

STI Technical Report No. 146-2

FEASIBILITY OF CONVENTIONAL CONTROL TECHNIQUES FOR LARGE HIGHLY COUPLED ELASTIC BOOST VEHICLES

(Final Report)

*Donald E. Johnston
Walter A. Johnson*

March 1967

N67-37786 (ACCESSION NUMBER)	(THRU)
197- (PAGES)	(CODE)
CR-88760 (NASA CR OR TXR OR AD NUMBER)	B2 (CATEGORY)

FACILITY FORM 608

Prepared under Contract No. NAS 8-11419 by
SYSTEMS TECHNOLOGY, INC.
Hawthorne, Calif.
for George C. Marshall Space Flight Center

NATIONAL AERONAUTICS AND SPACE ADMINISTRATION
Washington, D.C.

FEASIBILITY OF CONVENTIONAL CONTROL TECHNIQUES
FOR LARGE HIGHLY COUPLED ELASTIC BOOST VEHICLES

Donald E. Johnston and Walter A. Johnson

Distribution of this report is provided in the interest of information exchange. Responsibility for the contents resides in the author or organization that prepared it.

Prepared under Contract No. NAS8-11419 by
/SYSTEMS TECHNOLOGY, INC.
Hawthorne, Calif.

for Marshall Space Flight Center

NATIONAL AERONAUTICS AND SPACE ADMINISTRATION
Washington, D. C.

FOREWORD

This report was prepared under Contract NAS8-11419 between Systems Technology, Inc., Hawthorne, California, and the National Aeronautics and Space Administration, Marshall Space Flight Center. The NASA project monitor was Mr. J. R. Redus. The STI project engineer was Mr. D. E. Johnston. Technical direction was provided by Messrs. I. L. Ashkenas, D. Graham, and D. T. McRuer of STI.

The authors gratefully acknowledge the assistance of their colleagues, Messrs. F. R. Alex, J. A. Tennant, and G. L. Teper, in the accomplishment of this analysis. Special acknowledgment is due Mr. L. G. Hofmann of our Princeton, New Jersey, office who authored Appendix B and provided much help throughout the study. Finally, we are indebted to the STI production staff for their careful preparation of the final draft.

ABSTRACT

The report covers analytical feasibility studies for control of very large boost vehicles in which the elastic and fuel slosh modes have frequencies very near to the desired control frequencies and in which there is a great deal of intermodal coupling. Exact versus simplified equations of motion and conventional, unconventional, and advanced control system mechanizations are investigated. A relatively simple control system is synthesized which employs normal acceleration and attitude rate feedbacks to damp the elastic and rigid body modes throughout the boost phase of flight. Attitude control and load relief loops are closed about the damped vehicle. Stability and sensitivity measures are worked out for the vehicle/controller system synthesized. The use of normal acceleration to damp or suppress the vehicle elastic modes is the key to the success of the system synthesized and warrants further study.

CONTENTS

	<u>Page</u>
I. INTRODUCTION AND SUMMARY	1
II. COMPETING EQUATIONS OF MOTION	7
A. Simplified Equations	8
B. Sensor Numerators	13
C. Generation of Sensor Numerator Factors	19
D. Comparison of Transfer Functions	27
E. Summary and Conclusions	34
III. SYSTEM SYNTHESIS	35
A. Introduction.	35
B. Stabilization and Attitude Control System	38
C. Load Relief System.	70
IV. SENSITIVITY ANALYSIS	77
A. Determination of Potential Problem Areas	79
B. Sensitivity	84
C. Summary	90
V. ADAPTIVE MECHANIZATION CONSIDERATIONS	91
VI. CONCLUSIONS	97
REFERENCES	100
APPENDIX A. BASIC VEHICLE DATA	102
APPENDIX B. SIMPLIFIED EQUATIONS OF MOTION	122
APPENDIX C. SAWTOOTH BODE CONCEPT	132
APPENDIX D. PRELIMINARY ANALYSIS VIA SIMPLIFIED TRANSFER FUNCTIONS	137
APPENDIX E. SYSTEM SYNTHESIS WITH EXACT TRANSFER FUNCTIONS	153
APPENDIX F. THE USE OF BAFFLES TO DAMP SLOSH MODES.	164

FIGURES

	<u>Page</u>
1. Simplified Equation Model.	9
2. Simplified Characteristic Matrix Evaluated at t = 80 sec (q_{max})	15
3. Simple-Simplified Equation of Motion	16
4. Root Locus Sketch (Ref. 5)	21
5. Excursion of Numerator Roots With Inclusion of Successive Modes.	23
6. Simplified Versus Exact Pole/Zero Locations; $N\dot{\phi}_{46.5}/\beta$, t = 0 .	28
7. Simplified Versus Exact Pole/Zero Locations; $N\dot{\phi}_{46.5}/\beta$, t = 80. .	29
8. Simplified Versus Exact Pole/Zero Locations; $N\dot{\phi}_{46.5}/\beta$, t = 157 .	30
9. Simplified Versus Exact Pole/Zero Locations; $N\dot{z}_{46.5}/\beta$, t = 0 .	32
10. Simplified Versus Exact Pole/Zero Locations; $N\dot{z}_{46.5}/\beta$, t = 80. .	33
11. Block Diagram of Vehicle Stabilization and Control System . .	37
12. Normal Acceleration Feedback Loop	38
13. Attitude Rate Feedback Around Acceleration Stabilized Vehicle. .	39
14. Attitude Feedback Around Acceleration and Attitude Rate Stabilized Vehicle	40
15. Linear Acceleration Feedback Amplitude and Phase, t = 80 . . .	43
16. Root Locus for Acceleration Closure, t = 80.	44
17. Attitude Rate Feedback Amplitude and Phase, t = 80	46
18. Root Locus for Attitude Rate Closure, t = 80	47
19. Attitude Feedback Amplitude and Phase, t = 80	49
20. Root Locus for Attitude Closure, t = 80	50
21. Linear Acceleration Feedback Amplitude and Phase, t = 0. . . .	53
22. Root Locus for Acceleration Closure, t = 0	54
23. Attitude Rate Feedback Amplitude and Phase, t = 0.	56
24. Root Locus for Attitude Rate Closure, t = 0.	57
25. Attitude Feedback Amplitude and Phase, t = 0	59
26. Root Locus for Attitude Closure, t = 0	60
27. Attitude Rate Feedback Amplitude and Phase, t = 157	62
28. Root Locus for Attitude Rate Closure, t = 157	63
29. Attitude Feedback Amplitude and Phase, t = 157.	66
30. Root Locus for Attitude Closure, t = 157.	67
31. Gain Values as a Function of Time	68

32.	Load Relief Acceleration Feedback Amplitude and Phase.	71
33.	Root Locus for Load Relief Closure	72
34.	Wind Shear Input	73
35.	Closed-Loop Time Response to Wind Shear Input	75
36.	Typical Notch Filter Dynamics.	92
37.	Effect of Notch Width on Phase Characteristics	93
38.	Typical Pole/Zero Cancellation Effect	94
39.	Modal Separations: Exact-Coupled Equations	96
A-1.	Model Vehicle No. 2	107
A-2.	Simplified Characteristic Matrix at $t = 0$ sec	108
A-3.	Summary of Simplified Gyro Numerators and Mode Slopes, $t = 0$.	109
A-4.	Summary of Simplified Accelerometer Numerator Factors and Mode Amplitudes, $t = 0$	110
A-5.	Simplified Characteristic Matrix at $t = 80$ sec	111
A-6.	Summary of Simplified Gyro Numerators and Mode Slopes, $t = 80$.	112
A-7.	Summary of Simplified Numerator Factors and Mode Amplitude, $t = 80$	113
A-8.	Simplified Characteristic Matrix at $t = 157$ sec.	114
A-9.	Summary of Simplified Gyro Numerators and Mode Slopes, $t = 157$.	115
A-10.	Simplified Accelerometer Numerator Factors and Mode Amplitudes, $t = 157$	116
A-11.	Bending Mode Slopes	117-120
A-12.	Engine and Angle of Attack Moments, $t = 78$ sec	121
B-1.	Simplified Equation Model	123
B-2.	Simplified Characteristic Matrix.	127
C-1.	Simple Unity-Feedback System	132
C-2.	Root Locus Diagram	132
C-3.	Open-Loop Amplitude Bode Plot.	133
C-4.	Booster Control System Block Diagram	134
C-5.	Original Controller-Servo-Airframe Open-Loop Bode Plot	135
C-6.	Modified Controller-Servo-Airframe Open-Loop Bode Plot	136
D-1.	Locus of Zeros.	139
D-2.	Survey Plot for Pure Rate Feedback, $t = 80$	145
D-3.	Generation of Numerator Roots for Rate Gyro; $x_G = 46.5$ m, $t = 80$ sec	146
D-4.	Block Diagram for Dual Gyro Sensing.	148

D-5.	Numerator Roots of the Summed Gyro Feedback Transfer Function as a Function of Relative Gyro Gain; 2 Gyros - Location No. 1 ($x = 46.5$ m) and Location No. 4 ($x = 88.5$ m).	150
E-1.	System B, $t = 80$ sec; $\dot{\phi}_{46.5}$ Loop Closure	156
E-2.	System B, $t = 80$ sec; $\dot{\phi}_{46.5}$ Root Locus.	157
E-3.	Effective Vehicle Dynamics for $\phi_{120.5}$ Feedback; $t = 80$ sec	158
E-4.	Root Locus for Unity Feedback; $\phi_{120.5}$; $t = 80$ sec	159
E-5.	System B, $t = 157$, $\dot{\phi}_{46.5}$ Loop Closure Bode	160
E-6.	System B, $t = 157$, $\dot{\phi}_{46.5}$ Root Locus.	161
E-7.	System B, $t = 157$, $\dot{\phi}_{120.5}$ Loop Closure Bode	162
E-8.	System B, $t = 157$, $\phi_{120.5}$ Root Locus	163
F-1.	Root Locus of Slosh Mode Region for Accelerometer (at 46.5) Loop at $t = 80$.	165
F-2.	Root Locus of Slosh Mode Region for Rate Gyro (at 46.5) Loop at $t = 80$.	166
F-3.	Root Locus of Slosh Mode Region for Accelerometer (at 46.5) Loop at $t = 0$.	167
F-4.	Root Locus of Slosh Mode Region for Rate Gyro (at 46.5) Loop at $t = 0$.	168
F-5.	Effect of Lower Tank Baffling on the Simplified Pole/Zero Locations; $t = 80$.	174
F-6.	Slosh Damping as a Function of Wave Amplitude	177
F-7.	Determination of Damping Due to Phasing from Root Locus	178

TABLES

	<u>Page</u>
I. Comparison of Denominator Roots.	12
IIa. Gyro Numerators (Simplified Versus Exact); $x_G = 46.5m$	17
IIb. Gyro Numerators; $x_G = 120.5m$	18
III. Accelerometer Numerators; $x = 46.5m$	20
IV. Comparison of Numerator Roots Obtained by Three Techniques.	87
A-I. Summary of Parameter and Coefficient Values.	103-106
B-I. Nomenclature for Simplified Characteristic Matrix.	128
D-I. Magnitude Criteria for Achieving Sawtooth Bode Form	142
E-I. Summary of System B Feedback Shaping	155
F-I. Numerical Values for Model Vehicle No. 2 Second Slosh Mode at $t = 80$ (Ref. 1)	172
F-II. Summary of Results	175

SYMBOLS

a_z	Normal acceleration as sensed by linear accelerometer
A_i } A_{η_i} }	Lead coefficient of the uncoupled i^{th} bending mode numerator
A_{S_j}	Lead coefficient of the uncoupled j^{th} slosh mode numerator
$A_{\ddot{z}}$	Lead coefficient of \ddot{z}/β numerator
A_{Δ}	Lead coefficient of transfer function denominator
A_{ϕ}	Lead coefficient of ϕ/β numerator
c	Number of main engines gimbaled in a single plane
$D_H()$	Denominator of feedback shaping transfer function
F	Total number of main engines
\bar{g}	Longitudinal acceleration of vehicle = $(T-X)/M$
$H_{a_z}(s)$	Feedback shaping transfer function for normal acceleration damping loop
$H_{\phi}(s)$	Feedback shaping transfer function for attitude loop
$H_{\dot{\phi}}(s)$	Feedback shaping transfer function for attitude rate loop
I	Moment of inertia of vehicle, including <u>nonsloshing</u> propellant components and engines
I_E	Moment of inertia of a single main engine about its gimbal point
$\bar{K}()$	Feedback gain
l	Length, in general measured positive in forward direction from total vehicle or vehicle component CG to point indicated by subscript
m	Meter, unit of distance or length
M	Total mass of vehicle
$M()$	Generalized mass of the mode, particularized by the subscript
MB	Bending moment
M_{α}'	Aerodynamic pitching moment due to angle of attack

M_{β}'	Pitching moment due to engine deflection
$N_{az}(\)$ N_{zA}''	Numerator of vehicle normal acceleration transfer function at accelerometer location
$N_H(\)$	Numerator of feedback shaping transfer function
N_{α}	Aerodynamic normal force derivative
$N_{\phi G}$	Numerator of vehicle attitude transfer function at gyro location
q	Dynamic pressure
t	Time in seconds
T	Total thrust of main booster engines (for the active stage)
\bar{V}	Nominal flight path velocity
w	Component of wind velocity parallel to Z axis
W	Wind velocity
x	Coordinate in direction of weighted average vehicle center line, positive forward
X	Total axial aerodynamic force acting on vehicle
X	Flight path angle measured from the vertical
$Y_i(x)$	Normalized amplitude of i^{th} bending mode deflection at station x . Normalization may be made in an arbitrary way. Customary ways include choosing the normalization factors such that the generalized mass of each mode equals the total system mass; normalization such that $Y_i(x)$ at a particular station is the same arbitrarily chosen value for all modes. MSFC uses the latter method, defining all modal amplitudes to the +1.0 at the main engine gimbal station, x_{β} .
$Y_j(x)$	Normalized amplitude of the j^{th} slosh pseudomode at station x
$Y(j\omega)$ $Y(-\sigma)$	} Open-loop transfer function with s replaced by $j\omega$ and $-\sigma$, respectively
z_{sj}	Generalized displacement coordinate in the vehicle system of the fundamental sloshing modal mass in the j^{th} propellant tank
z_1	Generalized displacement of the vehicle mass independent of the slosh mass
Z	Generalized coordinate of the vehicle system in the quasi-inertial axis system; X, Y, Z . Translation of weighted average vehicle centerline from nominal flight path of vehicle.

α	Angle of attack of weighted average centerline
β	Generalized coordinate of vehicle system. Rotation of main engine centerlines from the deflected vehicle centerline tangent at the main engine gimbal station.
β_c	Commanded value of β at position servo output
Γ_j	See Eq. B-9
$\Delta(s)$	Denominator of open-loop vehicle transfer function
$\Delta'(s)$	Effective denominator of closed-loop vehicle transfer function; the number of primes indicates the number of loop closures
ζ	Damping ratio, particularized by the subscript
η_i	Generalized displacement coordinate of the vehicle system in the i^{th} mode of the local booster structure from the weighted average vehicle centerline
λ_j	See Eq. B-10
ϕ	Generalized coordinate of the vehicle system in the quasi-inertial axis system; X,Y,Z. Rotation of the weighted average vehicle centerline from the nominal flight path direction, X axis.
ψ_j	See Eq. B-10
ω	Undamped natural frequency, particularized by the subscript

Subscripts:

A	Accelerometer location
cp	Aerodynamic center of pressure
CG	Center of gravity
E	Main engine or engines
G	Location of gyro of IMU
i	Index indicating the i^{th} bending mode
sj	Indicates the first sloshing mode of the fluid in the j^{th} propellant tank
TWD	Abbreviation for Tail-Wags-Dog
β	Main engine gimbal location

Special Notation:

($\dot{\quad}$) Derivative of quantity with respect to time

(\prime) Derivative of quantity with respect to x

SECTION I

INTRODUCTION AND SUMMARY

This report presents the results of a research study accomplished under Marshall Space Flight Center Contract NAS8-11419, "Control Study for Reduced Bending Frequencies and Increased Coupling for Rigid and Elastic Modes." The contract covers analytical studies of the control of large space boosters for which the elastic and fuel slosh modes have frequencies very near to the desired control frequencies, and for which there is a great deal of intermodal coupling. The basic objectives of this study are:

- The development of a model of the vehicle dynamics which can provide the control engineer with the physical insights into the modal coupling and vehicle characteristics which are necessary for a solution of this complex control problem.
- The determination of the limits of conventional control systems for this general class of vehicle, and to provide guidelines for determining what degree of vehicle dynamic complexity requires more advanced control techniques.
- The evaluation of advanced control concepts for solution of the stability and control problems for the extreme cases in which conventional techniques are inadequate.

The Marshall Space Flight Center "Model Vehicle No. 2" serves as the study vehicle.

The first objective was accomplished and is documented in Ref. 1. The second and third objectives, which relate to the analysis and synthesis of stabilization, control, and load relief systems for the Model Vehicle No. 2, are the subject of this report.

The work has been directed along three major subdivisions: Competing equations or vehicle models, competing control systems, and sensitivity analysis. The three are interrelated to a considerable extent but will be discussed separately here.

a. Competing equations. In past and present boost vehicles intermodal coupling terms in the equations of motion have been sufficiently small that coupling effects could be drastically simplified, if not completely ignored, during a major portion of the systems synthesis work. Since the Model Vehicle No. 2 purposely exhibits extreme coupling, it is pertinent to the program objectives to investigate whether this approach remains valid for the class of vehicles represented and, if not valid, to define the limitations of the approach. The competing equation study is thus addressed to obtaining answers to the questions posed.

From a system synthesis standpoint the "competing equations" consist of the exact or coupled (Ref. 1) and the simplified or uncoupled (Appendix B). The initial thinking was that the simplified, uncoupled transfer functions could be employed in the preliminary system synthesis work and that the coupling corrections or even the exact transfer functions could be brought into play in later system refinement stages. The system synthesis was initiated along these lines. When the exact transfer functions became available, comparison of the exact and simplified factors presented surprising results: the vehicle numerator and denominator factors were in fair agreement while sensor numerator factors were in remarkably close agreement. At first this led to considerable optimism. Unfortunately, closer scrutiny revealed that, in the many instances where pole/zero separation was slight, the simplified factors could not be relied upon to indicate the correct pole/zero sequence. Since the simplified equations of motion, and hence transfer functions, were obtained via a mathematical manipulation (change of variable), faith in the simplified transfer functions faded and it was decided that the excellent agreement of the sensor numerators was partly coincidental. Thus the simplified approach was abandoned and all system synthesis proceeded with the more unwieldy exact expressions. Faith was restored in the simplified equations only after the coupling approximations (Ref. 1) were worked out and the necessary physical understanding of the coupling phenomena achieved.

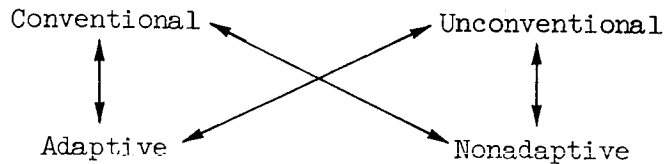
The findings of this portion of the investigation may be briefly summarized as follows:

- With few exceptions, the simplified transfer functions are adequate for preliminary system synthesis work.
- The approximate expressions of Ref. 1 can be used either to formulate an intermediate set of coupled transfer function factors for the exceptions or to provide insight to the effects coupling will have on the poles and zeros obtained via simplified equations.
- The sensor numerator zeros obtained from the simplified equations of motion are generally in better agreement with the exact sensor zeros than are the simplified and exact poles in agreement. The reason for this is not yet fully understood, but it is believed to be due to the sensor coupling being much stronger than the vehicle intermodal coupling.
- The pole/zero separation which results when the simplified transfer function factors are employed provides an automatic basis for determining the validity of the simplified transfer functions in system synthesis. That is, if the simplified transfer functions indicate moderate to large pole/zero separation for any mode, the simplified expressions may be safely employed. But, if the pole/zero separation is small for any mode, the exact transfer functions should be used because small differences may reverse the pole/zero order of the mode.
- Sensor numerators generated from the simplified equations of motion via the "successive loop closure" technique (Ref. 2) are very helpful in identifying the origin of the individual sensor numerator zeros, and hence in assessing the effects of changes or uncertainties in vehicle characteristics or sensor location.

b. Competing systems. One of the major interests of the study is to define the limitations and/or limiting factors in the application of conventional control techniques to flexible vehicles of a general class as represented by Model Vehicle No. 2. Another major interest is in determining the feasibility of elastic mode suppression via the control system, as opposed to present concepts of eliminating the modes from the feedback. A third interest lies in determining the requirements for, and potential of, advanced control techniques in stabilizing and controlling vehicles akin to Model Vehicle No. 2.

For the purpose of this study "conventional" is defined to represent the feedback (sensor, equalization, filtering) from the viewpoint of current performance-verified hardware in, or nearing, use on boost vehicles. "Unconventional" is defined to be any other feedback (sensor, equalization, filtering) which may, or may not, be proven in hardware or principle on any other vehicle. "Adaptive systems" are defined to be those mechanizations exhibiting any self-adjustment of internal controller parameters based on in-flight, self-measured vehicle or controller closed-loop dynamic characteristics.

Based on the above, we can construct a structure for system designation of the form shown below:



In this scheme, any system mechanization can be identified by two words. The possible combinations are indicated by the interconnecting arrows.

Although the above goals were achieved at a preliminary design or feasibility level, the effort was not as straightforward as hoped for because of the obvious difficulty in stabilizing a vehicle especially contrived by MSFC personnel to not yield to present-day control techniques. Several approaches had to be abandoned before a workable (unconventional nonadaptive) system emerged. Synthesis procedures were carried through for this system at three flight conditions: lift off ($t = 0$ sec), maximum q ($t = 80$ sec), and preburnout ($t = 157$ sec).

The conclusions from this portion of the study are:

- The general class of vehicles typified by MSFC Model Vehicle No. 2 does exceed the capabilities of conventional control techniques.
- Vehicles of this general class can be expected to require phase stabilization of all modes up to, and including, the fourth bending mode.

- Due to the extreme proximity of all modes from rigid-body through the fourth bending plus the above phase stabilization requirement, conventional feedbacks (attitude and attitude rate obtained from the attitude gyro) and state-of-art adaptive schemes are inadequate.
- A technical breakthrough will be required in isolating and identifying modes with less than a factor of 1.5 frequency separation before adaptive notch filtering devices will show promise.
- The use of dual gyro blending does not appear promising for vehicles of this type because more than a single flexible mode must be phase-stabilized.
- The unconventional use of lagged normal acceleration feedback looks extremely promising to suppress the vehicle flexible modes and is the key to the successful stabilization and control systems synthesized in this study.
- Some baffling of fuel tanks will be required regardless of the control system mechanization employed.

c. Sensitivity Analysis. Once the control system is synthesized it is desirable to establish the system sensitivity to change in vehicle or controller dynamic parameters, and to relate these changes to physical characteristics. Here we are interested mainly in those factors which result in major (or critical) deviations. Primarily, interest is centered on the sensitivity of closed-loop stability and/or controller mechanization to (1) variations in open-loop poles (zeros) or (2) the principal factors contributing to the open-loop poles (zeros).

It was determined that a generalized sensitivity study (e.g., Ref. 3) is impractical in the face of the complexity of the Model Vehicle No. 2 dynamics. For vehicles of this type the sensitivity considerations should be tailor-made to the specific problems on an individual basis.

The approach taken here is to identify, qualitatively and on the basis of the system synthesis plots, the potentially critical stabilization areas. In all instances these involve pole/zero pair having little frequency separation where either pole/zero sequence reversal can easily occur or increased separations would result in loss of amplitude ratio cancellation and, hence, gain margin. Simple sensitivity measures were then worked out and related to vehicle physical characteristics.

The results of this portion of the study indicate:

- The "successive closure technique" and the simplified (uncoupled) vehicle transfer function factors are a valuable tool in determining the sensitivity of the controller/vehicle system to changes in the vehicle characteristics.
- The unconventional control system synthesis is sensitive to location of the aftmost node and antinode of the third bending mode at lift-off and burnout, respectively.

d. Organization of the Report. Section II presents the simplified (uncoupled) vehicle equations of motion and a quantitative comparison of transfer function factors obtained via the simplified and exact (Ref. 1) equations. The successive loop closure technique is employed to generate and identify example numerator zeros for an attitude rate sensor. The synthesis of the stabilization, control, and the load relief system is discussed in Section III. Potential problem areas are outlined and system sensitivity measures are developed in Section IV. Section V contains a brief discussion of adaptive techniques investigated. Section IV presents conclusions of the study. Support material for the discussion in the body of the report are presented in the Appendixes along with some preliminary (and some unsuccessful) system synthesis studies.

SECTION II

COMPETING EQUATIONS OF MOTION

A fundamental requirement for the quantitative analysis of any control system is that the dynamic phenomena in the controlled element (the booster airframe in this case) be described in sufficient detail. This is not to say that the controlled element must necessarily be described in painstaking detail, but it does imply that all major dynamic mechanisms involved must be adequately described.

In past and present boost vehicles, intermodal coupling terms in the equations of motion have been sufficiently small that coupling effects could be drastically simplified, if not completely ignored, during initial portions of the systems synthesis work. Since the Model Vehicle No. 2 purposely exhibits extreme coupling, it is pertinent to the program objectives to investigate whether this approach remains valid for the class of vehicles represented and, if not valid, to define the limitations of the approach. This section is thus addressed to obtaining answers to the questions posed (validity/limitations).

From a systems synthesis standpoint the "competing equations" consist of the exact or coupled (Ref. 1) and the simplified or uncoupled (Appendix B). The simple models need only be accurate enough to reveal the major real effects of bending mode parameters on vehicle transfer function poles and zeros. Fortunately, simple models which meet this criterion are available and will be described shortly. Because these simple models can be expressed and analyzed in literal terms, they provide an immediate physical understanding of the relationships among the most important stability derivatives and structural parameters. The exact models provide final numerical verification of system stability and performance; and intermediate models may be required to explain "exact" effects not adequately covered by the simple model. These also are available in Ref. 1.

Since the objective of the study is not simply to design a control system for a specific vehicle, but rather to investigate control problems for certain vehicle types, the development of a physical understanding of

the key parameters and their effects is essential to provide a degree of generality in the results. This physical understanding is particularly critical in this study because the main objective is to determine, in general, which flexible mode parameters are critical in determining the stability of the system, and how variations in these parameters can be compensated for in the controller. There is no real substitute for the use of simple models to develop an understanding of the problem. The only alternative is a gigantic computer orgy which yields a solution for the particular vehicle being considered. In that case, the results have little generality and any changes in the vehicle characteristics would require another knob-twirling session. Thus, the simple models become the key to the successful completion of this program.

A. SIMPLIFIED EQUATIONS

A quick perusal of the exact booster equations of motion is generally sufficient to discourage even the bravest from pursuing an analysis in literal terms which attempts to retain a reasonably accurate description of the dynamic phenomena of the controlled element. How else then can any analysis be made which retains the elements of a physical "feel" for the problem?

Fortunately, there is a method (Ref. 4) for simplifying the booster dynamics in an analytically convenient manner while retaining adequate accuracy. In these simplified equations the modes are uncoupled and the booster dynamics can be represented by a block diagram of the form shown in Fig. 1. The assumptions which are necessary to produce the decoupled form of Fig. 1 are given in Appendix B together with the simplified equations and a list of symbols.

For convenience, the Laplace-transformed simplified equations of motion are summarized below.

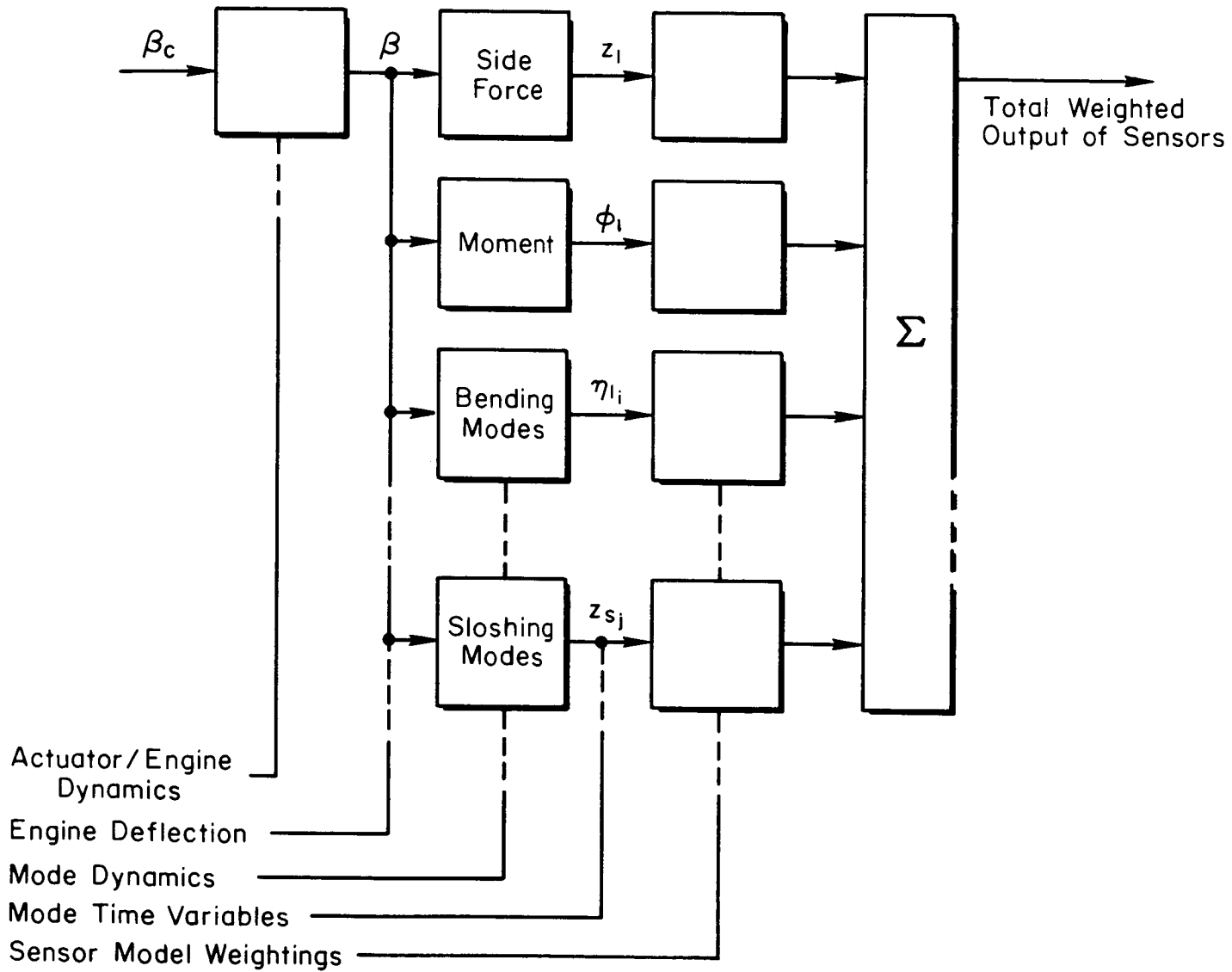


Figure 1. Simplified Equation Model

$$\left(s^2 + \frac{N_\alpha}{M\bar{V}} s\right) z_1 = \frac{cM_{E1E}}{M} \left(s^2 + \frac{T}{FM_{E1E}}\right) \beta + \frac{N_\alpha}{M\bar{V}} w$$

$$\left(s^2 - \frac{N_\alpha l_{cp}}{I}\right) \phi_1 = \frac{cM_{E1E}}{I} \left[-(-1\beta) \left\{ 1 + \frac{I_E}{M_{E1E}} \frac{1}{(-1\beta)} \right\} \right]$$

$$\left[s^2 + \frac{T}{FM_{E1E}} \left\{ \frac{1}{1 + \frac{I_E}{M_{E1E}} \frac{1}{(-1\beta)}} \right\} \right] \beta + \frac{N_\alpha l_{cp}}{I\bar{V}} w$$

$$\left(s^2 + \omega_{sj}^2\right) z_{sj} = \frac{cM_{E1E}}{M_{sj}} \left[Y_j(x_\beta) \left\{ 1 - \frac{I_E}{M_{E1E}} \frac{Y_j'(x_\beta)}{Y_j(x_\beta)} \right\} \right]$$

$$\left[s^2 + \frac{T}{FM_{E1E}} \left\{ \frac{1}{1 - \frac{I_E}{M_{E1E}} \frac{Y_j'(x_\beta)}{Y_j(x_\beta)}} \right\} \right] \beta + \frac{N_\alpha Y_j(x_{cp})}{M_{sj}\bar{V}} w$$
(1)

$$\left(s^2 + \omega_i^2\right) \eta_{i1} = \frac{cM_{E1E}}{M_i} \left[Y_i(x_\beta) \left\{ 1 - \frac{I_E}{M_{E1E}} \frac{Y_i'(x_\beta)}{Y_i(x_\beta)} \right\} \right]$$

$$\left[s^2 + \frac{T}{FM_{E1E}} \left\{ \frac{1}{1 - \frac{I_E}{M_{E1E}} \frac{Y_i'(x_\beta)}{Y_i(x_\beta)}} \right\} \right] \beta + \frac{N_\alpha Y_i(x_{cp})}{M_i\bar{V}} w$$

$$(s^2 + 2\zeta_E \omega_E s + \omega_E^2) \beta = \omega_E^2 \beta_c$$

In the simplified equations,

1. The variables z_1 , ϕ_1 , and η_{i1} are mathematically contrived from the "real" physical variables (Z , ϕ , η_i , and z_{sj}) to include certain important cross-couplings. Definitions of these variables are given in Eqs. B-1, B-3, and B-4.
2. The transfer functions for all modes (rigid, elastic, and sloshing) have identical forms. This consists of a gain multiplying an undamped second-order numerator divided by an undamped second-order denominator.
3. The numerator factors, or tail-wags-dog zeros, for each mode are all approximately equal to $\sqrt{T/FM_{E1E}}$ if

$$\left| \frac{I_E}{M_E l_E l_\beta} \right|, \left| \frac{I_E}{M_E l_E} \frac{Y_i'(x_\beta)}{Y_i(x_\beta)} \right|, \text{ and } \left| \frac{I_E}{M_E l_E} \frac{Y_j'(x_\beta)}{Y_j(x_\beta)} \right|$$

are small with respect to unity.

4. The transfer function describing the compliance in the actuator/nozzle linkage appears as a factored portion of the booster dynamics.
5. On the basis of Item 3, the tail-wags-dog zeros may be factored out of the equations of motion and lumped with the compliance transfer function.

The accuracy of the simplified equations is surprisingly good for a vehicle of this type. Table I compares the roots of the transfer function denominator as determined by the simplified equations and by factorization of the exact equations of motion (Ref. 1). For this comparison, the simplified actuator dynamics were included with the compliance mode and factored via the "literal" approximation method of Ref. 1, i.e.,

$$1/T_a = K_1/A \quad (2)$$

$$\omega_a^2 = \omega_E^2 \left(\frac{K_0}{K_0 + K_L} \right) \quad (3)$$

$$2\zeta_a \omega_a = 2\zeta_E \omega_E + \frac{K_L}{A} \left(\frac{(K_0 K_3/A) - K_1}{K_0 + K_L} \right) \quad (4)$$

where K_1 = actuator open-loop gain
 A = effective actuator area
 K_0 = effective hydraulic spring constant
 K_L = effective spring constant of actuator/nozzle compliance

Despite the presence of four modes (three slosh and one bending) within a very narrow frequency band at each flight condition, the accuracy of the simplified equations is more than adequate for preliminary design synthesis procedures. The major discrepancy is within the lead coefficient (A_Δ), which is relatively unimportant from the standpoint of establishing system equalization (feedback shaping).

TABLE I
COMPARISON OF DENOMINATOR ROOTS

	LIFT-OFF		MAXIMUM q		BURNOUT	
	t = 0		t = 80		t = 157	
	Simplified	Exact	Simplified	Exact	Simplified	Exact
A_{Δ}	67	46.51	67	35.506	67	38.752
First-order	0	0	0	-0.042015	0	-0.01428
	0	0	-0.2692	-0.27859	-----	-----
	0	0	0.2692	0.36441	-----	-----
	14.04	14.563	14.04	14.516	14.04	14.142
ω_0	-----	-----	-----	-----	0.036	0.040733
ω_1	2.1564	2.0299	2.318	2.2338	2.915	3.4091
ω_2	2.1363	2.1316	2.76	2.7504	3.5814	3.6800
ω_3	2.1363	2.2211	2.76	3.0471	3.7699	4.0265
ω_4	2.1363	2.6066	2.83	3.1313	4.7124	4.9510
ω_5	5.0617	5.2894	5.645	6.0224	6.592	7.4185
ω_6	8.7826	9.1876	9.184	9.9440	11.711	11.858
ω_7	12.356	12.589	12.504	12.894	24.862	24.991
ω_8	47.09	47.040	47.09	47.526	47.09	52.504
ξ_0	-----	-----	-----	-----	0	0.17621
ξ_1	0	0.00445	0	0.01408	0	0.0039
ξ_2	0	0.00496	0	0.00497	0	0.0048
ξ_3	0	0.00519	0	0.00571	0	0.00432
ξ_4	0	0.00544	0	0.00870	0	0.00508
ξ_5	0	0.00479	0	0.00838	0	0.0028
ξ_6	0	0.00490	0	0.00712	0	0.00457
ξ_7	0	0.00495	0	0.00638	0	0.00525
ξ_8	0.1028	0.09843	0.1028	0.09864	0.1028	0.09795

Actually, the differences between the simple and exact models are probably within the minimum uncertainty band to be expected of future superlarge boost vehicle flexible mode data.

B. SENSOR NUMERATORS

1. Gyro Numerators

Because sensors such as gyros and accelerometers detect elastic as well as rigid-body motions, the equations for a sensor output usually contain several terms. For example, the angle sensed by a gyro at station x_G is

$$\varphi_G = \varphi + \sum_i Y_i'(x_G) \eta_i \quad (5)$$

Consequently the sensor numerator is the sum of several high-order numerators. In the simplified equations, the equivalent of Eq. 5 is (from Appendix B)

$$\begin{aligned} \varphi_G &= \varphi_1 + \sum_i Y_i'(x_G) \eta_{i_1} + \sum_j \left[Y_j' + Y_j(x_{CG}) \sum_i Y_i'(x_G) Y_i(x_{S_j}) \frac{M}{M_i} \right] z_{S_j} \\ &= \varphi_1 + \sum_i Y_i'(x_G) \eta_{i_1} + \sum_j \Gamma_j'(x_G) z_{S_j} \end{aligned} \quad (6)$$

where the additional terms arise from the use of the uncoupled variables, φ_1 and η_{i_1} .

While Eq. 5 contains fewer terms than Eq. 6, in the transfer function form each term in Eq. 6 is only an undamped second-order (tail-wags-dog term) over another undamped second-order; in fact, the numerators are usually sufficiently alike to be factored out of the summation, as illustrated in a forthcoming example. Consequently, it is easier to combine the terms when using Eq. 6; and it is far easier to determine what parameters are affecting the sensor zeros and where to locate the sensors. An example of the summation technique and the physical insights provided follows shortly.

Before showing a comparison of the simplified and exact sensor numerators, a comment on the accuracy of the simplified sensor numerators is appropriate. The earlier general comments on accuracy requirements

apply equally to system denominators and sensor numerators; the numerators need only be sufficiently accurate to expose major control problems and the important relationships among key parameters. An example of the simplified matrix obtained from evaluation of Eq. 1 at the maximum q flight condition ($t = 80$ sec) is shown in Fig. 2. The right side of this matrix represents the gain terms and tail-wags-dog zeros which result from strict evaluation of the terms within Eq. 1.

By making the further simplifying assumption that

$$\left[\frac{I_E}{M_E l_E} \left(\frac{1}{-l_\beta} \right) \right] ; \left[\frac{I_E}{M_E l_E} \left(\frac{-Y_i(x_\beta)}{Y_i(x_\beta)} \right) \right] ; \left[\frac{I_E}{M_E l_E} \left(\frac{-Y'_{sj}(x_\beta)}{Y_{sj}(x_\beta)} \right) \right] \ll 1$$

the gain coefficients are modified slightly and the tail-wags-dog zero becomes a constant term ($\omega_{TWD} = \sqrt{T/FM_E l_E} = 25.6$ at $t = 80$ sec). The resulting matrix, in literal form, is shown in Fig. 3 and is presented in evaluated form in Figs. A-2, A-5, and A-8 of Appendix A for each flight condition. The latter are used for all remaining discussions of the simplified equations.

Tables IIa and IIb compare gyro numerator zeros computed from the simplified (Eq. 6) and the exact (Eq. 5) transfer functions. Table IIa presents a comparison for the most aft sensor location allowable. Table IIb presents a comparison for the most forward sensor location. Again the agreement is quite good. In fact, with the sole exception of the tail-wags-dog zeros, the numerators are in better agreement than are the previously discussed denominators. The effect of this discrepancy will be discussed later when we consider the complete sensor transfer function.

2. Accelerometer Numerators

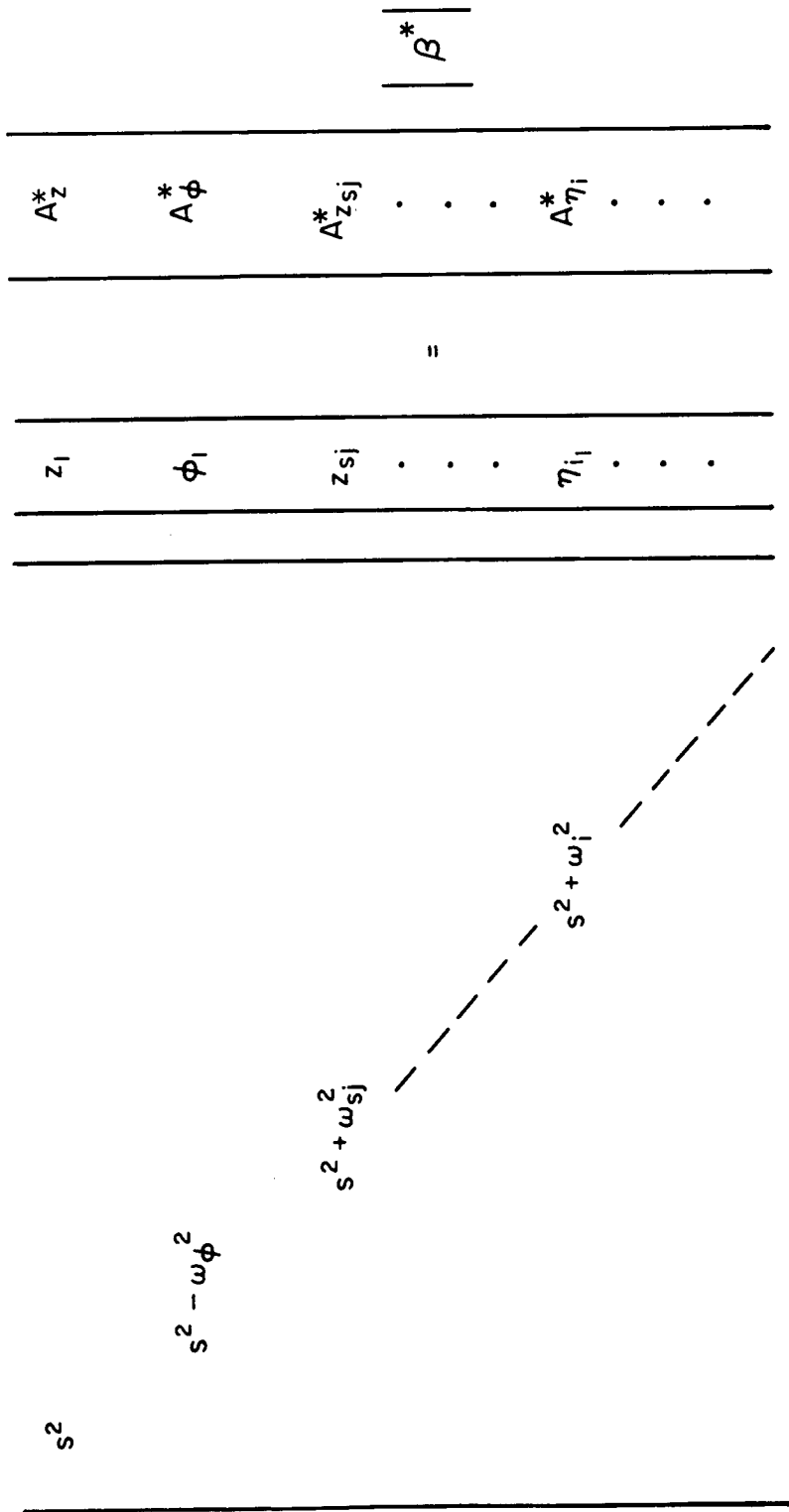
The acceleration sensed by a linear accelerometer at station x_A is

$$\ddot{z}_A = \ddot{z} + l_A \ddot{\phi} + \sum_i Y_i(x_A) \ddot{\eta}_i - \bar{g} \left[\phi + \sum_i Y'_i(x_A) \eta_i \right] \quad (7)$$

In the simplified equations, the equivalent of Eq. 7 is (from Appendix B)

s^2					
	$s^2 + (0.4047)^2$	z_1	0.01671	$\left\{ s^2 + (25.6)^2 \right\}$	
	$s^2 + (2.76)^2$	φ_1	-0.00074278	$\left\{ s^2 + (24.65)^2 \right\}$	
	$s^2 + (2.76)^2$	z_{s1}	-0.039764	$\left\{ s^2 + (25.05)^2 \right\}$	
	$s^2 + (2.76)^2$	z_{s2}	-0.024219	$\left\{ s^2 + (25.35)^2 \right\}$	
	$s^2 + (2.83)^2$	z_{s3}	-0.001744	$\left\{ s^2 + (32.8)^2 \right\}$	
	$s^2 + (2.318)^2$	η_{11}	0.021290	$\left\{ s^2 + (27.3)^2 \right\}$	
	$s^2 + (5.645)^2$	η_{21}	0.029092	$\left\{ s^2 + (28.02)^2 \right\}$	
	$s^2 + (9.184)^2$	η_{31}	0.032025	$\left\{ s^2 + (28.7)^2 \right\}$	
	$s^2 + (12.504)^2$	η_{41}	0.0052446	$\left\{ s^2 + (29.3)^2 \right\}$	
					$\left 10^{-5} \beta \right $

Figure 2. Simplified Characteristic Matrix Evaluated at $t = 80$ sec (q_{max})



$$A_z^* = \frac{1}{M} \quad K^* = c M E l E$$

$$A_\phi^* = \frac{l \beta}{I} \quad \omega_{TWD}^2 = \frac{T}{F M E l E}$$

$$A_{zsj}^* = \frac{Y_j(X\beta)}{M_{sj}} \quad \omega_\phi^2 = \frac{N a l c p}{I}$$

$$A_{\eta_i}^* = \frac{Y_i(X\beta)}{M_i} \quad \text{etc.}$$

$$\frac{\beta^*}{\beta_c} = \frac{K^* K_1 \omega_a^2 [s^2 + (\omega_{TWD})^2]}{(s + \frac{1}{T_a}) [s^2 + 2 \zeta_a \omega_a s + \omega_a^2]}$$

Figure 3. Simple-Simplified Equation of Motion

TABLE IIa

GYRO NUMERATORS (SIMPLIFIED VERSUS EXACT)

$x_G = 46.5m$

	<u>t = 0</u>		<u>t = 80</u>		<u>t = 157</u>	
	<u>Simplified*</u>	<u>Exact</u>	<u>Simplified*</u>	<u>Exact</u>	<u>Simplified*</u>	<u>Exact</u>
A_φ	2225	2961.9	1365	1561.5	-19,100	-16,554
First-order	0	0	0	0	0	0
	0	0	0	0.016	0	0.00007
	9.1125	7.8936	14.625	13.7	-----	-----
	-9.1125	-7.9444	-14.625	-13.7	-----	-----
ω_0	-----	-----	-----	-----	1.8599	2.2771
ω_1	1.5908	1.7239	1.6575	1.59	3.5586	3.5952
ω_2	2.1363	2.1144	2.7008	2.78	3.7519	3.7564
ω_3	2.1363	2.1738	2.76	2.78	4.7596	4.9528
ω_4	2.1377	2.2971	2.835	3.08	5.8939	6.1328
ω_5	5.3281	5.4684	5.6055	5.55	11.652	11.694
ω_6	11.047	11.192	11.481	11.4	25.815	27.048
ω_7	25.6	21.621	25.6	22.4	25.6	21.763
ξ_0	-----	-----	-----	-----	0	0.00261
ξ_1	0	0.00374	0	0.0213	0	0.00496
ξ_2	0	0.0043	0	0.0127	0	0.00502
ξ_3	0	0.00593	0	0.0026	0	0.00508
ξ_4	0	0.00515	0	0.0060	0	0.00504
ξ_5	0	0.00513	0	0.0094	0	0.00501
ξ_6	0	0.00506	0	0.0079	0	0.00446
ξ_7	0	0.00014	0	0.0006	0	0.00072

* Y_i' taken from discontinuous (unsmoothed) data

TABLE IIb
 GYRO NUMERATORS
 $x_G = 120.5m$

	<u>t = 0</u>		<u>t = 80</u>		<u>t = 157</u>	
	<u>Simplified*</u>	<u>Exact</u>	<u>Simplified*</u>	<u>Exact</u>	<u>Simplified*</u>	<u>Exact</u>
A_φ	-1073	1965.7	950	789.73	19,200	11,661
First-order	0	0	0	0	0	0
	0	0	0	0.00403	0	0.000082
	1.5608	1.599	1.6765	1.755	2.3962	3.0797
	-1.5608	-1.6125	-1.6765	-1.755	-2.3962	-3.1109
	-----	-----	-----	-----	-----	-----
ω_0	-----	-----	-----	-----	-----	-----
ω_1	2.1353	2.09	2.76	2.692	3.5776	3.5843
ω_2	2.1363	2.225	2.7615	2.9386	3.8096	3.785
ω_3	2.1363	2.225	2.8288	3.0074	4.6739	5.0271
ω_4	7.8711	7.26	9.4523	9.8171	12.298	12.171
ω_5	7.8711	7.27	9.4536	9.8293	10.550	12.310
ω_6	12.718	12.175	12.588	12.324	10.550	12.326
ω_7	25.6	21.9	25.6	23.025	25.6	19.647
ζ_0	-----	-----	-----	-----	-----	-----
ζ_1	0	0.0049	0	0.00308	0	0.005025
ζ_2	0	0.02145	0	0.01147	0	0.005
ζ_3	0	-0.01112	0	0.000797	0	0.0053
ζ_4	0.9144	0.797	0.89324	0.9088	0	0.005
ζ_5	-0.9144	-0.792	-0.89316	-0.90423	0.75755	0.82078
ζ_6	0	0.00499	0	0.009775	-0.75755	-0.81554
ζ_7	-----	-0.000004	-----	0.0001718	-----	0.0004

* Y_i^1 taken from discontinuous (unsmoothed) data

$$\begin{aligned}
\ddot{z}_A &= \ddot{z}_1 + 1_A \ddot{\phi}_1 + \sum_i Y_i(x_A) \ddot{\eta}_{i1} - \bar{g} \sum_i Y_i'(x_A) \eta_{i1} \\
&+ \sum_j \left[Y_j(x_A) + Y_j(x_{CG}) \sum_i Y_i(x_A) Y_i(x_{S_j}) \frac{M}{M_1} \right] \ddot{z}_{S_j} \\
&- \bar{g} \sum_j Y_j(x_{CG}) \sum_i Y_i'(x_A) Y_i(x_{S_j}) \frac{M}{M_1} z_{S_j} \\
&= \ddot{z}_1 + 1_A \ddot{\phi}_1 + \sum_i Y_i(x_A) \ddot{\eta}_{i1} - \bar{g} \left[\sum_j \lambda_j(x_A) z_{S_j} + \sum_i Y_i'(x_A) \eta_{i1} \right] + \sum_j \psi_j(x_A) \ddot{z}_{S_j}
\end{aligned} \tag{3}$$

where again the additional terms arise from the use of the uncoupled variables, ϕ_1 and η_{i1} .

The accelerometer numerators which result from Eq. 8 are tabulated in Appendix A for each allowable sensor location at each of the three flight conditions. For comparison purposes, Table III presents the numerator zeros computed from the simplified (Eq. 8) and the exact (Eq. 7) transfer functions at the most aft station allowable.

C. GENERATION OF SENSOR NUMERATOR FACTORS

As an illustration of the use of Eq. 6 to obtain numerator zeros, the following example determines the numerator for a gyro on the MSFC Model Vehicle No. 2 at maximum dynamic pressure. The forward location ($x_G = 120m$) is selected to illustrate an unfavorable phenomenon observed in Table IIb and in Ref. 5 — the appearance of two pairs of complex zeros with high (positive and negative) damping ratios, symmetrically placed about the imaginary axis. These zeros can be clearly seen in Fig. 4, which is a sketch of a root locus plot taken from Ref. 5. A similar situation will occur in the example.

The sensor numerator will be determined from Eq. 6, i.e.,

$$\Phi_G = \phi_1 + \sum_i Y_i'(x_G) \eta_{i1} + \sum_j \Gamma_j'(x_G) z_{S_j} \tag{9}$$

The second-order zeros of the individual terms are sufficiently close

TABLE III

ACCELEROMETER NUMERATORS

$x = 46.5m$

	<u>t = 0</u>		<u>t = 80</u>		<u>t = 157</u>	
	<u>Simplified*</u>	<u>Exact</u>	<u>Simplified*</u>	<u>Exact</u>	<u>Simplified*</u>	<u>Exact</u>
A_z	-64,500	-21,286	-43,100	-40,293	132,000	71,546
First-order	0	0	0	0	0	0
	0	0	0	-0.0408	0	-0.0191
	0	-0.0046	-0.3002	-0.5889	-0.025	-0.06672
	0	0.0046	0.3002	0.6802	0.025	0.08288
	2.3786	1.8115	3.431	3.1835	-----	-----
	-2.3786	-1.8241	-3.431	-3.2243	-----	-----
ω_0	-----	-----	-----	-----	2.938	3.1704
ω_1	2.1331	2.1047	2.76	2.744	3.559	3.630
ω_2	2.1363	2.107	2.809	2.749	3.730	3.7109
ω_3	2.1363	2.2133	2.943	2.950	4.607	4.9067
ω_4	2.5860	3.7912	3.156	3.3107	7.457	8.1619
ω_5	6.8760	9.1319	8.526	8.943	12.749	13.184
ω_6	11.971	15.084	13.172	13.20	29.478	37.059
ω_7	25.6	22.208	25.6	23.4	25.6	21.365
ξ_0	-----	-----	-----	-----	0	0.00383
ξ_1	0	-0.02323	0	0.036	0	0.00484
ξ_2	0	0.03380	0	-0.028	0	0.00515
ξ_3	0	0.00439	0	0.0084	0	0.00507
ξ_4	0	0.00502	0	0.0145	0	0.00574
ξ_5	0	0.00518	0	0.0135	0	0.00565
ξ_6	0	0.0055	0	-0.0024	0	0.00605
ξ_7	0	0.00022	0	0.0045	0	0.00119

* y_i' from discontinuous data

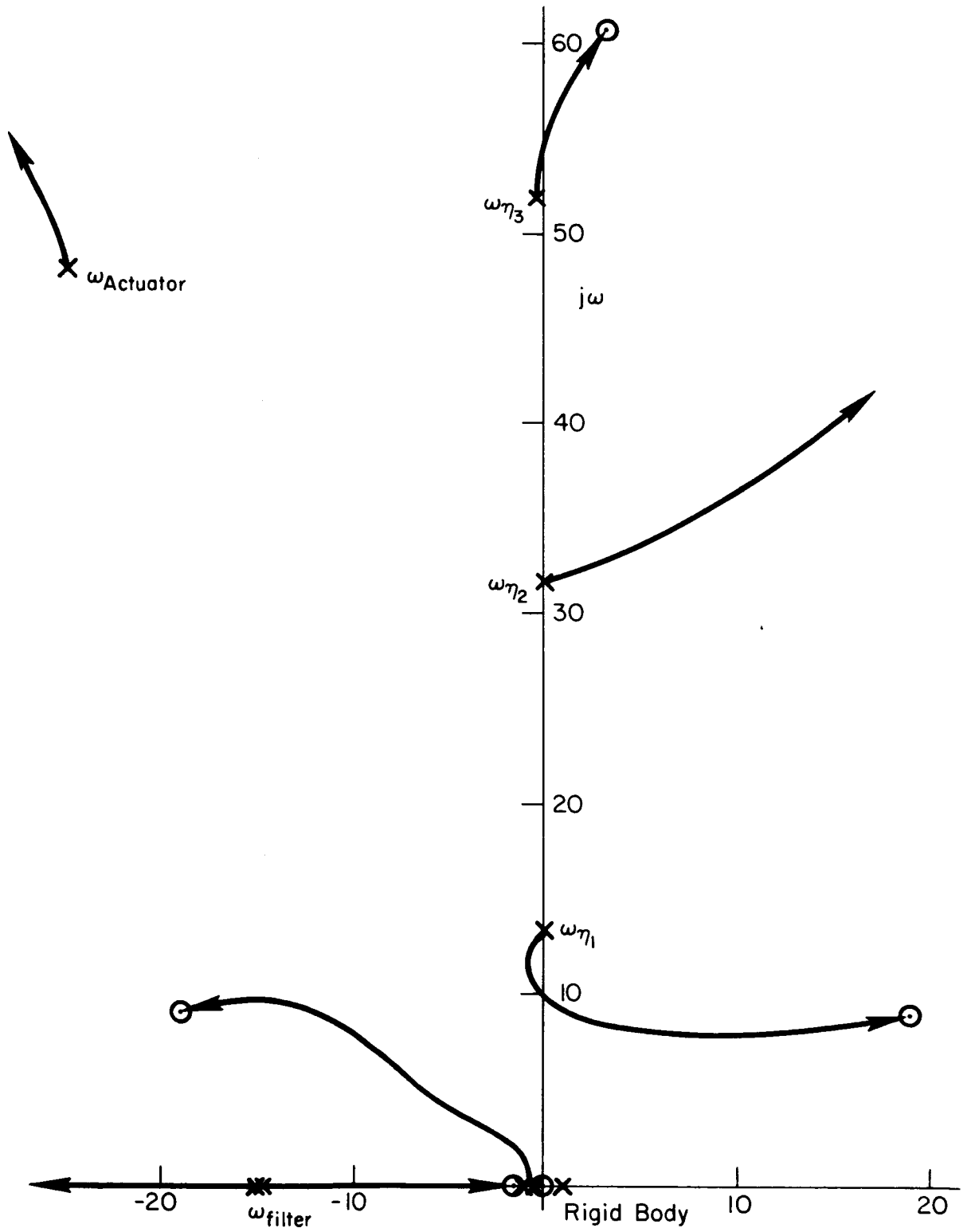
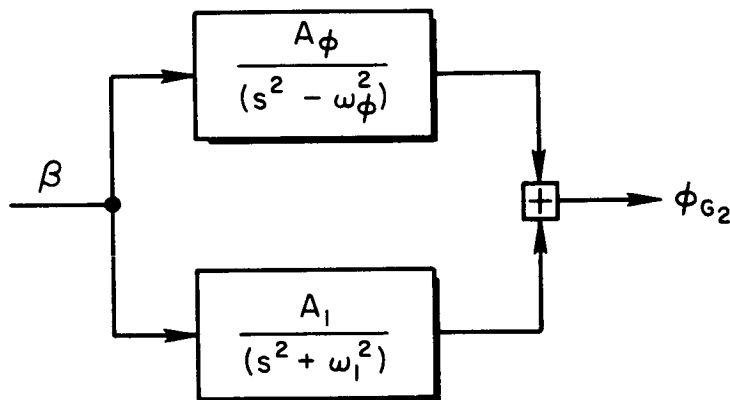


Figure 4. Root Locus Sketch (Ref. 5)

together to allow them to be factored out as a common element. Then each term of the summation becomes simply a gain and a second-order undamped root. The sum of the first two terms will be a second-order numerator with a fourth-order denominator. Each additional term will shift the zeros and increase the numerator and denominator order by 2. The final summation of the rigid-body, four bending, and three slosh modes will have a fourteenth-order numerator.

Summing the terms in the order of increasing frequency, the first two modes are rigid-body and first bending. Thus, one obtains



$$\begin{aligned}
 N_{\phi_{G2}} &= [A_{\phi}(s^2 + \omega_1^2) + A_1(s^2 - \omega_{\phi}^2)] \\
 &= A_{\phi}(s^2 + \omega_1^2) \left[1 + \frac{A_1(s^2 - \omega_{\phi}^2)}{A_{\phi}(s^2 + \omega_1^2)} \right] \\
 &= (A_{\phi} + A_1)(s^2 - \omega_1^{*2})
 \end{aligned}$$

where the closed-loop poles of the expression in the brackets are the desired roots, ω_1^* , of the numerator. The locus of roots is shown in Fig. 5a as a function of the gain parameter

$$\frac{A_1}{A_{\phi}} = \frac{Y_1(x_{\beta})Y_1'(x_G)I}{l_{\beta}M_1}$$

The specific roots for the selected gyro location are indicated by the solid rectangles (■) in Fig. 5a. The excursion of the roots can be better shown by employing the Bode/Siggy (Ref. 6) sketched below. It is of interest to note here that, for example, either decreasing the first bending mode

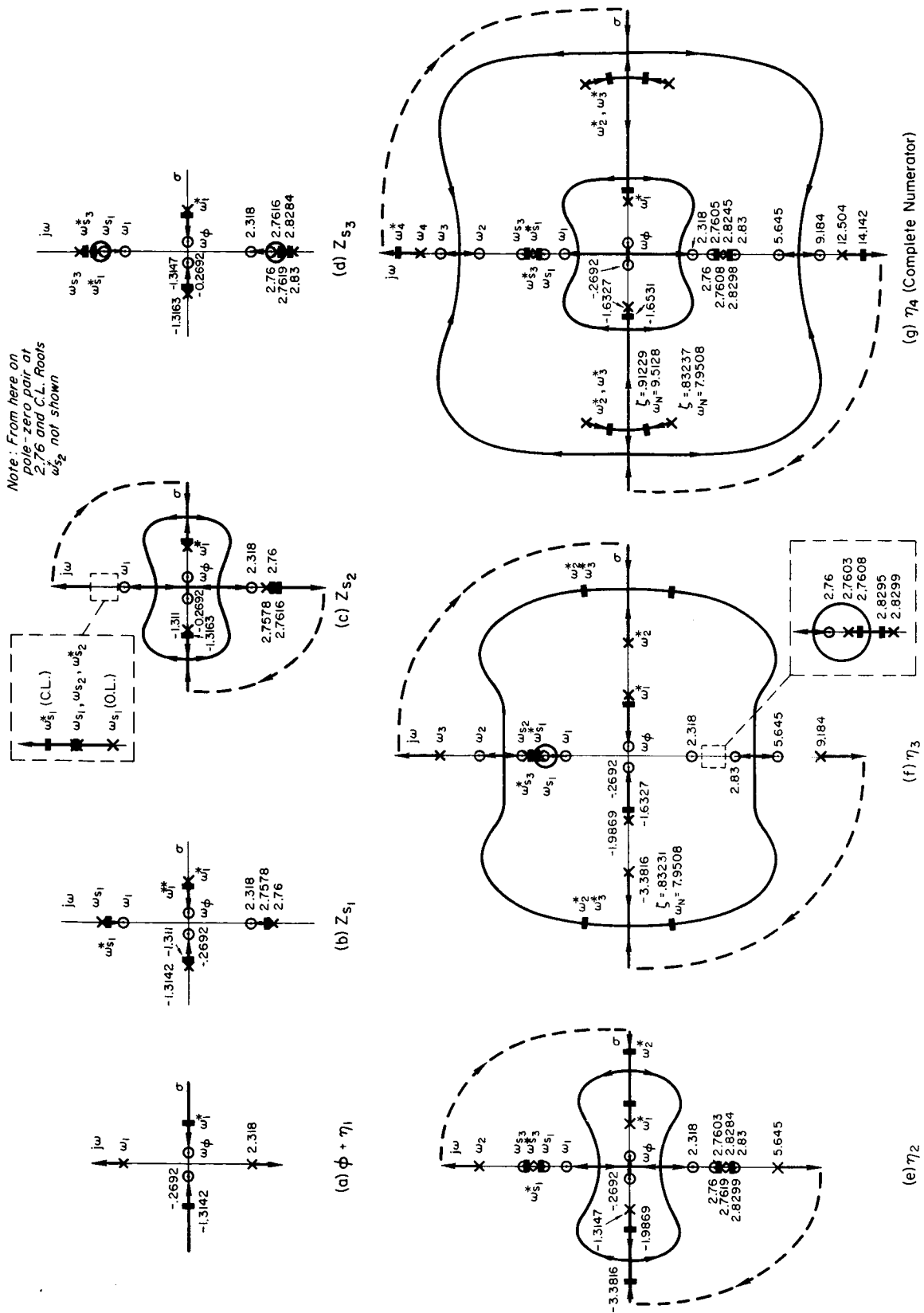
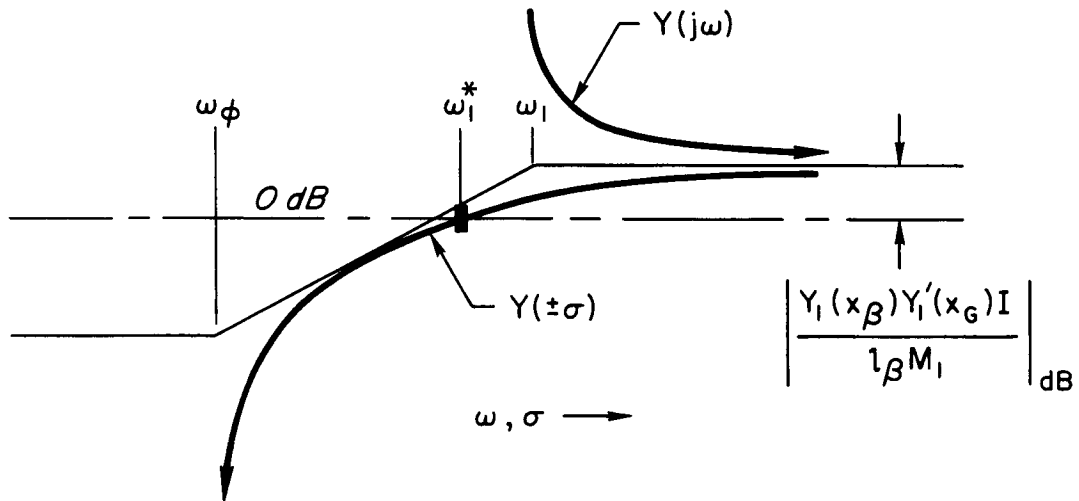


Figure 5. Excursion of Numerator Roots With Inclusion of Successive Modes

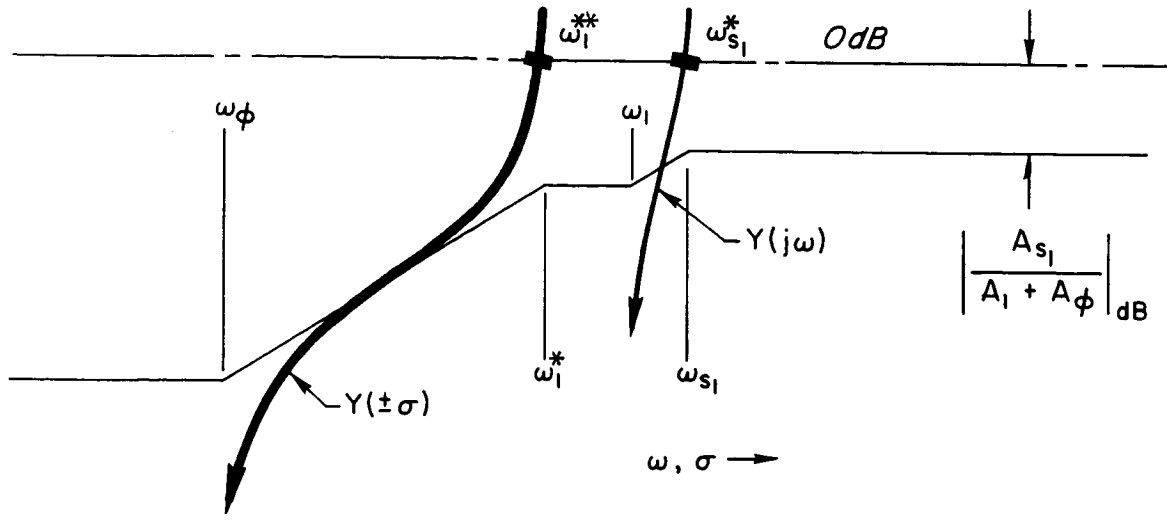
frequency or increasing the slope of the first bending mode at the gyro, $Y_1'(x_G)$, will move ω_1^* to lower frequencies. However, any change that effects a lowering of the gain A_1/A_ϕ will rapidly move ω_1^* to much higher frequencies.



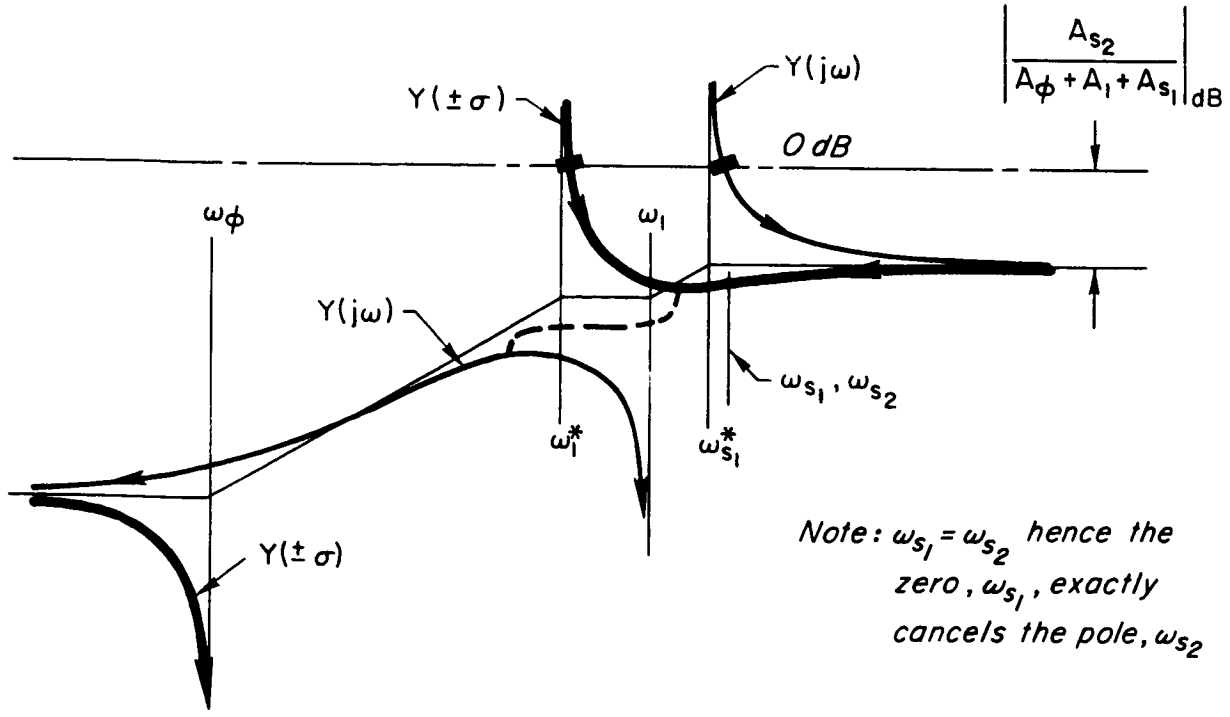
The next higher mode is the first slosch mode, ω_{S1} , which may now be added by employing the same technique:

$$\begin{aligned}
 N_{\phi G_3} &= (A_\phi + A_1)(s^2 - \omega_1^{*2})(s^2 + \omega_{S1}^2) + A_{S1}(s^2 - \omega_\phi^2)(s^2 + \omega_1^2) \\
 &= (A_\phi + A_1)(s^2 - \omega_1^{*2})(s^2 + \omega_{S1}^2) \left[1 + \frac{A_{S1}(s^2 - \omega_\phi^2)(s^2 + \omega_1^2)}{(A_\phi + A_1)(s^2 - \omega_1^{*2})(s^2 + \omega_{S1}^2)} \right] \\
 &= (A_\phi + A_1 + A_{S1})(s^2 - \omega_1^{**2})(s^2 + \omega_{S1}^{*2})
 \end{aligned}$$

The location of these roots may be seen in Fig. 5b and in the sketch below. Here the "gain" is sufficiently low that $\omega_1^{**} \doteq \omega_1^*$. This will also be the case as still other modes are added. Hence, to simplify the notation from here on the extra asterisks will not be employed because it is quite simple to keep track of the root movements. It should be noted, however, that in the progression from Fig. 5a through Fig. 5g the roots denoted by the solid rectangle (■) become the poles of the succeeding plot.



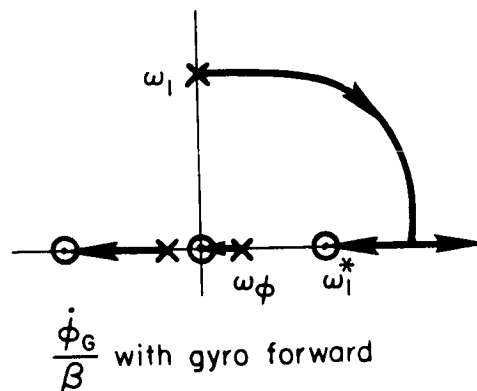
The probability of the zeros moving into the complex plane becomes evident when the second slosh mode is added (see Fig. 5c). Again, this may be visualized with the aid of the sketch below, where it can be seen that the root emanating from ω_{s1}^* moves out the $j\omega$ axis, then returns on the σ axis to meet the root from ω_1^* . The two roots then break off from the real axis and travel in the complex plane to the $j\omega$ axis, where they split; one goes into ω_1 , while the other goes to the origin and then comes back on the σ axis to ω_ϕ .



The major point here is that for certain values of the "gain" term it is possible to obtain a complex zero in the right half plane. In this case the zero is due to coupling of the first bending and the slosh modes. For the case at hand, the "gain" change required is relatively high and, in fact, is not achieved. However, progressing similarly to consideration of the second bending mode (Fig. 5e) and third bending mode (Fig. 5f), the possibility turns into reality through the coupling of the second and third bending modes.

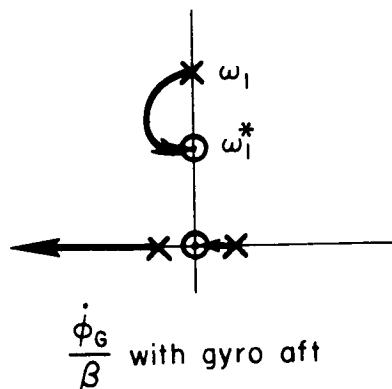
Thus it is possible not only to see how these zeros arise, but to identify the parameters which are involved. As noted before, the

selected gyro location is not a good one; it was picked only to illustrate a phenomenon. For example, considering an overly simplified case of the rigid body and first bending, a rate gyro feedback would result in the closure sketched. Moving the gyro to another location will modify the numerator drastically, since the loci



shown in Fig. 5 depend on the sign and magnitudes of the mode shapes as

seen by the sensor. The use of this figure can guide one in determining a better location for the sensor. For example, locating the sensor aft of the antinode of the first bending mode will change the sign of the "gain" term for Fig. 5a, which will then move ω_i^* from ω_1 toward the origin. A rate feedback for this overly simplified case would be as sketched. Obviously this latter case is to be preferred.



D. COMPARISON OF TRANSFER FUNCTIONS

The previous subsections (A and B) have discussed the transfer function denominators and sensor numerators separately. A more critical test of the validity and usefulness of the simplified equations is obtained by comparison of the complete transfer function (numerator and denominator). In this manner the relative position of poles and zeros may be checked. One of the more critical requirements for any approximation is that pole/zero sequence and separation be adequately represented. A relatively large error in both the pole and zero locations is acceptable if the sequence and separation are faithfully reproduced.

Figures 6-8 present open-loop pole/zero plots for a rate gyro located at the most favorable sensor location ($x_G = 46.5m$) for each of the three flight conditions. Zero damping is assumed for all oscillatory modes to facilitate plotting. The exact poles (\times) and zeros (\odot) are located on the σ and $j\omega$ axes, while the simplified poles (\times) and zeros (\bullet) are placed next to the axes with an arrow indicating precise location. Where necessary for clarity, expanded σ and $j\omega$ scales are shown.

Figure 6 represents the lift-off case and, neglecting the region between 2.0 and 2.6 rad/sec, indicates the simplified transfer function factors provide adequate accuracy in regard to both pole/zero sequence and separation. In fact, the rigid-body and bending mode zeros obtained from the simplified equations are remarkably close to the corresponding exact zeros. Reference 1 indicates that comparable agreement between the approximate and exact poles of the second through the fourth bending modes could be obtained by the simple refinement of removing the slosh mass from the generalized bending mass when calculating the uncoupled mode frequency.

In the region between 2.0 and 2.6 rad/sec the simplified transfer function indicates the three slosh mode poles and zeros to be coincident, whereas the exact modes exhibit some separation of both poles and zeros and the mode frequencies. Furthermore, the exact pole/zero sequence is

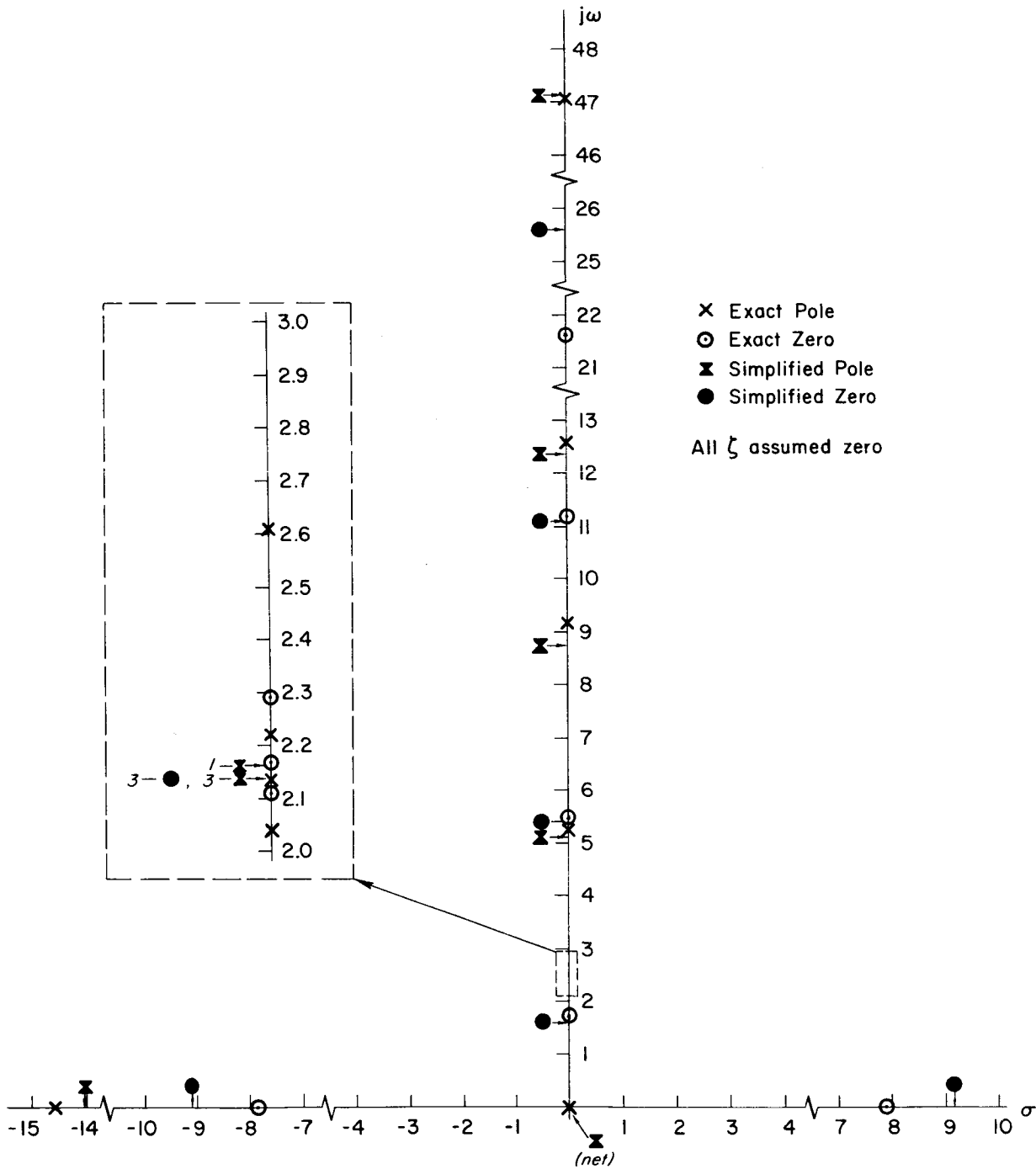


Figure 6. Simplified Versus Exact Pole/Zero Locations

$$N_{\phi_{46.5}} / \beta, t = 0$$

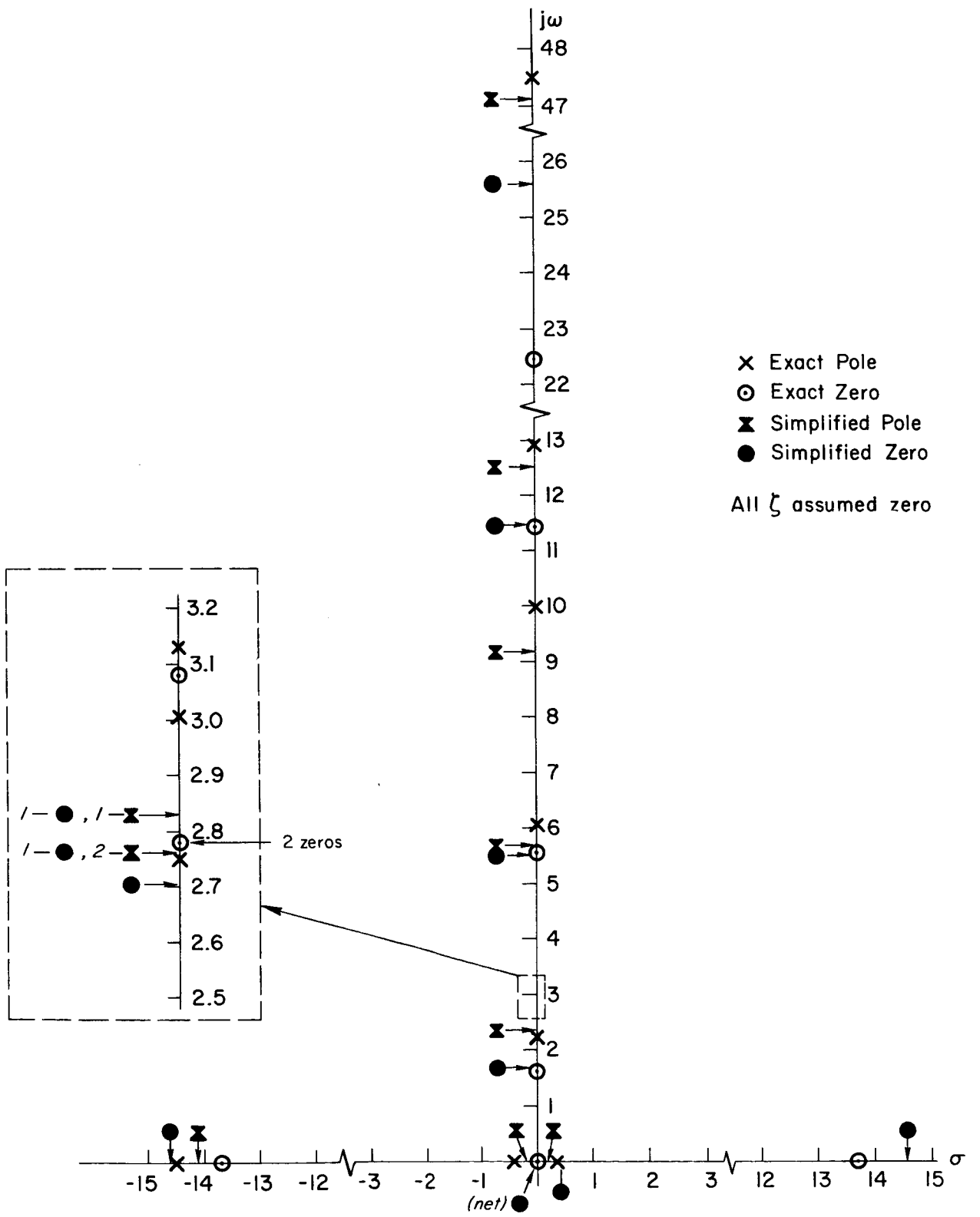


Figure 7. Simplified Versus Exact Pole/Zero Locations
 for $N_{\phi 46.5} / \beta, t = 80$

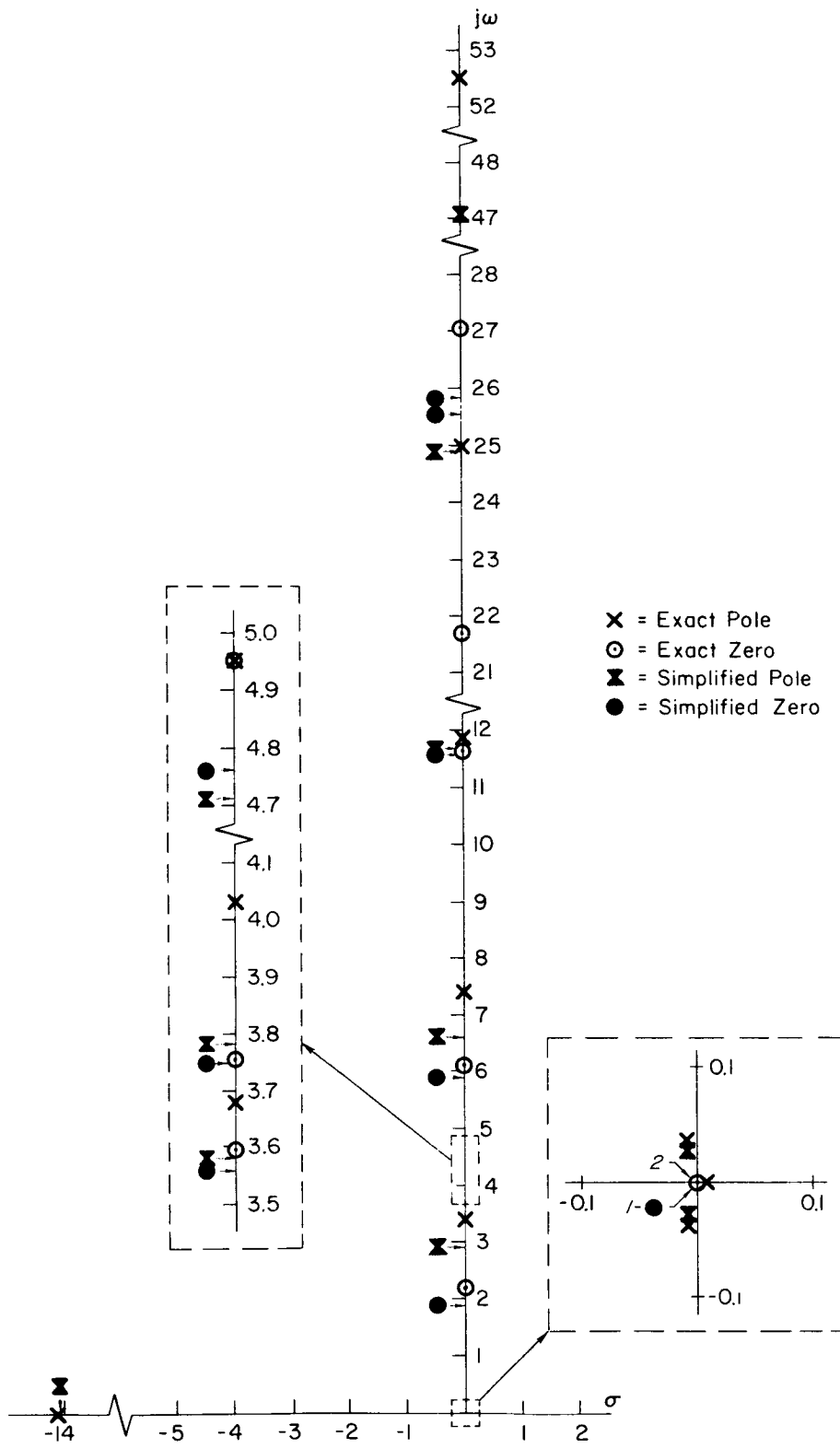


Figure 8. Simplified Versus Exact Pole/Zero Locations
 for $N_{\phi_{46.5}}/\beta$, $t = 157$

such that the damping of these modes is really increased by the rate feedback, but a 1 percent change in the first slosh (exact) pole or zero could result in this mode tending toward closed-loop instability. The simplified transfer functions thus appear to be questionable for these modes insofar as closed-loop stability prediction is concerned.

Reference 1 indicates the slosh/slosh and bending/slosh coupling to be extremely complicated. The best approximations obtained in Ref. 1 still exhibited slosh frequency discrepancies of 0.5 to 1 percent due to undetermined factors. Furthermore, it was found that correction to the slosh dynamics for the second bending mode contribution (or even third bending) could change slosh mode frequencies by 1 percent or more. Thus we may conclude that when the simplified transfer functions exhibit pole/zero separations of the order of 1 percent or less, little confidence can be placed in their validity in any subsequent stability analysis. In such cases the exact transfer function factors must be employed and even these may be questionable if based on calculated (rather than experimentally determined) slosh or flexible mode characteristics.

Figure 7 represents the maximum-q case and is sufficiently similar to the lift-off case that the comments regarding Fig. 6 apply here equally well. It might be pointed out that in Fig. 7 the exact slosh pole/zero sequence is such that the lowest slosh mode will tend toward instability. However, a 1 percent change in either the pole or zero could make this mode tend toward stability.

Figure 8 presents the comparison for the burnout case. Here the only significant discrepancy between the exact and simplified transfer functions lies in the tail-wags-dog zeros. The exact value is 21.76 rad/sec, whereas the simplified expression gives 25.6 rad/sec. This discrepancy destroys the favorable pole/zero sequence in the simplified factors at high frequencies. This could result in some minor differences between the equalization derived via the simplified transfer functions and that derived via the exact.

Figures 9 and 10 present similar comparisons of the acceleration sensor transfer functions at lift-off and maximum q, respectively. In Fig. 9 there appears to be little similarity between the pole/zero

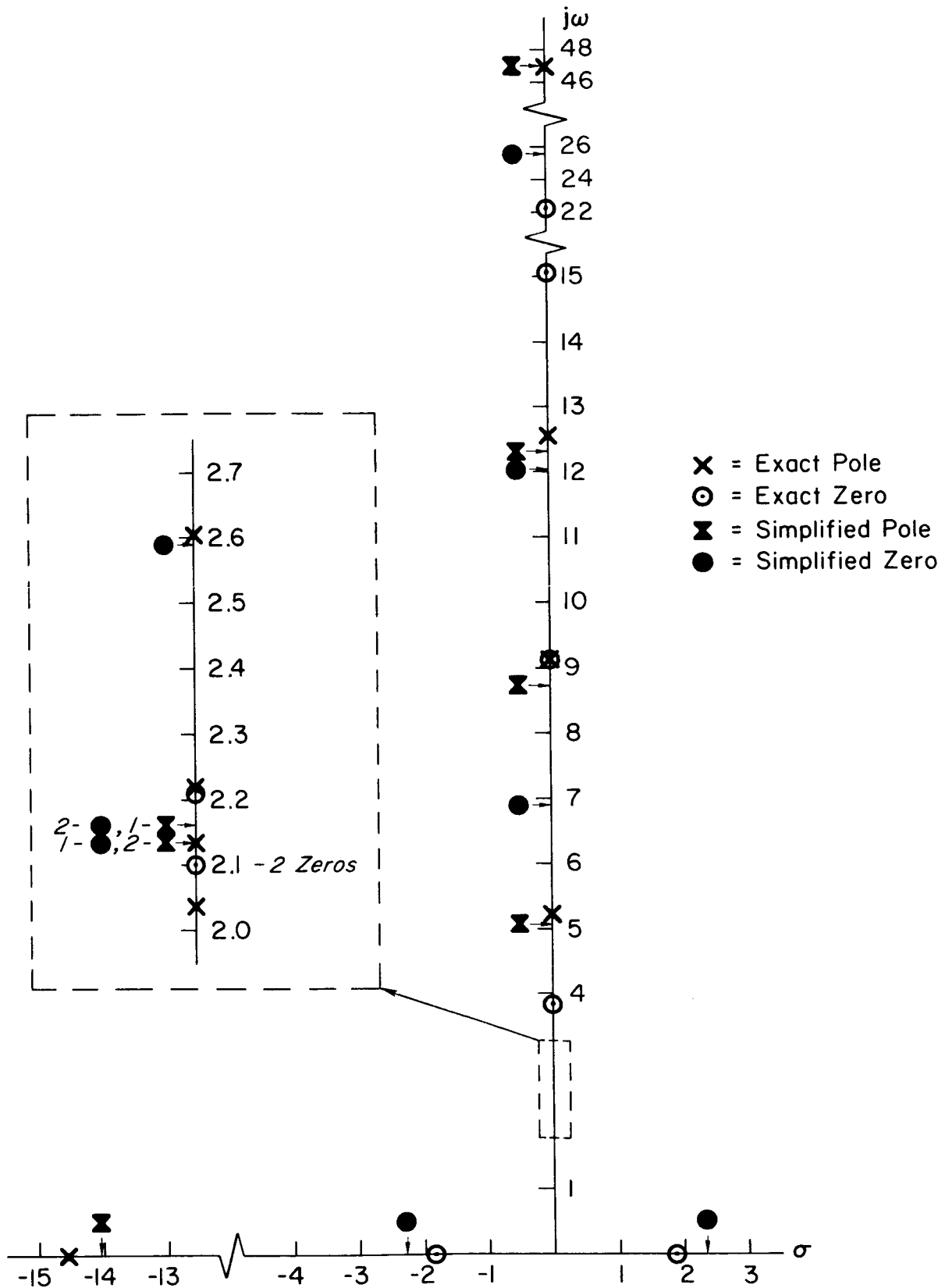


Figure 9. Simplified versus Exact Pole/Zero Locations; $\frac{Nz_{46.5}^{**}}{\beta}$, $t = 0$

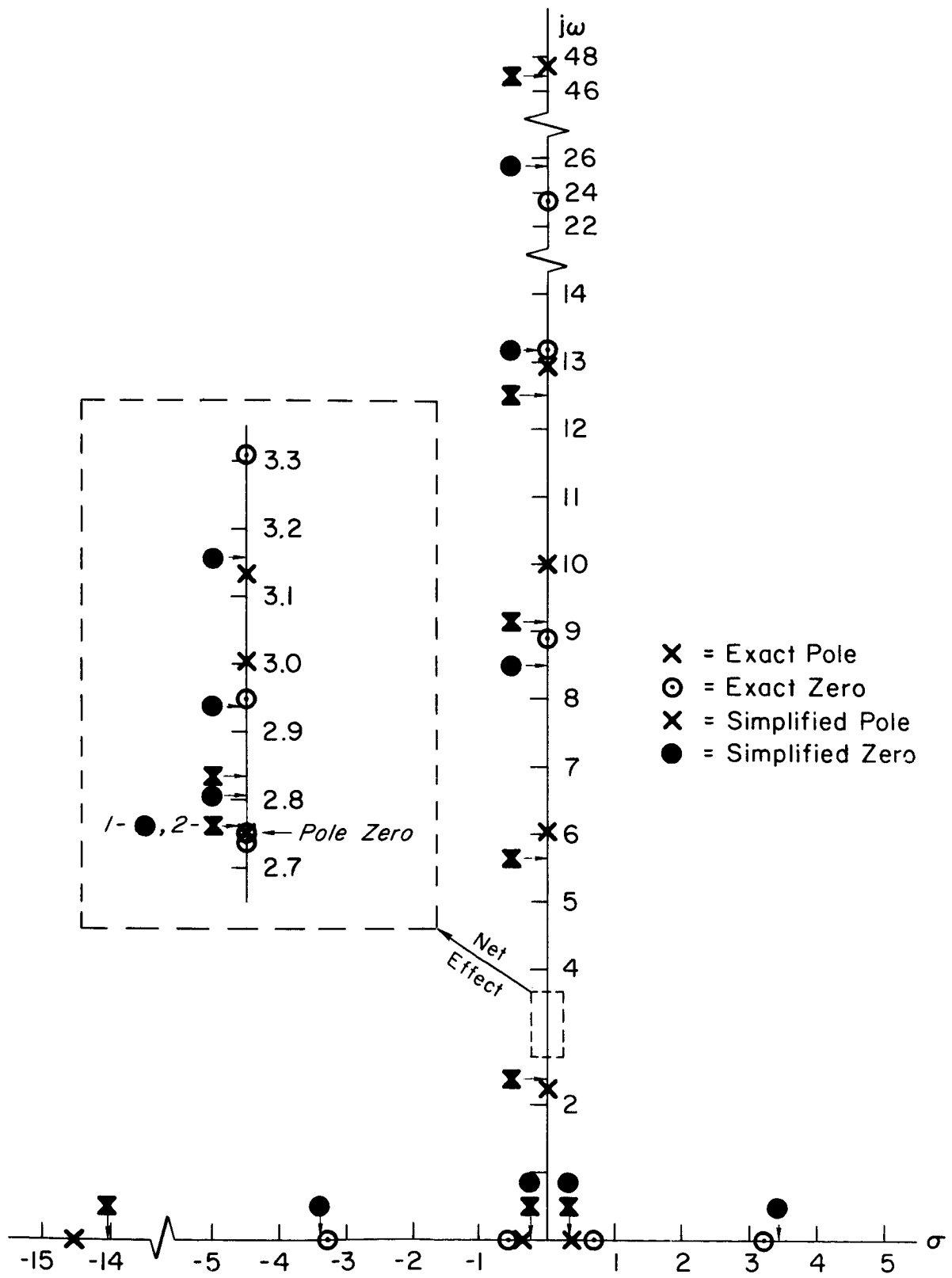


Figure 10. Simplified versus Exact Pole/Zero Locations; $\frac{N\bar{z}_{46.5}}{\beta}$, $t = 0$

sequences or separations. This is due primarily to differences between the simplified and exact zeros. As will be shown in Section IV.B, there is some question whether the simplified zeros shown here were evaluated correctly.

E. SUMMARY AND CONCLUSIONS

The simplified gyro sensor transfer function factors are adequate for preliminary systems synthesis work. Although not required, the accuracy of these approximations can be further improved by incorporating quite simple corrections (Ref. 1) to the simplified transfer function poles.

The simplified gyro sensor transfer functions are therefore valuable in selecting sensor location, determining effects of sensor blending, and establishing the general form of loop equalization. They can also be employed in determining sensitivity of transfer function factors to major vehicle parameter or configuration changes.

The pole/zero separation which results when the simplified gyro sensor transfer function factors are employed provides an automatic basis for determining the validity of the simplified transfer functions in system synthesis. That is, if the simplified transfer functions indicate moderate to large pole/zero separation for any mode, the simplified expressions may be safely employed. But if the pole/zero separation is small for any mode, then more exact methods should be used to determine the exact separation for that mode (e.g., Ref. 1).

The use of the simplified transfer functions and application of the successive loop closure technique provides insight to

1. The factors which control specific zero locations
2. Means of avoiding sensor zeros in the right half plane
3. The rapidity of sensor zero movement with change in vehicle parameters (sensitivity)
4. The effect of shifting sensor location
5. The effect, through comparison with the exact zeros, of coupling terms neglected through use of the simplified equations

SECTION III

SYSTEM SYNTHESIS

A. INTRODUCTION

The objective of this synthesis is to stabilize the flexible vehicle and to obtain a bandwidth of the order of 1 rad/sec with sufficient low frequency gain for attitude control. Rather than a detailed design of a control system, the object is to show that an acceptable system is feasible. As a result, only a "first cut" solution is presented. Refinements that would improve system characteristics are noted, but not incorporated.

There are five structural sections where sensors may be located (see Fig. A-1). An attitude gyro can be located only in Section No. 5 (most forward). Rate gyros may be located in any of the five sections, while accelerometers can be located only in Sections No. 1 through No. 4. Three flight conditions are considered: $t = 0$ (lift-off), $t = 80$ sec (maximum dynamic pressure), and $t = 157$ sec (burnout).

The preliminary investigations carried out prior to selecting the loop closures demonstrated here (including mention of the approaches that were not successful) are presented in the Appendixes. These preliminary investigations were "generic" in that the simplified (uncoupled) transfer functions were employed and actual loop closures were not made. The major interest was the selection of feedbacks and sensor locations to obtain the proper zero/pole sequence to damp or suppress the nonrigid modes with a minimum of feedback shaping. Single and blended rate gyro feedbacks and single and blended acceleration feedbacks were investigated. The results indicated

- The best rate gyro location for all three flight conditions is $x_G = 46.5m$
- A single rate gyro is as good as, or better than, two rate gyros (blended) because
 - The weighting of the blended signals favored one gyro sufficiently to cast doubt on the usefulness of the second gyro

- Only one to two modes are improved by the second feedback
- The second feedback proved detrimental to some modes
- The feedback shaping for a single rate gyro feedback would be complex, time varying, and potentially critical
- Lagged normal acceleration feedback (sensor at $x_A = 46.5\text{m}$) offered the possibility of damping the first through the third bending modes sufficiently, at $t = 0$ and $t = 80$, to relieve the criticalness of the shaping in the rate gyro loop
- The a_z and $\dot{\phi}$ feedbacks combined provided adequate damping and/or stabilization of all nonrigid modes except one slosh mode

Because the "simplified" transfer functions did not include modal coupling effects, it was then necessary to "check out" the results using exact transfer functions and to determine the necessary shaping, loop gains, etc. The system mechanizations thus investigated were

$$\text{System B: } \beta = H_{\dot{\phi}}(s)\dot{\phi}_{46.5} + H_{\phi}(s)\phi_{120.5}$$

$$\text{System C: } \beta = H_{a_z}(s)a_{z46.5} + H_{\dot{\phi}}(s)\dot{\phi}_{46.5}$$

$$\text{System D: } \beta = H_{a_z}(s)a_{z46.5} + H_{\dot{\phi}}(s)\dot{\phi}_{46.5} + H_{\phi}(s)\phi_{120.5}$$

The simplified synthesis adequately predicted results obtained via the exact (or coupled) transfer function analysis. In this section we shall present only the synthesis of mechanization D, since this resulted in the simplest system. The "simplified" analyses and the "exact" analysis of mechanizations B and C are summarized in Appendixes D and E.

It is pertinent to note at this point that the bending mode slope criteria (Ref. 7) for determining "good" gyro locations were applied but did not give satisfactory results. It is presumed that the high coupling of Model Vehicle No. 2 bending and slosh modes was the culprit. No single station could be found (within the allowable sensor locations) which exhibited the desired bending mode slopes throughout the flight. Furthermore, for those locations which came closest to satisfying the criteria regarding desired slope sign and consistency of sign (e.g., Station 120.5), many of the sensor zeros were located in the right half plane. The station actually selected as best in our analysis (Station 46.5) would be considered a poor location on the basis of the

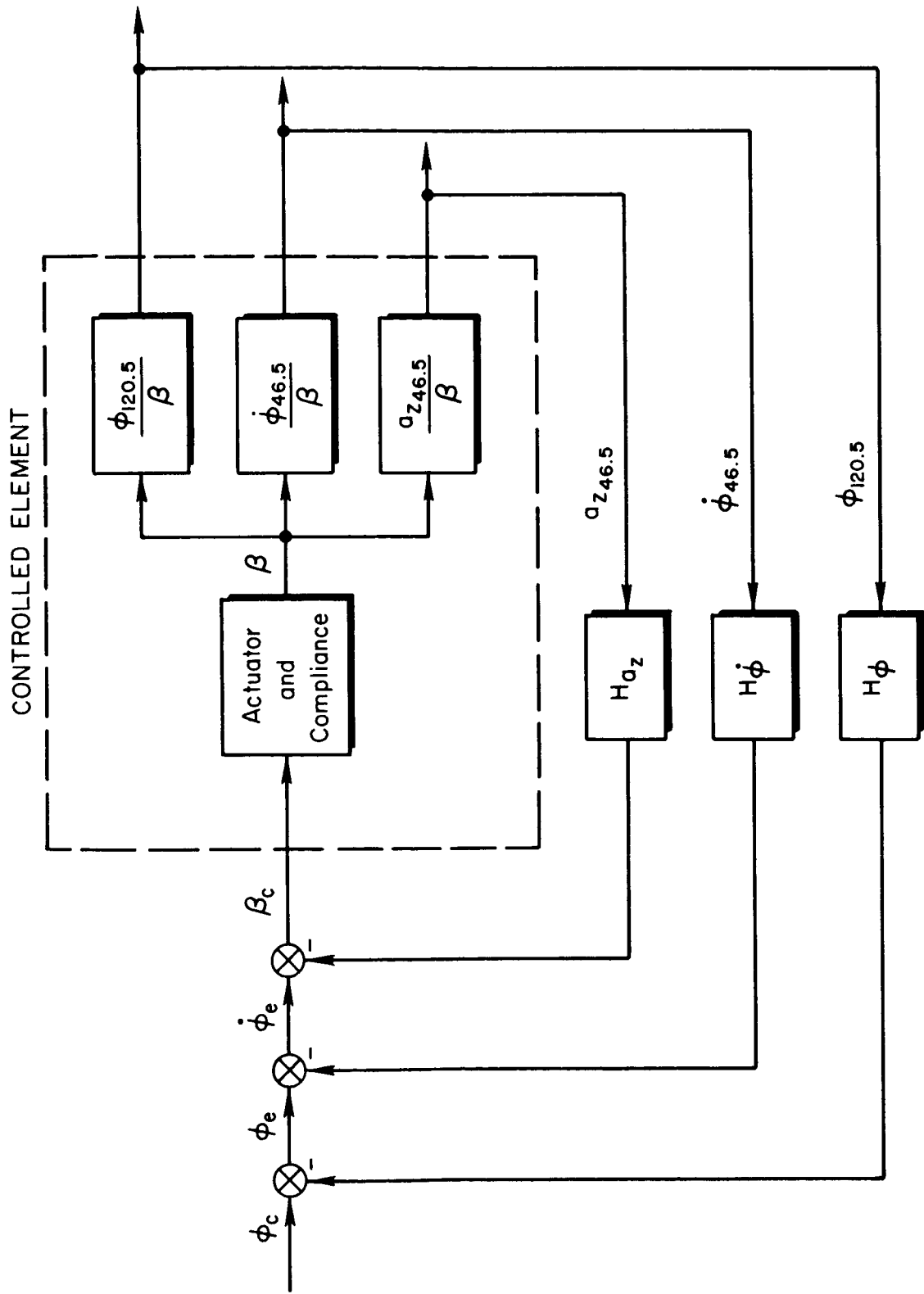


Figure 11. Block Diagram of Vehicle Stabilization and Control System

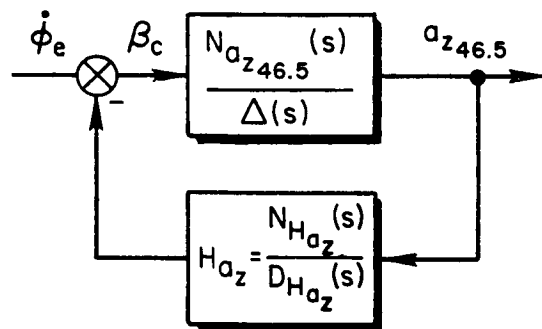
criteria of Ref. 7. Mechanization D is composed of a single linear accelerometer, a single rate gyro plus an attitude gyro feedback. The acceleration loop is employed to damp the flexible modes, the rate gyro loop to further damp nonrigid modes and to stabilize the rigid body, and the attitude gyro loop to control attitude. The loops are closed independently to better visualize the individual contributions of each.

B. STABILIZATION AND ATTITUDE CONTROL SYSTEM

The loop closures are represented by the block diagrams of Figs. 11 through 14. Figure 11 indicates the sequence of loop closures from "inner" to "outer." The remaining figures indicate the effective system dynamics as each loop is closed sequentially.

The "exact" or coupled transfer function factors were calculated from an 11-by-11 matrix (Ref. 1) which included the actuator and compliance equations. Therefore the vehicle, actuator, and compliance dynamics are lumped into a single block labeled "controlled element."

The sequence of loop closures, resulting block algebra, nomenclature, etc., for the Bode and root locus plots shown later in this section is as follows. The first loop closure is the acceleration loop, depicted by Fig. 12.



Note:
$$\frac{N_{a_{z46.5}}(s)}{\Delta(s)} = \frac{\beta}{\beta_c} \frac{a_{z46.5}}{\beta}$$

Figure 12. Normal Acceleration Feedback Loop

The closed-loop dynamics which result from this feedback and which are of interest for the second loop closure are obtained from the relationship

$$\begin{aligned}
\frac{\beta_c}{\dot{\phi}_e} &= \frac{1}{N_{a_z}_{46.5}(s) N_{H_{a_z}}(s)} \\
&= \frac{1}{1 + \frac{\Delta(s)}{\Delta'(s)} \frac{D_{H_{a_z}}(s)}{N_{H_{a_z}}(s)}} \\
&= \frac{\Delta(s) D_{H_{a_z}}(s)}{\Delta(s) D_{H_{a_z}}(s) + N_{a_z}_{46.5}(s) N_{H_{a_z}}(s)} \quad (10) \\
&= \frac{\Delta(s) D_{H_{a_z}}(s)}{\Delta'(s)}
\end{aligned}$$

The second closure, the attitude rate loop, is then represented by Fig. 13.

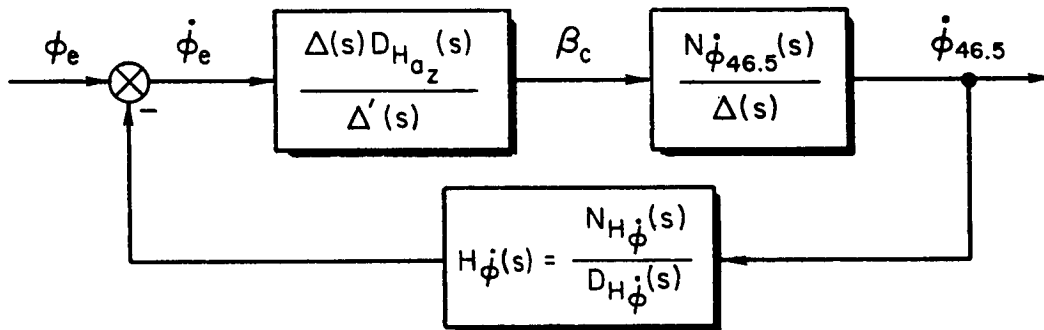


Figure 13. Attitude Rate Feedback Around Acceleration Stabilized Vehicle

For Bode and root locus plots of the attitude rate closure, the forward loop is represented by the equivalent expression

$$\frac{\dot{\phi}_{46.5}}{\dot{\phi}_e} = \frac{D_{H_{a_z}}(s) N_{\dot{\phi}_{46.5}}(s)}{\Delta'(s)} \quad (11)$$

The closed-loop dynamics of interest for the third (attitude) loop closure are then obtained from the relationship

$$\begin{aligned}
\frac{\beta_c}{\varphi_e} &= \frac{\frac{\Delta(s)D_{H_{a_z}}(s)}{\Delta'(s)}}{1 + \frac{D_{H_{a_z}}(s)N_{\phi_{46.5}}(s)}{\Delta'(s)} \frac{N_{H\dot{\phi}}(s)}{D_{H\dot{\phi}}(s)}} \\
&= \frac{\Delta(s)D_{H_{a_z}}(s)D_{H\dot{\phi}}(s)}{\Delta'(s)D_{H\dot{\phi}}(s) + D_{H_{a_z}}(s)N_{\phi_{46.5}}(s)N_{H\dot{\phi}}(s)} \quad (12) \\
&= \frac{\Delta(s)D_{H_{a_z}}(s)D_{H\dot{\phi}}(s)}{\Delta''(s)}
\end{aligned}$$

Finally, the third closure, the attitude loop, is represented by Fig. 14.

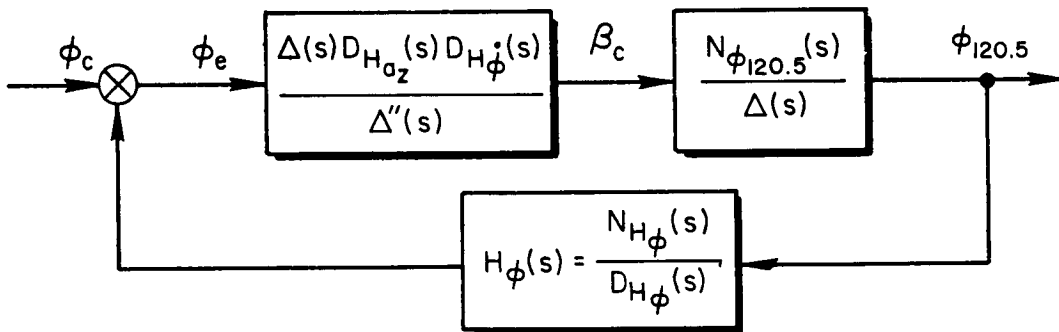


Figure 14. Attitude Feedback Around Acceleration and Attitude Rate Stabilized Vehicle

Again, for Bode and root locus purposes, the forward loop dynamics may be expressed as

$$\frac{\varphi_{120.5}}{\varphi_e} = \frac{D_{H_{a_z}}(s)D_{H\dot{\phi}}(s)N_{\phi_{120.5}}(s)}{\Delta''(s)} \quad (13)$$

The closed-loop dynamics of interest in any further loop closures are obtained from the relationship

$$\frac{\beta_c}{\varphi_c} = \frac{\Delta(s)D_{H_{a_z}}(s)D_{H\dot{\phi}}(s)D_{H\phi}(s)}{\Delta'''(s)} \quad (14)$$

It will be noted from the foregoing that the characteristic equation of the effective vehicle is always denoted by delta (Δ) with the primes (') indicating the number of loops closed. It may also be noted that the equalization poles of the inner loop(s) become zeros of each succeeding loop closure.

The system mechanization will now be discussed for each of the three flight conditions.

1. Maximum q (t = 80 sec)

In this and subsequent subsections the loop closures will be covered in the following manner. First, the open-loop effective-vehicle transfer function will be given, followed by the loop feedback equalization, the loop gain, and the resulting closed-loop roots. Then the Bode plot and a root locus sketch will be given. (The word "sketch" is emphasized because the pole (zero) departure (arrival) locus, the closed-loop roots, and the $j\omega$ axis crossings are the only points on the locus that are determined accurately.) This will be followed by a list of the pertinent aspects of the loop closure for the specific flight condition.

a. Acceleration feedback. The controlled element transfer function for this first loop closure is

$$\frac{a_z}{\beta_c} = \frac{N_{az_{46.5}}(s)}{\Delta(s)} = \frac{-40,293s(s-0.0408)(s-0.5889)(s+0.6802)}{35.506s(s-0.0420)(s-0.279)(s+0.364)} \times \frac{(s+3.1835)(s-3.2243)[0.036; 2.744]}{(s+14.5)[0.014; 2.234][0.0050; 2.75]} \times \frac{[-0.028; 2.749][0.0084; 2.950]}{[0.0057; 3.047][0.0087; 3.13]} \times \frac{[0.0145; 3.3107][0.0135; 8.943]}{[0.0084; 6.02][0.0071; 9.94]} \times \frac{[-0.0024; 13.20][0.0045; 23.4]}{[0.0064; 12.89][0.099; 47.5]} \quad (14)$$

where $[\zeta ; \omega]$ is a shorthand notation for $[s^2 + 2\zeta\omega s + \omega^2]$. The feedback equalization and gain is

$$H_{a_z}(s) = \frac{-0.0338 \left(\frac{s}{0.4} + 1 \right)}{\left(\frac{s}{0.8} + 1 \right) \left(\frac{s}{4} + 1 \right) \left(\frac{s}{13} + 1 \right)} \quad (15)$$

where the low frequency lead/lag is employed to avoid further destabilizing the initially unstable rigid-body mode. The poles at 4 and 13 are located to phase-stabilize and attenuate the fourth bending mode and to augment the damping of the first through third bending modes.

The resulting closed-loop dynamic characteristics are

$$\begin{aligned} \Delta'(s) = & 35.506s(s + 0.3108)(s + 1.08)(s + 22.85) [-0.884 ; 0.051] [0.229 ; 1.92] \\ & \times [0.0026 ; 2.75] [-0.014 ; 3.035] [0.041 ; 3.13] [0.673 ; 3.34] \\ & \times [0.216 ; 7.44] [0.0527 ; 10.47] [0.005 ; 12.79] [0.087 ; 47.8] \end{aligned} \quad (16)$$

One of the more significant aspects of this loop closure is the appreciable damping achieved in the first three bending modes.

From the root locus (Fig. 16) it is seen that the pole/zero alternation along the $j\omega$ axis is broken by the fourth bending mode. The resulting phase lag makes it necessary to avoid cutting the peak at $\omega \doteq 13$ with the closure gain line (Fig. 15). Although it appears on these plots that the fourth bending mode is destabilized by this closure, it actually is stabilized slightly (the open-loop damping is 0.0064, while the closed-loop damping is 0.0071).

Note in Fig. 16 that the two lowest frequency slosh modes are adversely affected by this closure. The lowest frequency mode remains stable, but the damping of this mode is cut in half. The second lowest frequency slosh mode is actually destabilized. The two real poles in the right half plane are coupled and move toward the origin. The actuator pole and one of the equalization poles also couple to provide an additional oscillatory mode between the first and second bending modes.

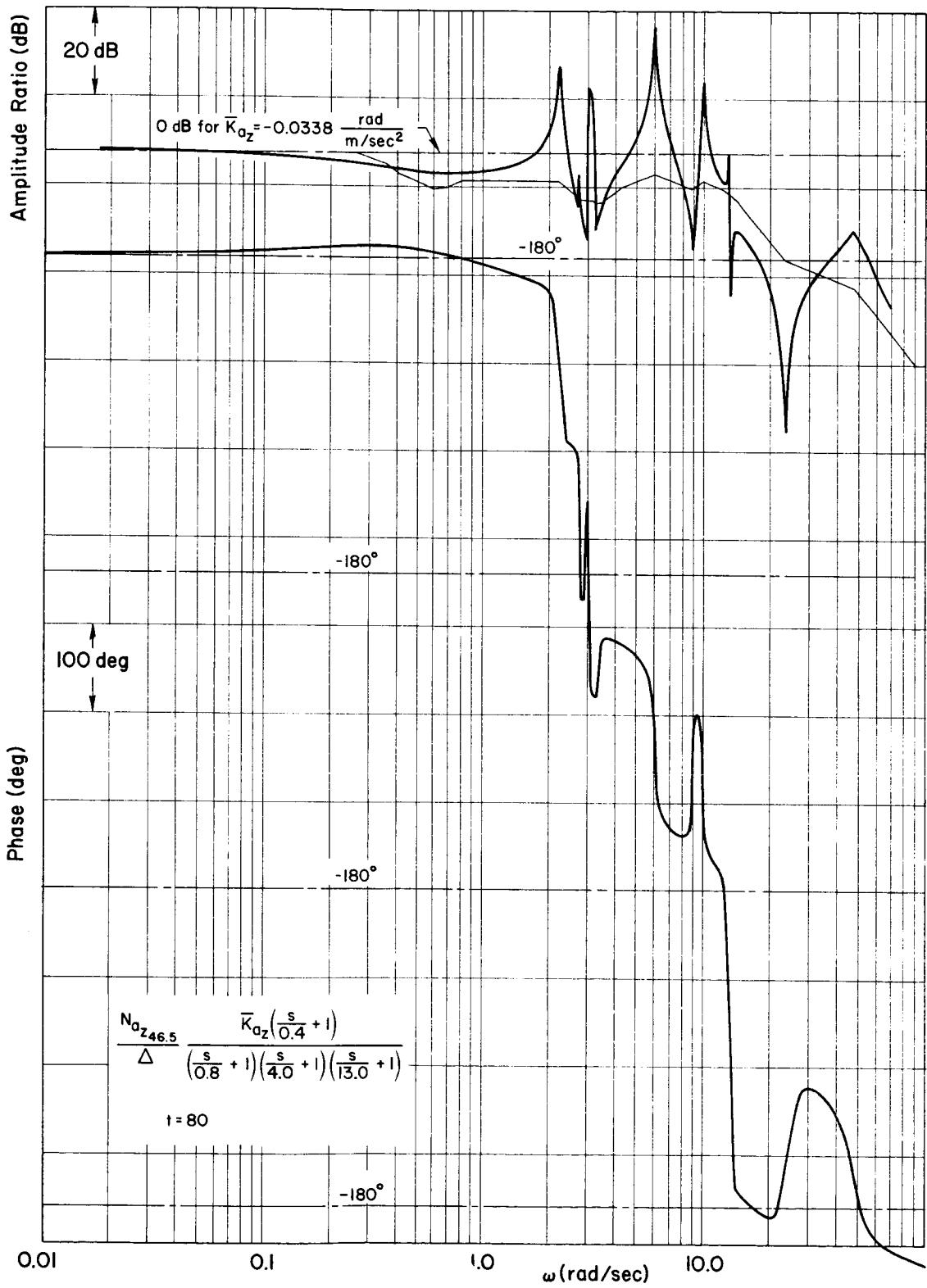


Figure 15. Linear Acceleration Feedback Amplitude and Phase, t = 80

$$\frac{N_{az} 46.5}{\Delta} \frac{\bar{K}_a \left(\frac{s}{4} + 1\right)}{\left(\frac{s}{.8} + 1\right)\left(\frac{s}{4} + 1\right)\left(\frac{s}{13} + 1\right)}$$

t = 80

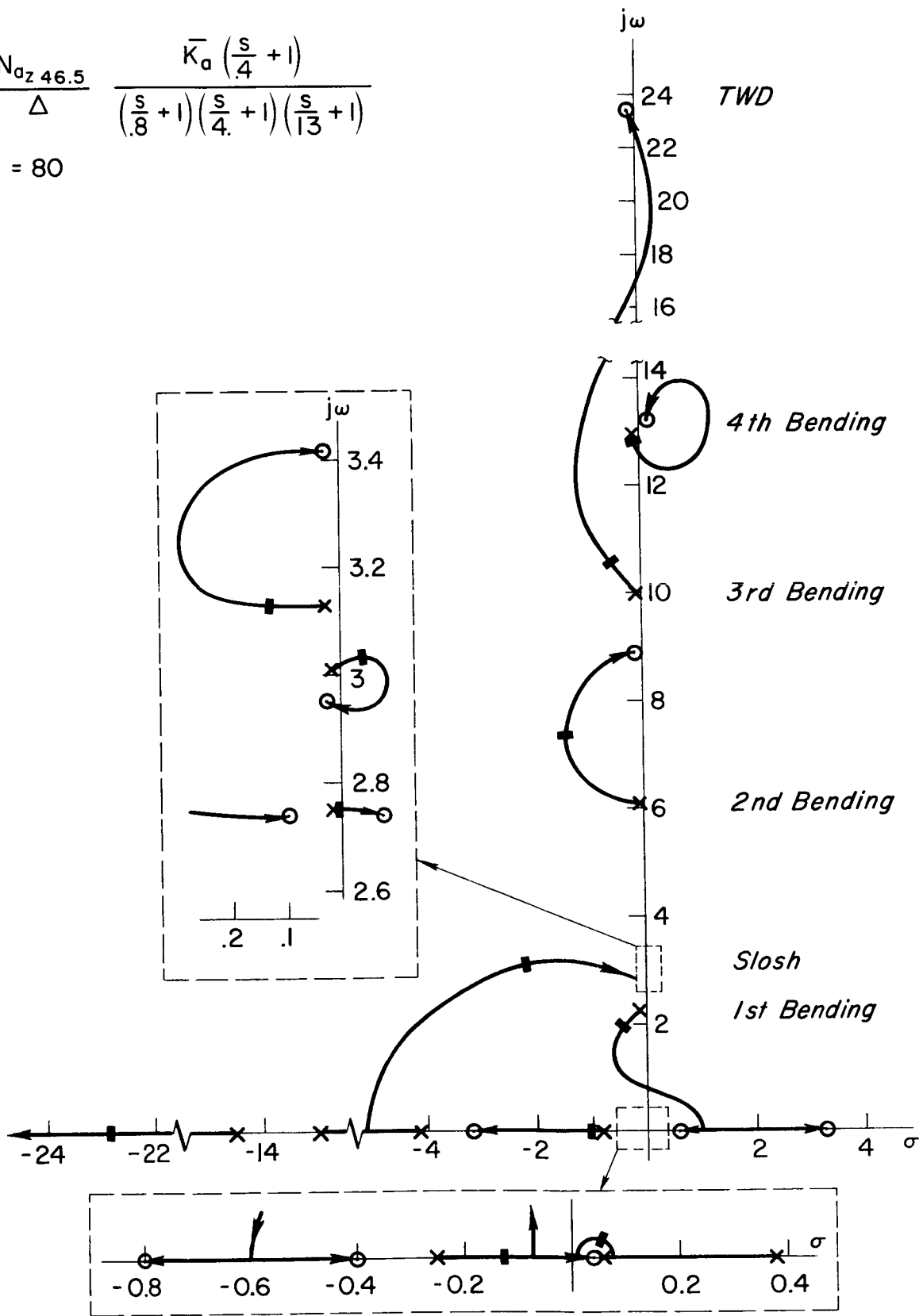


Figure 16. Root Locus for Acceleration Closure, t = 80

b. Attitude rate feedback. From Fig. 13 the effective controlled element is

$$\frac{D_{\text{Hez}}(s)N_{\dot{\phi}_{46.5}}(s)}{\Delta'(s)} = \frac{1561.5s^2(s+0.8)(s+4)(s+13)(s+0.016)(s+13.6)(s-13.7) \times [0.0213; 1.59] [0.0127; 2.78] [0.0026; 2.78] [0.006; 3.08] \times [0.0094; 5.55] [0.0079; 11.4] [0.0006; 22.4]}{\Delta'} \quad (17)$$

The selected feedback equalization and gain are

$$H_{\dot{\phi}_{46.5}}(s) = \frac{-0.0954 \left(\frac{s}{0.1} + 1 \right)}{s \left(\frac{s}{3} + 1 \right)} \quad (18)$$

The free s is employed to increase the low frequency amplitude ratio to improve the attitude control capability. The zero at 0.1 is to stabilize the unstable rigid-body mode. The pole at 3 is to phase-stabilize the fourth bending mode.

The resulting closed-loop dynamics are characterized by

$$\Delta'' = 35.506s^2(s+0.653)(s+22.82) [0.573; 0.0486] [0.409; 1.397] [0.284; 2.50] \times [0.00183; 2.75] [-0.0116; 3.06] [0.0513; 3.22] [0.94; 3.34] [0.197; 7.69] \times [0.0613; 10.39] [0.0071; 12.73] [0.087; 47.8] \quad (19)$$

It may be noted from Fig. 17 that, with the exception of the fourth bending mode at $\omega = 13$, there are no significant amplitude peaks in the Bode plot. This is the direct benefit of the previous acceleration feedback closure which damped the first three bending modes. Due to this lack of peaks and the fact that the fourth bending mode remains stable and is damped by this attitude rate closure, a higher gain could be employed here if necessary to reduce the fourth bending peak in subsequent loop closures. However, Fig. 18 indicates that a higher gain might drive the lowest frequency slosh mode unstable. Figure 18 also indicates that the rigid-body mode has now been stabilized, but the second slosh mode remains unstable.

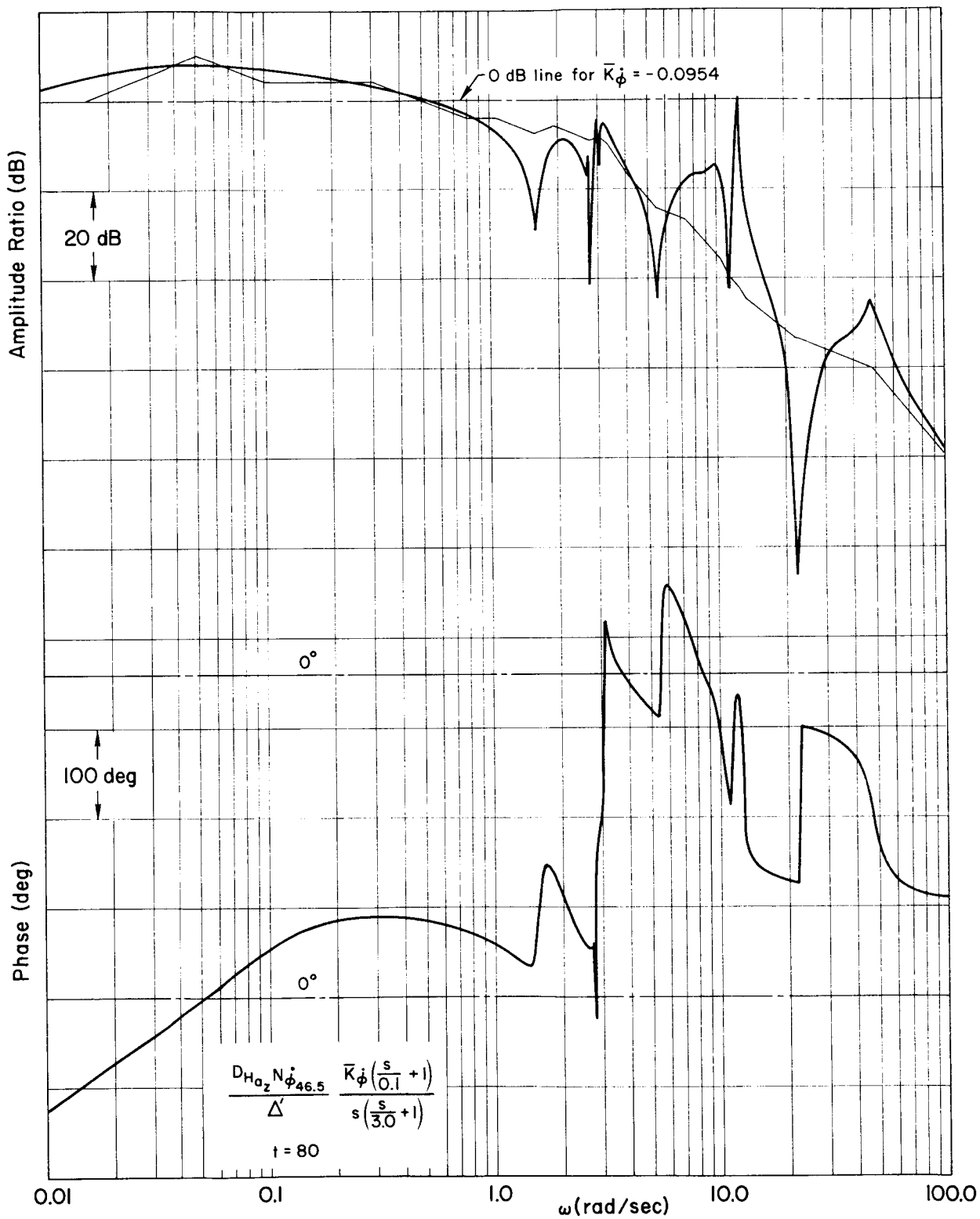


Figure 17. Attitude Rate Feedback Amplitude and Phase, $t = 80$

$$\frac{D_{H_{a_2}} N_{\phi_{46.5}}}{\Delta'} \frac{\bar{K}_{\phi} (\frac{s}{0.1} + 1)}{s (\frac{s}{3.0} + 1)}$$

t = 80

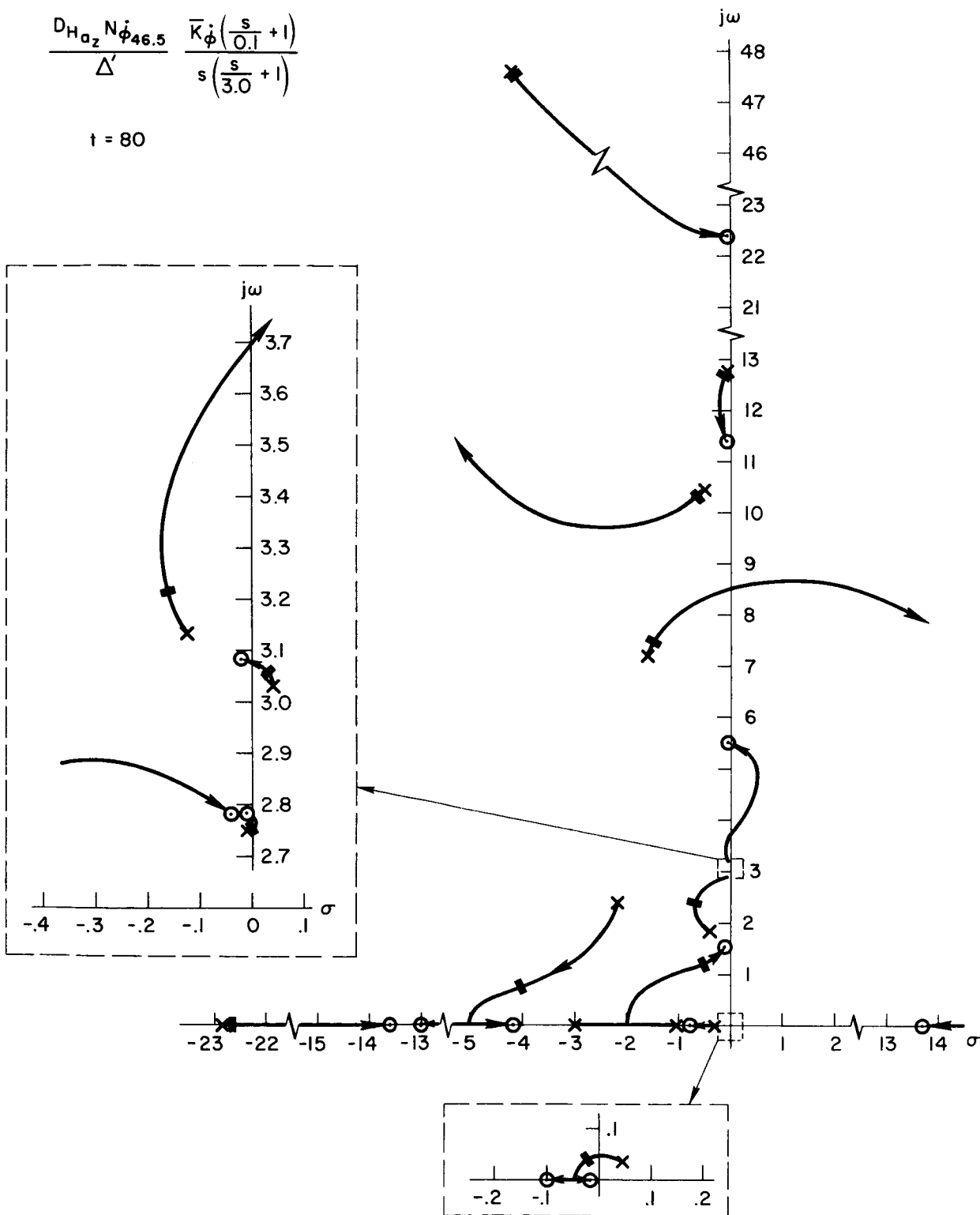


Figure 18. Root Locus for Attitude Rate Closure, t = 80

c. **Attitude feedback.** From Fig. 14 the effective controlled element is

$$\frac{D_{H_\phi}(s)D_{H_{a_z}}(s)N_{\phi_{120.5}}(s)}{\Delta''} = \frac{789.73s^2(s+0.8)(s+3)(s+4)(s+13)(s+0.00403)(s+1.755) \times (s-1.755)[0.00308;2.692][0.1147;2.9386][0.0008;3.0074] \times [0.9088;9.817][[-0.904;9.829][0.009775;12.324][0.0002;23.025]}{\Delta''} \quad (20)$$

The feedback equalization and gain selected are

$$H_\phi(s) = \frac{-0.01668\left(\frac{s}{0.05} + 1\right)}{s\left(\frac{s}{1} + 1\right)} \quad (21)$$

Again, the free s is employed to increase the low frequency amplitude ratio for tight attitude control. This necessitated the lead at 0.05 to keep the rigid-body mode stable. The lag at 1.0 is employed to phase-stabilize the higher frequency modes.

The closed-loop dynamic characteristics are

$$\Delta''' = 35.506s^2(s+0.00354)(s+0.0567)(s+0.891)(s+22.82)[0.545;0.628][0.567;1.079] \times [0.263;2.58][0.0040;2.75][[-0.012;3.05][0.056;3.23][0.940;3.35] \times [0.197;7.68][0.061;10.39][0.0072;12.73][0.087;47.8] \quad (22)$$

From Fig. 19 it will be noted that this closure results in a 6 dB gain margin. Figures 18 and 20 indicate that an oscillatory pair resulting from inner loop equalization is the limiting mode insofar as increasing gain is concerned. That is, this mode will be the first to go unstable. However, due to its origin it should be well known and controllable. The closed-loop roots show the rigid-body mode to have a break frequency of $\omega = 0.628$ at $\zeta = 0.545$. This should provide reasonable attitude response for a vehicle of this size, and, in fact, may provide too rapid response. The 20 dB amplitude ratio at low frequency should insure adequate steady-state control capability.

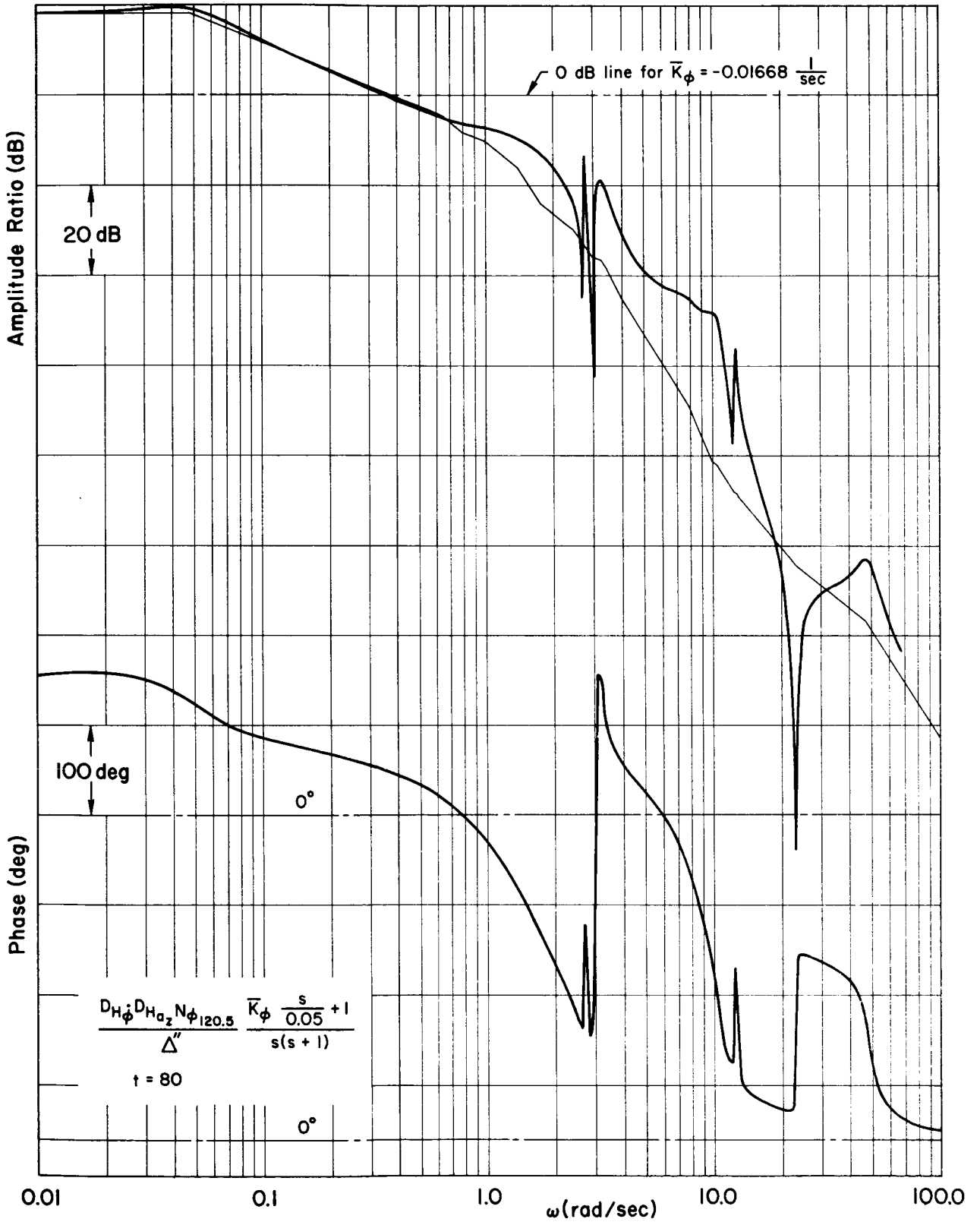


Figure 19. Attitude Feedback Amplitude and Phase, $t = 80$

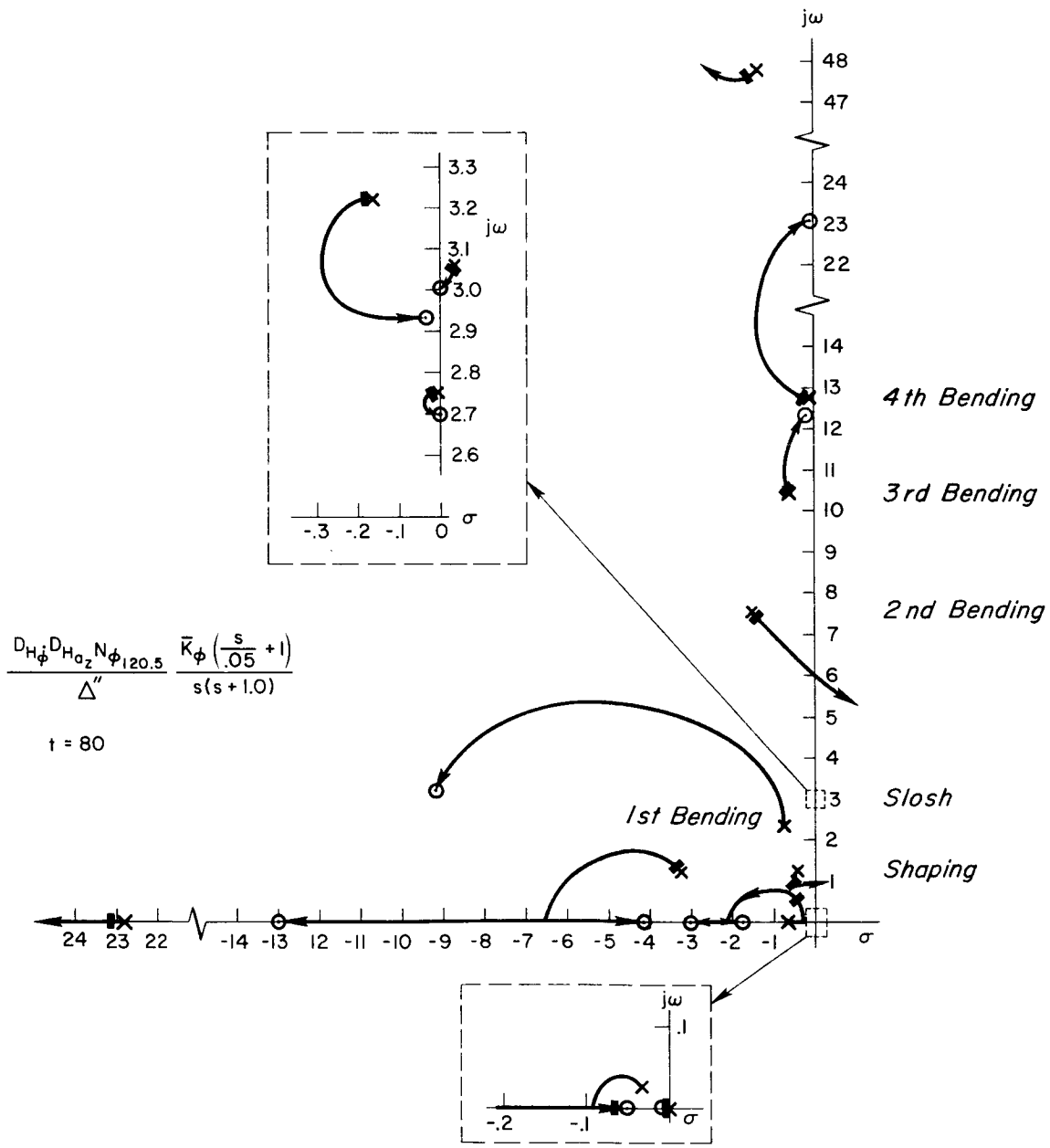


Figure 20. Root Locus for Attitude Closure, t = 80

Figure 20 also indicates that the second slosh mode still remains unstable. Thus it probably will be necessary to provide some tank baffling to maintain stability of this mode. Reflecting back to Fig. 16, it is apparent that if damping ($\zeta\omega$) of approximately 0.06 could be achieved through tank baffling, this mode would remain stable throughout all of these loop closures. It is to be noted further that the first closure has the dominant effect on the slosh pole movement and that subsequent loop closures have no appreciable effect.

It is to be emphasized that these results are the outgrowth of a "first cut" effort. The equalization and gain of the a_z closure were selected to maximize damping of the first three bending modes (with some tradeoff for the fourth bending and second slosh instability considerations). The equalization and gain of the ϕ closure were selected to further damp the nonrigid modes, but primarily to stabilize the rigid-body mode. Of course the final ϕ closure equalization and gain were selected to provide high amplitude ratio at low frequencies and a reasonable crossover frequency. Undoubtedly some improvement in system "performance" could be gained by iteration of the various loop equalizations and gains. However, this will not be done because (1) the purpose of this investigation is to prove control feasibility rather than control optimization and (2) the other two flight conditions must be investigated to determine the effectiveness of this same equalization.

2. Lift-Off ($t = 0$ sec)

a. **Acceleration feedback.** The open-loop controlled element transfer function is

$$\frac{a_z}{\beta_c} = \frac{N_{a_z}_{46.5}(s)}{\Delta(s)} = \frac{-21,286s^2(s-0.0046)(s+0.0046)(s+1.81)(s-1.82)}{46,510s^4(s+14.56)[0.0045; 2.03][0.0050; 2.13]} \\ \times \frac{[-0.02323; 2.1047][0.0338; 2.107][0.00439; 2.2133][0.0050; 3.79]}{[0.0052; 2.22][0.0054; 2.607][0.0048; 5.29]} \\ \times \frac{[0.0052; 9.13][0.0055; 15.08][0.00022; 22.21]}{[0.0049; 9.19][0.0050; 12.59][0.098; 47.0]} \quad (23)$$

Again, as a first cut the feedback equalization for this flight condition is purposely selected to be the same as that employed at $t = 80$ sec. The feedback gain is adjusted to avoid instabilities. The feedback is

$$H_{a_z}(s) = \frac{-0.00613 \left(\frac{s}{0.4} + 1 \right)}{\left(\frac{s}{0.8} + 1 \right) \left(\frac{s}{4} + 1 \right) \left(\frac{s}{13} + 1 \right)} \quad (24)$$

The resulting closed-loop dynamics are characterized as

$$\begin{aligned} \Delta' = & 46.510s^2(s + 0.814)(s + 4.60)(s + 9.87)(s + 16.8) [0.000255; 0.000584] \\ & \times [0.0078; 2.021] [0.0016; 2.132] [0.005; 2.224] [0.0259; 2.574] \\ & \times [0.029; 5.29] [0.0051; 9.19] [0.0040; 12.56] [0.097; 47.0] \quad (25) \end{aligned}$$

From Figs. 21 and 22 it is apparent that the low frequency lead/lag provides little or no benefit for this closure. But, it also has no harmful effect. The poles at 4 and 13 phase-stabilize the bending modes and attenuate the fourth bending mode. Due to the conservative gain selection (approximately 5 dB gain margin on the second slosh and fourth bending modes), at first glance it appears that this loop is of little benefit. However, the small amount of damping achieved in the first and second bending modes is necessary and sufficient to allow a reasonable rate gyro closure in the next loop. Adding an equalization pole at approximately 18 rad/sec would improve the phase near the fourth bending mode and allow considerably higher gain if we again assumed tank baffling to maintain stability of the second slosh mode. However, it appears that the present equalization is quite satisfactory since, if needed later, the loop gain can be increased up to 5 dB without incurring instability.

It might be noted that a slight increase in the third bending zero ($\omega \doteq 9$) could lead to instability problems with this mode. The location of this zero is critical and could cause trouble if the accelerometer location is changed slightly or if the vehicle parameters (e.g., third mode shape) vary from the values used here.

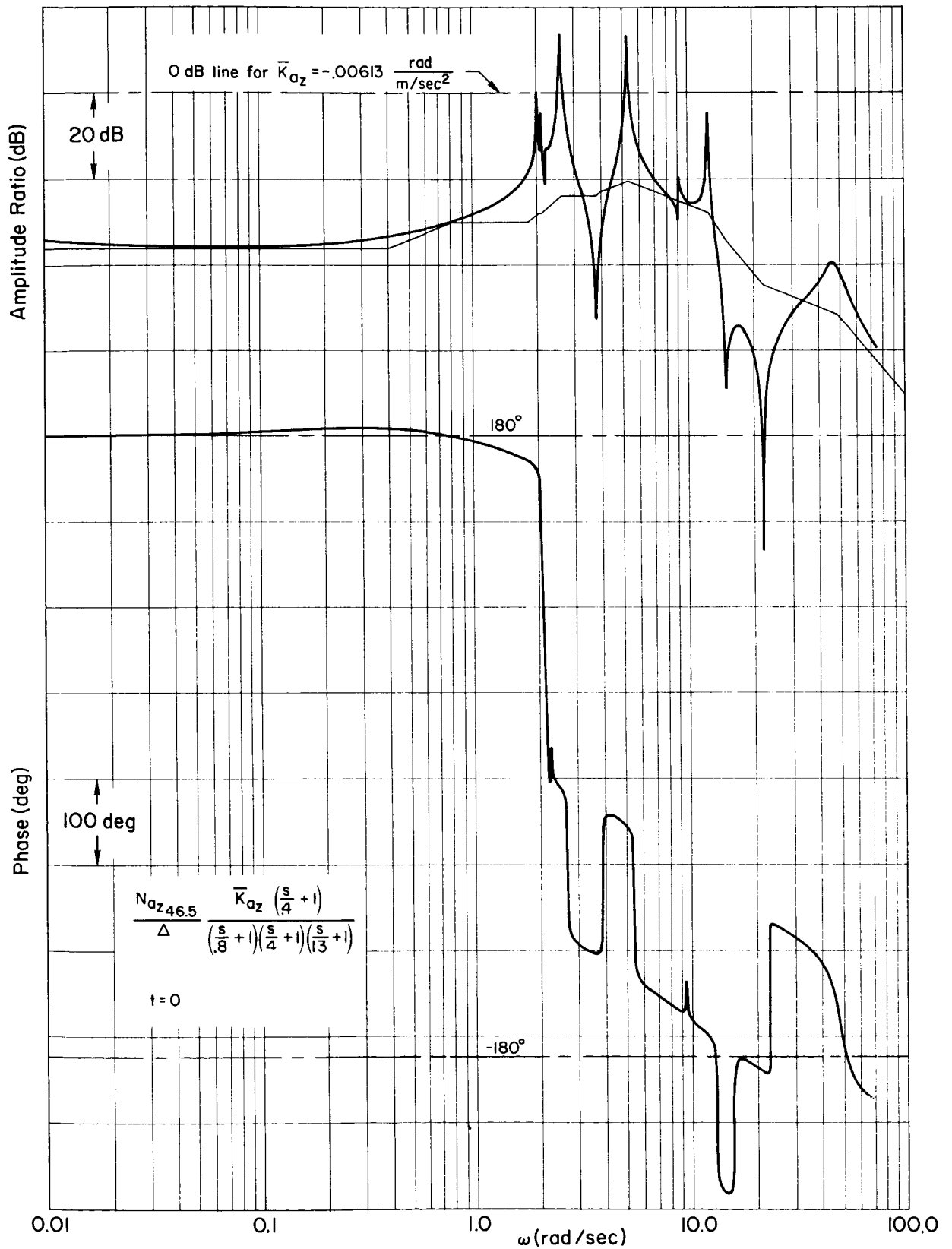


Figure 21. Linear Acceleration Feedback Amplitude and Phase, t = 0

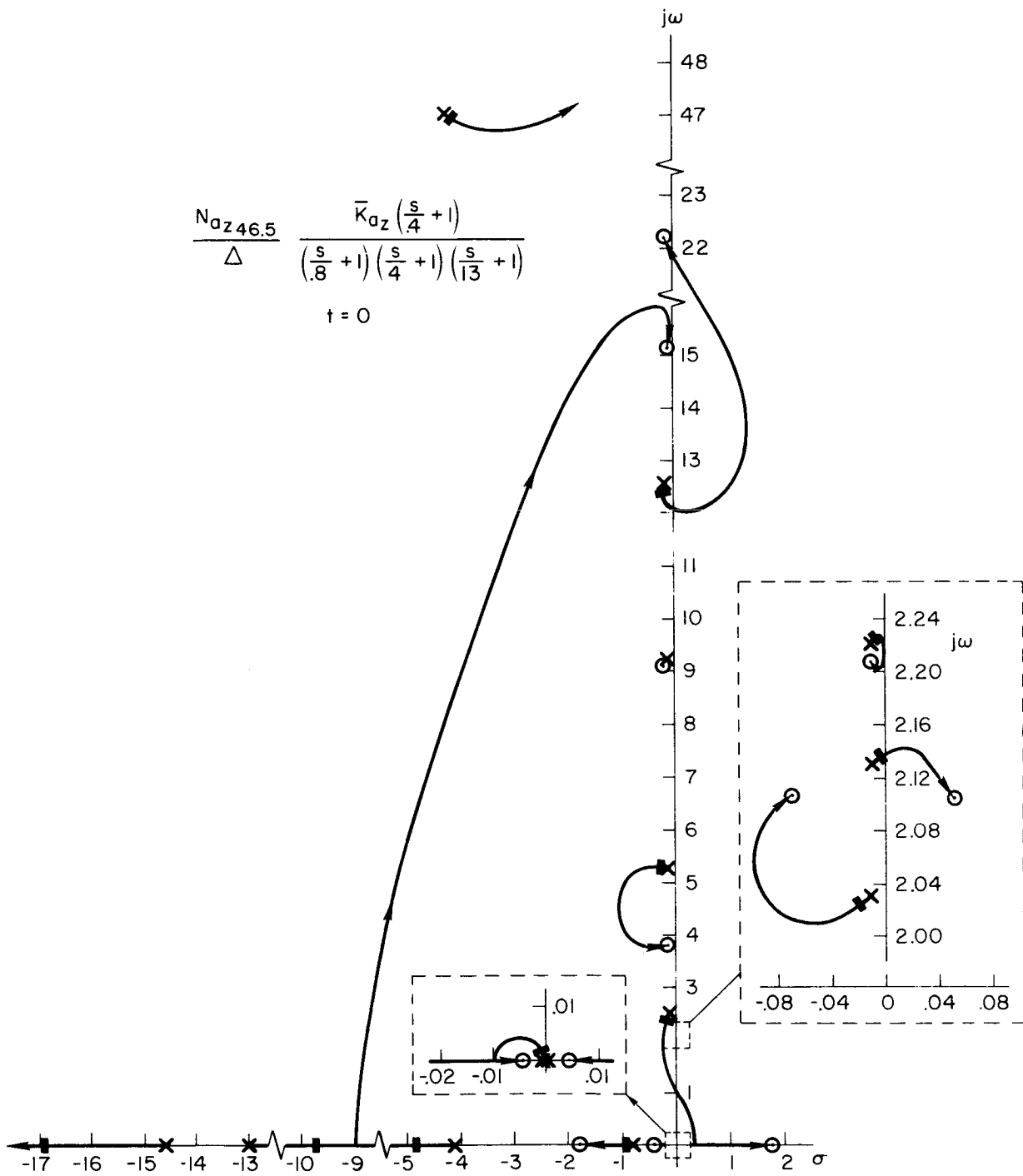


Figure 22. Root Locus for Acceleration Closure, $t = 0$

b. Attitude rate feedback. The effective-vehicle numerator for this loop closure is

$$\begin{aligned}
 D_{H_{a_z}}(s)N_{\dot{\phi}_{46.5}}(s) &= 2961.9s^3(s+0.8)(s+4)(s+7.89)(s-7.94)(s+13) \\
 &\times [0.0037; 1.724] [0.0051; 5.47] [0.0051; 11.19] \\
 &\times [0.00014; 21.6] \quad (26)
 \end{aligned}$$

Closing the $\dot{\phi}_{46.5}/\varphi_\epsilon$ loop (Fig. 13) with the $t = 80$ equalization and an appropriate gain,

$$H_{\dot{\phi}}(s) = \frac{-0.277\left(\frac{s}{0.1} + 1\right)}{s\left(\frac{s}{3} + 1\right)} \quad (27)$$

gives closed-loop dynamic characteristics defined by

$$\begin{aligned}
 \Delta'' &= 46.510s^3(s+0.118)(s+0.759)(s+4.30)(s+9.53)(s+16.7) \\
 &\times [0.812; 1.317] [0.169; 3.126] [0.0394; 5.18] [0.0154; 8.85] \\
 &\times [0.0082; 12.47] [0.099; 47.0] \quad (28)
 \end{aligned}$$

Note that the slosh modes have been neglected in the above transfer functions. This is to simplify calculation. Both the $t = 0$ and $t = 80$ sec a_z closures have indicated the desirability of employing tank baffling for the second slosh mode. Furthermore, the analysis for the $t = 80$ sec case indicated that these modes have relatively little movement for loop closures subsequent to the a_z closure. Thus, neglect of these modes should have little bearing on the results obtained.

From Figs. 23 and 24, the rigid-body and integration poles provide adequate low frequency amplitude ratio. The zero at 0.1 rad/sec stabilizes the rigid-body mode. The pole at 3 rad/sec phase-stabilizes and attenuates the third and fourth bending modes. The pole/zero pair near $\omega \doteq 5$ (second bending) represents a potentially critical aspect of this loop closure. If the zero were to shift to a value less than that of the pole, the lower departure at the $\omega \doteq 5$ pole would be shifted approximately 180 deg. Thus this mode would move almost directly toward the right half

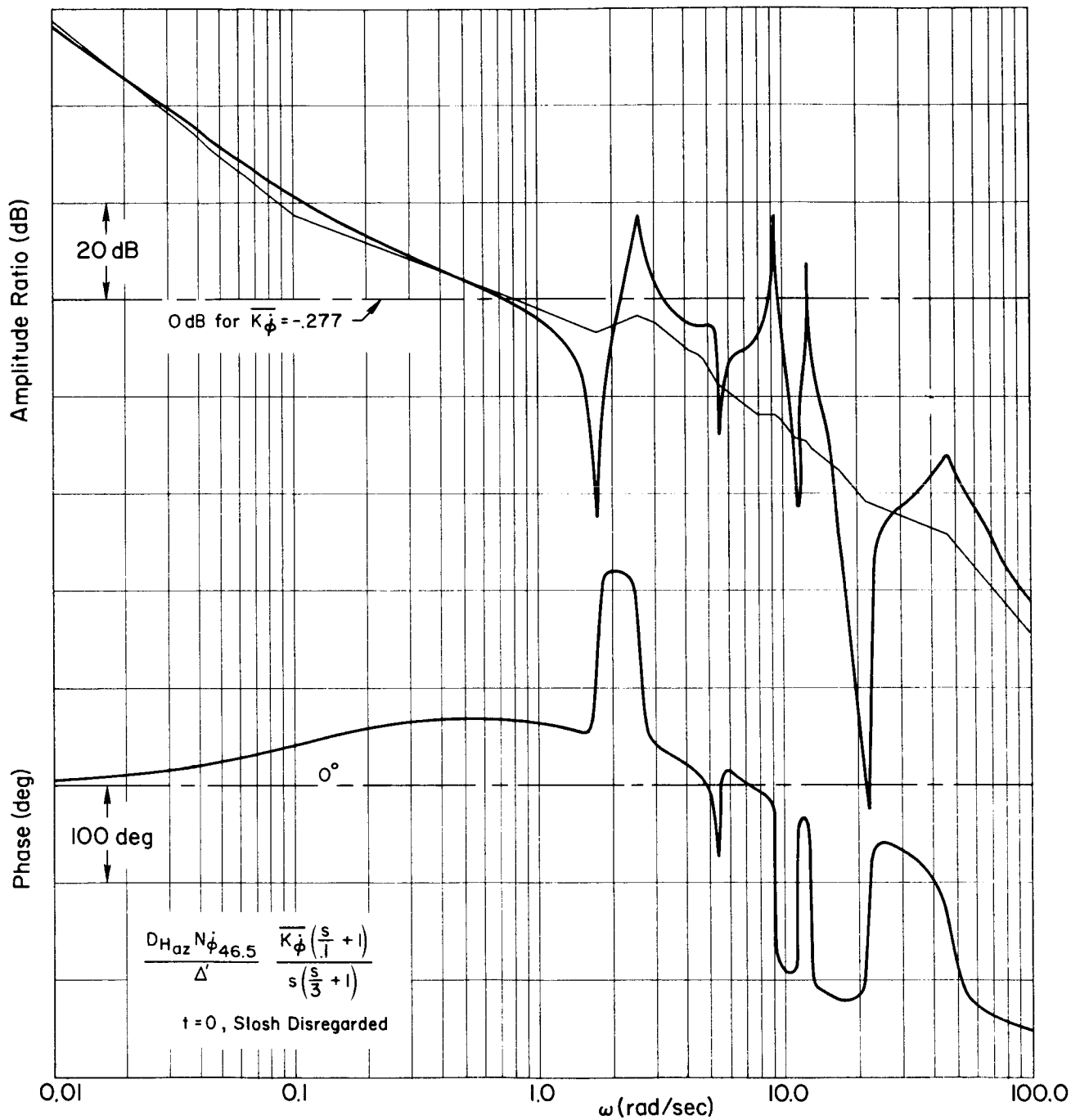


Figure 23. Attitude Rate Feedback Amplitude and Phase, t = 0

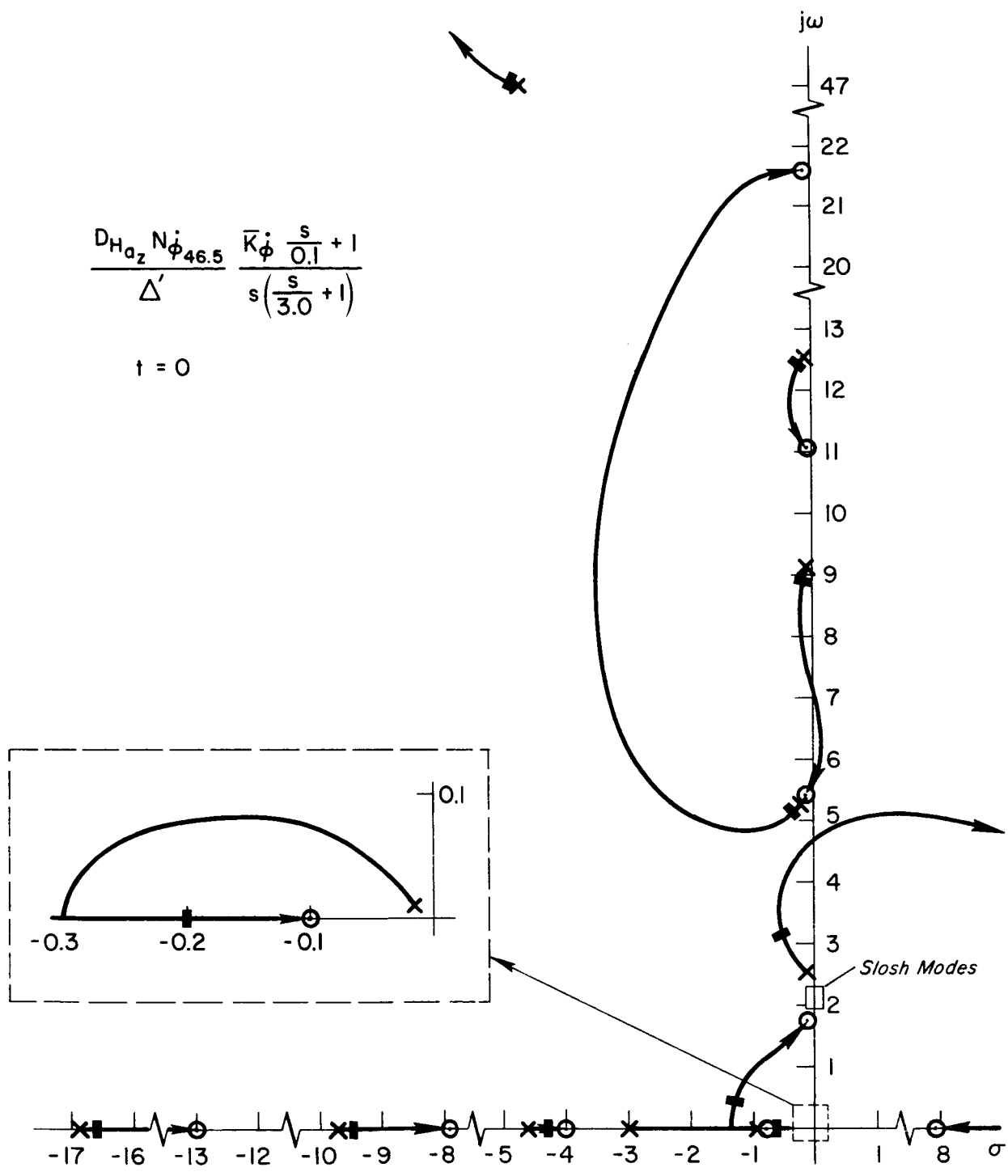


Figure 24. Root Locus for Attitude Rate Closure, $t = 0$

plane and instability. Or, if this second bending mode were to have greater damping (e.g., higher gain in the a_z loop closure) the phase lag would be increased in the region between 3 and 5 rad/sec. This would reduce the phase margin of the first bending mode.

For the closure as shown the gain margin is 6 dB and the phase margin is approximately 35 deg at 3.2 rad/sec.

c. Attitude feedback. Again neglecting the slosh modes, the effective-vehicle numerator is

$$\begin{aligned}
 D_{H_{a_z}}(s)D_{H_{\dot{\phi}}}(s)N_{\phi_{120.5}}(s) &= 1965.7s^3(s+0.8)(s+1.599)(s-1.6125)(s+3) \\
 &\times (s+4)(s+13)[0.797; 7.26][-0.792; 7.27] \\
 &\times [0.00499; 12.175][-0.0000037; 21.9]
 \end{aligned} \tag{29}$$

Closing the loop with the $t = 80$ equalization,

$$H_{\phi}(s) = \frac{-0.056\left(\frac{s}{0.05} + 1\right)}{s(s+1)} \tag{30}$$

gives closed-loop dynamic characteristics defined by

$$\begin{aligned}
 \Delta''' &= 46.510s^3(s+0.0437)(s+0.811)(s+4.29)(s+9.53)(s+16.66) \\
 &\times [0.312; 0.6725][0.928; 1.363][0.217; 3.178][0.025; 5.17] \\
 &\times [0.0165; 8.85][0.0082; 12.467][0.099; 46.98]
 \end{aligned} \tag{31}$$

From Figs. 25 and 26, the rigid-body and integration poles again provide adequate low frequency amplitude ratio. The zero at 0.05 stabilizes the rigid-body mode. The pole at 1 attenuates all of the bending modes. The pole near $\omega = 5$ (second bending) is probably the most critical aspect of this closure. Any decrease in damping of this mode (e.g., lower gain in either of the inner loops) will decrease the gain margin here. As it is now, there is about a 10 dB gain margin associated with this mode. Thus a slightly higher gain in the inner loops might be desirable.

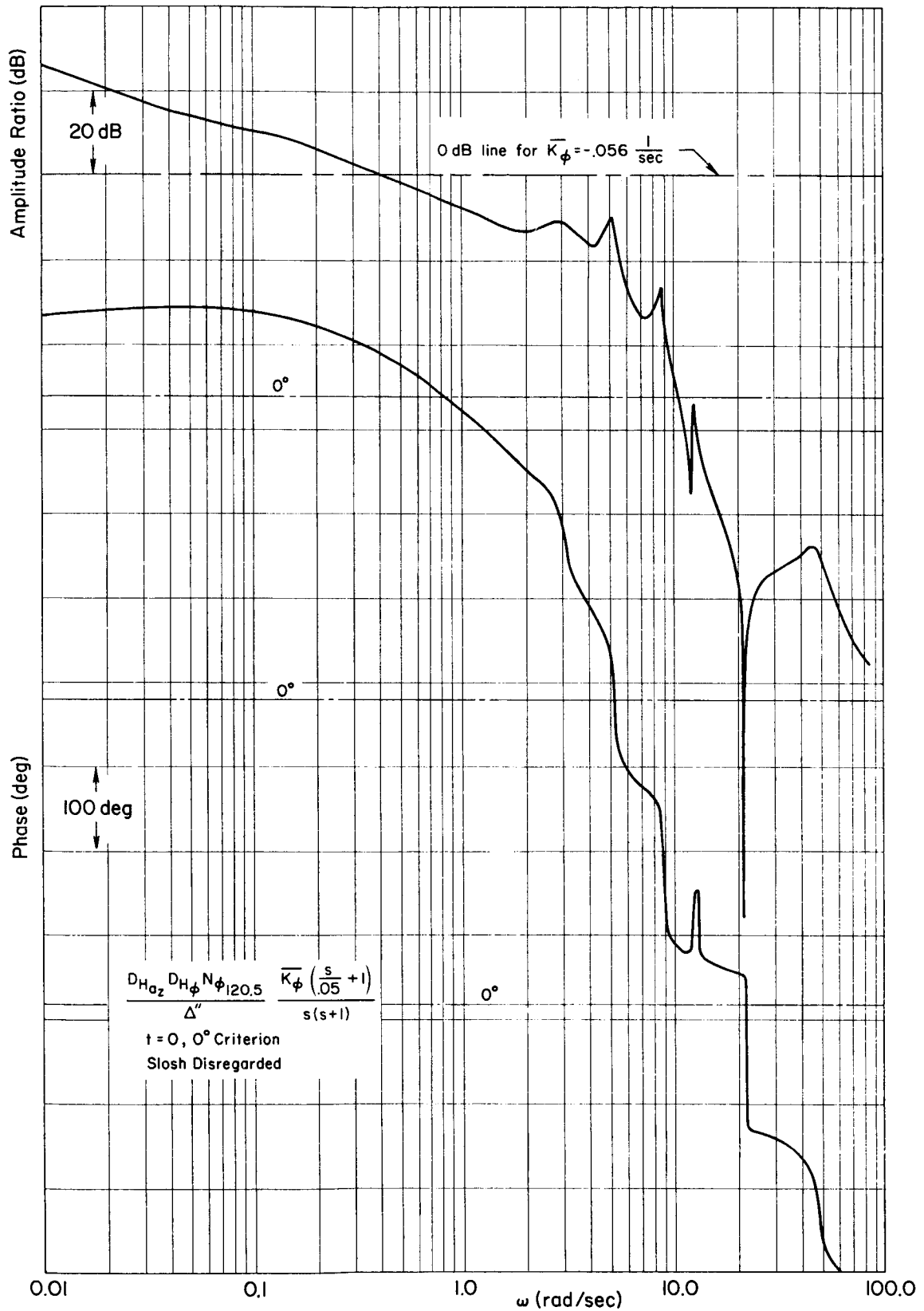


Figure 25. Attitude Feedback Amplitude and Phase, t = 0

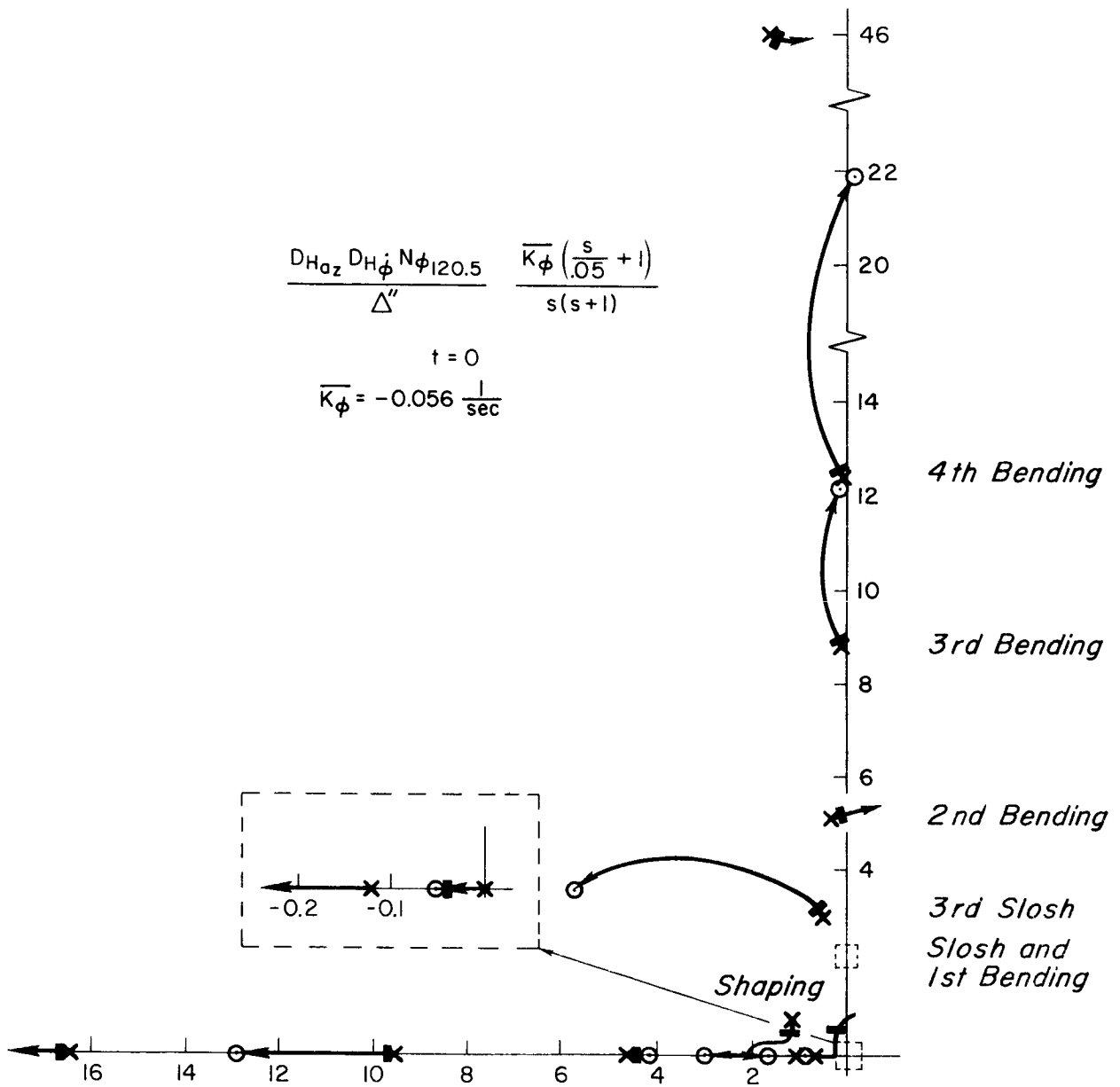


Figure 26. Root Locus for Attitude Closure, $t = 0$

As can be seen via the Bode plot, this is a relatively good loop closure with respect to low frequency amplitude ratio, phase and gain margins, and attenuation of elastic modes. The closed-loop rigid-body response ($\omega = 0.6725$, $\zeta = 0.312$) should be adequate for a vehicle of this size and the steady-state accuracy should be good.

As before, it probably would prove beneficial to adjust the inner loop gains somewhat. However, the equalizations selected for the maximum q ($t = 80$ sec) flight condition have proven satisfactory for this lift-off case.

3. Preburnout ($t = 157$ sec)

a. Attitude rate feedback. It is not desirable to close an accelerometer loop at this flight condition for two reasons. First, the accelerometer station (46.5m) is behind the vehicle c.g. Second, the rate gyro numerator exhibits the desired zero/pole sequence for all modes (at this flight condition the TWD zero is below the fourth bending pole). Therefore, only a rate gyro and an attitude gyro feedback are employed.

The open-loop transfer function is

$$\begin{aligned} \frac{\dot{\phi}_{46.5}}{\beta_c} &= \frac{N_{\dot{\phi}_{46.5}}(s)}{\Delta(s)} = \frac{-16,554s^2(s + 0.00007) [0.0026 ; 2.277] [0.0050 ; 3.595]}{38.752s(s - 0.0143)(s + 14.14) [0.176 ; 0.0407]} \\ &\times \frac{[0.0050 ; 3.756] [0.00508 ; 4.9528] [0.0050 ; 6.13]}{[0.0039 ; 3.409] [0.0048 ; 3.680] [0.0043 ; 4.027]} \\ &\times \frac{[0.0050 ; 11.69] [0.0007 ; 21.76]}{[0.005080 ; 4.9510] [0.0028 ; 7.42] [0.0046 ; 11.86]} \\ &\times \frac{[0.0045 ; 27.05]}{[0.0053 ; 24.99] [0.098 ; 52.5]} \end{aligned} \quad (32)$$

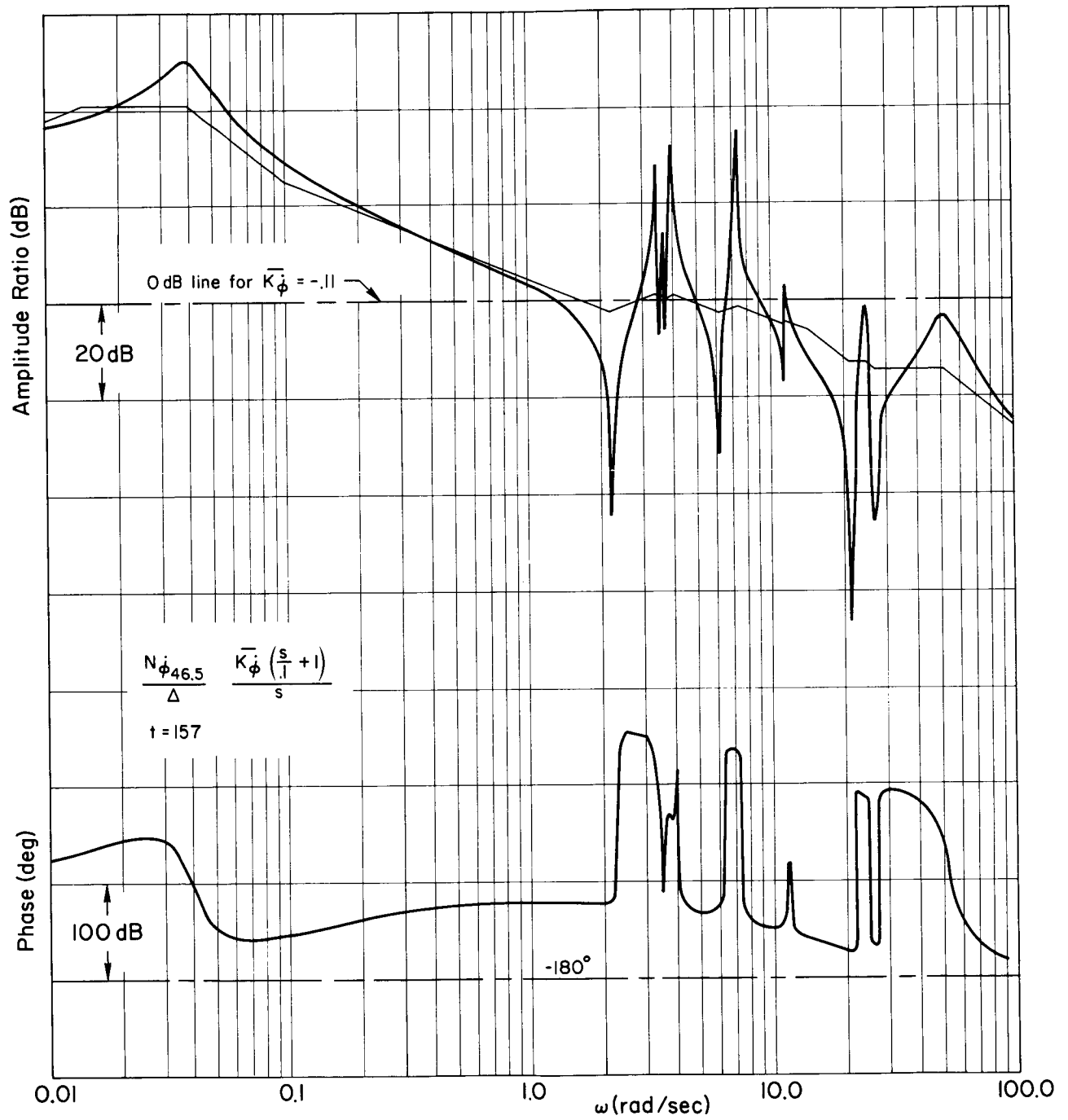


Figure 27. Attitude Rate Feedback Amplitude and Phase, $t = 157$

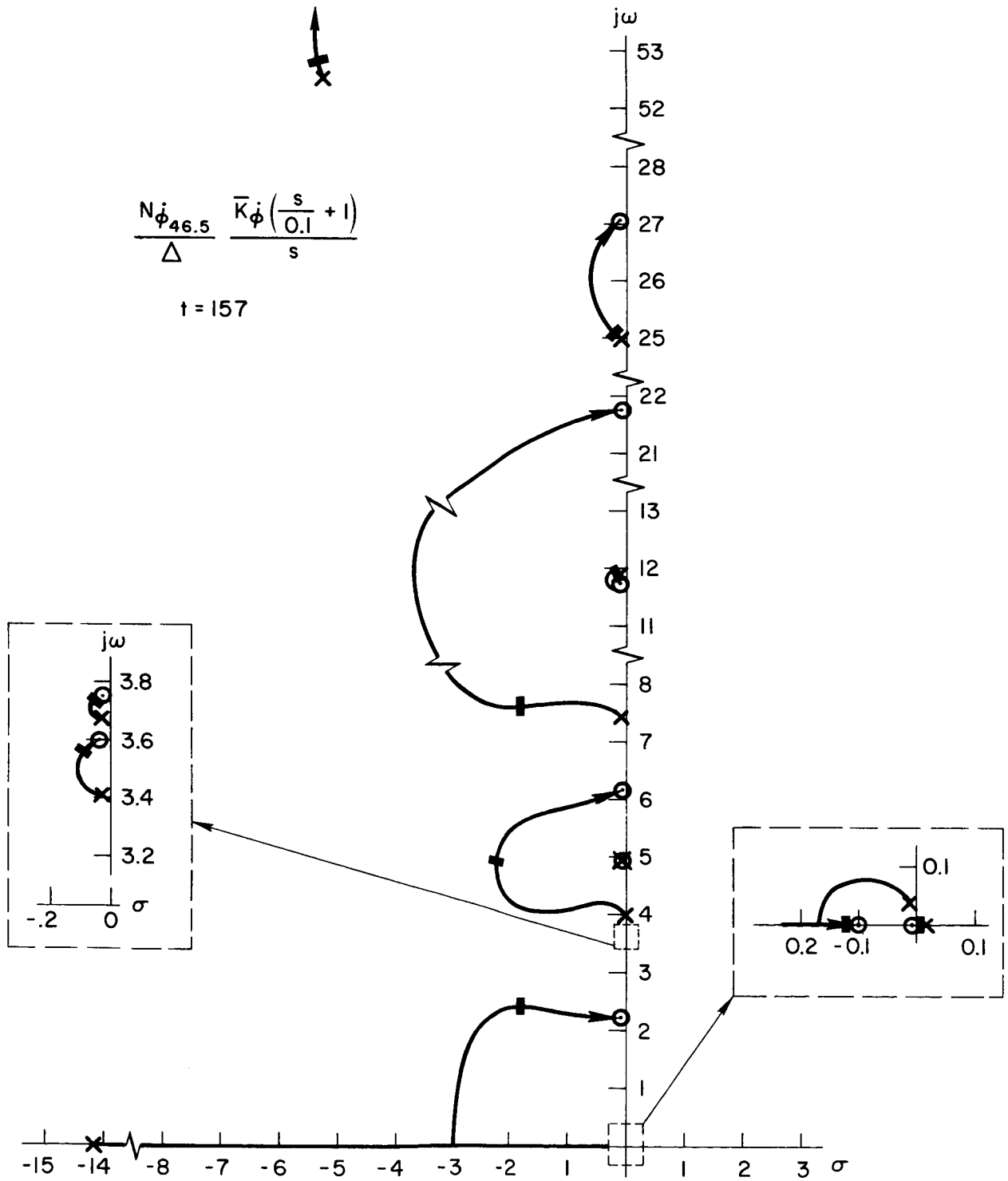


Figure 28. Root Locus for Attitude Rate Closure, $t = 157$

The feedback equalization and gain are

$$H_{\dot{\varphi}}(s) = \frac{-0.11\left(\frac{s}{0.1} + 1\right)}{s} \quad (33)$$

The previously employed lag at 3 rad/sec is detrimental to this closure and has been removed.

The closed-loop roots (exclusive of the slosh modes) are

$$\Delta' = 38.752s^2(s - 0.00007)(s + 0.108) [0.614; 3.00] [0.419; 5.42] \\ \times [0.236; 7.77] [0.012; 11.9] [0.007; 25.1] [0.11; 56.0] \quad (34)$$

From Figs. 27 and 28, this feedback exhibits the desired pole/zero alternation along the entire $j\omega$ axis. Thus all nonrigid modes remain stable for all gain values. The gain for this closure was selected to maximize the damping of the first bending mode. As a consequence the slosh poles are nearly driven into the slosh zeros and the contribution of these modes will be negligible.

Again the third bending pole/zero sequence is the critical aspect of this closure. Any shift in sensor location or vehicle characteristics which would interchange the relative positions of this pair could lead to instability.

b. Attitude feedback. The effective-vehicle numerator for this loop closure is given by (neglecting slosh modes)

$$D_{H_{\dot{\varphi}}} N_{\varphi_{120.5}} = 11,661s^2(s + 0.000082)(s + 3.08)(s - 3.11) \\ \times [0.005; 12.71] [0.82; 12.31] \\ \times [-0.82; 12.33] [0.0004; 19.6] \quad (35)$$

Closing the loop with the $t = 80$ sec equalization,

$$H_{\varphi}(s) = \frac{-0.0316\left(\frac{s}{0.05} + 1\right)}{s(s + 1)} \quad (36)$$

gives closed-loop dynamic characteristics defined by

$$\Delta'' = 38.752s^2(s + 0.000085)(s + 0.046) [0.45 ; 0.78] [0.71 ; 2.9] \\ \times [0.41 ; 5.60] [0.24 ; 7.71] [0.012 ; 11.9] [0.007 ; 25.1] [0.11 ; 56] \quad (37)$$

Figures 29 and 30 indicate that the rigid-body and integration poles provide adequate low frequency amplitude ratio, the zero at 0.05 stabilizes the rigid-body and the pole at 1.0 attenuates all of the nonrigid modes. The rigid-body mode is the first to reach instability; however, the feedback gain employed results in a 9 dB gain margin and a 50 deg phase margin. This provides a bandpass of $\omega = 0.78$ rad/sec.

4. Summary of System Mechanization

Because the foregoing loop closures are only a first-cut effort, there undoubtedly are many refinements that can be made. A few of the more obvious ones have been mentioned. The primary conclusion to be drawn, however, is that it is indeed feasible to use conventional sensors and relatively simple equalization to stabilize and control the Model Vehicle No. 2. Although the sensors are conventional, the use of normal acceleration feedback to damp the nonrigid modes of large flexible boost vehicles is considered unconventional.

The control equation employed is

$$\beta_c = H_{a_z}(s)a_{z46.5} + H_{\dot{\phi}}(s)\dot{\phi}_{46.5} + H_{\phi}(s)\phi_{120.5}$$

where

$$H_{a_z}(s) = \frac{\bar{K}_{a_z} [(s/0.4) + 1]}{[(s/0.8) + 1][(s/4) + 1][(s/13) + 1]} \quad \begin{array}{l} \text{All flight conditions} \\ (\bar{K}_{a_z} \equiv 0 \text{ at } t = 157 \text{ sec}) \end{array}$$

$$H_{\dot{\phi}}(s) = \begin{cases} \frac{\bar{K}_{\dot{\phi}} [(s/0.1) + 1]}{s [(s/3) + 1]} & \text{At } t = 0 \text{ and } t = 80 \text{ sec} \\ \frac{\bar{K}_{\dot{\phi}} [(s/0.1) + 1]}{s} & \text{At } t = 157 \text{ sec} \end{cases}$$

$$H_{\phi}(s) = \frac{\bar{K}_{\phi} [(s/0.05) + 1]}{s(s + 1)} \quad \text{All flight conditions}$$

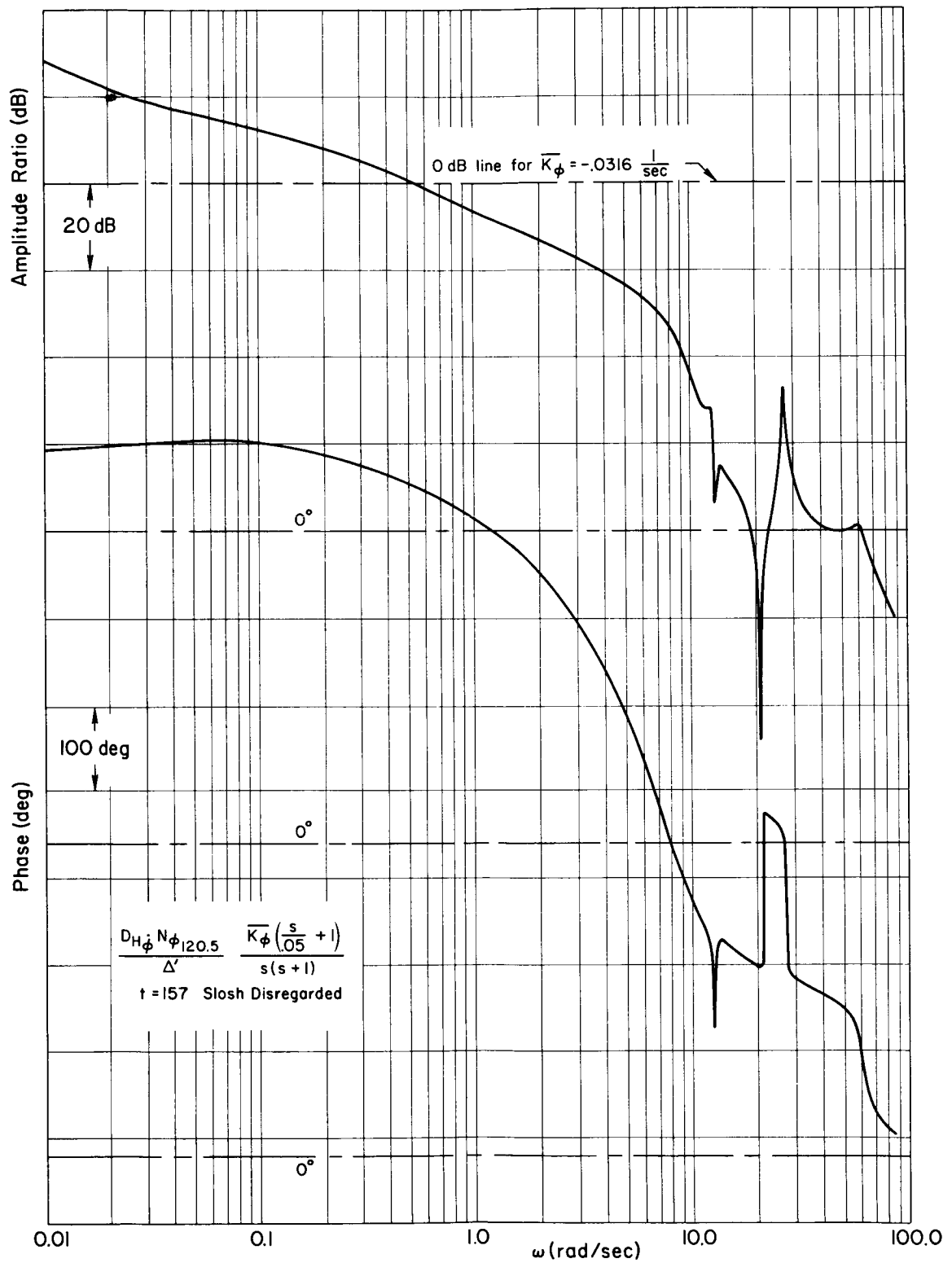


Figure 29. Attitude Feedback Amplitude and Phase, t = 157

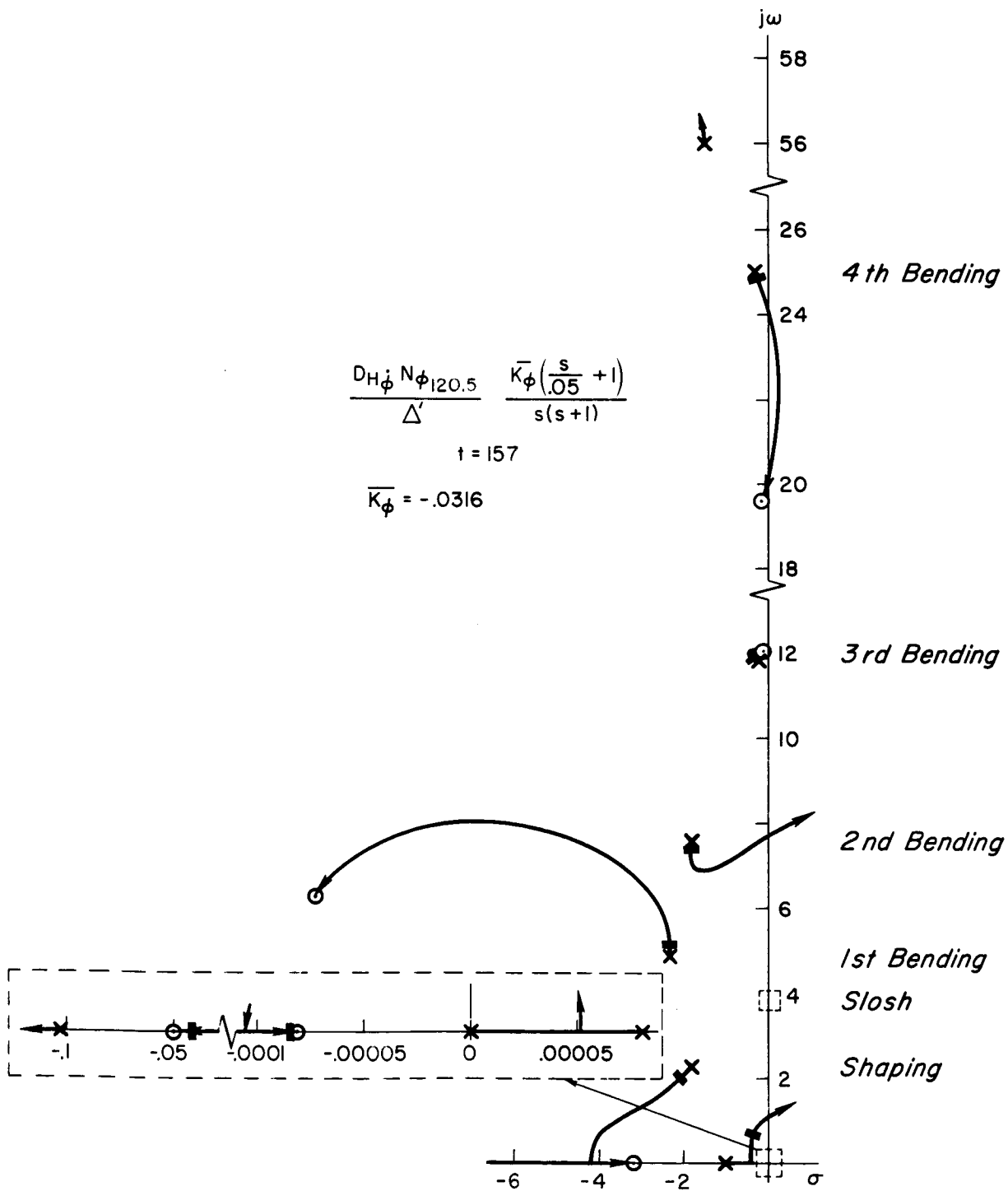


Figure 30. Root Locus for Attitude Closure, $t = 157$

The gain (preliminary) variation with flight time may be estimated, on the basis of values determined here, to be of the general form indicated in Fig. 31. Note that \bar{K}_{a_z} must be zero just before burnout ($t = 157$ sec). Also note that $\bar{K}_{\dot{\phi}}$ is essentially constant after reaching maximum q .

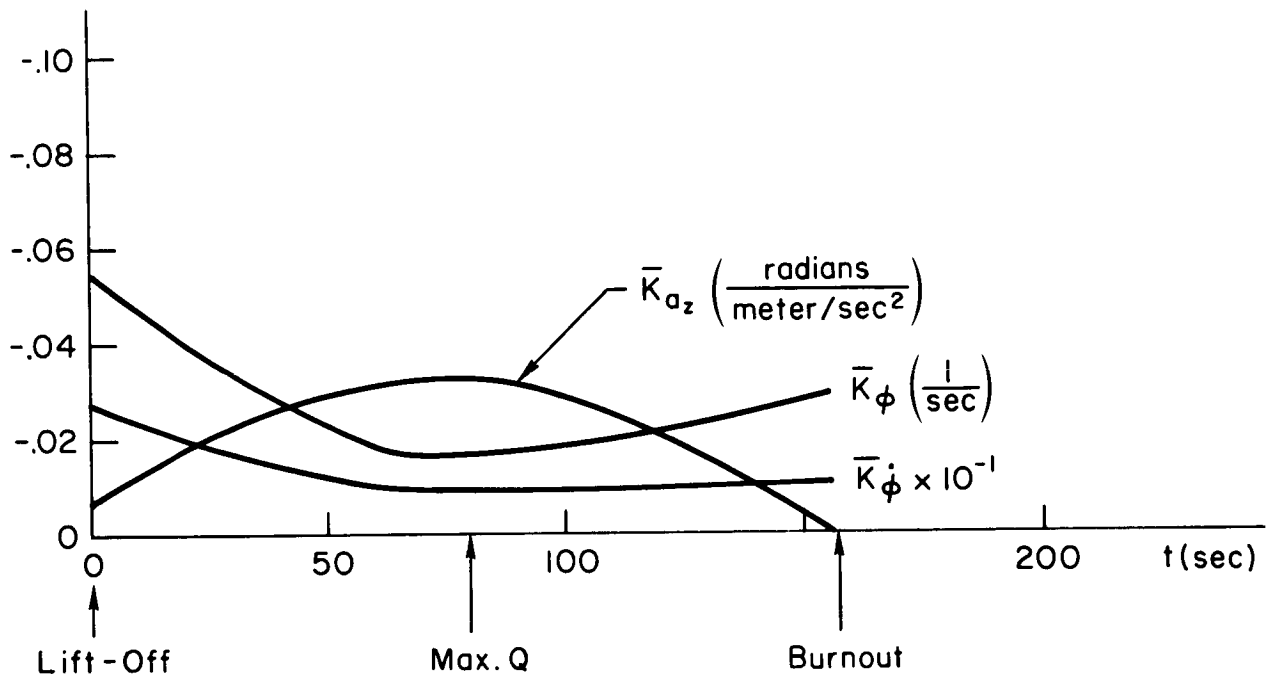


Figure 31. Gain Values as a Function of Time

Reflecting back on the Bode and root locus plots for all three flight conditions, it might be possible to adjust the loop gains so that $\bar{K}_{\dot{\phi}}$ will be constant throughout the flight. This might be accomplished by increasing \bar{K}_{a_z} and decreasing $\bar{K}_{\dot{\phi}}$ at $t = 0$. If this could be achieved, it would also result in \bar{K}_{a_z} remaining nearly constant over the period $0 < t < 80$ sec and then being decreased to zero in the period $80 < t < 157$ sec.

The required change in the rate gyro feedback equalization between $t = 80$ and 157 sec results from a combination of time-dependent effects (primarily total mass reduction and mass ratio changes). Since these changes are continuous and predictable, the equalization at $t = 157$ sec

can be obtained from that at $t = 80$ sec by making a programmed gain change. This may be seen as follows.

Consider the sum of the two equalizations with an additional gain parameter, K :

$$H(s,K) = (1 - K) \frac{K\dot{\phi}(s+0.1)}{s(s+3)} + K \frac{K\dot{\phi}(s+0.1)}{s} \quad (38)$$

Equation 1 can be rewritten as

$$H(s,K) = \frac{K\dot{\phi}(s+0.1)}{s} \left[\frac{K \left(s + 2 + \frac{1}{K} \right)}{s+3} \right] \quad (39)$$

The equalization at $t = 157$ is obtained from the equalization at $t = 80$ merely by changing K from zero to unity. When $K = 0$,

$$H(s,0) = \frac{K\dot{\phi}(s+0.1)}{s(s+3)} \quad (40)$$

and when $K = 1$,

$$H(s,1) = \frac{K\dot{\phi}(s+0.1)}{s} \quad (41)$$

As K goes from zero to unity, the "zero" is moved in along the negative real axis (from infinity) to cover the pole at 3 . However, for practical purposes the zero need only move to below 10 rad/sec to provide sufficient lead to stabilize the $t = 157$ case.

As a final comment, it is necessary to employ some tank baffling to assure that one or two critical slosh modes remain stable. However, this analysis has indicated that the baffling only need be located in the upper portions of the tank(s), i.e., sufficient to provide effectiveness through $t = 80$ sec. In addition, the coupling approximations of Ref. 1 indicate that increasing the uncoupled damping of any one slosh mode will, through modal coupling, also increase the damping of the other two slosh modes. Thus it may be possible to achieve the desired damping, yet restrict the baffling to a single tank. The subject of tank baffling is explored briefly in Appendix F.

C. LOAD RELIEF SYSTEM

In addition to vehicle attitude stabilization and control, the study objectives included consideration of loads induced by wind shear. The specific requirements were that the maximum bending moment be less than 2.7×10^6 kg-lb-m and the drift be less than 10m/sec in the presence of the MSFC synthetic wind profile given in Ref. 8. This profile is such that the maximum wind velocity is encountered at approximately $t = 80$ sec and the wind shear buildup essentially starts at $t = 66$ sec. Thus the "frozen" flight condition at $t = 80$ sec was employed for this preliminary analysis of a load relief system.

Load relief is achieved by feeding back normal acceleration, sensed at Station 58.5m, as an outer loop to the stabilization and control system presented in the foregoing (Subsection B-1). The effective-vehicle transfer function is, therefore,

$$\frac{D_{H_{a_z}} D_{H_{\phi}} D_{H_{\psi}} N_{a_z}_{58.5}(s)}{\Delta'''} = \frac{K_{a_z} s^3 (s - 0.0406)(s + 0.8)(s + 1)(s + 4)(s + 13) \times (s + 89.9)(s - 95.3) [0.8665; 1.185] \times [-0.8811; 1.116] [0.0125; 4.412] \times [0.0082; 10.87] [0.0004; 22.65]}{\Delta'''} \quad (42)$$

The feedback equalization was selected to be

$$H_{a_z}_{58.5}(s) = \frac{K_H}{s(s + 0.5)} \quad (43)$$

Bode and root locus plots are presented in Figs. 32 and 33. The dynamics of primary concern are the bandpass frequency of $\omega \doteq 0.38$ rad/sec and the low frequency first-order divergence. It suffices to verify that all other modes remain stable.

The performance assessment was accomplished for the pitch plane using a wind shear input $w = W \cos \chi$, where χ is the flight path angle from the vertical and W is the aforementioned MSFC synthetic wind profile (see Fig. 34). Time responses were obtained via simultaneous

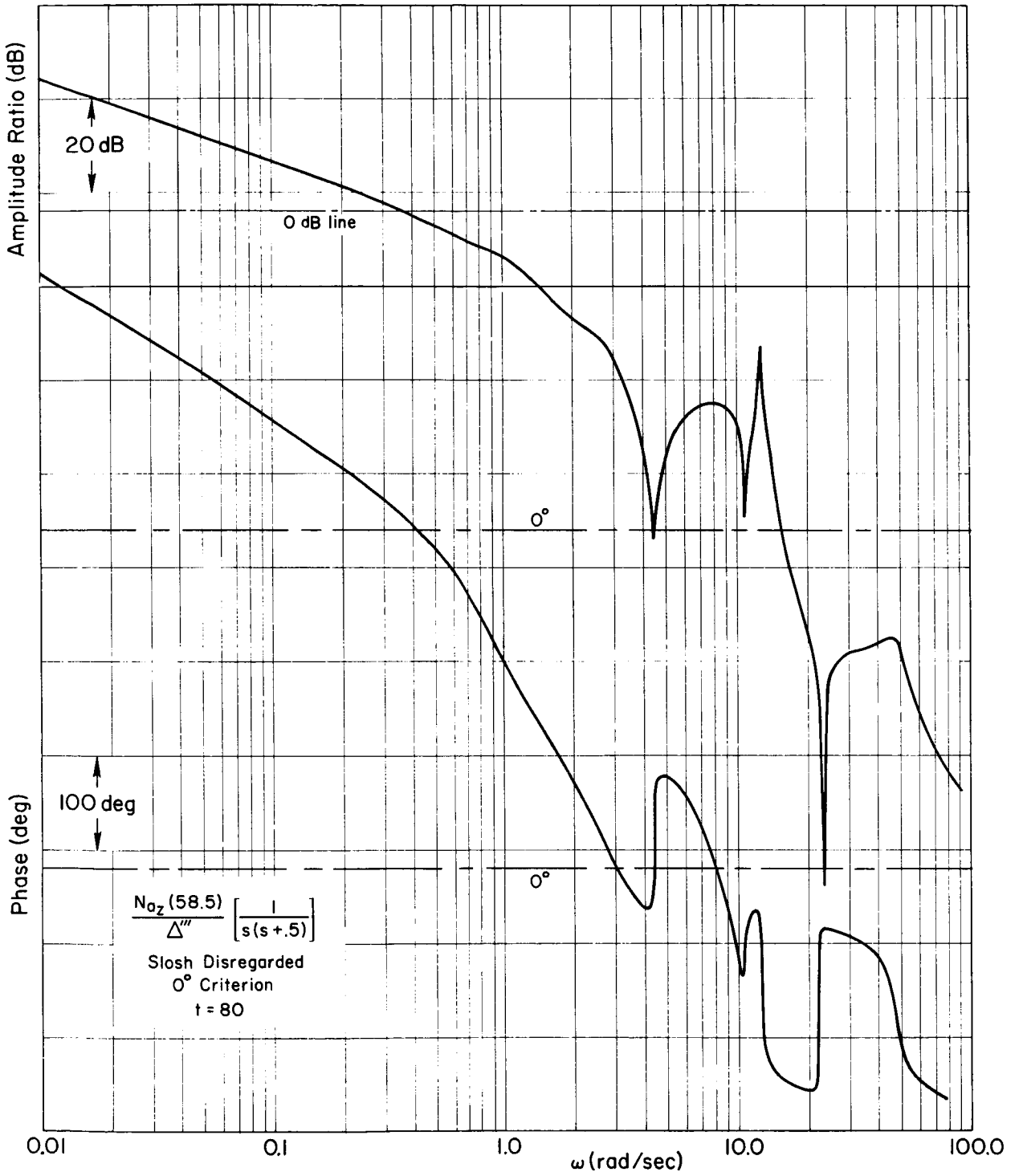


Figure 32. Load Relief Acceleration Feedback Amplitude and Phase

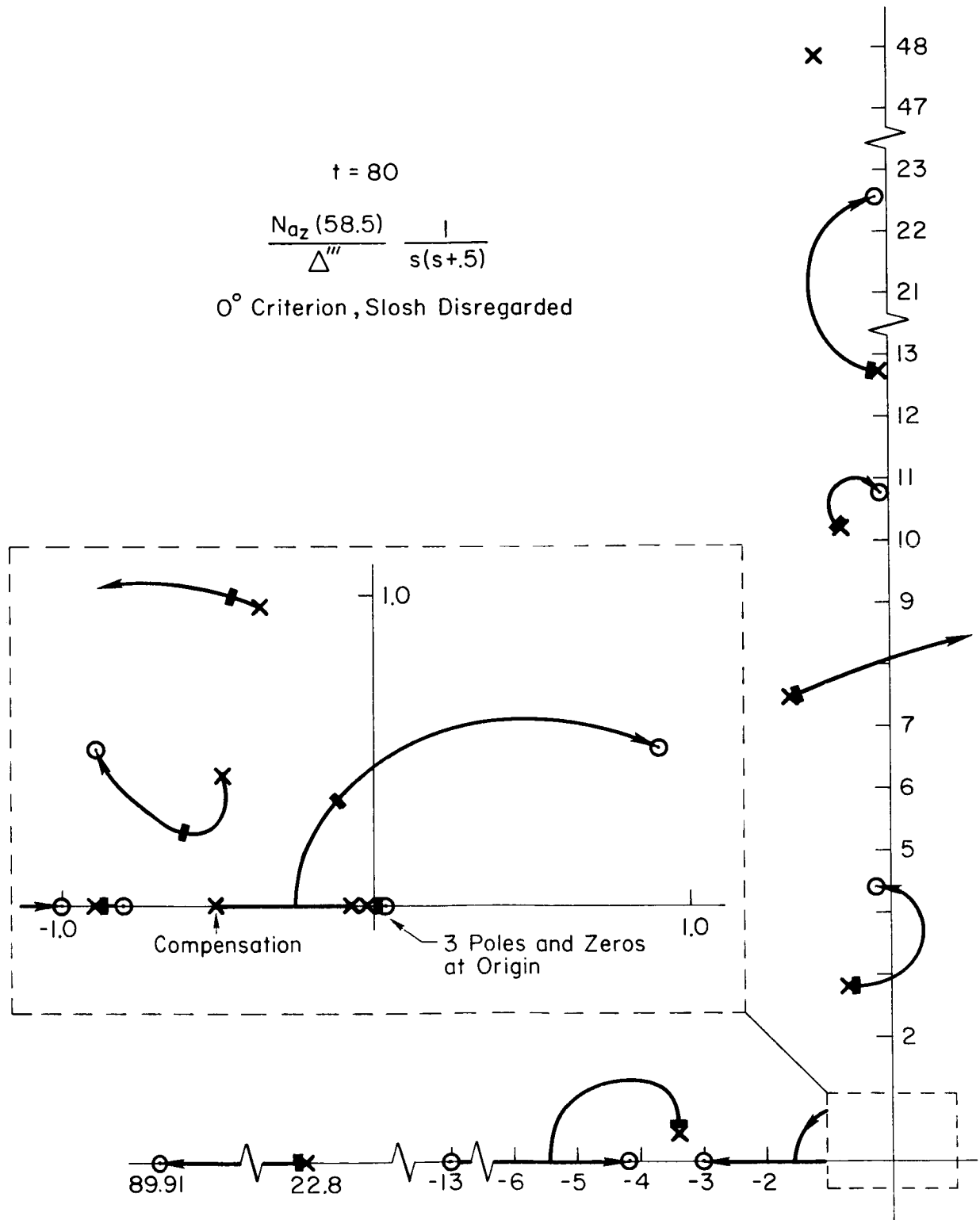


Figure 33. Root Locus for Load Relief Closure

$$w = W \cos \chi$$
$$\chi = 40 \text{ deg}$$

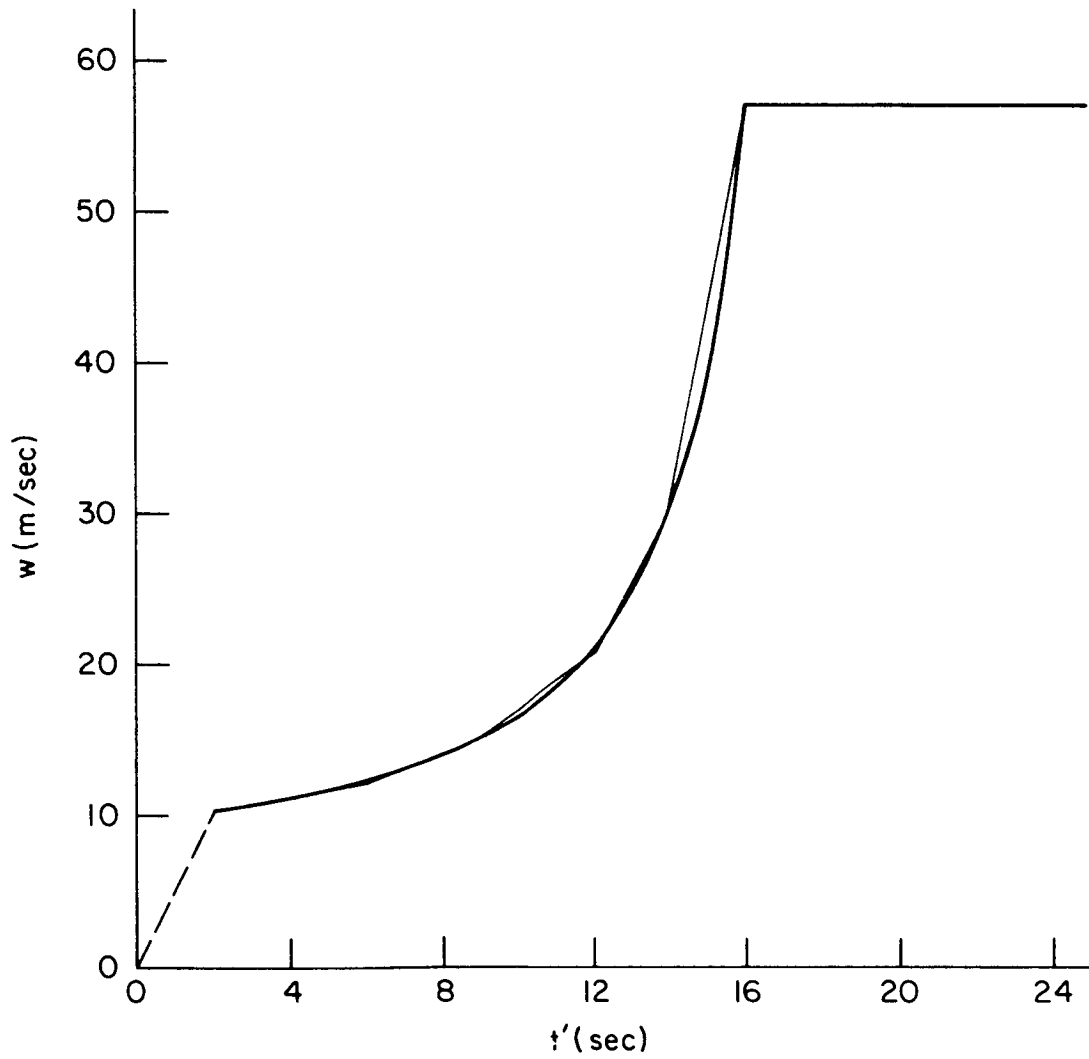


Figure 34. Wind Shear Input

solution of the fixed operating point equations of motion on an IBM 7094 (MIDAS program). The wind profile was approximated by the straight-line segments shown in Fig. 34. To avoid unnecessary complication, the equations of motion were truncated, via the static correction technique of Ref. 1, to include only the rigid-body and first bending contributions. The comparison of the truncated and exact closed-loop root locations is

$$\begin{aligned} \text{Exact: } \Delta''' &= s^3(s - 0.0275)(s + 0.894) [0.2954 ; 0.3699] \\ &\quad \times [0.9241 ; 0.6454] [0.4092 ; 1.0995] \end{aligned}$$

$$\begin{aligned} \text{Truncated: } \Delta''' &= s^3(s - 0.0274)(s + 0.934) [0.2676 ; 0.3573] \\ &\quad \times [0.9334 ; 0.5871] [0.2802 ; 1.428] \end{aligned}$$

Bending moment was calculated at three locations on the vehicle (see Fig. A-12) which bracketed the expected location of maximum bending moment (Station 31.5m). For this preliminary analysis the bending moment was assumed to be defined as

$$MB \doteq M_{\alpha}' + M_{\beta}'$$

Runs were made with three different values of load relief loop gain. The load relief loop remained closed throughout the runs. Figure 35 presents the results for the lowest gain employed (approximately 10 dB below the gain line shown in Fig. 32).

The maximum bending moment of 2.6×10^6 kg-lb-m was registered at Station 31.5m and is just within the criteria value of 2.7×10^6 kg-lb-m. It appears that this bending moment can be reduced appreciably by reducing the attitude loop gain to achieve a better balance between the attitude and load relief loops.

While the vehicle drift shown does not meet the 10m/sec criteria, it is apparent that the large drift is due to the rigid-body first-order divergence mode which, in turn, is due to the load relief loop remaining closed long after the peak wind shear has been passed. This can be remedied by either time-programming the load relief loop closure to

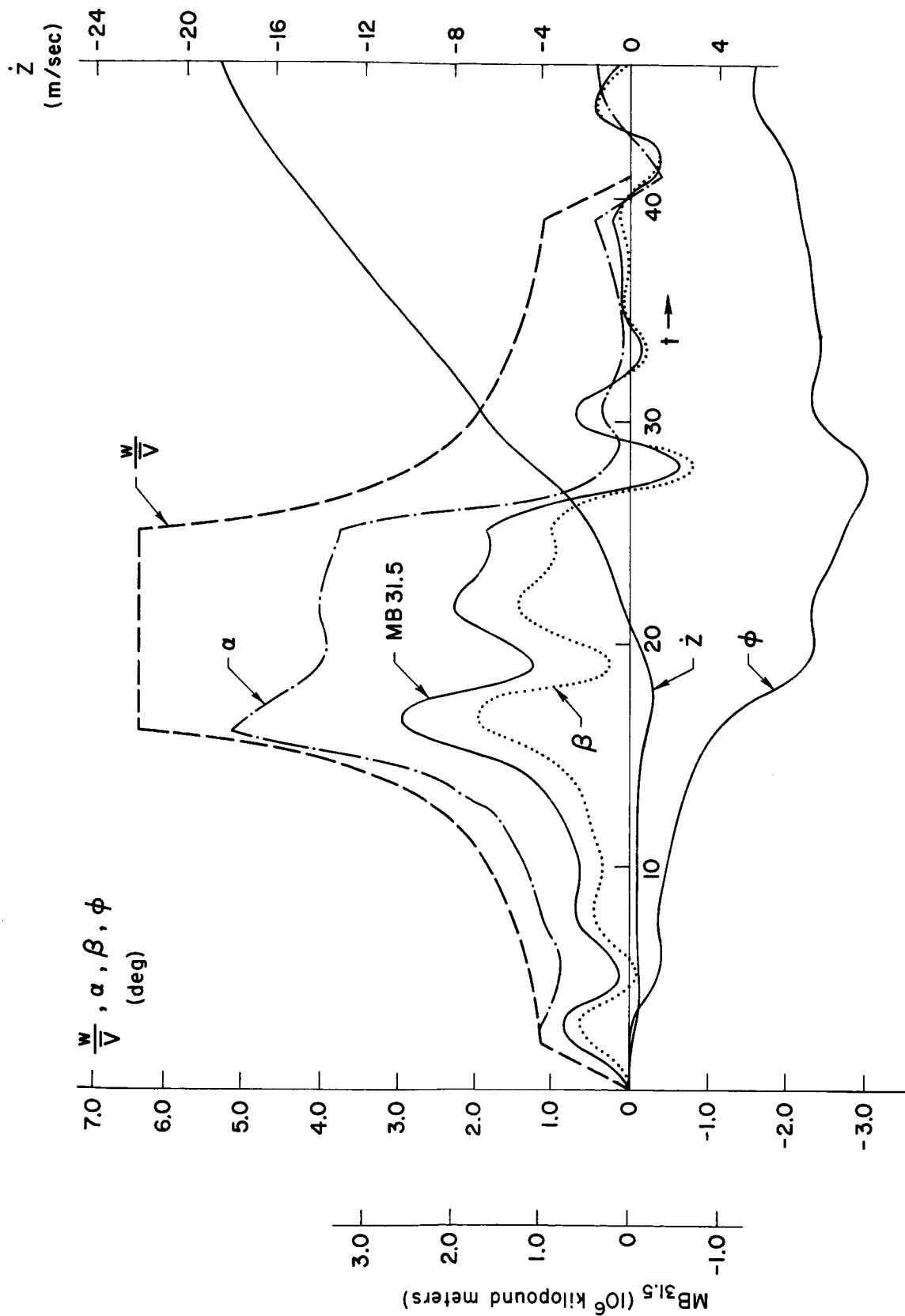


Figure 35. Closed-Loop Time Response to Wind Shear Input

coincide with predicted wind shear encounter or, preferably, by placing a threshold in the acceleration feedback.

Time limitations did not permit investigation of the above refinements, but there is no reason to believe that the load relief and drift requirements cannot be met in the pitch plane. There is some question whether this same mechanization would be adequate for yaw plane control, however. In this plane the vehicle profile is perpendicular to the wind shear so that $w = W$. The peak wind is therefore 75m/sec instead of 57.5m/sec as shown in Fig. 34. Accordingly, we would have to achieve roughly a 30 percent reduction in the pitch plane bending moment before we could expect this system to operate satisfactorily as a yaw plane load relief system.

SECTION IV
SENSITIVITY ANALYSIS

The preceding synthesis has shown that, on a first cut basis, a relatively simple controller may be feasible for Model Vehicle No. 2. In this section we shall investigate the sensitivity of this system to variation in system parameters. In particular, it is pertinent to determine or identify

- a. critical or potentially critical aspects of our vehicle/controller system
- b. the related physical parameters
- c. the likelihood of the critical situation developing (or the preciseness with which certain parameter values should be known)

One possible approach is to vary individual open-loop parameters and to determine, directly, the effect on closed-loop roots. Such a brute force method not only is impractical, but it provides little "feel" for system modifications which might alleviate any problem areas uncovered. Another possible approach is the sensitivity and modal response technique of Ref. 3. In Ref. 3, sensitivity is defined as a partial derivative of a system root with respect to some open-loop parameter. To give some feeling for what is involved, the variation in a closed-loop pole, dq_i , for a single-loop closure can be expressed as

$$dq_i = S_K^i \frac{dK}{K} + S_{z_j}^i dz_j + S_{p_j}^i dp_j \quad (44)$$

where K is the open-loop gain, z_j an open-loop zero, and p_j an open-loop pole. The sensitivities themselves are given by

$$\begin{aligned} S_K^i &= \frac{\partial q_i}{\partial K/K} = \frac{1}{(\partial G/\partial s)_{s=q_i}} \\ S_{z_j}^i &= \frac{\partial q_i}{\partial z_j} = \frac{S_K^i}{q_i + z_j} \\ S_{p_j}^i &= \frac{\partial q_i}{\partial p_j} = \frac{-S_K^i}{q_i + p_j} \end{aligned} \quad (45)$$

where G is the open-loop transfer function. Corresponding relationships for multiple loop closures are given in Ref. 3.

In general, the sensitivities will be complex numbers, or vectors in the s -plane, which indicate directly the changes in the damping and frequency of a root due to variations in an open-loop parameter. As may be readily appreciated, the calculation of such sensitivity measures for each closed-loop pole of the Model Vehicle No. 2, which involves a twenty-first order denominator and an eighteenth order numerator (for attitude sensing), is a monumental task. Further difficulty lies in the small separation of the open-loop poles and zeros and the closed-loop poles of the three slosh modes and either the first or second bending (or both).

This generalized method was briefly investigated and abandoned in favor of a more practical method in which the major (and crucial) effects of a change in open-loop parameters is obtained from manipulation of the simplified equations and the Bode and root locus plots employed in the system synthesis. In short, the sensitivity considerations are approached from the viewpoint of the change required in vehicle/controller dynamics to cause the system response to become critical (e.g., unstable) in a specific manner. The required dynamic change is then related to the dominant physical characteristic which can bring about the critical state.

For example, in the region for which $G \gg 1$ the closed-loop response is dominated by zero location. Consequently, sensitivity to zero location relative to the left-half-plane is of major concern. Gain sensitivity is low in this region. For the region in which $G \ll 1$ the closed-loop response is dominated by pole location. Here, sensitivity to pole location relative to the left-half-plane is of major concern. Again, gain sensitivity is low.

For Model Vehicle No. 2 the above sensitivities are readily handled. The zeros of interest arise from the rigid-body mode and low frequency controller equalization. Approximate expressions allow direct evaluation of zero shifts due to change in vehicle and/or controller parameters. The poles of interest ($G \ll 1$) are limited to the actuator/engine compliance mode. Again, a good approximation is available from which to determine dominant parameters and effects of parameter change.

Within the region where $G \dot{=} 1$, gain sensitivity is high and we are vitally interested in pole and zero location (sequence and separation). Unfortunately, all of the nonrigid vehicle modes, except for the compliance mode, fall within this region. To cope with this, the Bode and root locus plots for all sequential loop closures must be studied simultaneously with perturbations (shifts) in poles and zeros visualized and/or sketched. Key factors which are relatively sensitive or insensitive are noted and, for each of the highly sensitive aspects, an appropriate treatment and sensitivity measure worked out. Wherever possible this measure will be obtained from physical understanding and analytical information already at hand. Where this does not suffice, a procedure will be outlined for providing the sensitivity.

A. DETERMINATION OF POTENTIAL PROBLEM AREAS

The discussion accompanying the system synthesis plots of Section III indicated some potential instability problem areas. We shall pursue these further in this subsection as well as hypothesize other possibilities.

The closures of Section III were predicated on a minimum of 6 dB gain margin and, for the most part, 45 deg phase margin. Since the controller (sensor, actuator, circuitry, etc.) gain and phase characteristics are generally well known (in comparison with vehicle characteristics) and easily altered, we shall not concern ourselves here with possible variations originating within the control system. We shall focus attention on those aspects which relate to possible variations in vehicle characteristics.

As indicated previously, the major problem areas are expected to lie in the region $G \dot{=} 1$ where gain sensitivity is high. For the inner loops this generally concentrates attention on the vehicle nonrigid modes which, unfortunately, can be expected to be the least well known.

In keeping with the sequence of flight condition presentation in Section III, we shall investigate first the $t = 80$ sec case and follow with the $t = 0$ and $t = 157$ sec cases.

1. $t = 80 \text{ sec}$ (Figs. 15 through 20)

Starting with the innermost loop ($a_z \rightarrow \beta$), Fig. 15 indicates that the closure line is nearly coincident with the horizontal, low frequency, open-loop asymptote. Thus the low frequency (rigid body) closed-loop roots resulting from this first closure are highly sensitive to open-loop gain changes. As little as $\pm 0.5 \text{ dB}$ gain change could result in a pair of these closed-loop roots lying on the real axis in the right-half-plane (RHP) of Fig. 16 or all roots lying entirely in the left-half-plane (LHP). Despite the seemingly wide latitude of movement possible for these roots their precise location is not crucial since these rigid-body modes are readily stabilized by the $\dot{\phi}$ and ϕ feedbacks (Figs. 18-20). The only zero into which one root ultimately is driven is a controlled (equalization) zero and hence is assured of being stable.

The pair of real zeros at approximately $\pm 0.5 \text{ sec}^{-1}$ arise from the center-of-percussion effect of the acceleration feedback. These zeros will move out the real axis if the accelerometer is moved forward (toward the vehicle center-of-rotation for forces applied at the gimbal station) and toward the origin if the accelerometer is moved aft. The major concern here is that these zeros not lie inside the vehicle open-loop poles at roughly $\pm 0.3 \text{ sec}^{-1}$. If this should occur, the acceleration feedback would destabilize the rigid body—perhaps sufficiently that the $\dot{\phi}$ and ϕ closures could not restabilize it. Presumably the vehicle center-of-rotation and accelerometer location should be sufficiently well known to preclude the latter.

Turning attention to the nonrigid modes, it was noted in Section III that the fuel tanks would have to be baffled to achieve stability in the slosh modes. Therefore, this factor will not be belabored further here. The next most crucial aspect of Figs. 15 and 16 is the fourth bending mode. The controller shaping has been selected to place the 180 deg phase crossover in the amplitude ratio valley between the third and fourth bending peaks. For the existing vehicle this provides a gain margin of approximately 7 dB. Any combination of dynamic variations which would increase the amplitude ratio greater than 7 dB at 12.5 rad/sec would destabilize the fourth bending mode. If this should occur, Figs. 17-20 indicate it is doubtful the $\dot{\phi}$ and ϕ closures would restabilize the mode.

It is obvious from Fig. 15 that any increase in separation of the fourth bending pole-zero pair will be detrimental since this would increase the peaking at and below the fourth bending pole. Based on a comparison of fourth bending pole/zero separation effects in Figs. 15 and 21, it appears that the fourth bending zero (Fig. 15) would have to increase by more than 15 percent for instability to occur. A decrease in the fourth bending frequency (pole) should not, in itself, have appreciable effect on the pole/zero separation since pole/zero separation is controlled primarily by the mode shape at the sensor location. A decrease in separation between the third and fourth bending poles would also be detrimental; however, the separation decrease would have to be almost 50 percent of the present separation—which is unlikely.

Insofar as the other nonrigid modes are concerned, the acceleration closure can stand greater than 15 percent shifts in the various poles or zeros without seriously courting instability in any of the loops.

Figures 17-20 indicate considerable safety margin on all modes providing the fourth bending remains stable from the acceleration loop closure.

2. $t = 0$ sec (Figs. 21 through 26)

Again starting with the innermost (a_z) loop, it is apparent from Figs. 21 and 22 that the fourth bending mode (12.5 rad/sec) is a crucial mode for this feedback. The closure shown exhibits but 5 dB gain margin at the fourth bending peak. The gain sensitivity could be improved appreciably by adjusting the equalization lag to obtain an additional 30 deg of phase lag at roughly 11 rad/sec. This would place the 180 deg phase crossover in the bottom of the amplitude ratio valley at 11 rad/sec. The loop gain then could be increased appreciably but at the expense of destabilizing the second slosh mode and increasing the criticalness of the third bending pole/zero pair. [A quick check of the $t = 80$ sec case (Fig. 15) indicates that the additional 30 deg of phase lag could be tolerated at 11 rad/sec if the loop gain were reduced approximately 4 dB. Such a compromise should be acceptable since the $t = 80$ sec gain is actually higher than necessary.]

Looking ahead to the ϕ closure (Figs. 23 and 24), it is apparent that the second bending pole/zero pair (at roughly 5 rad/sec) and the third bending pole (at approximately 9 rad/sec) could easily become critical. For example, a reversal of the second bending pole/zero sequence would lead to a decrease in damping of this mode by the ϕ closure. From Figs. 25 and 26 it can be seen that the damping of this mode is further decreased by the ϕ closure and could lead to instability. Thus at lift-off ($t = 0$ sec) we have potential problems with the second, third, and fourth bending modes.

The problem of the fourth bending mode would be reduced and that of the second bending essentially eliminated if the previously indicated change in a_z loop equalization were made and the loop gain increased at lift-off. This can be visualized from Fig. 22 wherein a 30 deg counter-clockwise rotation of the fourth bending departure and an increase in gain could provide satisfactory damping in this mode. Also note in Fig. 21 that the 180 deg phase crossover would shift from 12.1 rad/sec to approximately 11 rad/sec. Thus the locus of Fig. 22 would shift sufficiently that the gain in the a_z loop could be increased to place the closed-loop root at, say, 12 rad/sec which should provide sufficient damping of this mode to remove it from further concern even in the ϕ loop (Figs. 25 and 26).

The problem of the second bending mode would be alleviated by this same a_z loop gain increase which should place the closed-loop root (Fig. 22) in the vicinity of the midpoint of its locus. Comparison of the resulting second bending root locations in Figs. 22, 24, and 26 indicate that this mode should then be of little further concern.

The remaining crucial aspects are the third bending mode and the second slosh mode (the latter should have been destabilized by the increased a_z loop gain). Again we shall sidestep the slosh problem by assuming tank baffling and concentrate on the third bending.

Referring back to Fig. 22, it is apparent that if the third bending zero at roughly 9 rad/sec were increased approximately 1 percent the closed-loop pole would be destabilized instead of stabilized. The closeness of the pole and zero indicates that the sensor is essentially at a node of the third bending mode shape. (The accelerometer is actually

0.5 meter aft of the node). Thus, the accelerometer should be moved farther aft to assure that the pole/zero sequence remains as shown in Fig. 22. This would also increase the separation between the pole and zero, and hence result in greater damping of the mode by the a_z closure. Since the node for the third bending mode moves forward with time, an aft shift of the sensor would tend to assure that the pole/zero sequence remains proper at least between $t = 0$ and $t = 80$. The sensor can only be shifted 2 meters aft if it is to remain within the allowable sensor compartment. This small shift should not appreciably alter the zeros of the other modes at this flight condition; however, it would be advisable to check the effect on the center-of-percussion zeros and the fourth bending zeros at $t = 80$ sec.

Even if the accelerometer were to be moved the 2 meters, the third bending mode will remain the critical mode and it will be necessary to know the location of the aftmost node within 2.5 meters.

3. $t = 157$ sec (Figs. 27 through 30)

For the $t = 157$ sec case the third bending (11.8 rad/sec) is again the critical mode (see Fig. 28). An increase of greater than 1.5 percent in the zero would reverse the zero/pole sequence and cause the closed-loop root to depart toward the RHP. If this root should be driven unstable by the $\dot{\phi}$ closure, it is unlikely that it could be restabilized by the ϕ closure (Fig. 29). In this case the rate sensor is located just aft of one of the third bending antinodes and the attitude sensor is located just forward of another. If the rate sensor were moved aft by 2 meters, the favorable zero/pole sequence in Fig. 28 would be preserved and the separation increased. This would assure stability of the third mode in the $\dot{\phi}$ closure so that the pole/zero sequence in the ϕ loop would be of little concern. A quick check indicates that this small shift in the rate sensor should have little effect on the other flight conditions. However, once again a detailed check would be required to be certain.

The sensitivity of this third bending mode would also be decreased somewhat by reducing the feedback gain of the $\dot{\phi}$ loop. It can be readily appreciated from Figs. 28 and 30 that a reduction in $\dot{\phi}$ loop gain would not be detrimental and might be favorable to the overall system performance.

4. Summary

Based on the foregoing analysis it appears that the following will remain critical after minor adjustments are made in sensor locations, feedback gains, and shaping:

t	LOOP	MODE	CRITICAL ASPECT
0	a_z	third bending	2.5 meter shift aftward in bending node
80	a_z	fourth bending	15 percent increase in fourth bending zero
157	ϕ	third bending	3.5 meter shift aftward in bending antinode

B. SENSITIVITY

In terms of the simplified equations of motion, the vehicle normal acceleration transfer function is of the form

$$\frac{N_{a_z}}{\beta} = \frac{s^2 A_z}{s^2} + \frac{s^2 l_A A_\phi}{s^2 - \omega_\phi^2} + \sum_i \frac{Y_i(x_A) A_{\eta_i} \left[s^2 - \bar{g} \frac{Y_i'(x_A)}{Y_i(x_A)} \right]}{s^2 + \omega_{i-1}^2} + \sum_j \frac{\psi_j(x_A) A_{S_j} \left[s^2 - \bar{g} \frac{\lambda_j(x_A)}{\psi_j(x_A)} \right]}{s^2 + \omega_{S_j}^2} \quad (46)$$

Collecting numerator terms over a common denominator results in a summation of polynomials from which the roots (zeros) of the i th bending mode may be obtained via the successive closure expression

$$\text{zeros} = \text{roots of} \left\{ 1 - \frac{Y_i(x_A) A_{\eta_i} s^2 (s^2 - \omega_\phi^2) \prod (s^2 + \omega_{i-1}^2) (s^2 + \omega_{S_j}^2)}{[\kappa - Y_i(x_A) A_{\eta_i}] (s^2 + \omega_i^2) (s^2 - \omega_\phi^{*2}) \prod (s^2 + \omega_{i-1}^{*2}) (s^2 + \omega_{S_j}^{*2})} \right\} \quad (47)$$

$$\text{where } \kappa = \left[A_z + l_A A_\phi + \sum_i Y_i(x_A) A_{\eta_i} + \sum_j \psi_j(x_A) A_{S_j} \right]$$

* indicates roots of previous closures

If one plots the Bode asymptotes and appropriate departures therefrom (as in the sketches accompanying Fig. 5), "closure" at the "gain"

$Y_i(x_A)A_{\eta_i} / |\kappa - Y_i(x_A)A_{\eta_i}|$ provides the desired zeros as the intersection of the closure line and the amplitude ratio curve at frequencies just above or below ω_i (depending upon the sign of the "gain"). The slope of the amplitude ratio curve in the vicinity of the zero is then a measure of its positional sensitivity to change in "gain." If $Y_i(x_A) \equiv 0$ (sensor located at the bending shape node) the "gain" is zero and there is no separation between the pole/zero pair for this bending mode. If $Y_i(x_A) \neq 0$ (sensor moved away from the bending shape node) the "gain" has a finite value, the zero moves away from the pole, and the contribution of this mode to the sensor output increases as the separation increases.

It will be noted from Eq. 47 and from the example plots of Section II and Appendix D that each mode can have some effect on all zeros although the principal contributors to the location of any specific zero generally are its modal gain coefficient, $Y_i(x_A)A_{\eta_i}$, and modal frequency, ω_i . It will also be noted that a shift in ω_i affects a corresponding shift in its associated zero.

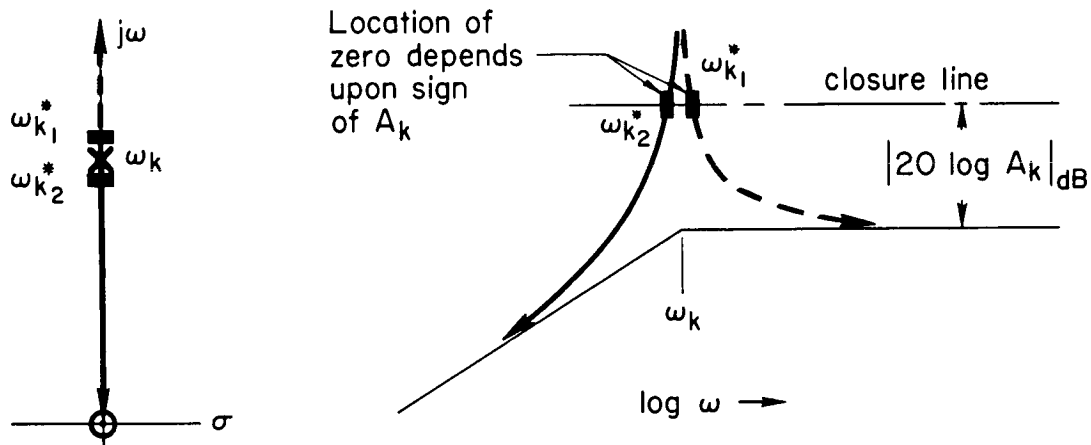
Although the assessment of sensitivity in this manner provides good insight into the physical relationships involved, it unfortunately is somewhat time consuming unless one has already obtained the simplified zeros via the successive closure technique. Since we are interested primarily in specific pole/zero pair for which the separation is small (e.g., the fourth bending mode at $t = 80$ sec) and since the successive closure technique may not always be employed, a simpler approach may be desired.

It will be noted in the sketches accompanying Fig. 5 (Section II) that the amplitude ratio is extremely large and steep in the immediate vicinity of a pole. Unless the mode separation (of other poles) is extremely small, the amplitude ratio in the immediate vicinity of a given pole is principally comprised of the contribution of that pole. Thus, if the modal gain coefficient, $Y_i(x_A)A_{\eta_i}$, is sufficiently small, the "closure" line will cut the amplitude ratio curve in a region close to the pole of interest where the amplitude contribution of other modes will be negligible. In this event we may revert to Eq. 46 and treat each mode individually. That is, we may consider the contribution of

each degree of freedom as a separate open-loop transfer function and obtain its effective closed-loop root (zero) as follows. For the kth nonrigid degree of freedom the open-loop transfer function is

$$Y_{OL} = \frac{A_k \left[s^2 - \frac{Y'_k(x_A)}{Y_k(x_A)} \right]}{s^2 + \omega_k^2} \quad (48)$$

and the closed-loop root (zero) is as indicated in the following sketch.



The sensor zero for this mode is then either $(s^2 + \omega_{k1}^{*2})$ or $(s^2 + \omega_{k2}^{*2})$ depending upon the sign of A_k . Unfortunately the sign of A_k cannot be depended upon to provide the correct direction of departure of the zero from the pole unless the other terms which make up κ (Eq. 47) are also taken into consideration. But, presumably, we already know the direction of the zero from the pole via the complete vehicle transfer function (either exact or simplified) and we are merely trying to determine its positional "gain" sensitivity. This can be accomplished by merely employing the magnitude A_k and the foreknowledge of zero position.

As an example of the applicability of this method, Table IV presents the zero calculated by this single degree of freedom technique together with the zeros obtained from the exact and simplified equations of motion (Section II). For $t = 0$ sec, the four bending and three slish

TABLE IV
COMPARISON OF NUMERATOR ROOTS OBTAINED BY THREE TECHNIQUES

t = 0 sec							
ω (pole)	A_k	$ A_k $	$ A_k $ dB	ZEROS			Exact Transfer Function
				Single Degree of Freedom	Simplified Transfer Function		
2.03	$Y_1(x_A)A_{\eta 1}$	0.2315	-13	1.81	± 2.38	± 1.81	
2.13	$\psi_1(x_A)A_{s1}$	0.0019	-54	2.13	2.13	2.1	
2.22	$\psi_2(x_A)A_{s2}$	0.0146	-37	2.2	2.14	2.11	
2.61	$\psi_3(x_A)A_{s3}$	0.0034	-49	2.6	2.14	2.21	
5.29	$Y_2(x_A)A_{\eta 2}$	0.243	-12	4.6	2.59	3.79	
9.19	$Y_3(x_A)A_{\eta 3}$	0.0138	-36	9.1	6.88	9.13	
12.59	$Y_4(x_A)A_{\eta 4}$	0.11	-19	13.7	11.97	15.1	
t = 80 sec							
2.32	$Y_1(x_A)A_{\eta 1}$	0.288	-11	2.78	2.81	3.3	
5.64	$Y_2(x_A)A_{\eta 2}$	0.448	-7	4.23	± 3.4	± 3.2	
9.2	$Y_3(x_A)A_{\eta 3}$	0.145	-17	8.55	8.53	8.94	
12.5	$Y_4(x_A)A_{\eta 4}$	0.0757	-22	13.1	13.17	13.2	

degrees of freedom are presented; for $t = 80$ sec, only the four bending degrees of freedom are presented. It will be noted that the single degree of freedom approximation for zero location (pole/zero separation) is nearly as good as, or better than, the simplified transfer function approximation. In fact, the considerably better results obtained via the single degree of freedom at $t = 0$ sec leads one to believe that an error was made in evaluating the simplified acceleration sensor numerator at this flight condition. (Note this only means that the simplified transfer function approach may be better than the factors of Table III, Section II, would indicate. It does not change the analysis of Sections III and IV since only the exact transfer functions were employed.) It can also be noted that the largest errors are incurred at the largest values of A_k . This indicates that these zeros are sufficiently separated from their poles that the amplitude contributions of neighboring poles must be taken into account.

In conclusion, it appears that for the crucial modes of interest here (i.e., the third bending at $t = 0$ sec, and the fourth bending at $t = 80$ sec), we may safely employ the modal gain coefficients, $Y_i(x_A)A\eta_i$, as measures of pole/zero separation.

From Ref. 6, the slope of the amplitude ratio at 20 dB departure from the Bode asymptote is approximately 0.02ω rad/sec/dB. Thus, at the fourth bending ($t = 80$ sec) the zero positional sensitivity is

$$0.02(12.5) = 0.25 \frac{\text{rad/sec}}{\text{dB}}$$

It was established in subsection III.A.4 that a 15 percent increase in the fourth bending zero might lead to instability. Since the zero is at 13.2 rad/sec, this corresponds to a 2 rad/sec increase or

$$\frac{2.0 \text{ rad/sec}}{0.25 \frac{\text{rad/sec}}{\text{dB}}} = 8 \text{ dB gain change}$$

and the gain coefficient $Y_4(x_A)A\eta_4$ must change by a factor of two and one-half.

Since

$$Y_4(x_A)A\eta_4 = Y_4(x_A) \frac{cM_E l_E}{M_4} \left[Y_4(x_\beta) \left(1 - \frac{I_E}{I_E M_E} \frac{Y_4'(x_\beta)}{Y_4(x_\beta)} \right) \right] \quad (49)$$

the principal source of uncertainty which can contribute to pole/zero separation is therefore the product $Y_4(x_A)Y_4(x_\beta)$. Any combination of changes in these factors which results in a 250 percent increase over those given for Model Vehicle No. 2 will lead to problems. This should be unlikely.

It was suggested in the previous subsection that the accelerometer be moved aft by 2 meters ($x_A = 44.5m$). This would increase $Y_4(x_A)$ by 33 percent (from -0.015 to -0.02) but would still provide approximately 6 dB margin on the modal gain coefficient.

For the third bending mode at $t = 0$ sec we are primarily concerned with pole/zero sequence (or reversal of sequence). From Table IV the modal gain is -36 dB. Thus the single degree of freedom amplitude curve has essentially infinite slope at the crossover which establishes the present zero location and the slope becomes infinite as the gain decreases (zero approaches the pole). Thus, amplitude ratio slope is not a good measure of sensitivity for change of pole/zero sequence.

The critical aspect at both $t = 0$ and 157 sec is a change in sign of the third bending modal gain coefficient. If both sensors are moved aft 2 meters from the location assumed in the analysis of Section III, the accelerometer will be 2.5 meters aft of the third bending (shape) node and the rate gyro will be 3.5 meters aft of the antinode. A simple sensitivity measure for these cases is therefore the percentage shift (or error) allowable in predicting the aftmost third bending node and antinode:

$$t = 0 \text{ sec ; } \frac{-2.5m}{47.0m} \times 100 = -5.3 \text{ percent change in node}$$

$$t = 157 \text{ sec ; } \frac{-3.5m}{48.0m} \times 100 = -7.3 \text{ percent change in antinode}$$

Thus an aftward shift of 5.3 percent in the third bending node at $t = 0$ sec would place the pole and zero coincident. Any further aftward shift in the node would place the zero above the pole and destabilize this mode.

On the basis of the foregoing, it appears that the limiting factor for the system synthesized herein is the accuracy of prediction of the third bending mode over the aft segment of the boost vehicle at lift-off ($t = 0$ sec) and preburnout ($t = 157$ sec) flight conditions. The fourth bending mode, which appears to be critical at max q ($t = 80$ sec) in the Bode analysis of Section III, is of considerably less concern since a change of over 200 percent is required in its modal gain coefficient before destabilization becomes imminent.

C. SUMMARY

Summarizing the findings of this portion of the effort, it has been found that

1. Rigorous methods of calculating sensitivity (e.g., Ref. 3) are impractical and unnecessary for vehicles as complex as the Model Vehicle No. 2.
2. Generation of sensor zeros via simplified equations, the successive closure technique, and Bode-Siggie plots provides direct measures (amplitude ratio slope) of zero location sensitivity.
3. The approach to determining system sensitivity worked out here
 - a. is amenable to paper and pencil analysis
 - b. provides insight to the physical parameters involved
 - c. is equally applicable to other types of sensors and other modes
 - d. provides a "first cut" which can be checked by, or provide guidance to, large scale computing activities.
4. The System D mechanization derived herein is quite sensitive to the third bending mode characteristics.

SECTION V

ADAPTIVE MECHANIZATION CONSIDERATIONS

In keeping with the second program objective—the determination of performance limitations of conventional (off-the-shelf) control systems as applied to this general study class vehicle—it is necessary to also consider current adaptive mechanizations. Quite arbitrarily, we shall interpret "off-the-shelf" as mechanizations which have reached the design/development test stage. Also, since attitude stabilization and/or elimination of flexible modes by or within the feedback is the first hurdle in control of the vehicle, the adaptive considerations herein are limited to this aspect (as opposed to adaptive load relief).

Adaptive concepts are attractive in flexible boost vehicle control because

- of the relatively high uncertainty in predicting frequency and shape of flexible modes throughout flight
- experimental determination or verification of flexible mode characteristics will be impractical for extremely large vehicles such as Model Vehicle No. 2.

Most state-of-art adaptive devices work on the principle of keeping constant some aspect of a closed-loop mode. A necessary prerequisite is measurement of some system dynamic property which, in turn, requires isolation of a specific dynamic mode from the composite vehicle motion. Several means (Refs. 9—12) have been devised to accomplish this, but all involve, basically, bandpass filtering (fixed or tracking). It is further necessary that the adaptive device dynamics be sufficiently separated from the dominant control mode (or other flexible modes) that:

- interference does not take place between the dominant control mode and the adaptive mode
- the adaptive adjustments are sufficiently rapid to maintain adequate stability
- interference (or confusion) does not exist between flexible modes.

If the adaptive device is to adjust loop gains to maintain system

stability, it must also be sensitive to change in closed-loop gain and/or phase with changing flight condition.

A review of the literature reveals that, for boost vehicle application, off-the-shelf adaptive devices narrow to consideration of "roving" or "tracking" filters—of which there are several designs, differing considerably in mechanizational detail. However, most operate on essentially the same dynamic principle—pole/zero cancellation, i.e., maintaining a pair of very lightly damped zeros precisely on top of the lightly damped vehicle poles. The creation of the zeros entails creation of a pair of poles also. The latter are generally at, or near, the frequency of the zeros but are well damped. The result is the familiar "notch" filter as indicated in Fig. 36. Unfortunately, the well damped poles introduce phase lag at frequencies below the notch and phase lead at frequencies

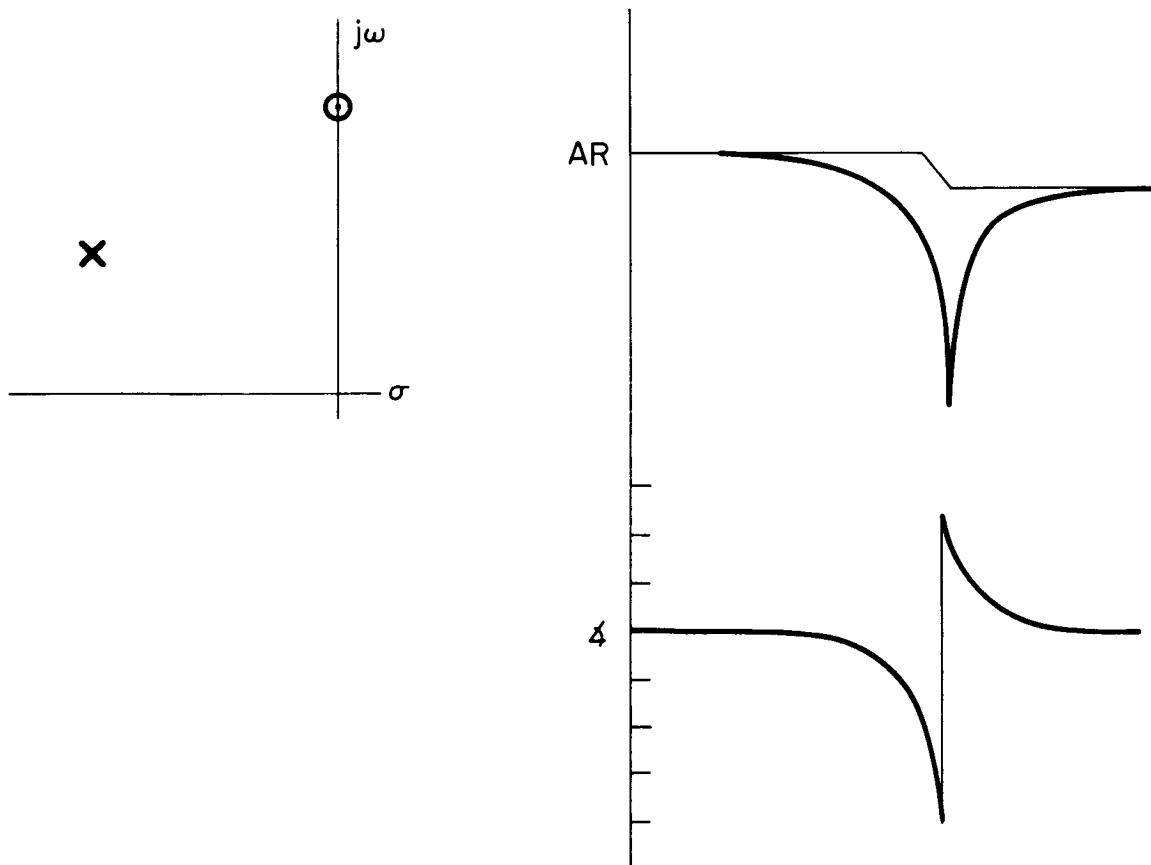


Figure 36. Typical Notch Filter Dynamics

above the notch. The width of the notch and the lag contribution are directly related as indicated in Fig. 37, which is taken from Ref. 9. In addition, some mechanizations introduce harmonics which also create amplitude and phase variations at slightly higher frequencies. Figure 38 indicates the contribution of the wider of the two notches shown in Fig. 37 in cancelling a second-order pole with $\zeta = 0.01$. While this notch does a good job of cancelling the amplitude peak, it will be appreciated that there is little margin for error in frequency adjustment. That is, if the notch is not exactly over the pole, the desired amplitude cancellation will not occur. Thus a wider notch probably would be preferred to allow for tracking error, etc. However, a wider notch would increase the already appreciable lag contribution of the filter.

For vehicles which have a wide separation of flexible modes, the identification, tracking, and cancellation of specific modes is not a

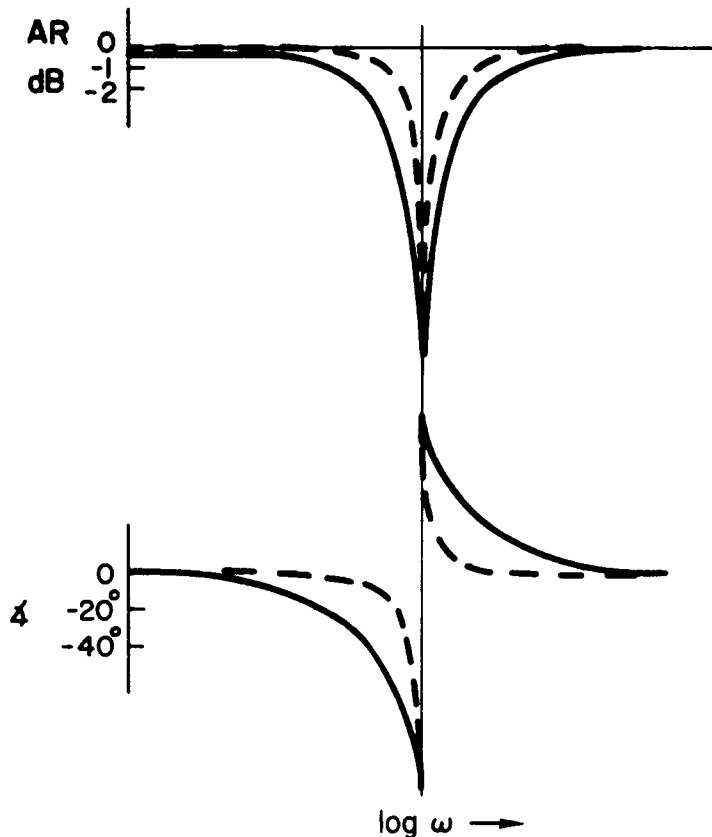


Figure 37. Effect of Notch Width on Phase Characteristics

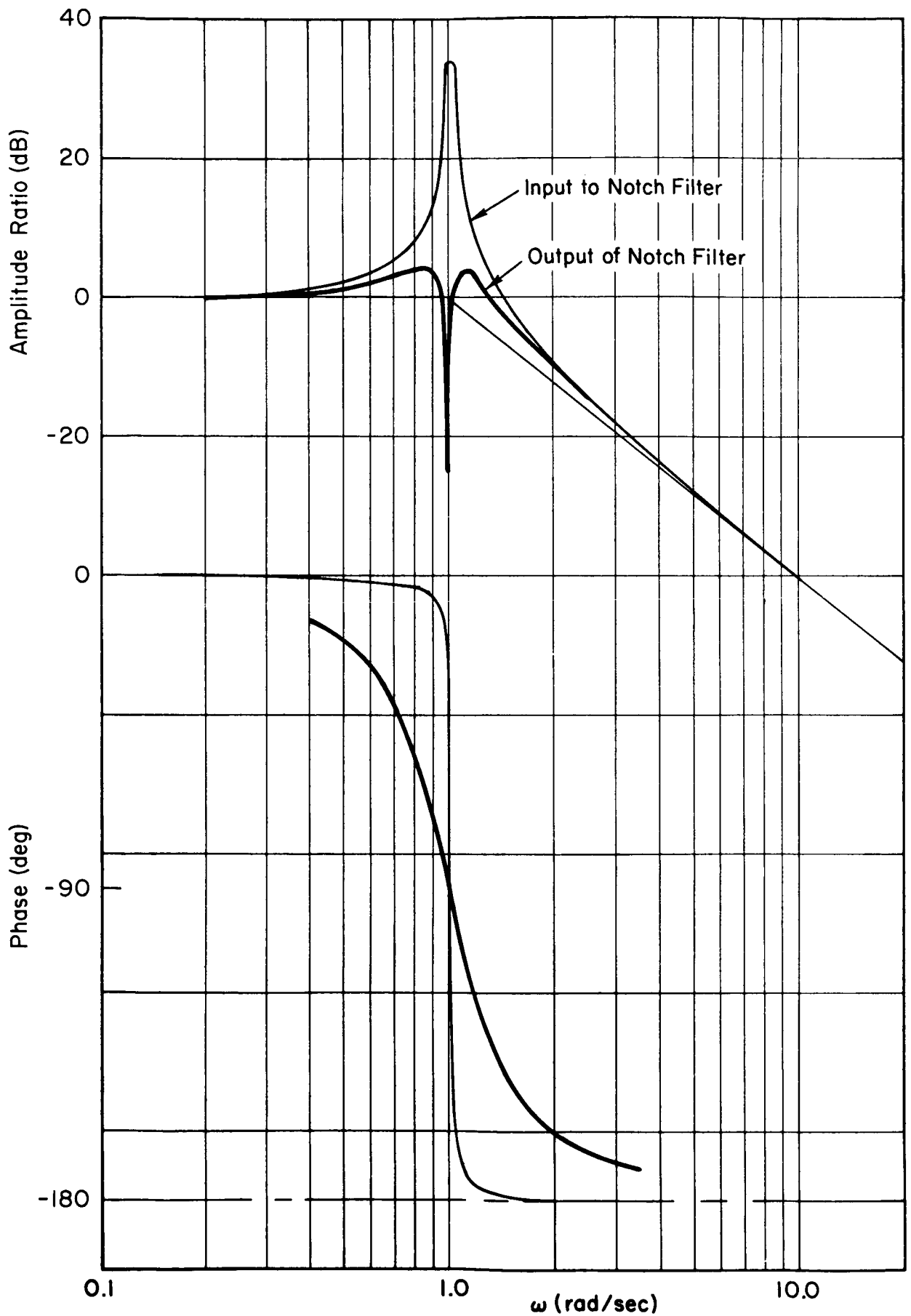


Figure 38. Typical Pole/Zero Cancellation Effect

particularly difficult task since relatively wide notches can be employed. However, Refs. 9, 11, and 15 indicate that the current state-of-art in identification and tracking requires a minimum mode separation of 2:1, or greater, and that development is still underway to reliably achieve this performance.

For the Model Vehicle No. 2 the modal separations are as indicated in Fig. 39. It is apparent that on the basis of predicted frequencies the proximity of modes exceeds the above 2:1 separation requirements. If, in addition, the initial basis for consideration of adaptive schemes is uncertainty in prediction of mode frequencies, then the possibility must exist that separations may be even less than those shown in Fig. 39.

Thus it appears that current, off-the-shelf identification/tracking devices will not suffice for this class of vehicle. Additional development and/or a technical breakthrough will be required before such devices are applicable.

Figure 39

MODAL SEPARATIONS: EXACT-COUPLED EQUATIONS

	t = 0	t = 80	t = 157
	<u>L.O.</u>	<u>Max. q.</u>	<u>B.O.</u>
$\omega_4 =$	$1.37 \omega_3$	$1.3 \omega_3$	$2.19 \omega_3$
$\omega_3 =$	$1.73 \omega_2$	$1.65 \omega_2$	$1.57 \omega_2$
$\omega_2 =$	$2.02 \omega_{s3}$	$1.92 \omega_{s3}$	$1.5 \omega_{s3}$
$\omega_1 =$	—	—	—
$\omega_{s3} =$	$1.14 \omega_{s2}$	$1.03 \omega_{s2}$	$1.23 \omega_{s2}$
$\omega_{s2} =$	$1.04 \omega_{s1}$	$1.11 \omega_{s1}$	$1.09 \omega_{s1}$
$\omega_{s1} =$	$1.05 \omega_1$	$1.23 \omega_1$	$1.08 \omega_1$
Avg.	1.39	1.37	1.44

SECTION VI

CONCLUSIONS

Despite being especially contrived to exhibit extremely low mode separation and high coupling, the Model Vehicle No. 2 has turned out to be quite similar to much stiffer boost vehicles in that uncoupled, simplified, equations and modal responses provide adequate approximations for preliminary synthesis work. Furthermore, this "first cut" analysis indicates it is feasible to employ conventional control techniques and off-the-shelf components but slightly unconventional sensing concepts (for boost vehicles) in achieving a successful control system for the Model Vehicle No. 2.

The understanding of the vehicle dynamics, coupling effects, etc., gained through the approximate transfer function factors (Ref. 1) developed in the first phase of this study provided faith in the simplified equations on which much of this second phase feasibility study was based. This synthesis study has therefore demonstrated the achievement of the first study objective (in Ref. 1) — to develop a model of the vehicle dynamics which can provide the control engineer with the physical insights into modal coupling and vehicle characteristics which are necessary for a solution of this complex control problem.

The second objective — the determination of the limits of conventional control systems for this general class of vehicle and guidelines for determining what degree of vehicle dynamic complexity requires more advanced control techniques — has been partially achieved. It was determined that the proximity of the various nonrigid modes exceeds the separation requirements of current adaptive tracking filter devices. A technical breakthrough will be required in isolating and identifying modes with less than a factor of 1.5 frequency separation before adaptive notch filtering devices will show promise. Vehicles of this class can be expected to require phase stabilization of all modes up to and including the fourth bending mode. The limits of "conventional" control (in terms of $\dot{\phi}$ and ϕ sensing and reasonable shaping complexity) would appear to have been exceeded by this vehicle. However, with the addition

of the "unconventional" use of acceleration sensing and feedback to damp flexible modes, it appears that "conventional" control techniques may still be feasible.

Thus the achievement of the third objective — the evaluation of advanced control concepts for solution of the stabilization and control problems for the extreme cases in which conventional techniques are inadequate — remains a matter of semantics. If one considers the use of acceleration feedback to damp flexible modes to be an advanced control concept — then the objective has been met. If one considers the use of such acceleration feedback to be conventional — then the limits of conventional control have not been found (objective 2), conventional control techniques are adequate, and the third objective is superfluous.

While the analysis has resulted in a system which is stable at three points in the flight spectrum and indicates promise of meeting reasonable attitude control, load relief, and drift requirements, it is subject to the shortcoming of most time "programmed" control systems — the requirement for rather precise knowledge of at least one of the flexible modes. However, this was a "first cut" effort and it is possible that further analysis could surmount this shortcoming since there is indication that the controller would be relatively insensitive to precise knowledge of most flexible modes. If vehicles of this type or class are anticipated in the future, this type of mechanization is certainly worthy of more detailed analysis.

Other results and/or ramifications over and above the objectives listed are possibly of greater importance however. In particular, the analytical techniques used in the study deserve special note. The use of the successive closure technique, whether to generate numerator zeros or to observe the effects of each individual feedback, provides feel for and understanding of the interaction between the vehicle and controller, assists in working out simple sensitivity measures, etc. Understanding and physical feel is further enhanced by the use of approximate and/or simplified transfer function factors which allow one to relate the system dynamic characteristics to physical characteristics. The resultant

insight not only obviates the many time consuming parameter variation orgies often accompanying system synthesis or simulation, but provides the basis for quickly assessing the criticality of change in any parameter as the vehicle progresses through its various design/development phases. While use of these generic and simplified "paper and pencil" techniques is not uncommon for simple systems, it is significant that they can be successfully employed for a complex, high-order, highly coupled system such as the vehicle for this study.

REFERENCES

1. Stapleford, R. L., L. G. Hofmann, J. J. Best, C. D. Wezeman, and W. A. Johnson, Transfer Function Approximations for Large Highly Coupled Elastic Boosters with Fuel Slosh, NASA CR-464, Apr. 1966.
2. Pass, H. R., and B. F. Pearce, Topics on Flexible Airplane Dynamics: Coupling of the Rigid and Elastic Degrees of Freedom of an Airframe-Autopilot System, ASD-TDR-63-334, Part IV, July 1963.
3. McRuer, D. T., and R. L. Stapleford, Sensitivity and Modal Response for Single-Loop and Multiloop Systems, ASD-TDR-62-812, Jan. 1963.
4. Hofmann, Lee Gregor, and Allen Kezer, Simplified Analysis of Flexible Booster Flight Control Systems, MIT, Instrumentation Lab. Rept. No. E-1210, June 1962.
5. Lewis, Robert C., and Thomas E. Carter, A Dual Rate Gyro Approach to the Elastic Feedback Problem, George C. Marshall Space Flight Center MTP-AERO-63-21, 4 Mar. 1963.
6. McRuer, Duane T., Unified Analysis of Linear Feedback Systems, ASD-TR-61-118, July 1961.
7. A Report on the Feasibility Study of the Multiloop Rate Gyro Control System, Northrop Space Lab. R and A Tech. Memo. No. 42, 23 Dec. 1964.
8. Studies on the Application of Advanced Control Techniques on the Solution of Various Control Problems Which Arise in Controlling Large Flexible Launch Vehicles, Exhibit A-RFQ, DCN-1-4-75-01002-01, George C. Marshall Space Flight Center, NASA, Huntsville, Alabama, 31 Oct. 1963.
9. Hosenthien, H. H., and M. T. Borelli, An Adaptive Tracking-Notch Filter for Suppression of Structured Bending Signals of Large Space Vehicles, NASA TM X-53,000, 1 Oct. 1963.
10. Borelli, M. T., S. N. Carroll, and H. H. Hosenthien, Recent Developments in Adaptive Tracking Notch Filter Techniques, NASA TM X-53217, 1 Mar. 1965.
11. Gaylor, R., R. L. Schaeperksetter, and D. C. Cunningham, "An Adaptive Tracking Filter for the Stabilization of Bending Modes in Flexible Vehicles," AIAA/JACC Guidance and Control Conference, Aug. 1966.
12. Smythe, R. K., and J. C. Davis, "A Self-Adaptive Control System for a Space Booster of the Saturn Class," Joint Automatic Control Conference, New York University, 27-29 June, 1962.

13. Hosenthien, Hans H., and Michael T. Borelli, "Self-Adaptive Tracking Filters," Society of Automotive Engineers Committee A-18 Meeting No. 14, New York, 8-10 July 1964.
14. Miles, J. W., Ring Damping of a Free Surface Oscillation in a Circular Tank, ASME Applied Mechanics Div. Paper No. 57-A-31, Mar. 1957.

APPENDIX A
BASIC VEHICLE DATA

TABLE A-I

SUMMARY OF PARAMETER AND COEFFICIENT VALUES

PARAMETER UNITS	t = 0 sec	t = 80 sec	t = 157 sec
$M \left(\frac{\text{kg}}{\text{m/sec}^2} \right)$	423,565.2	266,051.2	116,412.4
\bar{V} (m/sec)	0	519.3	2520.5
F (total number of engine)	8	8	8
c (number of gim-baled engine)	4	4	4
T (kg)	5,193,233	5,819,805	6,150,420.2
K_1	800	800	800
l_E (m)	1.20142	1.20142	1.20142
ω_E (rad/sec)	51.14	51.14	51.14
$M_E \left(\frac{\text{kg}}{\text{m/sec}^2} \right)$	925.07	925.07	925.07
$I_E \left(\frac{\text{kg}}{\text{m/sec}^2} \text{ m}^2 \right)$	3456.38	3456.38	3456.38
$I \left(\frac{\text{kg}}{\text{m/sec}^2} \text{ m}^2 \right)$	285×10^6	250×10^6	90×10^6
X_{cg} (m)	37.8	41.2	67.2
$X_E \equiv X_\beta$ (m)	2.54	2.54	2.54
$l_\beta = X_E - X_{cg}$ (m)	-35.26	-38.66	-64.66
$\frac{M}{I} \left(\frac{1}{\text{m}^2} \right)$	1.4862×10^{-3}	1.0642×10^{-3}	1.2935×10^{-3}
$\frac{I}{M}$ (m^2)	672.86	939.67	773.10

TABLE A-I
SUMMARY OF PARAMETER AND COEFFICIENT VALUES (Continued)

PARAMETERS UNITS	t = 0 sec	t = 80 sec	t = 157 sec
$M_1 \left(\frac{\text{kg}}{\text{m}/\text{sec}^2} \right)$	193,188	170,748.1	17,866.5
M_2	165,516.2	115,674.3	29,067.6
M_3	162,154.5	98,114.7	169,960.9
M_4	350,110.7	565,743.8	203,335.9
ω_1 (rad/sec)	2.156	2.318	2.915
ω_2	5.062	5.645	6.5923
ω_3	8.7826	9.184	11.711
ω_4	12.356	12.504	24.862
$Y_1(X_\beta)$	0.93051	0.92869	0.95810
$Y_2(X_\beta)$	0.91178	0.90509	0.93768
$Y_3(X_\beta)$	0.89073	0.88583	0.89977
$Y_4(X_\beta)$	0.87366	0.87095	0.78675
$Y_1'(X_\beta)$	-0.03477	-0.03569	-0.02100
$Y_2'(X_\beta)$	-0.04429	-0.04764	-0.03143
$Y_3'(X_\beta)$	-0.05509	-0.05758	-0.05093
$Y_4'(X_\beta)$	-0.06407	-0.06544	-0.11012
C_{N_α} (1/rad)		4.81	
C_{M_α} (1/rad)		-57.2805	
X_{cp} (m)		53.5503	
$l_{cp} = X_{cp} - X_{cg}$ (m)		12.3503	
$N_\alpha = qSC_{N_\alpha}$ (1/rad)		14.679×10^5	

TABLE A-I
SUMMARY OF PARAMETER AND COEFFICIENT VALUES (Continued)

PARAMETERS UNITS	t = 0 sec	t = 80 sec	t = 157 sec
ω_{s1} (rad/sec)	2.14	2.76	3.58
ω_{s2}	2.14	2.76	3.77
ω_{s3}	2.14	2.83	4.71
M_{s1} $\left(\frac{\text{kg}}{\text{m/sec}^2}\right)$	11,158	11,612	338
M_{s2}	17,048	18,399	772
M_{s3}	11,173	11,173	11,173
l_{s1} (m)	-21.71	-31.04	-60.96
l_{s2}	5.35	-10.12	-42.36
l_{s3}	23.55	20.15	-5.85
X_{s1} (m)	16.09	10.16	6.24
X_{s2}	43.15	31.08	24.84
X_{s3}	61.35	61.35	61.35
$Y_{sj}' = -\frac{M_{sj}l_{sj}}{I}$			
Y_1'	0.84997×10^{-3}	1.4417×10^{-3}	0.22894×10^{-3}
Y_2'	-0.32002×10^{-3}	0.74479×10^{-3}	0.36335×10^{-3}
Y_3'	-0.92324×10^{-3}	-0.90054×10^{-3}	0.72625×10^{-3}
$Y_{s1}(X_{\beta})$	-0.056313	-0.099382	-0.017707
$Y_{s2}(X_{\beta})$	-0.028965	-0.097950	-0.030126
$Y_{s3}(X_{\beta})$	0.0061751	-0.0071809	-0.14294

TABLE A-I
SUMMARY OF PARAMETER AND COEFFICIENT VALUES (Concluded)

PARAMETERS UNITS	t = 0 sec	t = 80 sec	t = 157 sec
$Y_1(X_{S1})$	0.45316	0.66	0.88018
$Y_2(X_{S1})$	0.28197	0.53	0.82030
$Y_3(X_{S1})$	0.07135	0.43	0.70820
$Y_4(X_{S1})$	-0.11228	0.34	0.36830
$Y_1(X_{S2})$	-0.39874	-0.08	0.49173
$Y_2(X_{S2})$	-0.45672	-0.38	0.24804
$Y_3(X_{S2})$	-0.19357	-0.55	-0.19102
$Y_4(X_{S2})$	0.21504	-0.61	-1.36246
$Y_1(X_{S3})$	-0.69948	-0.80	-0.15258
$Y_2(X_{S3})$	0.02956	-0.32	-0.29600
$Y_3(X_{S3})$	0.90061	0.57	-0.30459
$Y_4(X_{S3})$	0.70020	1.22	0.12724
M/M_1	2.1925	1.5582	6.5157
M/M_2	2.5591	2.3000	4.0049
M/M_3	2.6121	2.7116	0.68494
M/M_4	1.2098	0.47027	0.57251

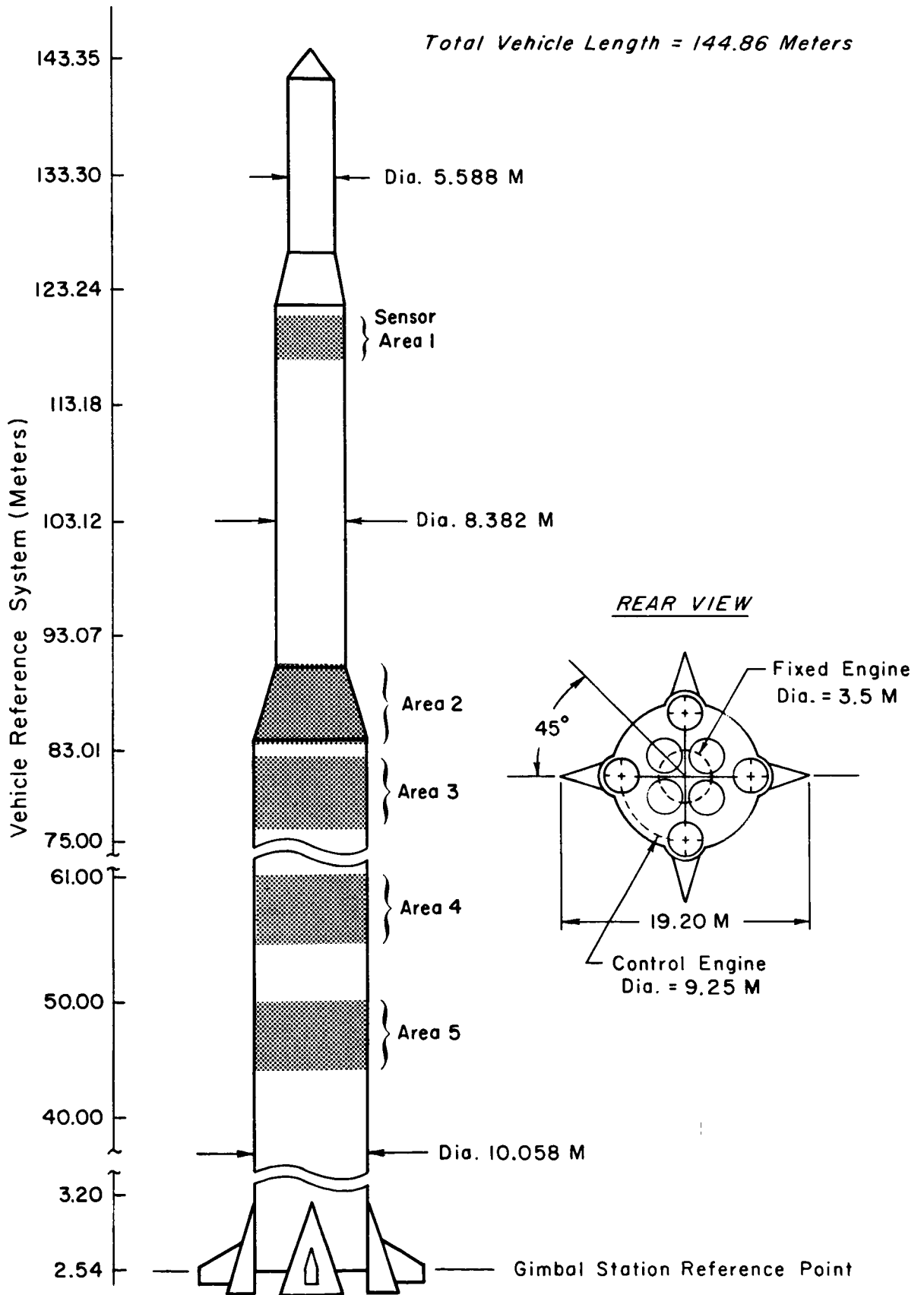


Figure A-1. Model Vehicle No. 2

$$\begin{array}{c}
 s^2 \\
 \hline
 s^2 \\
 s^2 + (2.1363)^2 \\
 s^2 + (2.1363)^2 \\
 s^2 + (2.1363)^2 \\
 s^2 + (2.1564)^2 \\
 s^2 + (5.0617)^2 \\
 s^2 + (8.7826)^2 \\
 s^2 + (12.3556)^2 \\
 \hline
 \begin{array}{c}
 z_1 \\
 \varphi_1 \\
 z_{s1} \\
 z_{s2} \\
 z_{s3} \\
 \eta_{11} \\
 \eta_{21} \\
 \eta_{31} \\
 \eta_{41}
 \end{array}
 \end{array}
 =
 \begin{array}{c}
 0.23609 \\
 -0.012495 \\
 -0.50469 \\
 -0.16990 \\
 0.055268 \\
 0.48166 \\
 0.55083 \\
 0.54932 \\
 0.24954
 \end{array}
 \cdot 10^{-5} \beta$$

Figure A-2. Simplified Characteristic Matrix at $t = 0$ sec

MODE SLOPES AT SAMPLE ALLOWABLE GYRO LOCATIONS

Gyro Location	xG	Y ₁ '	Y ₂ '	Y ₃ '	Y ₄ '	Γ ₁ '	Γ ₂ '	Γ ₃ '
1	46.5	-0.02300	+0.00833	+0.05260	+0.05987	+0.00098924	-0.0002188	-0.0062213
2	58.5	-0.00943	+0.04255	+0.05186	-0.01613	-0.0013389	+0.0029701	-0.0029280
3	76.5	+0.01031	+0.05945	-0.02838	-0.13313	-0.0027968	+0.0042103	+0.0059584
4	88.5	+0.03461	+0.04745	-0.08133	-0.04837	-0.0022542	+0.0024231	+0.0079826
5	120.5	+0.11408	-0.15163	+0.10592	-0.01202	+0.0050844	-0.0025828	-0.0070542
Sawtooth Bode Criteria		(-)	(-)	(-)	(-)	(+)	(+)	(-)

SUMMARY OF GYRO NUMERATORS N_{φ_GF} (s)

Gyro Location	N _{φ_GF} (s)
1	+2404.4 [s ² + (1.5908) ²] [s ² + (2.1363) ²] [s ² + (2.1377) ²] [s ² + (5.3281) ²] [s ² - (9.1125) ²] [s ² + (11.047) ²]
2	+3089.8 [s ² + (1.9265) ²] [s ² + (2.1363) ²] [s ² + (2.1361) ²] [s ² - (4.5866) ²] [s ² + (6.6812) ²] [s ² + (12.759) ²]
3	-2256.8 [s ² + (2.1395) ²] [s ² + (2.1363) ²] [s ² + (2.5530) ²] [s ² - (4.7442) ²] [s ² - (7.5289) ²] [s ² + (9.6488) ²]
4	-2526.7 [s ² + (2.1376) ²] [s ² + (2.1363) ²] [s ² - (s.7635) ²] [s ² + (3.5580) ²] [s ² - (7.4119) ²] [s ² + (11.421) ²]
5	-1159.8 [s ² - (1.5608) ²] [s ² + (2.1363) ²] [s ² + (2.1353) ²] [s ² + 2(-0.91440)(7.8711)s + (7.8711) ²] [s ² + 2(0.91440)(7.8711)s + (7.8711) ²] [s ² + (12.718) ²]

Figure A-3. Summary of Simplified Gyro Numerators and Mode Slopes, t = 0

$$\frac{N_{az}}{\Delta} = s^2 \left[z_1 + 1_a \phi_1 + \sum_{j=1}^3 \psi_j(x_a) Z_{sj} + \sum_{i=1}^4 Y_{i1}(x_a) \eta_{i1} \right] - g \left[\sum_{j=1}^3 \lambda_j(x_a) Z_{sj} + \sum_{i=1}^4 Y_{i1}'(x_a) \eta_{i1} \right]$$

	BENDING MODES (ξ AND ω)* AT LOCATIONS			
	1	2	3	4
$K \times 10^{-5}$	-0.6973	-0.2391	0.2541	-0.1237
RB	0	0	0	0
ω_{s1}	2.1331	0.5573	1.3706	1.5549
ω_{s2}	2.1363	2.1363	2.1363	2.1363
ω_{s3}	2.1363	2.1363	2.1363	2.1363
ω_1	$\pm(2.3736)$	2.1368	2.1374	2.1381
ω_2	2.5860	3.8805	5.2452	6.4726
ω_3	6.8760	9.2901	11.4420	(0.6014) (14.5240)
ω_4	11.971	18.3050	$\pm(14.2180)$	(-0.6014) (14.5240)
MODE AMPLITUDE				
Y_1	-0.4807	-0.6789	-0.6588	-0.4007
Y_2	-0.4418	-0.0980	0.8702	1.5980
Y_3	-0.0251	0.7896	0.8445	0.1320
Y_4	0.4397	0.9229	-0.9484	-2.4943
ψ_1	0.0038	0.0105	0.0001	-0.0122
ψ_2	-0.0859	-0.0690	-0.0079	0.0332
ψ_3	-0.0614	-0.1426	-0.1221	-0.0455
λ_1	0.0001	-0.0022	-0.0037	-0.0031
λ_2	0.0001	0.0033	-0.0045	0.0027
λ_3	-0.0053	-0.0020	0.0069	0.0089

*For $\xi \neq 0$ or 1, the Bending Modes are listed in the following fashion:

(ξ)

(ω)

Figure A-4. Summary of Simplified Accelerometer Numerator Factors and Mode Amplitudes, $t = 0$

s^2		
$s^2 - (0.2692)^2$	z_1	0.37587
$s^2 + (2.76)^2$	φ_1	-0.015464
$s^2 + (2.76)^2$	z_{s1}	-0.85586
$s^2 + (2.76)^2$	z_{s2}	-0.53237
$s^2 + (2.83)^2$	z_{s3}	-0.06427
$s^2 + (2.318)^2$	η_{11}	0.54589
$s^2 + (5.645)^2$	η_{21}	0.78248
$s^2 + (9.184)^2$	η_{31}	0.90285
$s^2 + (12.504)^2$	η_{41}	0.15395
	=	$10^{-5} \beta$

Figure A-5. Simplified Characteristic Matrix at $t = 80$ sec

MODE SLOPES AT SAMPLE ALLOWABLE GYRO LOCATIONS

Gyro Location	xg	Y ₁ ¹	Y ₂ ¹	Y ₃ ¹	Y ₄ ¹	Γ ₁ ¹	Γ ₂ ¹	Γ ₃ ¹
1	46.5	-0.259	-0.0011	+0.0398	+0.0791	0.000124	0.00615	-0.00675
2	58.5	-0.0140	+0.0299	+0.0430	-0.00517	-0.00165	0.00681	-0.00341
3	76.5	+0.0060	+0.0572	-0.0119	-0.180	-0.000073	-0.000495	0.00614
4	88.5	+0.0313	+0.0544	-0.0540	-0.0763	0.000350	-0.00279	0.00765
5	120.5	+0.118	-0.129	+0.0702	-0.0052	-0.000398	0.00107	-0.00279
Sawtooth Bode Criteria		(-)	(--)	(-)	(-)	(+)	(+)	(+)

SUMMARY OF GYRO NUMERATORS N_{ΦGB}(s)

Gyro Location	N _{ΦGB} (s)
1	1475.3 [s ² + (1.6575) ²] [s ² + (2.7008) ²] [s ² + (2.76) ²] [s ² + (2.8350) ²] [s ² + (5.6055) ²] [s ² + (11.481) ²] [s ² - (14.625) ²]
2	3635.0 [s ² + (1.9458) ²] [s ² + (2.7051) ²] [s ² + (2.76) ²] [s ² + (2.8358) ²] [s ² - (5.9749) ²] [s ² + (6.8261) ²] [s ² + (12.561) ²]
3	-596.63 [s ² + (2.4912) ²] [s ² + (2.76) ²] [s ² + 2(0.0118)(2.7942) s + (2.7942) ²] [s ² + 2(-0.0118)(2.7942) s + (2.7942) ²] [s ² - (4.7990) ²] [s ² + (9.7333) ²] [s ² - (20.881) ²]
4	-1567.9 [s ² + (2.7242) ²] [s ² + (2.76) ²] [s ² + (2.8539) ²] [s ² - (3.1186) ²] [s ² + (3.4752) ²] [s ² + (11.594) ²] [s ² - (12.063) ²]
5	1026.0 [s ² - (1.6765) ²] [s ² + (2.76) ²] [s ² + (2.7615) ²] [s ² + (2.8288) ²] [s ² + 2(0.89324) (9.4523) s + (9.4523) ²] [s ² + 2(-0.89316)(9.4536) s + (9.4536) ²] [s ² + (12.588) ²]

Figure A-6. Summary of Simplified Gyro Numerators and Mode Slopes, t = 80

$$\frac{N_{a_z}}{\Delta} = s^2 \left[z_1 + 1_a \phi_1 + \sum_{j=1}^3 \psi_j(x_a) z_{s_j} + \sum_{i=1}^4 Y_{i_1}(x_a) \eta_{i_1} \right] - g \left[\sum_{j=1}^3 \lambda_j(x_a) z_{s_j} + \sum_{i=1}^4 Y_{i_1}'(x_a) \eta_{i_1} \right]$$

	BENDING MODES (ζ AND ω)* AT LOCATIONS			
	1	2	3	4
$K \times 10^{-5}$	-0.4659	0.0131	0.1504	-0.03523
RB	$\pm(0.3002)$	$\pm(0.534)$	0.351	0.218
ω_1	2.760	$\pm(1.226)$	1.344	1.900
ω_{s_1}	2.809	2.759	2.758	2.760
ω_{s_2}	2.943	2.760	2.760	2.769
ω_{s_3}	3.156	2.845	2.835	2.832
ω_2	$\pm(3.341)$	4.677	6.719	8.613
ω_3	8.526	10.977	$\pm(13.547)$	$\pm(14.516)$
ω_4	13.172	$\pm(64.806)$	14.054	$\pm(22.299)$
	MODE AMPLITUDE			
Y_1	-0.5290	-0.7778	-0.8374	-0.6277
Y_2	-0.5736	-0.3992	0.4553	1.2094
Y_3	-0.1605	0.4670	0.6505	0.2313
Y_4	0.4920	1.3311	-1.0846	-3.2426
ψ_1	0.0229	0.0049	-0.0051	-0.0019
ψ_2	-0.1116	-0.0125	0.0240	-0.0054
ψ_3	-0.0930	-0.1722	-0.1209	-0.0202
λ_1	-0.0013	-0.0031	-0.0015	-0.0011
λ_2	0.0054	0.0061	-0.0012	-0.0035
λ_3	-0.0059	-0.0025	0.0070	0.0085

*For $\zeta \neq 0$ or 1, the Bending Modes are listed in the following fashion:

(ζ)

(ω)

Figure A-7. Summary of Simplified Numerator Factors and Mode Amplitude, $t = 80$

$$\begin{array}{l}
 s^2 \\
 \hline
 s^2 + (0.03597)^2 \\
 s^2 + (3.5814)^2 \\
 s^2 + (3.7699)^2 \\
 s^2 + (4.7124)^2 \\
 s^2 + (2.915)^2 \\
 s^2 + (6.592)^2 \\
 s^2 + (11.711)^2 \\
 s^2 + (24.862)^2 \\
 \hline
 z_1 \quad \varphi_1 \quad z_{s1} \quad z_{s2} \quad z_{s3} \quad \eta_{11} \quad \eta_{21} \quad \eta_{31} \quad \eta_{41} \\
 \hline
 0.85903 \\
 -0.071527 \\
 -5.2388 \\
 -3.9023 \\
 -1.2793 \\
 5.3624 \\
 3.2258 \\
 0.5294 \\
 0.38691 \\
 \hline
 10^{-5} \beta
 \end{array}$$

Figure A-8. Simplified Characteristic Matrix at t = 157 sec

MODE SLOPES AT SAMPLE ALLOWABLE GYRO LOCATIONS

Gyro Location	x_G	Y_1'	Y_2'	Y_3'	Y_4'	Γ_1'	Γ_2'	Γ_3'
1	46.5	-0.01776	-0.01554	-0.00489	+0.04280	+0.00065255	+0.0010586	-0.0031367
2	58.5	-0.01397	+0.00334	+0.04786	+0.15142	+0.00026857	+0.0014613	-0.00033023
3	76.5	-0.00689	+0.02929	+0.08544	+0.02813	-0.000074287	+0.00053483	+0.0049122
4	88.5	+0.00341	+0.03650	+0.00483	-0.18123	-0.000072856	-0.00088441	+0.0065649
5	120.5	+0.04382	-0.06600	+0.03549	+0.62230	-0.00030316	+0.0031152	-0.0062452

Sawtooth Bode
Criteria

(-) (-) (-) (-) (-) (+) (+) (+) (+)

SUMMARY OF GYRO NUMERATORS $N_{\Phi_{CB}}(s)$

Gyro Location	$N_{\Phi_{CB}}(s)$
1	$-20646 [s^2 + (1.8599)^2] [s^2 + (3.5586)^2] [s^2 + (3.7519)^2] [s^2 + (4.7596)^2] [s^2 + (5.8939)^2]$
2	$[s^2 + (11.652)^2] [s^2 + (25.815)^2]$ $-5843.0 [s^2 + (2.0330)^2] [s^2 + (3.5719)^2] [s^2 + (3.7336)^2] [s^2 + (4.7159)^2] [s^2 + (6.7877)^2]$
3	$[s^2 + (12.736)^2] [s^2 + (35.636)^2]$ $+3414.3 [s^2 + (2.4346)^2] [s^2 + (3.5792)^2] [s^2 + (3.7572)^2] [s^2 + (4.6506)^2] [s^2 + (9.1571)^2]$
4	$[s^2 - (16.459)^2] [s^2 + (22.452)^2]$ $-762.8 [s^2 + (3.1942)^2] [s^2 + (3.5844)^2] [s^2 + (3.8715)^2] [s^2 + (4.5728)^2] [s^2 - (7.1106)^2]$
5	$[s^2 + (11.602)^2] [s^2 - (65.183)^2]$ $+20753 [s^2 - (2.3962)^2] [s^2 + (3.5776)^2] [s^2 + (3.8096)^2] [s^2 + (4.6739)^2]$ $[s^2 + 2(0.75755)(10.550)s + (10.550)^2] [s^2 + 2(-0.75755)(10.550)s + (10.550)^2] [s^2 + (12.298)^2]$

Figure A-9. Summary of Simplified Gyro Numerators and Mode Slopes, $t = 157$

$$\frac{N_{a,z}}{\Delta} = s^2 \left[z_1 + 1_a \phi_1 + \sum_{j=1}^3 \psi_j(x_a) Z_{s_j} + \sum_{i=1}^4 Y_{i_1}(x_a) \eta_{i_1} \right] - g \left[\sum_{j=1}^3 \lambda_j(x_a) Z_{s_j} + \sum_{i=1}^4 Y_{i_1}'(x_a) \eta_{i_1} \right]$$

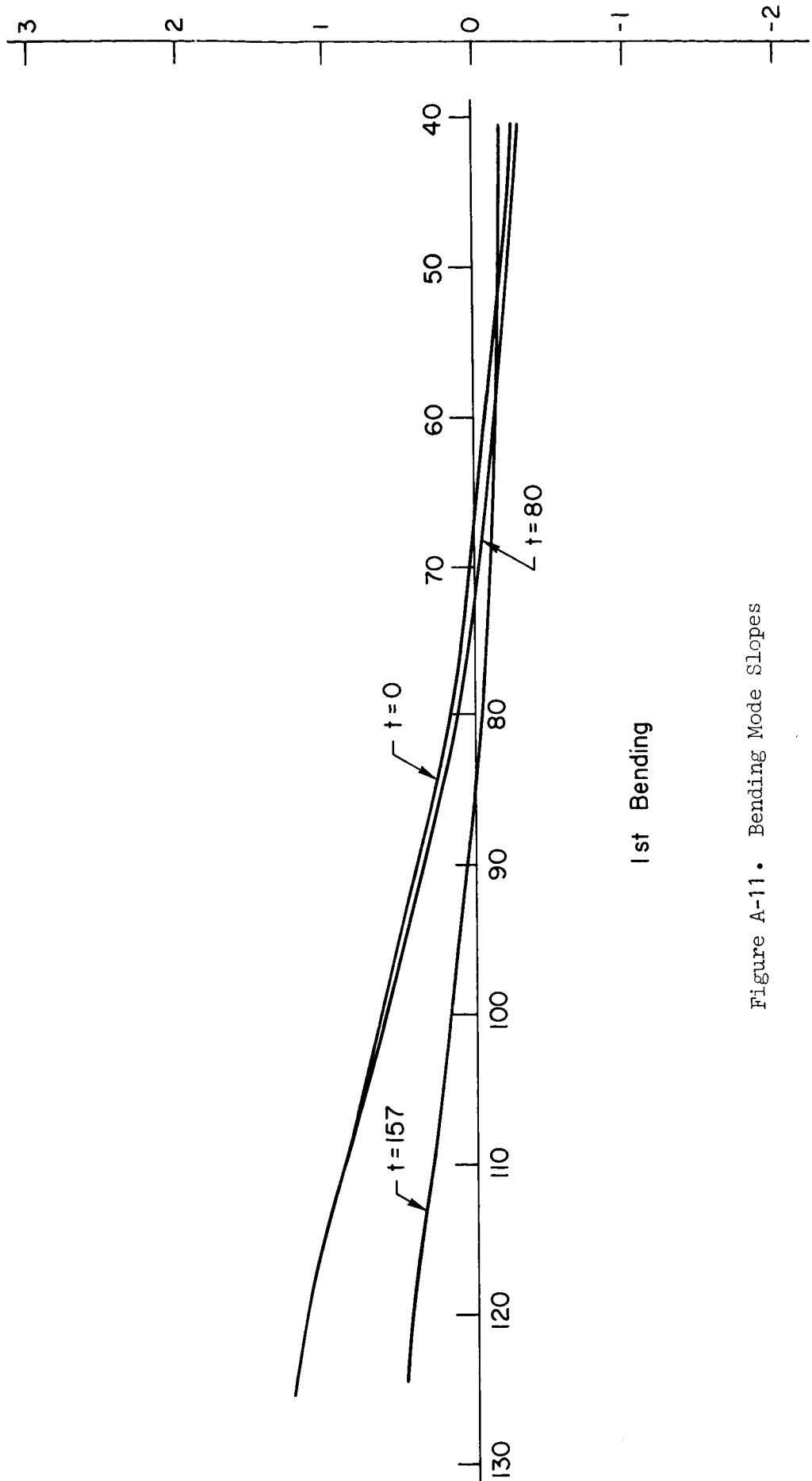
	BENDING MODES (ζ AND ω)* AT LOCATIONS			
	1	2	3	4
K X 10 ⁻⁵	1.4283	-0.3115	-0.01097	0.3335
RB	0.025	0.029	0.066	±(0.031)
ω_1	2.938	3.862	±(1.307)	1.789
ω_{s1}	3.559	3.572	3.581	3.583
ω_{s2}	3.730	(0.025) (4.116)	3.748	3.762
ω_{s3}	4.607	(-0.025) (4.116)	4.815	4.720
ω_2	7.457	10.091	6.928	8.654
ω_3	12.749	±(16.932)	14.397	20.989
ω_4	29.478	21.643	213.790	±(27.683)
	MODE AMPLITUDE			
Y ₁	0.078	-0.115	-0.301	-0.330
Y ₂	-0.224	-0.317	0.034	0.479
Y ₃	-0.668	-0.474	0.998	1.810
Y ₄	-1.394	-0.338	1.778	0.692
ψ_1	-0.0050	0.0009	0.0014	-0.0001
ψ_2	-0.0221	-0.0074	0.0130	0.0101
ψ_3	-0.1327	-0.0156	-0.1066	-0.0262
λ_1	0.0004	0.00004	-0.0003	-0.0003
λ_2	0.0007	0.0011	0.0002	-0.0012
λ_3	-0.0039	-0.0011	0.0042	0.0058

*For $\zeta \neq 0$ or 1, the Bending Modes are listed in the following fashion:

(ζ)

(ω)

Figure A-10. Simplified Accelerometer Numerator Factors and Mode Amplitudes, $t = 157$



1st Bending

Figure A-11. Bending Mode Slopes

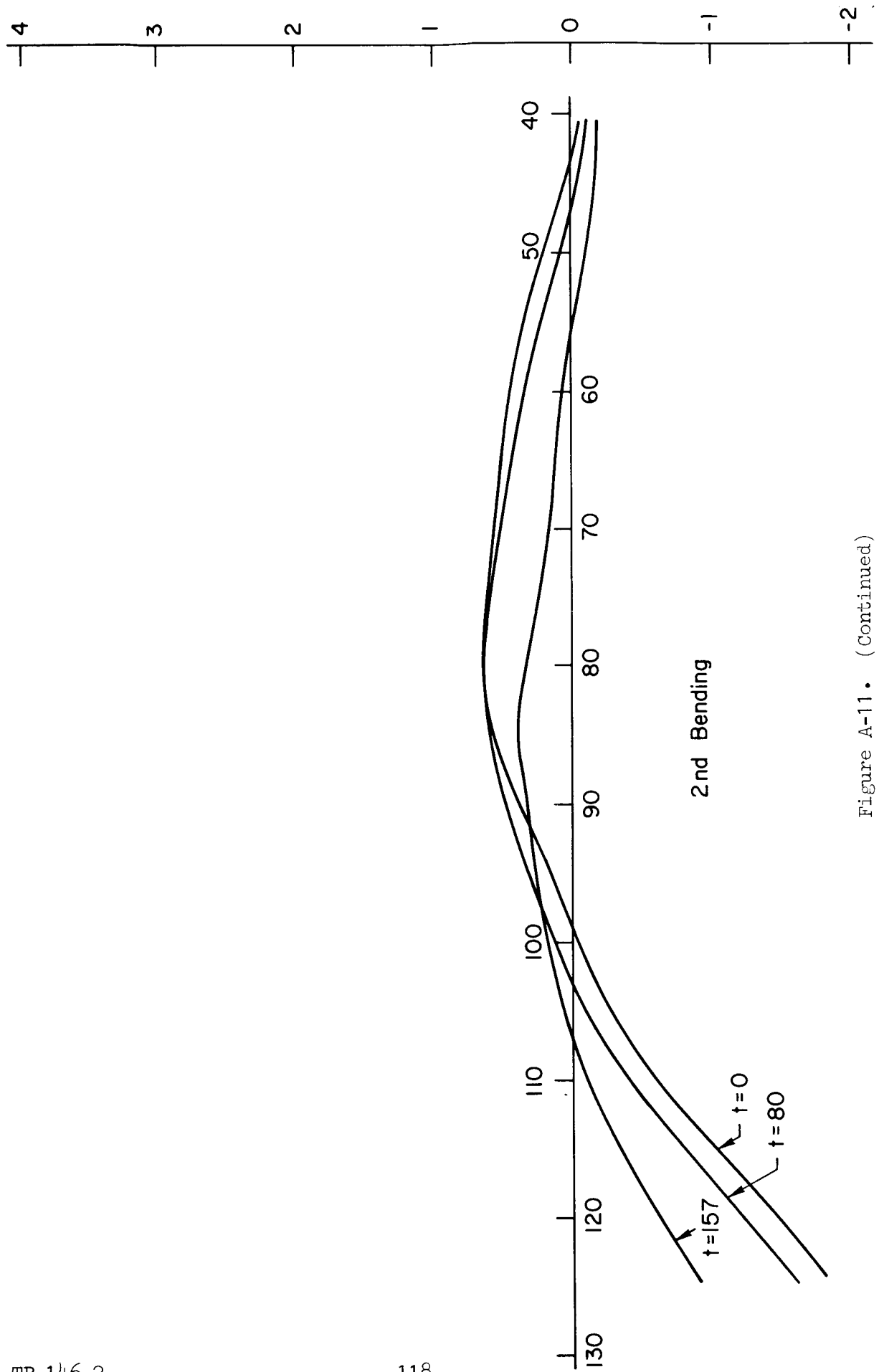


Figure A-11 • (Continued)

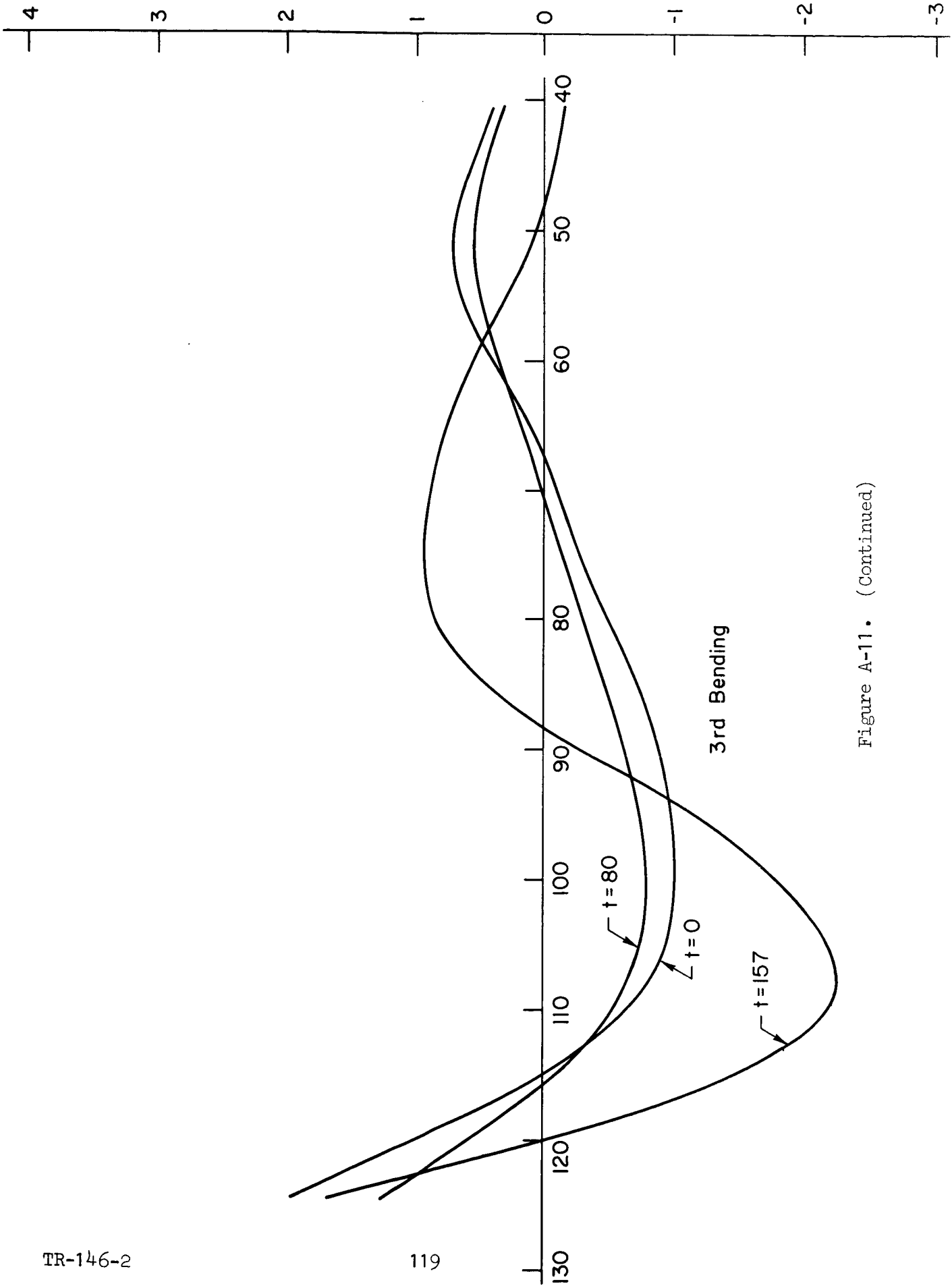
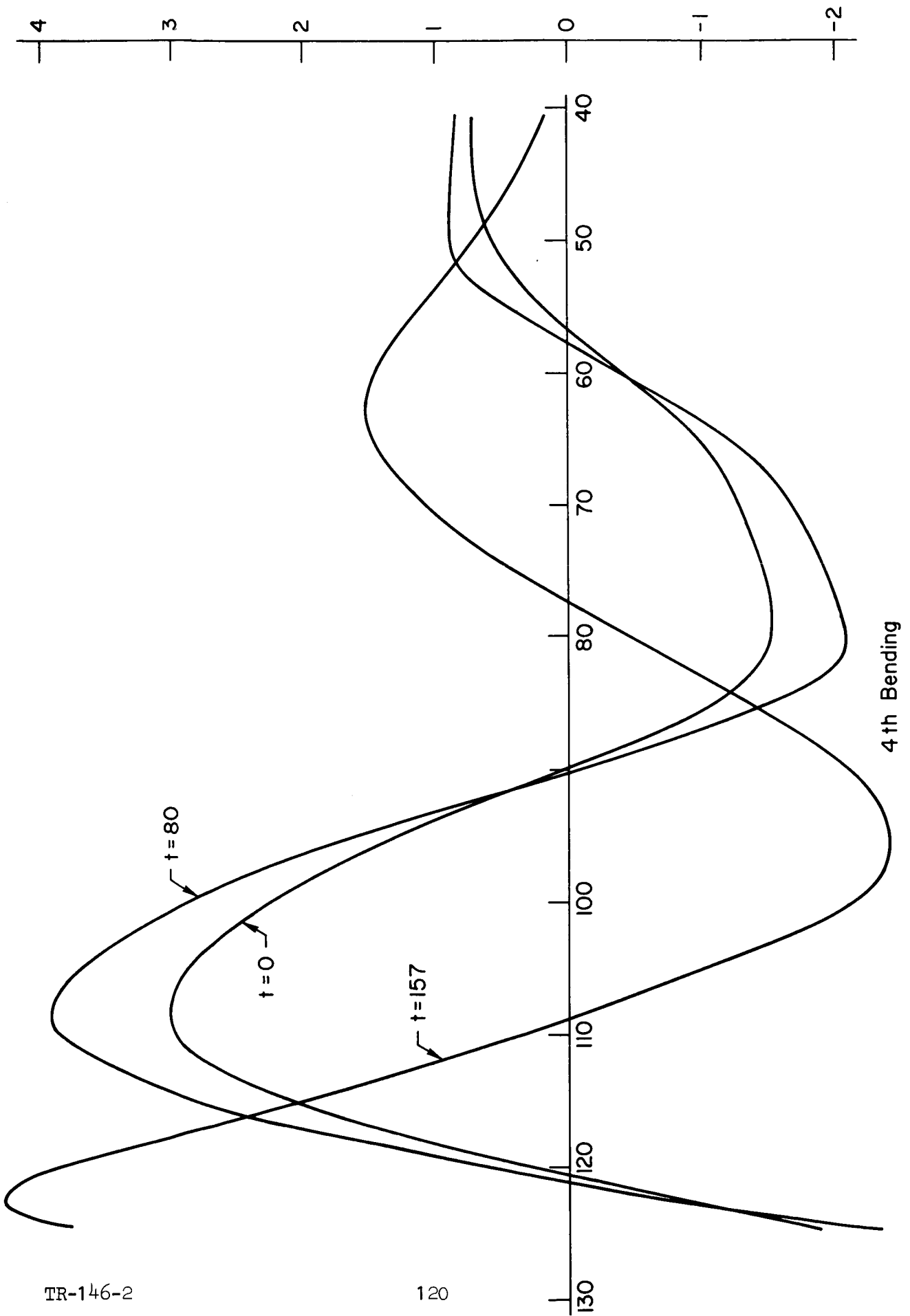


Figure A-11 • (Continued)



TR-146-2

120

Figure A-11. (Concluded)

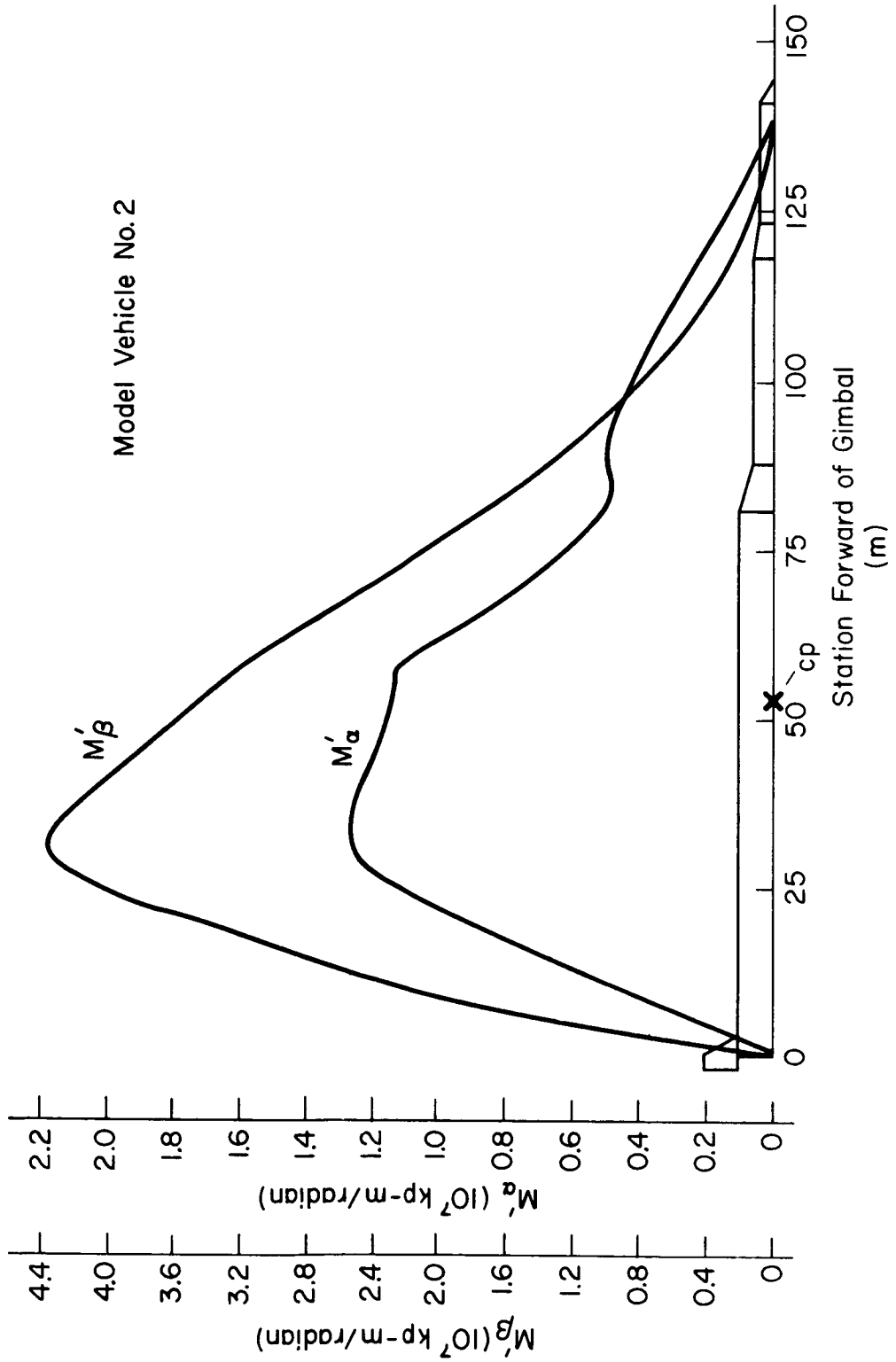


Figure A-12. Engine and Angle of Attack Moments, $t = 78$ sec

APPENDIX B

SIMPLIFIED EQUATIONS OF MOTION

L. G. Hofmann

The derivation (Ref. 4) of the simplified equations of motion involves the elimination of certain variables which may be regarded as being intermediate (i.e., formed from linear combinations of the independent degree of freedom variables) in such a way as to emphasize the mathematical similarities of the various modes. The only restriction placed on this line of attack is that the end results be expressed in terms readily identifiable with the physical system. The mathematical solution of a coordinate transformation to completely diagonalize the characteristic matrix for the system is not an acceptable approach because the relationships of the transformed to the physical coordinates are too obscure.

At the outset, let our thesis be that gross system behavior can be accounted for in terms of the following block diagram (Fig. B-1) and variables.

Examination of the equations of motion reveals that while the rigid body, engine, and bending modes of motion fit this form relatively well in an approximate sense, the sloshing modes do not. The reasons for this are twofold

1. The sloshing motion degrees of freedom are forced through motion of the container wall, i.e., through ϕ , Z , and the η_i 's.
2. The motion component due to sloshing effects at the sensor inputs is contained in the ϕ , Z , and η_i variables.

The obvious way around the second point is merely to identify a component in the equations for the ϕ , Z , and η_i variables which may be considered to arise from the sloshing motion. This component is identified by analogy, let us say, to the terms expressing the contribution of the bending to the angular rotation sensed by a gyro. Thus, for ϕ , let

$$\ddot{\phi} = \ddot{\phi}_1 + \sum_j Y_j \ddot{z}_{sj} \quad (B-1)$$

Then, match the appropriate terms in the ϕ equation after substitution of

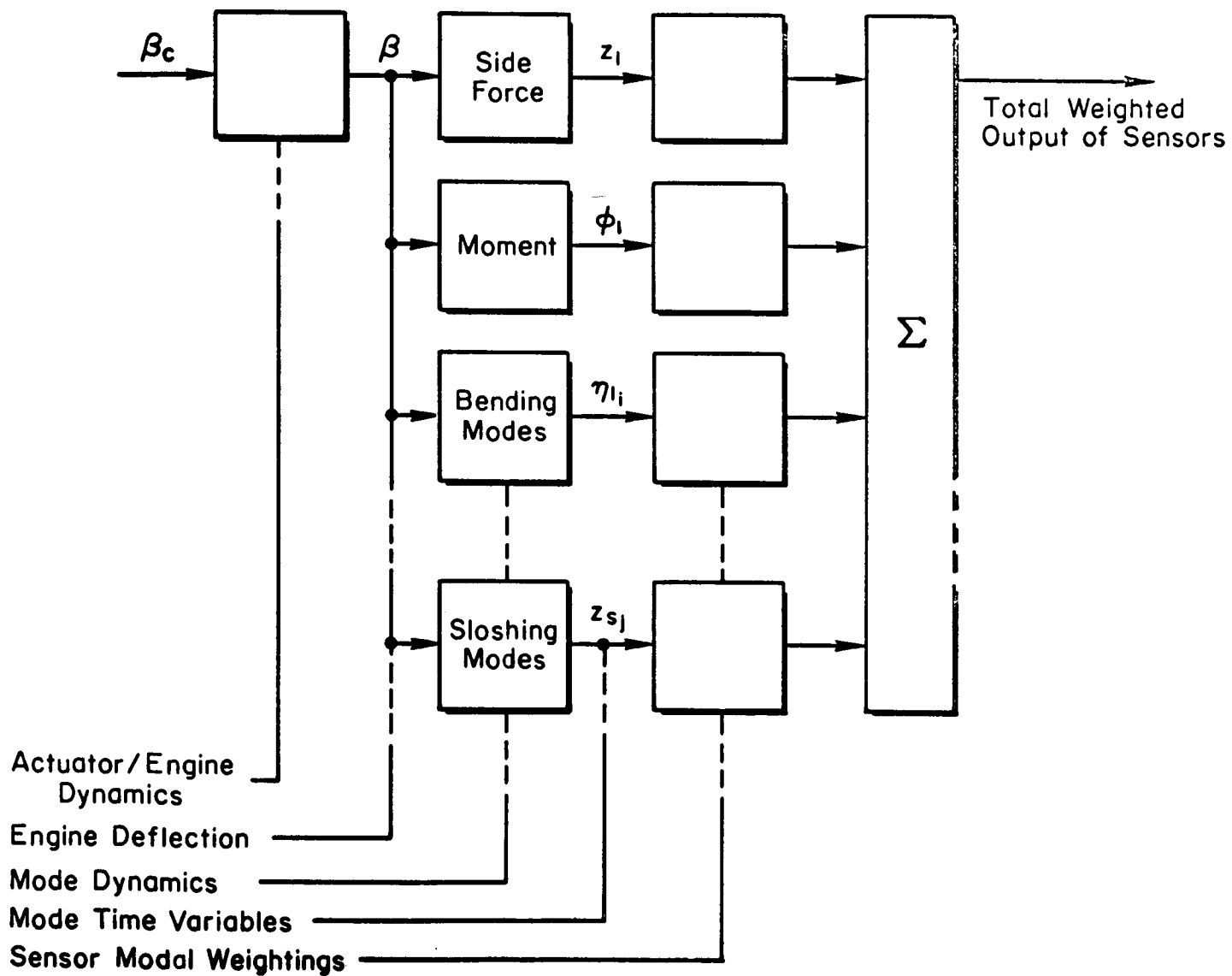


Figure B-1. Simplified Equation Model

the above expression,

$$Y_j' = - \frac{l_{sj} M_{sj}}{I} \quad (B-2)$$

Likewise, for Z and η_1 ,

$$\ddot{Z} = \ddot{z}_1 + \ddot{\phi} + \sum_j Y_j(x_{CG}) \ddot{z}_{sj} \quad (B-3)$$

and

$$\ddot{\eta}_1 = \ddot{\eta}_{1_1} + \sum_j Y_j(x_{CG}) Y_{1_1}(x_{sj}) \frac{M}{M_1} \ddot{z}_{sj} \quad (B-4)$$

$$Y_j(x) = - \frac{M_{sj}}{M} \left[1 + \frac{M l_{sj}}{I} (x - x_{CG}) \right] \quad (B-5)$$

It is evident that by combining the sloshing contributions from the ϕ , Z, and η_1 modes, a direct sloshing motion input to the sensors may be realized in keeping with the block diagram. This necessitates rewriting the equations of motion in the appropriate forms. This has been done in the following pages.

The way around the first point is to eliminate ϕ , Z, and η_1 from the sloshing equations. With the complete detailed equations of motion, this is difficult to accomplish by substitution, therefore we shall postpone performing the substitution until after a simplified set of equations of motion has been formed. The substitution approach is, however, the one we shall ultimately use.

As the next step we will simplify the equations of motion in a manner that will render them analytically convenient to use. Fortunately, the resulting equations are accurate enough to fulfill their intended function of indicating the important relationships among key parameters.

Mathematically Convenient Assumptions for Diagonalizing
the Modal Partition of the Characteristic Matrix

1. Aerodynamic couplings (except for self-couplings) and acceleration field couplings into the z_1 equation are neglected.
2. Aerodynamic couplings (except for self-couplings) and acceleration field couplings into the ϕ_1 equation are neglected.

3. Couplings of bending and sloshing modes into the sloshing modes due to tank wall motion are neglected.
4. Couplings of bending and sloshing modes into the sloshing modes due to the acceleration field are neglected.
5. Aerodynamic and acceleration field couplings of sloshing and bending modes (except for self-couplings) into the bending equations are neglected.
6. All modal couplings into the engine equation are neglected.
7. The small amount of damping inherent in the bending and sloshing modes is neglected.

The equations obtained as a result of employing these assumptions are further modified by eliminating the ϕ_1 and z_1 variables from the simplified sloshing equation.

$$\begin{aligned}
\ddot{z}_{s_j} + \omega_{s_j}^2 z_{s_j} &= -\ddot{z}_1 - l_{s_j} \ddot{\phi}_1 \\
&= -\frac{c_T}{FM} \beta - c \frac{M_E l_E}{M} \ddot{\beta} + \frac{N_\alpha}{MV} \dot{z}_1 \\
&\quad + l_{s_j} \frac{c_T}{FI} (-l_\beta) \beta + l_{s_j} c \frac{M_E l_E (-l_\beta) + I_E}{I} \ddot{\beta} \\
&\quad - l_{s_j} \frac{N_\alpha l_{cp}}{I} \phi_1 - \frac{N_\alpha}{mV} \left(1 + \frac{l_{cp} l_{s_j} M}{I} w \right)
\end{aligned} \tag{B-6}$$

8. Aerodynamic couplings into the sloshing equations are neglected.

Then the sloshing becomes:

$$\begin{aligned}
\ddot{z}_{s_j} + \omega_{s_j}^2 z_{s_j} &= \frac{c_T}{FM_{s_j}} \left(\frac{-M_{s_j}}{M} \right) \left[1 - \frac{(-l_\beta) l_{s_j} M}{I} \right] \beta \\
&\quad + \frac{c_T}{FM_{s_j}} \left(\frac{FM_E l_E}{T} \right) \left(\frac{-M_{s_j}}{M} \right) \left\{ 1 - \frac{(-l_\beta) l_{s_j} M}{I} \left[1 + \frac{I_E}{M_E l_E (-l_\beta)} \right] \right\} \ddot{\beta} \\
&\quad + \frac{N_\alpha Y_j(x_{cp})}{M_{s_j} V} w
\end{aligned} \tag{B-7}$$

The Laplace-transformed simplified equations of motion are summarized below.

$$\begin{aligned} \left(s^2 + \frac{N_\alpha}{M\bar{V}} s\right) z_1 &= \frac{cM_{E1E}}{M} \left(s^2 + \frac{T}{FM_{E1E}}\right) \beta + \frac{N_\alpha}{M\bar{V}} w \\ \left(s^2 - \frac{N_\alpha l_{cp}}{I}\right) \phi_1 &= \frac{cM_{E1E}}{I} \left\{ l_\beta \left[1 + \frac{I_E}{M_{E1E}} \frac{1}{(-l_\beta)} \right] \right\} s^2 + \frac{T}{FM_{E1E}} \left[\frac{1}{1 + \frac{I_E}{M_{E1E}} \frac{1}{(-l_\beta)}} \right] \beta + \frac{N_\alpha l_{cp}}{I\bar{V}} w \\ \left(s^2 + \omega_{s_j}^2\right) z_{s_j} &= \frac{cM_{E1E}}{M_{s_j}} \left\{ Y_j(x_\beta) \left[1 - \frac{I_E}{M_{E1E}} \frac{Y'_j(x_\beta)}{Y_j(x_\beta)} \right] \right\} s^2 + \frac{T}{FM_{E1E}} \left[\frac{1}{1 - \frac{I_E}{M_{E1E}} \frac{Y'_j(x_\beta)}{Y_j(x_\beta)}} \right] \beta \\ &\quad + \frac{N_\alpha Y_j(x_{cp})}{M_{s_j} \bar{V}} w \\ \left(s^2 + \omega_i^2\right) \eta_{1_i} &= \frac{cM_{E1E}}{M_i} \left\{ Y_i(x_\beta) \left[1 - \frac{I_E}{M_{E1E}} \frac{Y'_i(x_\beta)}{Y_i(x_\beta)} \right] \right\} s^2 + \frac{T}{FM_{E1E}} \left[\frac{1}{1 - \frac{I_E}{M_{E1E}} \frac{Y'_i(x_\beta)}{Y_i(x_\beta)}} \right] \beta \\ &\quad + \frac{N_\alpha Y_i(x_{cp})}{M_i \bar{V}} w \\ \left(s^2 + 2\zeta_E \omega_E s + \omega_E^2\right) \beta &= \omega_E^2 \beta_c \end{aligned} \tag{B-8}$$

The equations are presented in matrix form in Fig. B-II and Table B-I.

To conclude this presentation of simplified launch vehicle dynamics, we supply a simplified description of quantities sensed by a gyro and a lateral accelerometer. It has been assumed that the instruments themselves are "ideal"; that is, each sensor output signal is proportional (gain taken to be 1) to the appropriate physical (input) quantity. This assumption is consistent with the objectives of the simplified analysis concept.

In each case the sensor output is a dynamically weighted sum of the modal signals defined earlier. The weighting functions are, to some extent, adjustable in that their coefficients are functionally related to instrument locations x_G and x_A .

$s(s + \frac{1}{T_Z})$	z_1	$A_z(s^2 + \omega_{z\beta}^2)$	B_z
$s^2 - \omega_\phi^2$	ϕ_1	$A_\phi(s^2 + \omega_{\phi\beta}^2)$	B_ϕ
$s^2 + \omega_{s1}^2$	z_{s1}	$A_{zs1}(s^2 + \omega_{zs1}^2)$	B_{zs1}
$s^2 + \omega_{s2}^2$	z_{s2}	$A_{zs2}(s^2 + \omega_{zs2}^2)$	B_{zs2}
$s^2 + \omega_{s3}^2$	z_{s3}	$A_{zs3}(s^2 + \omega_{zs3}^2)$	B_{zs3}
$s^2 + \omega_1^2$	η_{11}	$A_{\eta_1}(s^2 + \omega_{\eta_1}^2)$	B_{η_1}
$s^2 + \omega_2^2$	η_{21}	$A_{\eta_2}(s^2 + \omega_{\eta_2}^2)$	B_{η_2}
$s^2 + \omega_3^2$	η_{31}	$A_{\eta_3}(s^2 + \omega_{\eta_3}^2)$	B_{η_3}
$s^2 + \omega_4^2$	η_{41}	$A_{\eta_4}(s^2 + \omega_{\eta_4}^2)$	B_{η_4}

=

$ \beta +$	$ w $
---------------	---------

$$\frac{\beta}{\beta c} = \frac{\omega_E^2}{s^2 + 2\zeta_{E\omega_E}s + \omega_E^2}$$

Figure B-2. Simplified Characteristic Matrix

TABLE B-I

NOMENCLATURE FOR SIMPLIFIED CHARACTERISTIC MATRIX

$$A_{\varphi} = \frac{cM_E l_E}{I} \left[-(-l_{\beta}) \left(i + \frac{I_E}{M_E l_E} \frac{1}{(-l_{\beta})} \right) \right]$$

$$A_{\eta_i} = \frac{cM_E l_E}{M_i} \left[Y_i(x_{\beta}) \left(1 - \frac{I_E}{M_E l_E} \frac{Y_i'(x_{\beta})}{Y_i(x_{\beta})} \right) \right] \quad i = 1, 2, 3, 4$$

$$A_z = \frac{cM_E l_E}{M}$$

$$A_{z_{s_j}} = \frac{cM_E l_E}{M_{s_j}} \left[Y_{s_j}(x_{\beta}) \left(1 - \frac{I_E}{M_E l_E} \frac{Y_{s_j}'(x_{\beta})}{Y_{s_j}(x_{\beta})} \right) \right] \quad j = 1, 2, 3$$

$$B_{\varphi} = \frac{N_{\alpha} l_{cp}}{I \bar{V}}$$

$$B_{\eta_i} = \frac{N_{\alpha} Y_i(x_{cp})}{M_i \bar{V}}$$

$$B_z = \frac{N_{\alpha}}{M \bar{V}} = \frac{1}{T_z}$$

$$B_{z_{s_j}} = \frac{N_{\alpha} Y_{s_j}(x_{cp})}{M_{s_j} \bar{V}}$$

$$\omega_{\varphi}^2 = \frac{N_{\alpha} l_{cp}}{I}$$

$$\omega_{\varphi_{\beta}}^2 = \frac{T}{FM_E l_E} \left[\frac{1}{1 + \frac{I_E}{M_E l_E} \frac{1}{(-l_{\beta})}} \right]$$

$$\omega_{\eta_i}^2 = \frac{T}{FM_E l_E} \left[\frac{1}{1 - \frac{I_E}{M_E l_E} \frac{Y_i'(x_{\beta})}{Y_i(x_{\beta})}} \right]$$

$$\omega_{z_{\beta}}^2 = \frac{T}{FM_E l_E}$$

$$\omega_{z_{s_j}}^2 = \frac{T}{FM_E l_E} \left[\frac{1}{1 - \frac{I_E}{M_E l_E} \frac{Y_{s_j}'(x_{\beta})}{Y_{s_j}(x_{\beta})}} \right]$$

Angular Motion Sensed by a Gyro:

$$\begin{aligned}\varphi_G &= \varphi_1 + \sum_i Y'_i(x_G) \eta_{1i} + \sum_j \left[Y'_j + Y_j(x_{CG}) \sum_i Y'_i(x_G) Y_i(x_{Sj}) \frac{M}{M_i} \right] z_{Sj} \\ &= \varphi_1 + \sum_i Y'_i(x_G) \eta_{1i} + \sum_j \Gamma'_j(x_G) z_{Sj}\end{aligned}\quad (B-9)$$

Lateral Acceleration Sensed by an Accelerometer:

$$\begin{aligned}\ddot{z}_A &= \ddot{z}_1 + l_A \ddot{\phi}_1 + \sum_j \left[Y_j(x_A) + Y_j(x_{CG}) \sum_i Y_i(x_A) Y_i(x_{Sj}) \frac{M}{M_i} \right] \ddot{z}_{Sj} \\ &\quad + \sum_i Y_i(x_A) \ddot{\eta}_{1i} - \bar{g} \sum_i Y'_i(x_A) \eta_{1i} \\ &\quad - \bar{g} \sum_j Y_j(x_{CG}) \sum_i Y'_i(x_A) Y_i(x_{Sj}) \frac{M}{M_i} z_{Sj} \quad (B-10) \\ &= \ddot{z}_1 + l_A \ddot{\phi}_1 + \sum_i Y_i(x_A) \ddot{\eta}_{1i} - \bar{g} \left[\sum_j \lambda_j(x_A) z_{Sj} + \sum_i Y'_i(x_A) \eta_{1i} \right] + \sum_j \psi_j(x_A) \ddot{z}_{Sj}\end{aligned}$$

where $\Gamma'_i(x_G) = Y_{Sj}'(x_G) + Y_{Sj}(x_{CG}) \sum_i Y'_i(x_G) Y_i(x_{Sj}) \frac{M}{M_i}$

$$\psi_j(x_A) = -M_{Sj} \left[\frac{1}{M} + \frac{l_{Sj}}{I} (x - x_{CG}) + \sum_i Y_i(x_A) \frac{Y_i(x_{Sj})}{M_i} \right]$$

$$\lambda_j(x_A) = -M_{Sj} \sum_i Y'_i(x_A) \frac{Y_i(x_{Sj})}{M_i}$$

$$l_A = x_A - x_{CG}$$

DEFINITION OF SYMBOLS

- c Number of main engines gimballed in a single plane
 C_{Z_α} Aerodynamic side force coefficient, Z_α/qS , of vehicle
F Total number of main engines

\bar{g}	Longitudinal acceleration of vehicle = $\frac{T - X}{M}$
I	Moment of inertia of vehicle, including <u>nonslashing</u> propellant components and engines
I_E	Moment of inertia of a single main engine about its gimbal point
l	Length, in general measured positive in forward direction from total vehicle or vehicle component CG to point indicated by subscript
M	Total mass of vehicle
M	Generalized mass of the mode, particularized by the subscript
q	Dynamic pressure
S	Reference area of vehicle
T	Total thrust of main booster engines (for the active stage)
\bar{V}	Nominal flight path velocity
x	Coordinate in direction of weighted average vehicle center line, positive forward
X	Total axial aerodynamic force acting on vehicle
$Y_i(x)$	Normalized amplitude of i^{th} bending mode deflection at station x. Normalization may be made in an arbitrary way. Customary ways include choosing the normalization factors such that the generalized mass of each mode equals the total system mass; normalization such that $Y_i(x)$ at a particular station is the same arbitrarily chosen value for all modes. MSFC uses the latter method, defining all modal amplitudes to be +1.0 at the main engine gimbal station, x_p .
z_{sj}	Generalized displacement coordinate in the vehicle system of the fundamental sloshing modal mass in the j^{th} propellant tank
z	Generalized coordinate of the vehicle system in the quasi-inertial axis system; X,Y,Z. Translation of weighted average vehicle centerline from nominal flight path of vehicle.
β	Generalized coordinate of vehicle system. Rotation of main engine centerlines from the deflected vehicle centerline tangent at the main engine gimbal station.
β_c	Commanded value of β at position servo output
ζ	Damping ratio, particularized by the subscript
η_i	Generalized displacement coordinate of the vehicle system in the i^{th} mode of the local booster structure from the weighted average vehicle centerline

- ϕ Generalized coordinate of the vehicle system in the quasi-inertial axis system; X,Y,Z. Rotation of the weighted average vehicle centerline from the nominal flight path direction, X axis.
- ω Undamped natural frequency, particularized by the subscript

Subscripts:

- A Accelerometer location
- CG Center of gravity
- E Main engine or engines
- G Location of gyro or IMU
- i Index indicating the i^{th} bending mode
- s_j Indicates the first sloshing mode of the fluid in the j^{th} propellant tank
- β Main engine gimbal location

Special Notation:

- ($\dot{\quad}$) Denotes derivative of quantity with respect to time
- (\quad)' Denotes derivative of quantity with respect to x

APPENDIX C
SAWTOOTH BODE CONCEPT

The basic objective of the Sawtooth Bode Concept is to increase the damping of several modes simultaneously. To show how this can be done, we will start with some fundamental aspects of the tie between Bode amplitude plots and the root locus diagram. Consider the simple block diagram in Fig. C-1,

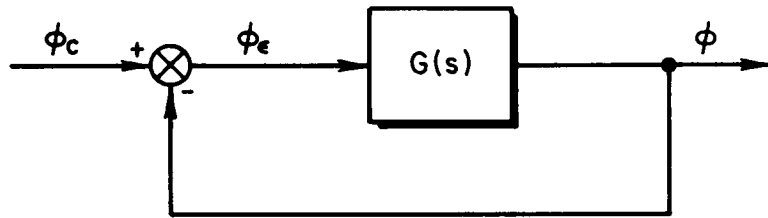


Figure C-1. Simple Unity-Feedback System

and assume $G(s)$ is of the form

$$G(s) = \frac{K(s^2 + 2\zeta_1\omega_1 s + \omega_1^2)}{s(s^2 + 2\zeta_2\omega_2 s + \omega_2^2)}$$

where ζ_1 and ζ_2 are both very low and $\omega_1 < \omega_2$. The root locus is shown in Fig. C-2, with indications of the closed-loop poles for three values of open-loop gain — low, K_L ; medium, K_M ; and high, K_H .

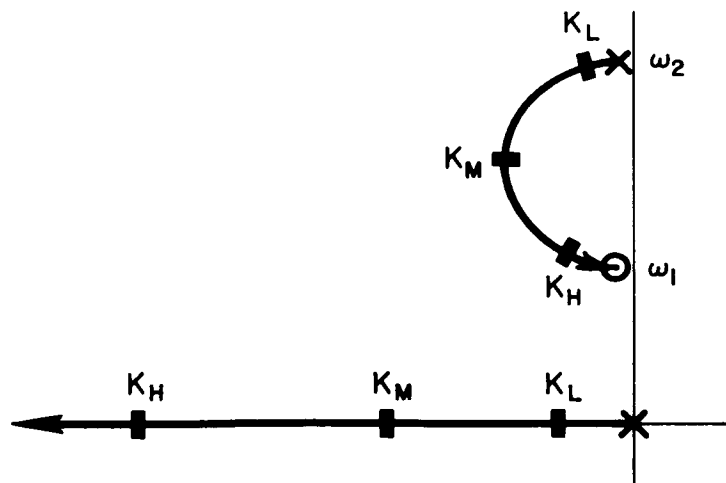


Figure C-2. Root Locus Diagram

Obviously, the maximum damping of the oscillatory closed-loop roots is achieved when the open-loop gain is K_M . If the open-loop gain is too low, the closed-loop oscillatory roots will be poorly damped, having a damping ratio only slightly higher than ζ_2 . If the open-loop gain is too high, the closed-loop oscillatory roots will again be poorly damped, with a damping ratio approaching ζ_1 .

Now consider the open-loop Bode plot, with the 0 dB lines shown for these three cases of gain, Fig. C-3. It becomes clear that when the 0 dB line passes above or through the top of an open-loop Bode peak due to poorly damped denominator roots (poles), the closed-loop damping characteristics will be very poor. Also, when the 0 dB line passes below or through the bottom of an open-loop Bode valley due to poorly damped numerator roots (zeros), the closed-loop damping again is very poor. The highest closed-loop damping occurs when the 0 dB line cuts deeply into the open-loop Bode peak, but well above the open-loop Bode valley.

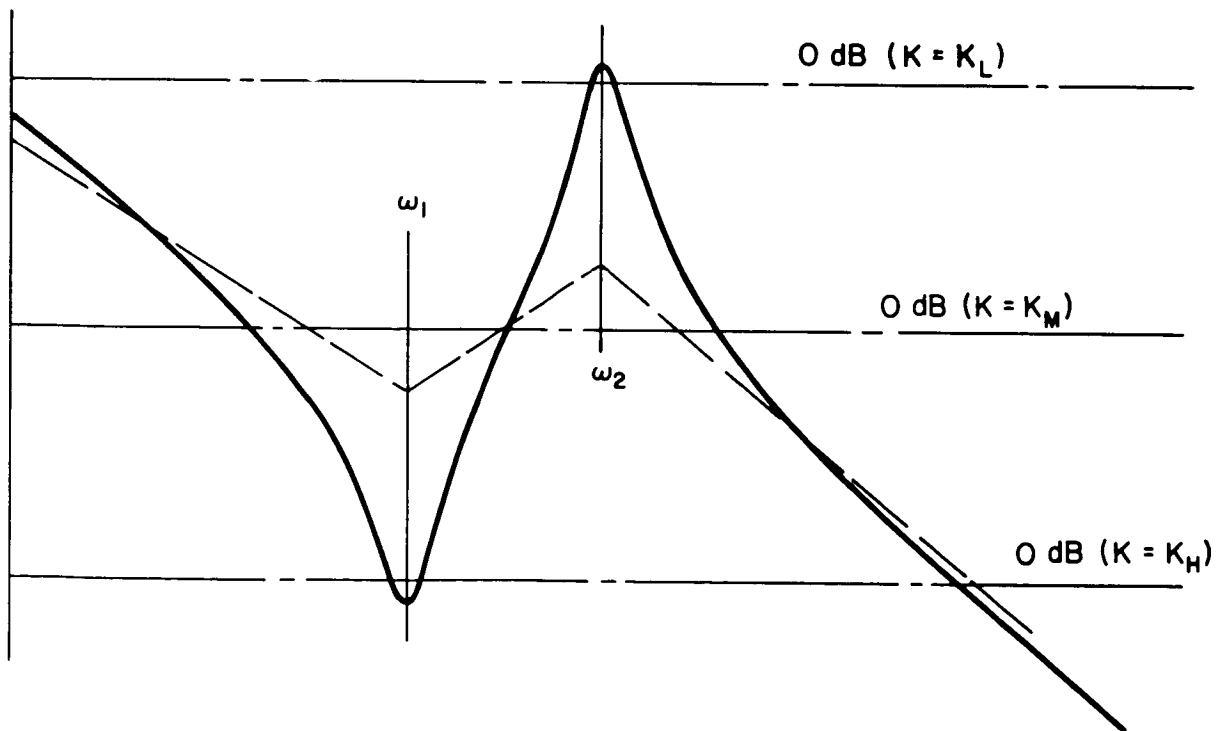


Figure C-3. Open-Loop Amplitude Bode Plot

The application of the above considerations in the synthesis of booster control systems where more complex open-loop transfer functions exist can now be shown fairly easily. Consider that the generalized single-loop block diagram shown in Fig. C-4 represents a booster control system. Here the response variable, q , is used as the feedback, the actuator servo is represented by a first-order element, and the controller is a pure gain with no equalization.

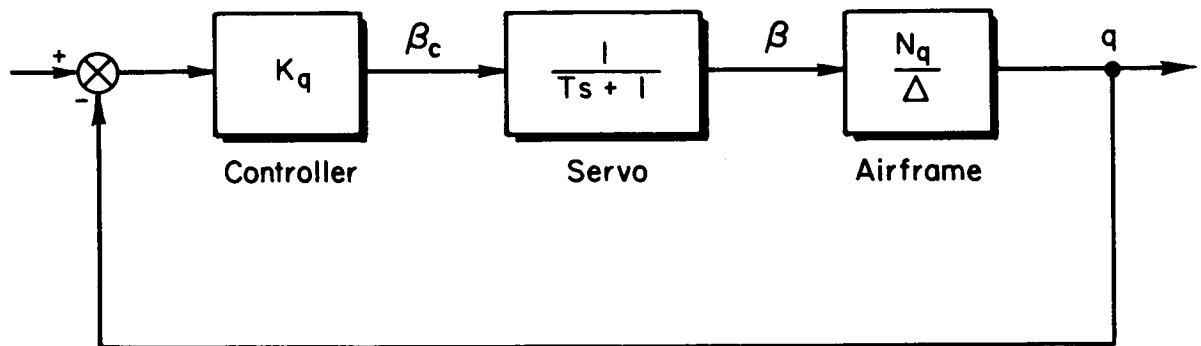


Figure C-4. Booster Control System Block Diagram

We will assume that the airframe transfer function now is of the more complicated form

$$\frac{N_q/\beta}{\Delta} = \frac{A_q s(s^2 + 2\zeta_a \omega_a s + \omega_a^2)(s^2 + 2\zeta_b \omega_b s + \omega_b^2)}{(s^2 + 2\zeta_1 \omega_1 s + \omega_1^2)(s^2 + 2\zeta_2 \omega_2 s + \omega_2^2)(s^2 + 2\zeta_3 \omega_3 s + \omega_3^2)}$$

and that all the damping ratios (ζ) are very small. With the servo bandwidth high ($1/T > \omega_3$), a possible Bode plot for the controller-servo-airframe open loop might appear as in Fig. C-5. In this case, closing the loop with a low gain is adequate to damp the first two modes, ω_1 and ω_2 , but leaves the damping of the highest mode essentially unaffected. If the open-loop gain were increased to damp the ω_3 mode by having the 0 dB line cut deeply into the Bode peak associated with ω_3 , the closed-loop damping of the ω_2 mode would be substantially decreased, for the 0 dB line now passes through the Bode valley

of the poorly damped ω_2 zeros. Thus, simultaneous damping of all three airframe oscillatory modes is not possible.

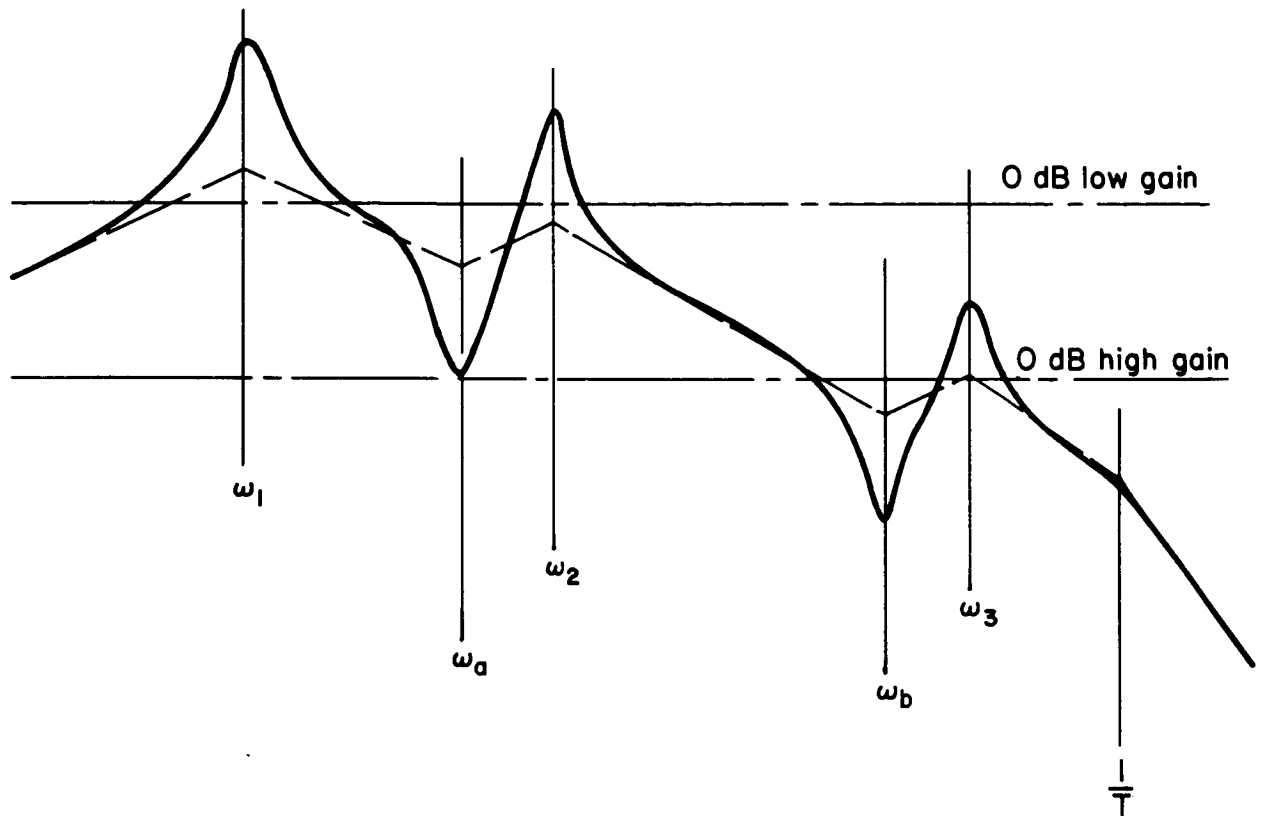


Figure C-5. Original Controller-Servo-Airframe Open-Loop Bode Plot

If it were possible to modify the numerator of the airframe by relocating the sensor of q so that the numerator roots occur midway (on the Bode plot) between the adjacent airframe poles (which are not affected by sensor location) then the Bode plot would appear as in Fig. C-6. Now the damping of all three modes can be increased simultaneously by having the 0 dB line cut deeply into all three Bode peaks. This, then, is the essence of the Sawtooth Bode Concept.

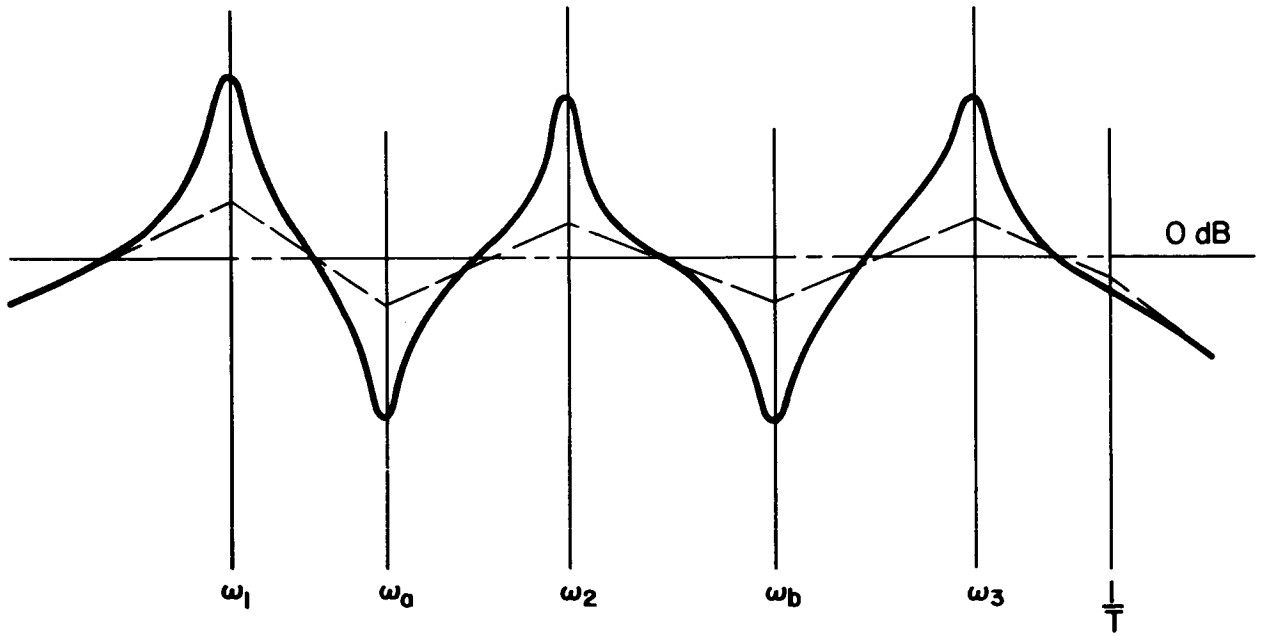


Figure C-6. Modified Controller-Servo-Airframe Open-Loop Bode Plot

APPENDIX D

PRELIMINARY ANALYSIS VIA SIMPLIFIED TRANSFER FUNCTIONS

In this appendix we shall concern ourselves with the selection and location of feedback sensors. The approach taken is to focus, as rapidly as possible, on the frequency band between a logical rigid mode controller break frequency and a logical amplitude-phase cutoff frequency (the band over which the "sawtooth Bode" concept is most useful). To facilitate this, the analysis is based on the simplified vehicle equations of motion (Appendix B). In addition, system dynamics having limited contribution in the frequency range of interest are relegated to consideration in later analyses. Since one of the objectives of this analysis is to gain insight to the effects of the non-rigid vehicle modes, the actuator-engine and tail-wags-dog dynamics will be excluded, temporarily, to avoid clouding the picture. The previous sections have indicated the advantages and limitations of using simplified transfer functions. It bears repeating, however, that the simplified equations facilitate an analytical understanding of the fundamental modes and the effects of loop closures about these modes. They are not intended to reflect coupling effects or, for that matter, to be other than "ballpark" approximations to the exact equations. The dominant coupling effects and other neglected terms are included in the later detailed synthesis.

A. SAWTOOTH BODE CRITERIA - ATTITUDE RATE SENSING

The Sawtooth Bode Concept is outlined in Appendix C. The object is to select the sensor location such that the zero of each mode is located on the $j\omega$ axis precisely midway between its associated pole and the next lower pole. If this can be achieved, closure of the feedback loop will result in damping of each mode without the necessity for shaping in the feedback. In this subsection we shall present a generic development of criteria for sensor location (or locations) to achieve the "Sawtooth Bode" form. The criteria are developed by the successive loop closure technique outlined in Section II in which the contributions or effects of successively higher modal dynamics are brought into consideration through repetitive multiloop analysis procedures.

From Appendix B, the attitude rate (rate gyro) sensing equation is:

$$\dot{\phi}_G = K_{RG} s \left\{ \phi_1 + \sum_j \Gamma_j'(x_{RG}) z_{sj} + \sum_i Y_i'(x_{RG}) \eta_{i1} \right\} \quad (D-1)$$

where

$$\Gamma_j'(x_{RG}) = Y_{sj}' + Y_{sj}(x_{cg}) \sum_i Y_i'(x_{RG}) Y_i(x_{sj}) \frac{M}{M_i}$$

Engine deflection to sensor output transfer function is:

$$\frac{\dot{\phi}_G}{\beta} = K_{RG} s \left\{ \frac{A_{\phi_1}}{s^2 - \omega_{\phi}^2} + \sum_j \frac{\Gamma_j'(x_{RG}) A_{z_{sj}}}{s^2 + \omega_{sj}^2} + \sum_i \frac{Y_i'(x_{RG}) A_{\eta_{i1}}}{s^2 + \omega_i^2} \right\} \quad (D-2)$$

Arranging the modal frequencies in ascending order, for example,

$$\omega_{\phi} < \omega_{s1} < \omega_{s2} < \omega_{s3} < \omega_1 < \omega_2 < \omega_3 < \omega_4$$

and employing the first two modes

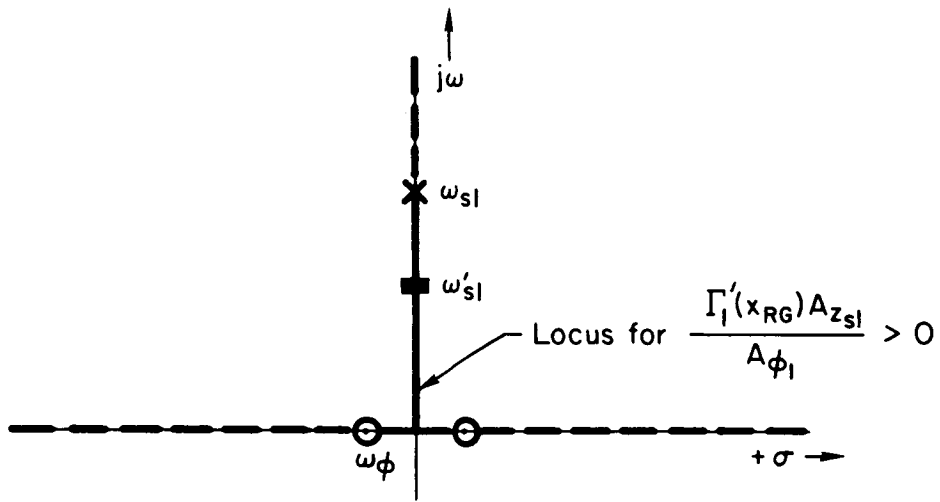
$$\frac{\dot{\phi}_G}{\beta} = K_{RG} s \left\{ \frac{A_{\phi_1} \left[(s^2 + \omega_{s1}^2) + \frac{\Gamma_1'(x_{RG}) A_{z_{s1}}}{A_{\phi_1}} (s^2 - \omega_{\phi}^2) \right]}{(s^2 - \omega_{\phi}^2)(s^2 + \omega_{s1}^2)} \right\} \quad (D-3)$$

The numerator may be factored by graphical techniques, as indicated in Fig. D-1, to obtain the sign and magnitude of the gain term,

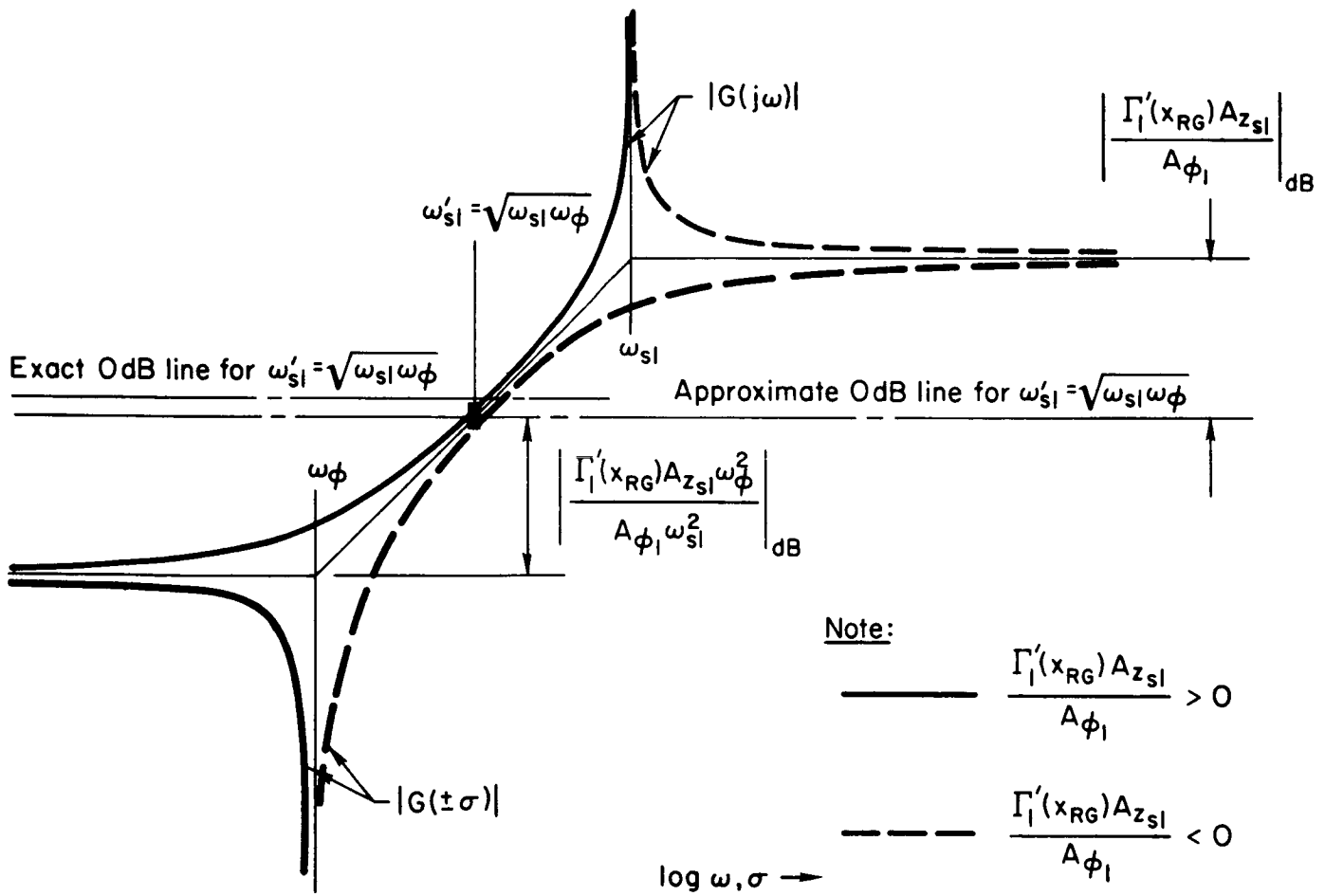
$$\frac{\Gamma_1'(x_{RG}) A_{z_{s1}}}{A_{\phi_1}} \quad (D-4)$$

which places the zero, ω_{s1}' , exactly midway between the poles ω_{ϕ} and ω_{s1} . This occurs if the gain term is positive and if

$$\Gamma_1'(x_{RG}) = \left| \frac{A_{\phi_1}}{A_{z_{s1}}} \frac{\omega_{s1}}{\omega_{\phi}} \right| \quad (D-5)$$



a) Root Locus



Note:

— $\frac{\Gamma_1'(x_{RG})A_{zsl}}{A_{\phi_1}} > 0$

- - - $\frac{\Gamma_1'(x_{RG})A_{zsl}}{A_{\phi_1}} < 0$

b) Bode

Figure D-1. Locus of Zeros

various slopes on the location of numerator zeros. The location of these zeros for any sensor station is determined by vehicle characteristics alone. Referring back to Fig. D-1, if the Sawtooth Bode sign criteria is violated, the zero will not be located on the $j\omega$ axis between the appropriate pair of poles and hence the desired $j\omega$ axis pole/zero/pole, etc., sequence will not be obtained. Again from Fig. D-1, if the sign of the gain term is incorrect and the magnitude is sufficiently large, the zeros will move out the $j\omega$ axis until the gain line coincides with the high frequency asymptote. At this point the zeros are of infinite magnitude. For larger gain, the zeros move back in the real axis to a value set by the magnitude of the gain. From the summary of gyro numerators of Fig. A-3, the latter occurs for two pair of zeros when the sensor is located at either $x_G = 76.5$ or 88.5 meters but only for one pair of zeros when the sensor is located at $x_G = 46.5$ meters. Furthermore, this one set of real zeros occurs at a relatively high frequency and hence allows the Sawtooth effect to be obtained over a wider frequency band. Thus the most aft sensor location is the best compromise.

Figure A-6 indicates the situation is much the same for the maximum-q case ($t = 80$ sec). That is, the most aft sensor location is best. Here the 180 deg crossover should be between the second and third bending modes. Figure A-9 again indicates the most aft sensor location comes the closest to meeting the sawtooth criteria at burnout ($t = 157$ sec). In this case the 180 deg crossover should be between the third and fourth bending modes.

The bending mode slope data of Fig. A-11 indicates that slight shifts in the sensor location within any of the allowable sensor station bands will not improve the slope sign situation. Hence, for a single sensor, full potential of the Sawtooth Bode effect cannot be realized. The most aft sensor location does appear to be the best from the standpoint of minimizing the feedback shaping required to achieve positive damping of the nonrigid modes.

C. PRELIMINARY LOOP CLOSURES FOR $t = 80$ SEC

1. Single Sensor Feedback

From the foregoing, station $x_G = 46.5$ meters appears to be the best compromise location for a single rate gyro. We shall therefore perform a preliminary analysis of such a feedback at the maximum-q flight condition ($t = 80$ sec) to increase our "feel" for the behavior of the nonrigid modes.

Bode, Siggie, and root-locus sketches for the airframe alone and a pure gain (i.e., no shaping) feedback are shown in Fig. D-2. The sign of the feedback is selected to stabilize the rigid body modes (loci ① and ②) and the lower frequency nonrigid modes. This feedback results in a zero degree phase criteria, therefore, the Bode phase crossovers of concern are the zero degree crossovers. Recall that the Sawtooth Bode sign criteria indicated a phase reversal to be required between the second and third bending modes in order to stabilize the third and fourth bending modes. This is demonstrated by Fig. D-2. Selection of the feedback shaping to provide a zero degree phase crossover between the second and third bending modes will cause a phase reversal for poles above ω_3 so that the closed-loop roots emanating from ω_3 and ω_4 (loci ⑦ and ⑧a) depart into the left half plane of the root locus and are stable. Unfortunately, a sharp phase cutoff will be required to accomplish stabilization of the third bending mode without adversely affecting the second bending mode. Figure D-1 also indicates the third slosh mode (loci ⑤) will be destabilized (again as predicted by the Sawtooth Bode sign criteria) while the first slosh mode (loci ④) will remain stable. The second slosh is unaffected since the pole and zero of this mode have identical values.

The root locus and Bode sketches both show the desirability of decreasing all zeros except the zero on the real axis. The latter would preferably be moved to the $j\omega$ axis. Therefore, it is of interest to identify the source of the real axis zero and to investigate the possibility of improving the location of all zeros. This can be accomplished by generating the numerator zeros via the successive loop closure

A primary and limiting assumption is that the next higher pair of pole/zero combinations have little effect on the departure of the $G(j\omega)$ amplitude from the Bode asymptote for this pair.

Repeated applications of this technique (adding ω_{s2} next, then ω_{s3} , etc.) results in the magnitude criteria presented in Table D-I. The sign criteria of the normalized modal slopes, the Γ'_j , Y'_i 's is set by the sign of the appropriate modal gain coefficients, the $A_{(i,j)}$'s, since it is necessary that the complete gain term be positive. For this vehicle A_{ϕ_1} is always negative, therefore it is desired that Γ'_j , Y'_i be of opposite sign to the respective $A_{z_{sj}}$, $A_{\eta_{i1}}$ (see Eq. D-4).

TABLE D-1

MAGNITUDE CRITERIA FOR ACHIEVING SAWTOOTH BODE FORM

$$\begin{aligned}
 1. \quad \Gamma'_1(x_{RG}) &= \frac{A_{\phi_1}}{A_{z_{s1}}} \frac{\omega_{s1}}{\omega_{\phi}} \\
 2. \quad \Gamma'_2(x_{RG}) &= \frac{[A_{\phi_1} + \Gamma'_1(x_{RG})A_{z_{s1}}]}{A_{z_{s2}}} \frac{\omega_{s2}}{\omega_{s1}} \\
 3. \quad \Gamma'_3(x_{RG}) &= \frac{[A_{\phi_1} + \Gamma'_1(x_{RG})A_{z_{s1}} + \Gamma'_2(x_{RG})A_{z_{s2}}]}{A_{z_{s3}}} \frac{\omega_{s3}}{\omega_{s2}} \\
 4. \quad Y'_1(x_{RG}) &= \frac{[A_{\phi_1} + \sum_{j=1}^3 \Gamma'_j(x_{RG})A_{z_{sj}}]}{A_{\eta_{11}}} \frac{\omega_1}{\omega_{s3}} \\
 5. \quad Y'_2(x_{RG}) &= \frac{[A_{\phi_1} + \sum_{j=1}^3 \Gamma'_j(x_{RG})A_{z_{sj}} + Y'_1(x_{RG})A_{\eta_{11}}]}{A_{\eta_{21}}} \frac{\omega_2}{\omega_1} \\
 6. \quad Y'_3(x_{RG}) &= \frac{[A_{\phi_1} + \sum_{j=1}^3 \Gamma'_j(x_{RG})A_{z_{sj}} + \sum_{i=1}^2 Y'_i(x_{RG})A_{\eta_{i1}}]}{A_{\eta_{31}}} \frac{\omega_3}{\omega_2}; \\
 7. \quad Y'_4(x_{RG}) &= \frac{[A_{\phi_1} + \sum_{j=1}^3 \Gamma'_j(x_{RG})A_{z_{sj}} + \sum_{i=1}^3 Y'_i(x_{RG})A_{\eta_{i1}}]}{A_{\eta_{41}}} \frac{\omega_4}{\omega_3}
 \end{aligned}$$

Of the two criteria, the sign criteria is the more basic and practical. That is, it is more important that the zero be between the two poles than that it be exactly midway between them. The magnitude criteria does offer a guide in improving the pole/zero spacing once the proper sequence has been obtained.

It should be noted that the magnitude criteria expressions of Table D-I are valid only for the ascending sequence of model frequencies initially assumed, i.e., $\omega_p, \omega_{s1}, \omega_{s2}, \omega_{s3}, \omega_1$, etc. If the sequence is different, it is necessary to modify the expressions accordingly. For example, if the sequence is $\omega_p, \omega_1, \omega_{s1}, \omega_{s2}$, etc., the magnitude criteria become:

$$Y_1'(x_{RG}) = \left| \frac{A_{\phi_1} \omega_1}{A_{\eta_{11}} \omega_p} \right|$$

$$\Gamma_1'(x_{RG}) = \left| \frac{[A_{\phi_1} + Y_1'(x_{RG})A_{\eta_{11}}] \omega_{s1}}{A_{z_{s1}} \omega_1} \right|$$

$$\Gamma_2'(x_{RG}) = \left| \frac{[A_{\phi_1} + Y_1'(x_{RG})A_{\eta_{11}} + \Gamma_1'(x_{RG})A_{z_{s2}}] \omega_{s2}}{A_{z_{s2}} \omega_{s1}} \right|$$

etc.

Note that the sign criteria do not change.

If the sensor(s) can be located so that the foregoing criteria are satisfied, each mode will be equally damped by a single, unshaped feedback provided that the system phase angle does not exceed 180 deg or that all phase lag in the region of interest is introduced by these modes. If other dynamics (e.g., actuator, rigid body mode shaping, etc.) introduce phase lags so that the system phase exceeds 180 deg, the sawtooth sign criteria will be reversed for all modes having frequencies above the 180 deg phase crossover.

Thus, if the criteria can be satisfied, it indicates

- location(s) for the sensor which will minimize the feedback shaping

If the criteria cannot be satisfied by sensor location, the criteria indicates:

- the best compromise sensor location(s)
- desirable region(s) for the 180 deg phase crossover, and
- modes which are likely to lead to instability problems.

These aspects will be demonstrated in the following subsection.

B. PRELIMINARY SELECTION OF THE ATTITUDE RATE SENSOR LOCATION

The mode slopes at $t = 0, 80, \text{ and } 157$ sec for sample allowable sensor locations (x_G) are presented in Appendix A; Figs. A-3, A-6, and A-9, respectively. Unfortunately, none of the allowable sensor locations completely satisfy the Sawtooth Bode sign criteria. Thus the magnitude criteria are of little value. The "best" single sensor location must, of necessity, be a compromise.

Starting with the lift-off case ($t = 0$ sec), Fig. A-3 indicates the Sawtooth Bode sign criteria requires the four bending mode slopes and the third slosh mode pseudoslope to be negative. The first and second slosh mode pseudoslopes should be positive. The most aft gyro location ($x_G = 46.5$ meters) would suffice, insofar as the sign criteria is concerned, if the 180 deg phase crossover is located between the first and second bending modes. The criteria indicates potential problems with the second and third slosh modes, however, since these have pseudoslopes of the wrong sign and are of lower frequency than the second bending mode. But, referring back to Section II, it will be recalled that the separation between the poles and zeros of any mode is an indication of the validity (or accuracy) of the simplified transfer function factors. For this case there is no separation between the poles and zeros of all three slosh modes. Thus we may neglect the slosh modes for the present and defer their consideration to later detailed analysis.

It might appear at first glance that sensor locations of $x_G = 76.5$ or 88.5 meters would also suffice if the sensor feedback were of opposite sign (thus change the effective slopes from positive to negative, etc.). However, we must bear in mind that we are considering the effect of the

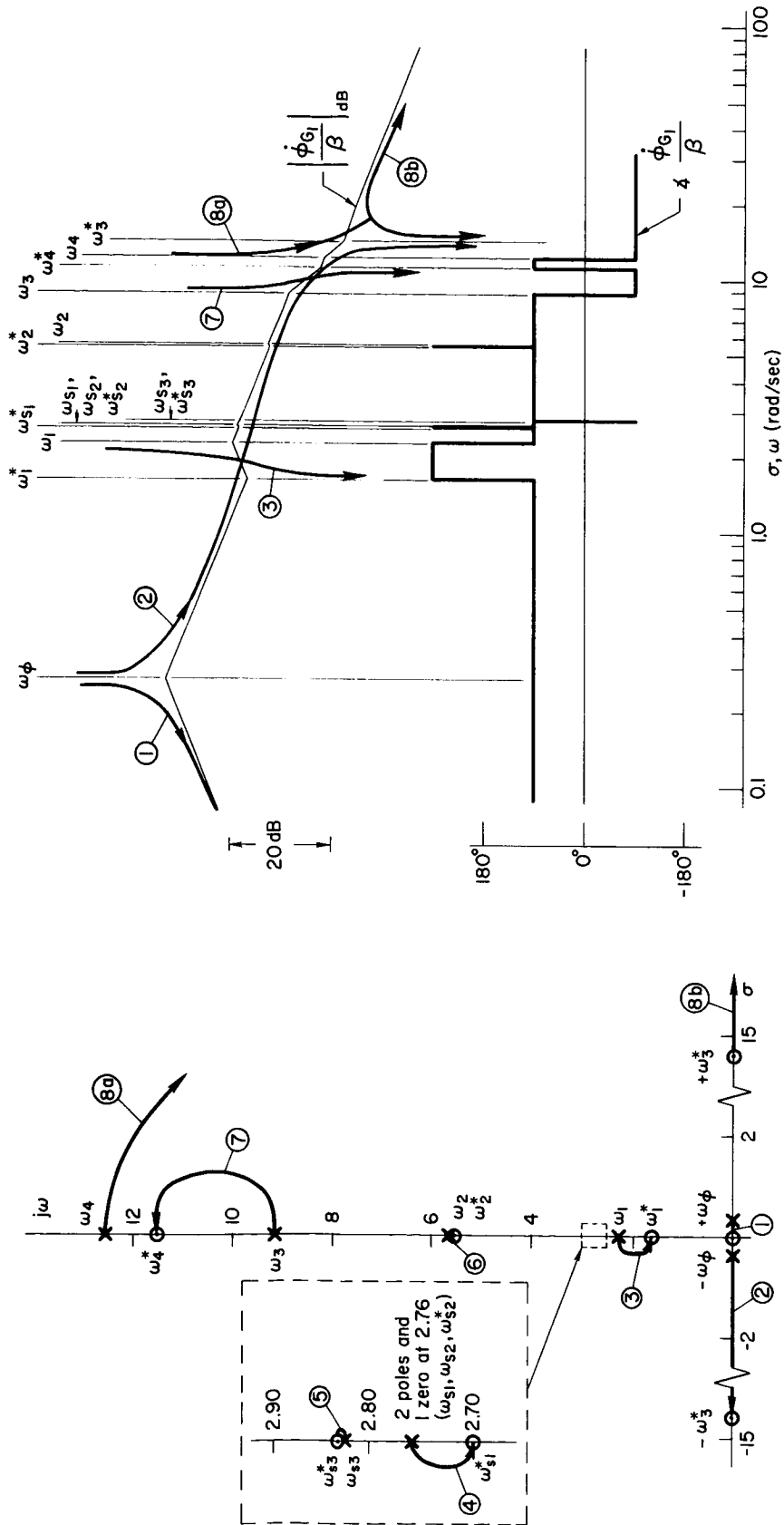
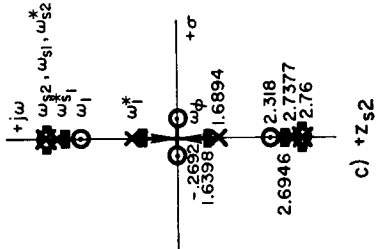
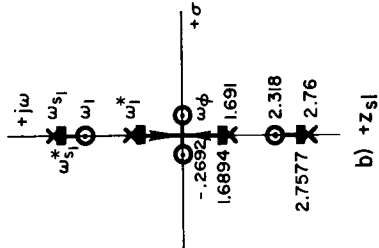


Figure D-2. Survey Plot for Pure Rate Feedback, $t = 80$

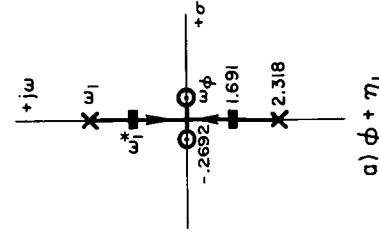
From here on pole - zero pair at 2.76 and net C.L. root ω_{s2}^* not shown



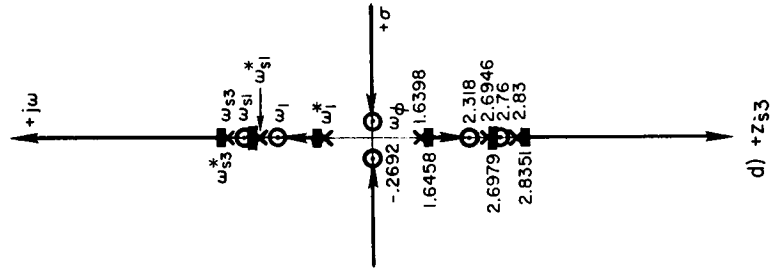
c) $+Z_{s2}$



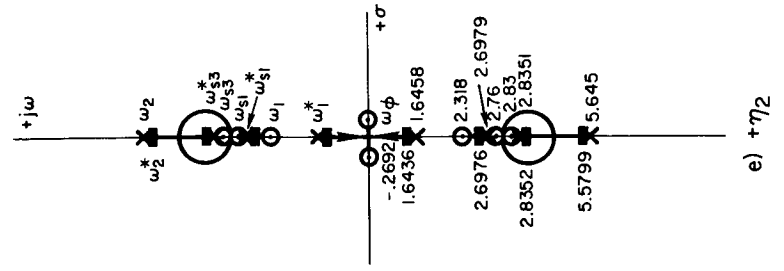
b) $+Z_{s1}$



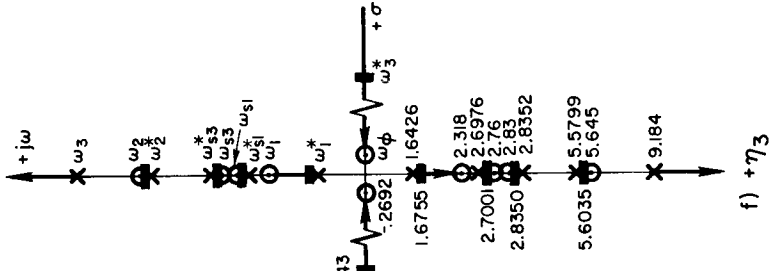
a) $\phi + \eta_1$



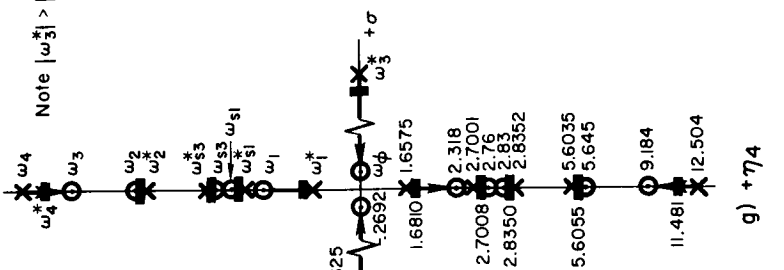
d) $+Z_{s3}$



e) η_2



f) η_3



g) η_4

Figure D-3. Generation of Numerator Roots for Rate Gyro
 $x_G = 46 \cdot 5 \text{ m}, t = 80 \text{ sec}$

technique of Section II. Figure D-3 presents the results. It is to be emphasized that these figures are merely sketches to aid in visualizing the various interactions. The exact values for the zeros have been obtained through a digital factorization program.

Recall that as we include each successively higher frequency mode (i.e., we progress from sketch a to g) the open-loop poles (X) of a given sketch transpose to the succeeding sketch as open-loop zeros (O) while the closed-loop roots (■) transpose as open-loop poles. In each sketch, the closed-loop roots (■) are the sensor numerator roots, and hence the numerator zeros, for the summation of modes considered to that point.

From Fig. D-3 it can be seen that

- the means of accomplishing a decrease in all zeros is to reverse the sign of the third slosh and the third and fourth bending modes. (This would consistently move all numerator roots to lower frequencies as successive modes are included. Admittedly, the effect is small in most instances — which supports the assumption made in deriving the Sawtooth Bode magnitude criteria.)
- the root on the real axis (sketch f) derives from the third bending mode (the third bending mode slope is positive, which moves this root out the $j\omega$ axis to infinity and back in the σ axis).
- the "coupling" between the third slosh and second bending (sketch e) is such that if the "gain" of the second bending were increased to obtain greater separation between ω_2 and ω_2^* (the second bending mode pole/zero pair) this would also move the third slosh zero to a higher frequency which would be undesirable (see locus 5 of Fig. D-2).

From the bending mode slope plots of Fig. A-11 it is apparent that within allowable sensor area No. 1 the desired slope reversal cannot be achieved for bending modes three or four. It would appear advantageous, however, to move the sensor to the most aft location within this instrumentation area ($x_G \doteq 44.5$ meters). This would increase the first bending slope by a small increment which would move the first bending zero (ω_1^*) to a lower frequency. It would also place the sensor a little further aft of the second bending slope node which would provide somewhat greater assurance that this slope would remain negative. It would also increase

the magnitude of the slope by a small increment which would move the second bending zero to a lower frequency but might increase the frequency of the third slosh zero.

In summary, it is apparent that while this aft location for the single sensor may be best, it still leaves much to be desired from the standpoint of affording stabilization and suppression of the nonrigid modes and/or relatively simple feedback shaping.

2. Second Sensor Considerations (Gyro Blending)

It remains, then, to investigate the control that can be achieved over zero locations through the use of an additional rate gyro. The second gyro will be added in instrumentation area No. 4 ($x_G = 88.5m$) since comparison of the various mode slope signs of Fig. A-6 indicates that this location offers the potential of offsetting the undesirable slope signs obtained at the $x_G = 46.5m$ station. Unfortunately this can also be expected to result in some decrease in the favorable effects of the aft gyro alone.

Figure D-4 represents the system with two rate gyros; one at location No. 1 ($x_G = 46.5m$) and one at location No. 4 ($x_G = 88.5m$).

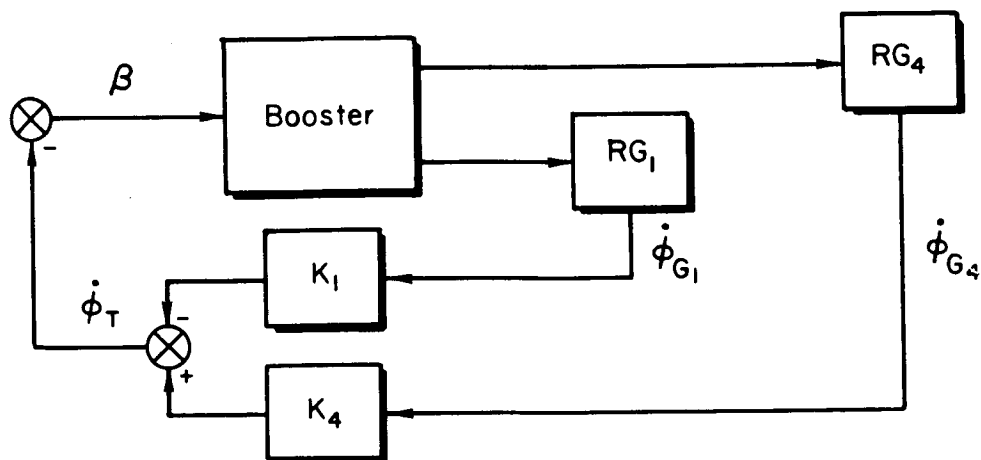


Figure D-4. Block Diagram for Dual Gyro Sensing

The total feedback signal, $\dot{\phi}_T$, is given by:

$$\dot{\phi}_T = K_4 \dot{\phi}_{G4} - K_1 \dot{\phi}_{G1} \quad (D-6)$$

and the transfer function by:

$$\frac{\dot{\phi}_T}{\beta} = \frac{s(K_4 N_{\phi G_4} - K_1 N_{\phi G_1})}{\Delta} = \frac{K_T s N_{\phi T}}{\Delta} \quad (D-7)$$

The roots of $N_{\phi T}$ can be found by writing the equation for the numerator in the following form,

$$\begin{aligned} K_T N_{\phi T} &= K_4 N_{\phi G_4} - K_1 N_{\phi G_1} \\ &= -K_1 N_{\phi G_1} \left\{ 1 - \frac{K_4 N_{\phi G_4}}{K_1 N_{\phi G_1}} \right\} \end{aligned} \quad (D-8)$$

which can again be solved by USAM techniques. Figure D-5 is the USAM plot of the roots as a function of the gyro gain ratio, K_4/K_1 . The corresponding root movements on the root locus and Bode plots are identified by the circled numbers and letters. Note that increasing the gain ratio, K_4/K_1 , moves the numerator roots from the zeros for a single gyro at location No. 1 to the zeros for a single gyro at location No. 4.

Starting with the lowest frequency zeros, Fig. D-5 indicates that as the ratio K_4/K_1 is increased the first bending mode zero, ω_1^* , and the first slosh mode zero, $\omega_{S_1}^*$, move toward each other along the $j\omega$ axis (locus (1a)). As the gain is further increased they break off the $j\omega$ axis and move into the complex plane (locus (1b)) until they again reach the $j\omega$ axis at a point above $\omega_{S_2}^*$ (locus (1c)). Thus the first bending zero is increased while the first slosh zero is decreased and then increased. Increasing these zeros is undesirable.

The third slosh zero, $\omega_{S_3}^*$, is decreased (locus (2)) which is a favorable trend. The second bending zero, ω_2^* , and the fourth bending zero, ω_4^* , move toward each other along locus (3a) until they meet and break off into the complex plane (locus (3b)). If the ratio K_4/K_1 is further increased, this pair move into the real axis and progress along locus (3c). The third bending zeros, ω_3^* , move out the real axis (locus (4a)) until the

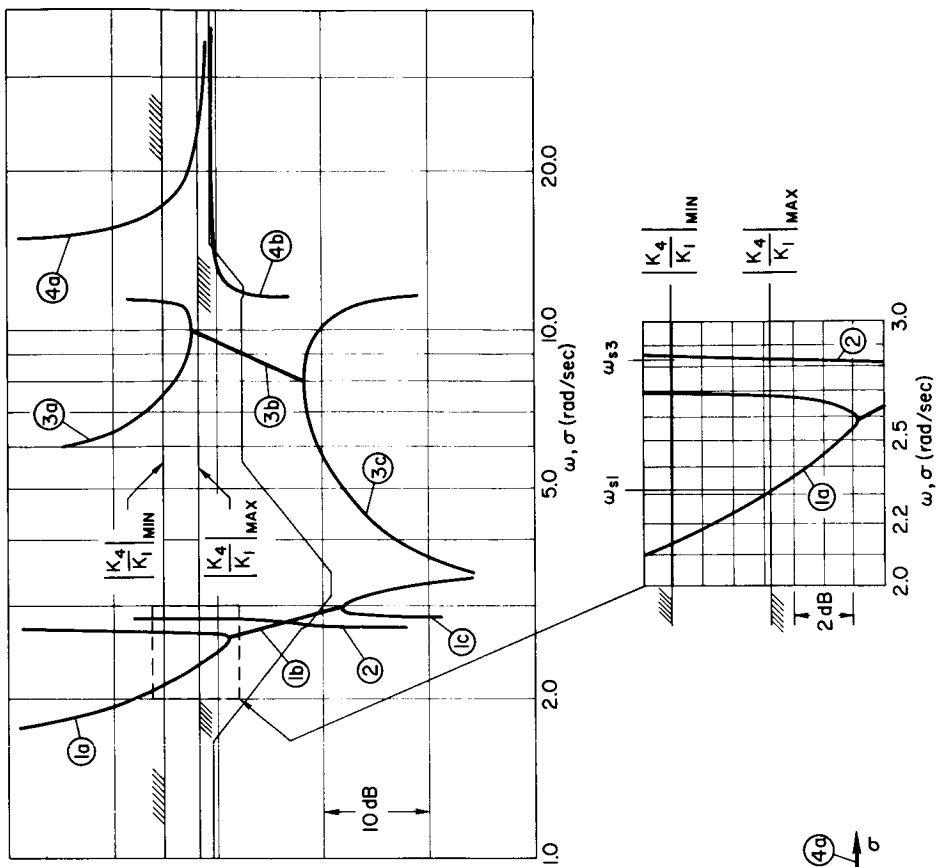


Figure D-5. Numerator Roots of the Summed Gyro Feedback Transfer Function as a Function of Relative Gyro Gain;
 2 Gyros—Location No. 1 ($x = 46.5$ m)
 and Location No. 4 ($x = 88.5$ m)

gain line reaches the high frequency asymptote on the Bode plot. For higher gain (gain line below the high frequency asymptote) this pair return along the $j\omega$ axis (locus (4b) and its mirror image). Thus the movement of ω_3^* and ω_4^* is desirable while that of ω_2^* is not.

From Fig. D-2 it may be seen that we do not want ω_1^* to exceed the value of ω_1 . The maximum allowable frequency for ω_1^* thus sets the maximum allowable relative gyro gain which is again found on the Bode-root locus of Fig. D-5 as the point where branch (1a) reaches the frequency of ω_1 . This is indicated in the figure as $|K_4/K_1| \text{ max.}$ For this value of the gain the second and fourth bending zeros have progressed to a point in the complex plane on locus (3b) while the third bending zeros still remain on the real axis (locus (4a)) at approximately 23 rad/sec. The only beneficial effect is obtained on the third slosh zero (locus (2)) which has moved to a value slightly lower than its associated pole, ω_{S3} . The latter occurs at the gain indicated as $|K_4/K_1| \text{ min.}$

Thus to have any beneficial effect at all, the gain ratio is restricted to the region indicated in the Bode plot of Fig. D-5. Unfortunately, the several unfavorable effects outweigh the single favorable effect.

If we were to reverse the sign of one of the feedbacks, the loci of roots in Fig. D-5 would be on the σ and $j\omega$ axis in the regions of the light lines of the root locus. For example, the root emanating from ω_1^* would now move toward the origin. This would be desirable in that both the first and second bending zeros could be moved to appreciably lower frequencies while all other zeros would remain essentially unchanged (i.e., the values shown in Fig. D-2). Although this would be of some benefit in allowing higher potential of damping these two modes, it would not relieve the necessity for having a relatively sharp phase reversal in the region between the second and third bending modes of Fig. D-2. Furthermore, it is questionable whether the potential increase in damping of these two modes could be realized since the feedback gain may be limited by other considerations.

D. NORMAL ACCELERATION FEEDBACK

Since the feedback of attitude rate (either single or blended sensing) would require complex, and possibly time-varying, shaping, attention was turned to the use of normal acceleration feedback as a possibility of shifting the poles of the flexible modes (stiffening the vehicle) or of damping the modes. This type of feedback has been successfully employed in controlling the rigid and flexible modes of other types of airborne vehicles but is not known to have been employed to control the flexible modes of large launch vehicles.

As a trial case, the maximum q flight condition ($t = 80$ sec) was selected since the simplified transfer function factors most closely approximated the exact factors for this condition. Analysis based on the use of USAM sketches similar to Fig. D-2 quickly indicated a sensor location of $x_A = 46.5\text{m}$ afforded the best pole/zero sequence. It further indicated that the use of lagged normal acceleration feedback might provide sufficient damping of the second and third bending modes to effectively eliminate these modes from concern in closing the attitude rate loop (Fig. D-2). Thus the lagged normal acceleration feedback might reduce considerably the criticalness of shaping in the attitude rate loop. The analysis also indicated the lagged normal acceleration feedback would destabilize the rigid body and fourth bending modes unless appropriate shaping was incorporated in this loop. Overall, the results were sufficiently encouraging to warrant further investigation via the exact transfer functions.

The detailed analysis and synthesis of this feedback is presented in Section III of the report.

APPENDIX E

SYSTEM SYNTHESIS WITH EXACT TRANSFER FUNCTIONS

As a check on the simplified analysis of Appendix D, several competing mechanizations were checked with the exact transfer functions. The competing mechanizations were:

$$\text{System A: } \phi_{120.5} \rightarrow \beta$$

$$\text{System B: } \dot{\phi}_{46.5} + \phi_{120.5} \rightarrow \beta$$

$$\text{System C: } ay_{46.5} + \dot{\phi}_{46.5} \rightarrow \beta$$

Mechanization A was quickly eliminated as impractical because of the several zeros in the right half plane and on the real axis. This mechanization would require several notch filters to eliminate the bending modes from the feedback.

Mechanizations B and C are presented herein. The analysis of these mechanizations supported the preliminary (simplified) analysis and lead to Mechanization D which is discussed in Section III.

A. SYSTEM B

System B employs attitude and attitude rate feedback. Attitude rate is sensed at Station $x = 46.5\text{m}$; attitude is sensed at Station $x = 120.5\text{m}$. Two flight conditions ($t = 80$ and 157 sec) were investigated and are summarized herein. The $t = 0$ sec flight condition was not investigated because the feedback shaping changes required between maximum q ($t = 80$ sec) and burnout ($t = 157$ sec) were considered to be excessive and undesirable.

A summary of the feedback shaping required for each loop is presented in Table E-I. Bode and root locus plots of the closures are presented in Figs. E-1 through E-8. Limiting factors and pertinent considerations are as follows:

$t = 80$ sec The $\dot{\phi}$ loop (Figs. E-1 and E-2) is closed to provide 11 dB gain margin at the second bending mode but with the first sloop essentially on the $j\omega$ axis. Damping of all four bending modes could be increased by increasing $K_{\dot{\phi}}$ if fuel tank baffling were employed to stabilize the sloop. However, a low frequency lead would be

required in the $\dot{\phi}$ loop to improve the damping of the root near 0.5 rad/sec for subsequent closure of the ϕ loop. Such low frequency lead would then create problems with the third and fourth bending modes unless additional lag is introduced to restabilize these modes.

The exact shaping for the ϕ loop was not worked out but would be similar to that shown in Table E-I. Note that Figs. E-3 and E-4 reflect the rate-damped vehicle but do not reflect the ϕ loop shaping suggested. The exact shaping was not worked out since it was obvious from the foregoing plus the $t = 157$ sec analysis that excessive change in shaping would be required with change in flight condition.

$t = 157$ sec On the basis of the given vehicle dynamics, no problems exist at this flight condition (see Figs. E-5-E-8). The feedback shaping is relatively simple and straightforward but considerably different from that required at $t = 80$ sec.

B. SYSTEM C

System C consists of the inner two loops (a_z and $\dot{\phi}$) of the system synthesized in Section III. The difference between the systems lies primarily in mechanizational concept. System C sensing was envisioned to be comprised of an accelerometer and an integrating rate gyro located at Station $x = 46.5m$. Although the feedback gains for System C were somewhat higher than those presented in Section III (System D), the plots of Figs. 15-18, 21-24, and 27 and 28 are representative of this system. The gains were set higher in an attempt (unsuccessful) to obtain adequate static gain for attitude control. However, the static gain at maximum q ($t = 80$ sec) and burnout ($t = 157$ sec) was so low that it would require the introduction of an additional integration to correct. This integration would be detrimental at lift-off ($t = 0$ sec) and would also necessitate the introduction of additional lead at $t = 80$ and 157 sec to stabilize the flexible modes. Since the necessary static gain could be obtained by employing attitude feedback from the forward stable platform, the integrating rate gyro idea was discarded.

TABLE E-I
SUMMARY OF SYSTEM B FEEDBACK SHAPING

FLIGHT CONDITION	FEEDBACK	FIGURES	SHAPING	REASON FOR SHAPING
t = 80 sec	$\dot{\phi}_{46.5}$	E-1	$K_{\phi} \frac{\left(\frac{s}{1.35} + 1\right)}{s \left(\frac{s}{6.7} + 1\right)}$	Lead to phase-stabilize first and second bending modes Integration to improve stability of rigid body to ease requirements on outer loop equalization Lag to phase-stabilize the third and fourth bending modes
		E-2		
t = 157 sec	$\dot{\phi}_{120.5}$		$K_{\phi} \frac{\left(\frac{s}{0.5} + 1\right)^2}{s \left(\frac{s}{3} + 1\right)^2}$	(Note: Exact shaping not worked out) Integration to reduce steady-state error (increase dc gain) Lead to phase-stabilize rigid body Lag to phase- and gain-stabilize flexible modes
		E-5 E-6	$K_{\phi} \frac{\left(\frac{s}{0.1} + 1\right)}{s}$	Integration to tighten rigid-body control Lead to phase-stabilize all modes
t = 157 sec	$\dot{\phi}_{120.5}$	E-7 E-8	$K_{\phi} \frac{\left(\frac{s}{0.05} + 1\right)}{s \left(\frac{s}{1.0} + 1\right)}$	Integration to increase dc gain Lead to stabilize rigid-body mode Lag to phase- and gain-stabilize flexible modes

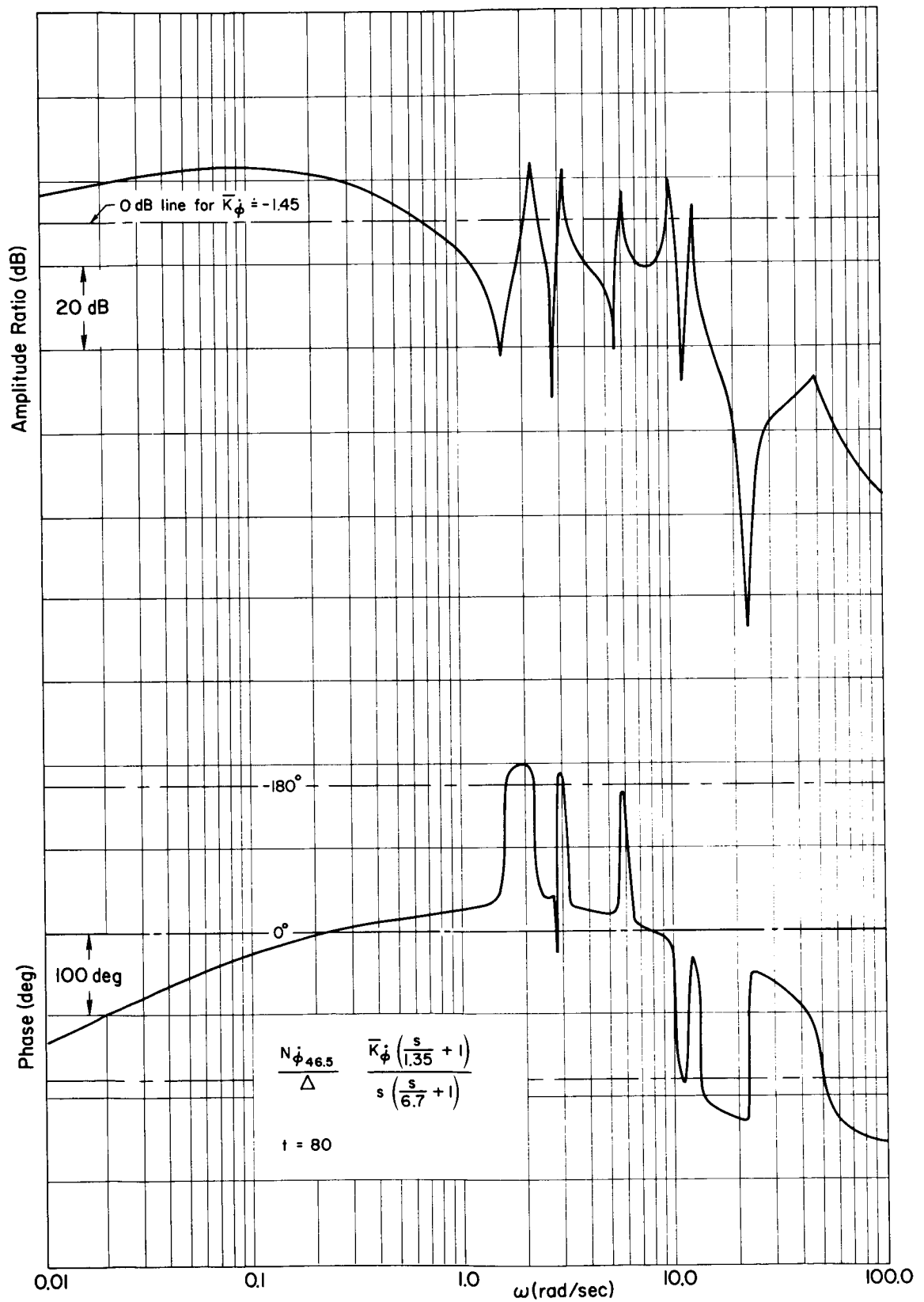


Figure E-1. System B; $t = 80$ sec; $\phi_{46.5}$ Loop Closure

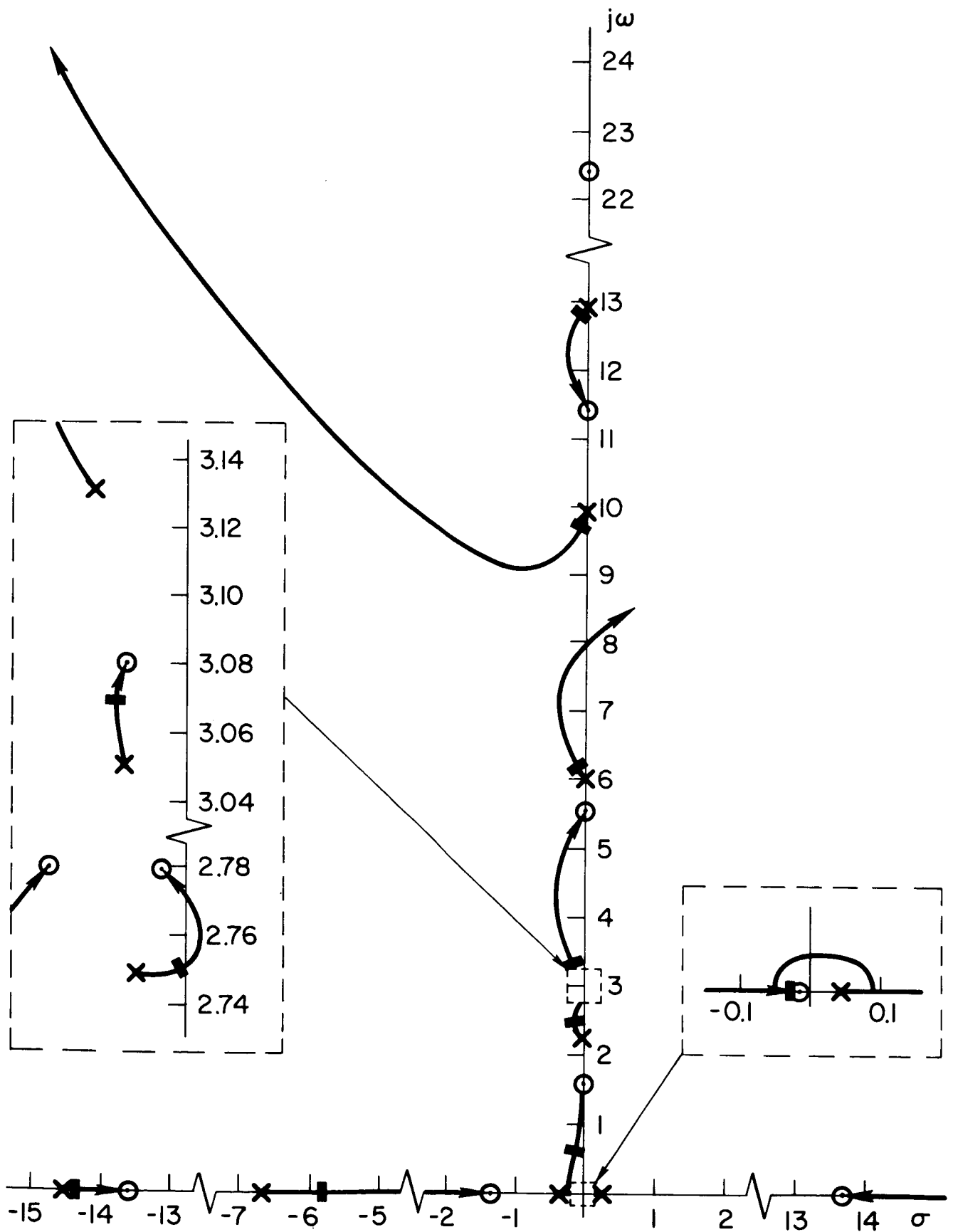


Figure E-2. System B, $t = 80$, $\phi_{46.5}$ Root Locus

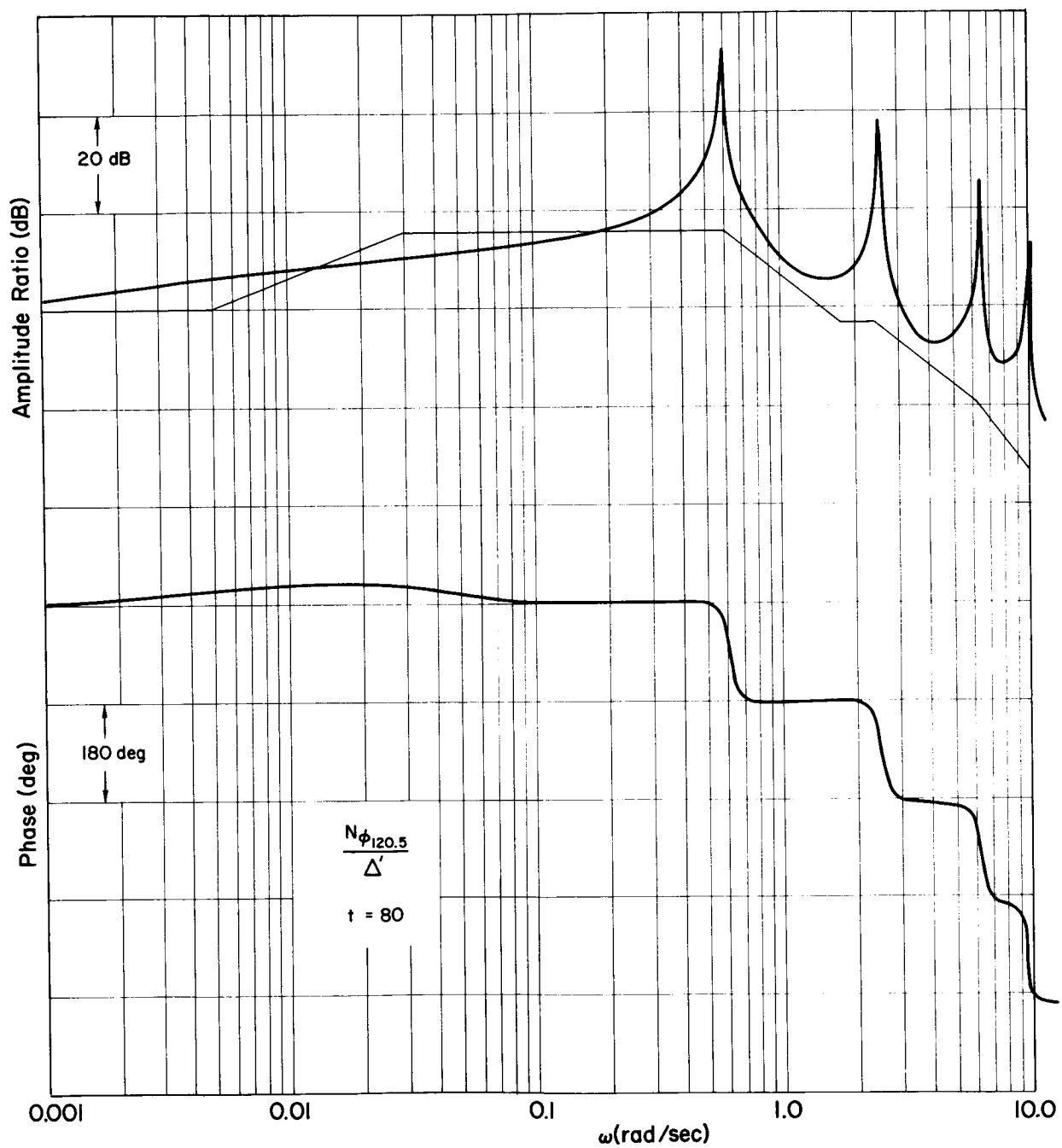


Figure E-3. Effective Vehicle Dynamics for $\phi_{120.5}$ Feedback; $t = 80$ sec

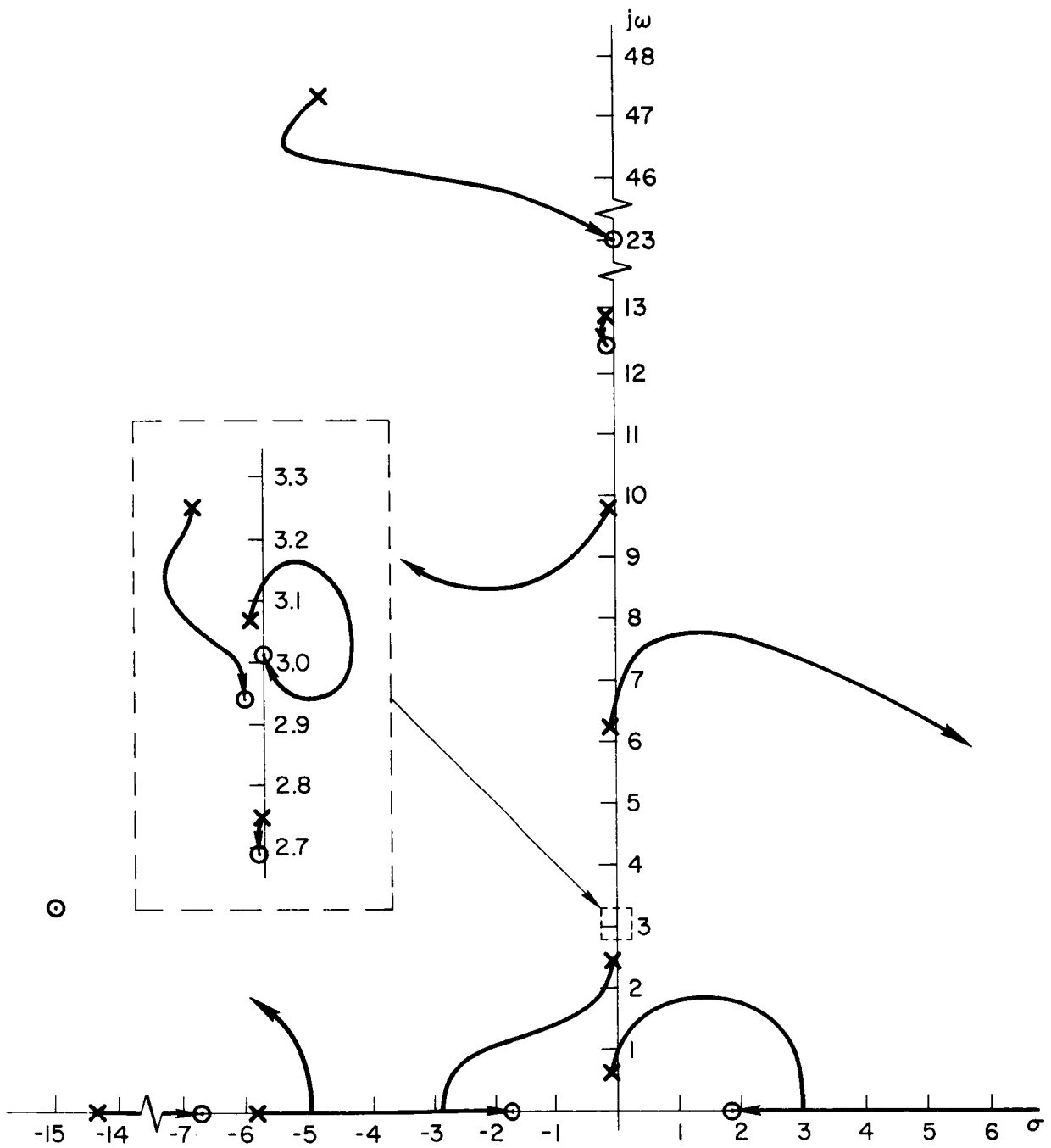


Figure E-4. Root Locus for Unity Feedback; $\phi_{120.5}$; $t = 80$ sec

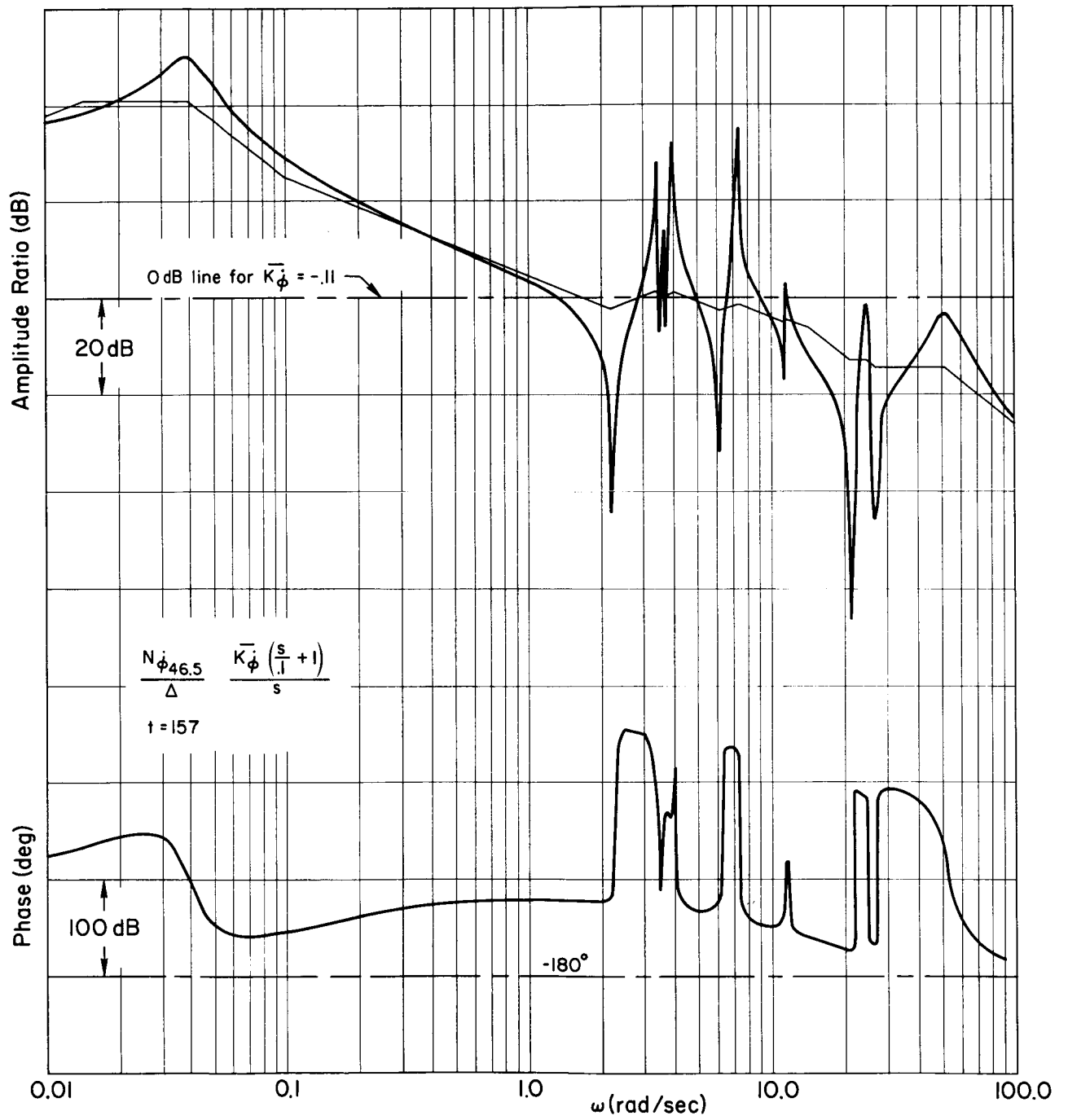


Figure E-5. System B, $t = 157$, $\dot{\phi}_{46.5}$ Loop Closure Bode

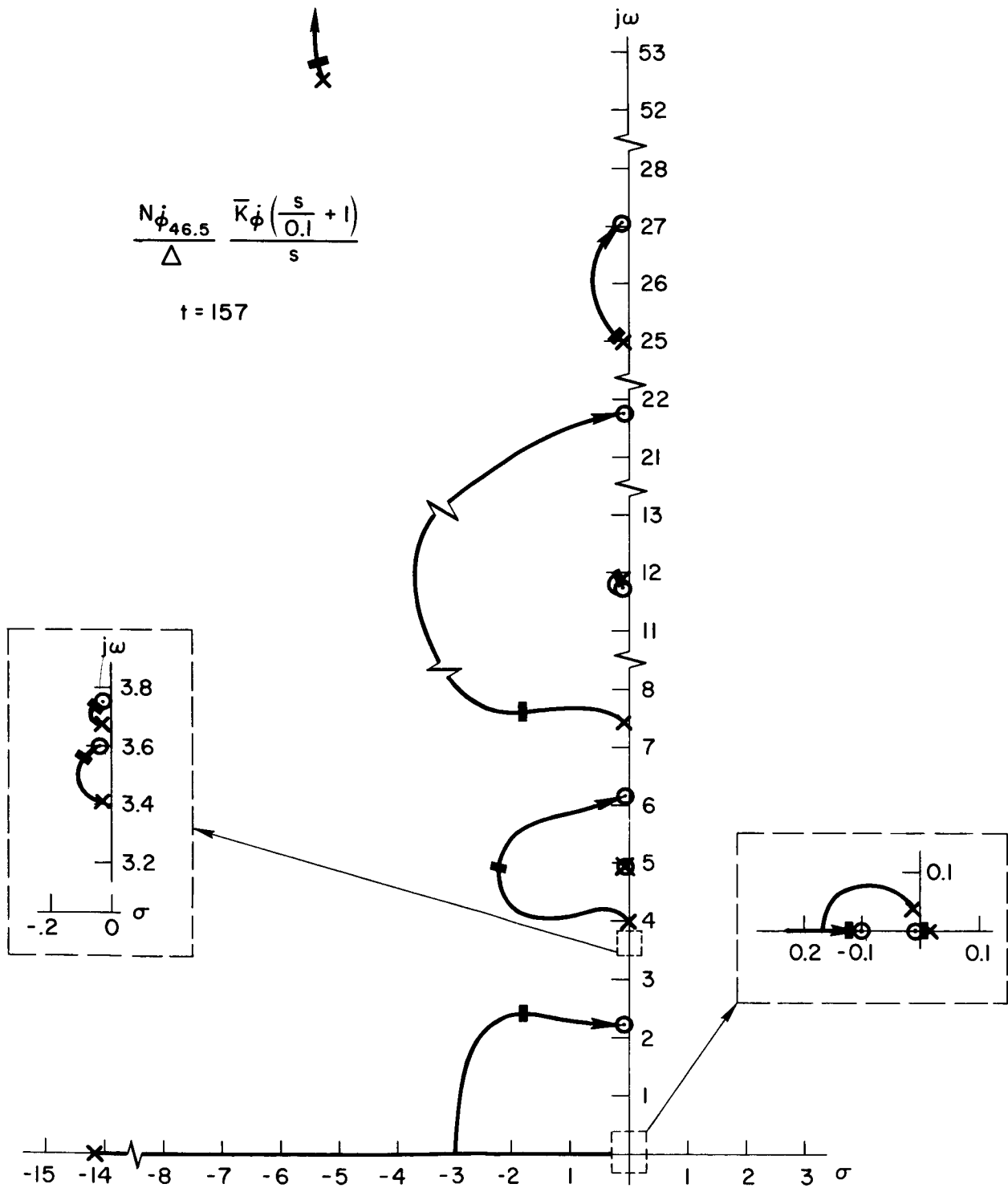


Figure E-6. System B, $t = 157$, $\phi_{46.5}$ Root Locus

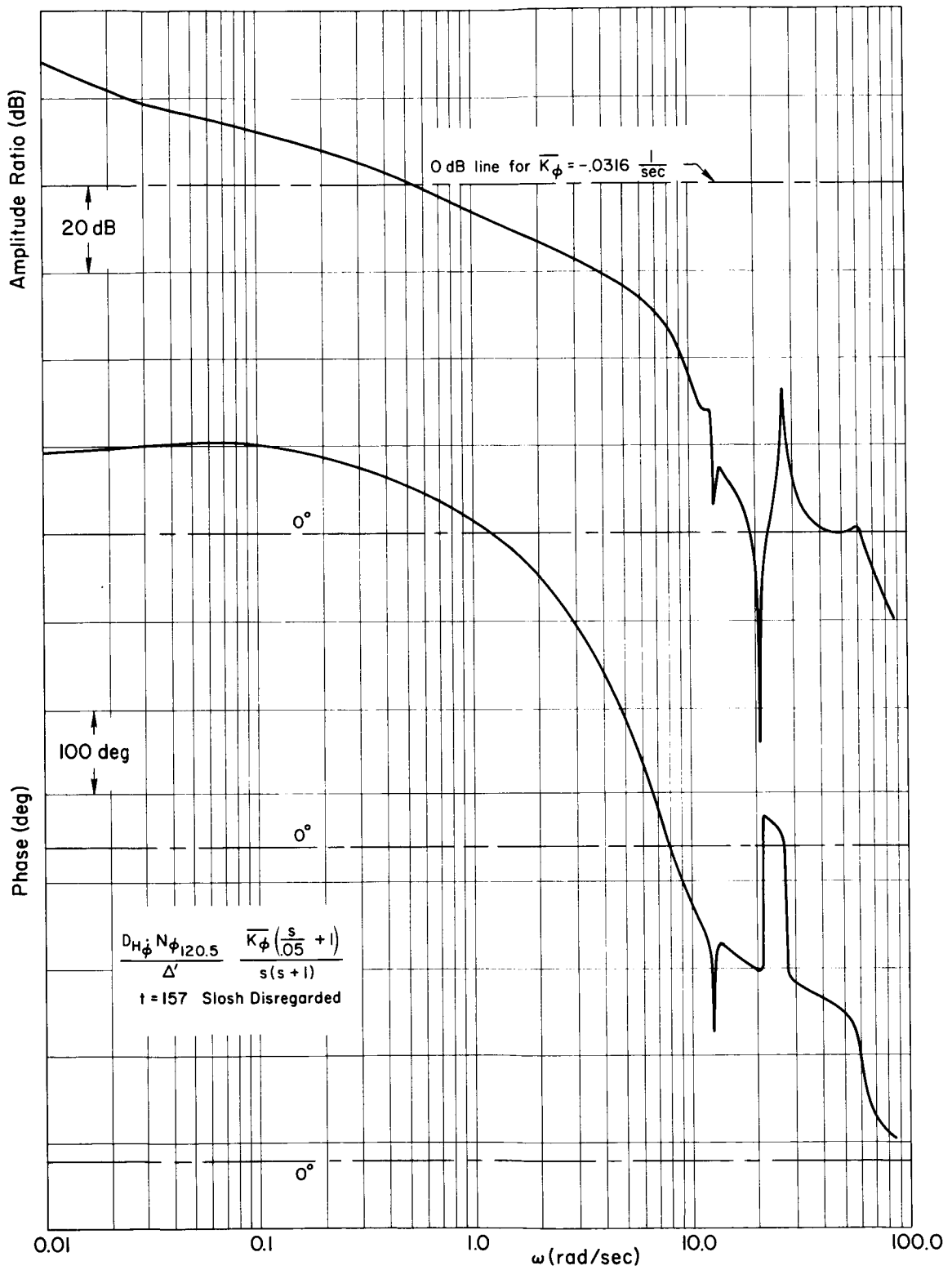


Figure E-7. System B, $t = 157$, $\dot{\phi}_{120.5}$ Loop Closure Bode

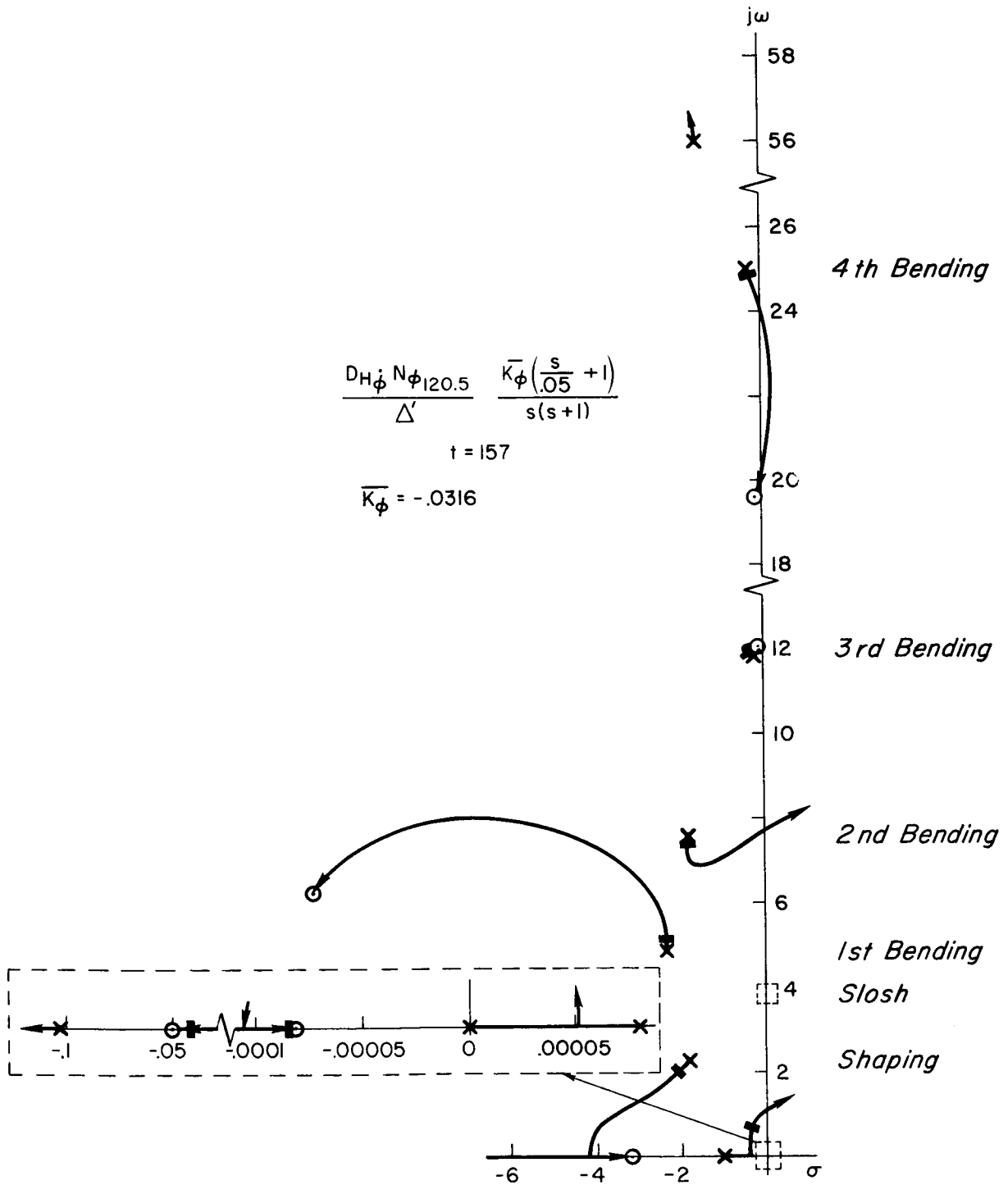


Figure E-8. System B, $t = 157$, $\dot{\phi}_{120.5}$ Root Locus

APPENDIX F

THE USE OF BAFFLES TO DAMP SLOSH MODES

W. A. Johnson

This appendix documents a short investigation of the effectiveness of fuel tank baffles in increasing the damping of slosh modes. The over-all task was performed in four separate steps:

1. Determine a need for increased slosh mode damping (where and how much)
2. Decide what to do to obtain the desired damping.
3. Compute the "new" slosh mode factors that result from carrying out the step 2 decision
4. Determine wave amplitude effects

These will be presented in the following four sections.

A. DETERMINE A NEED FOR SLOSH MODE DAMPING

Expanded scale root locus plots for the System D mechanization are presented in Figs. F-1 - F-4. From Fig. F-1 it can be seen that the accelerometer loop closure at $t = 80$ drives the "middle" slosh mode unstable. Figure F-2 then shows that the subsequent rate gyro loop does not restabilize the unstable middle mode. The "upper" and "lower" slosh modes are seen to remain stable with the two loop closures.

Figures F-3 and F-4 show that at $t = 0$ there is no slosh mode instability. Although the root locus paths cross the $j\omega$ axis, the gain in the accelerometer loop is low enough to keep the closed-loop roots in the left half plane. Figure F-4 then shows that the slosh modes are stable in the rate gyro loop at all gains. It is shown in Section III that there is no instability at $t = 157$.

From these root locus plots it is evident that the only instability problem occurs in the middle slosh mode at the $t = 80$ flight condition. This instability could be avoided if the middle pole and zero were moved to the left (via added damping) by $\Delta\zeta\omega = 0.04$.

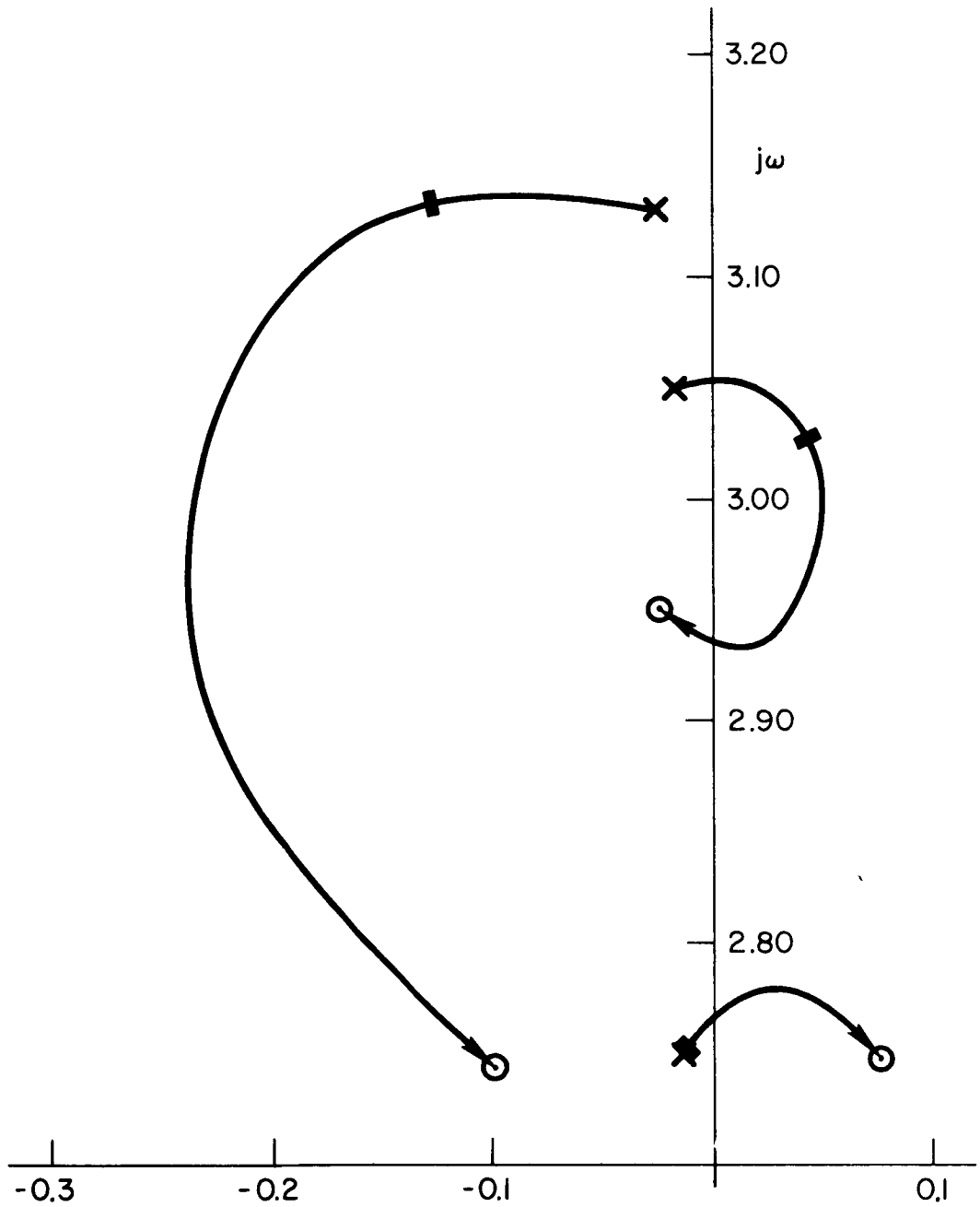


Figure F-1. Root Locus of SLOSH Mode Region for Accelerometer (at 46.5) Loop at $t = 80$

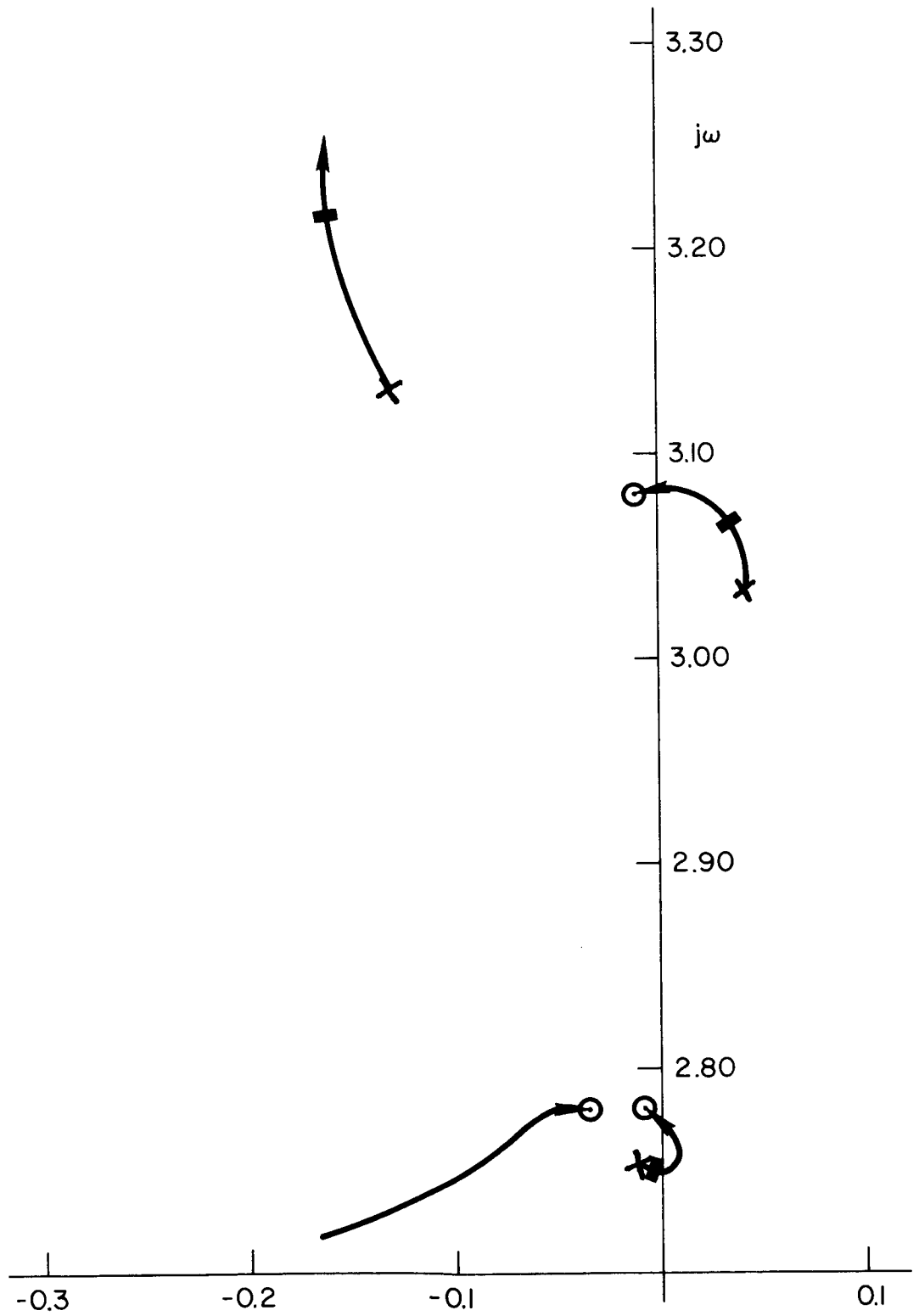


Figure F-2. Root Locus of Slosh Mode Region
for Rate Gyro (at 46.5) Loop at $t = 80$

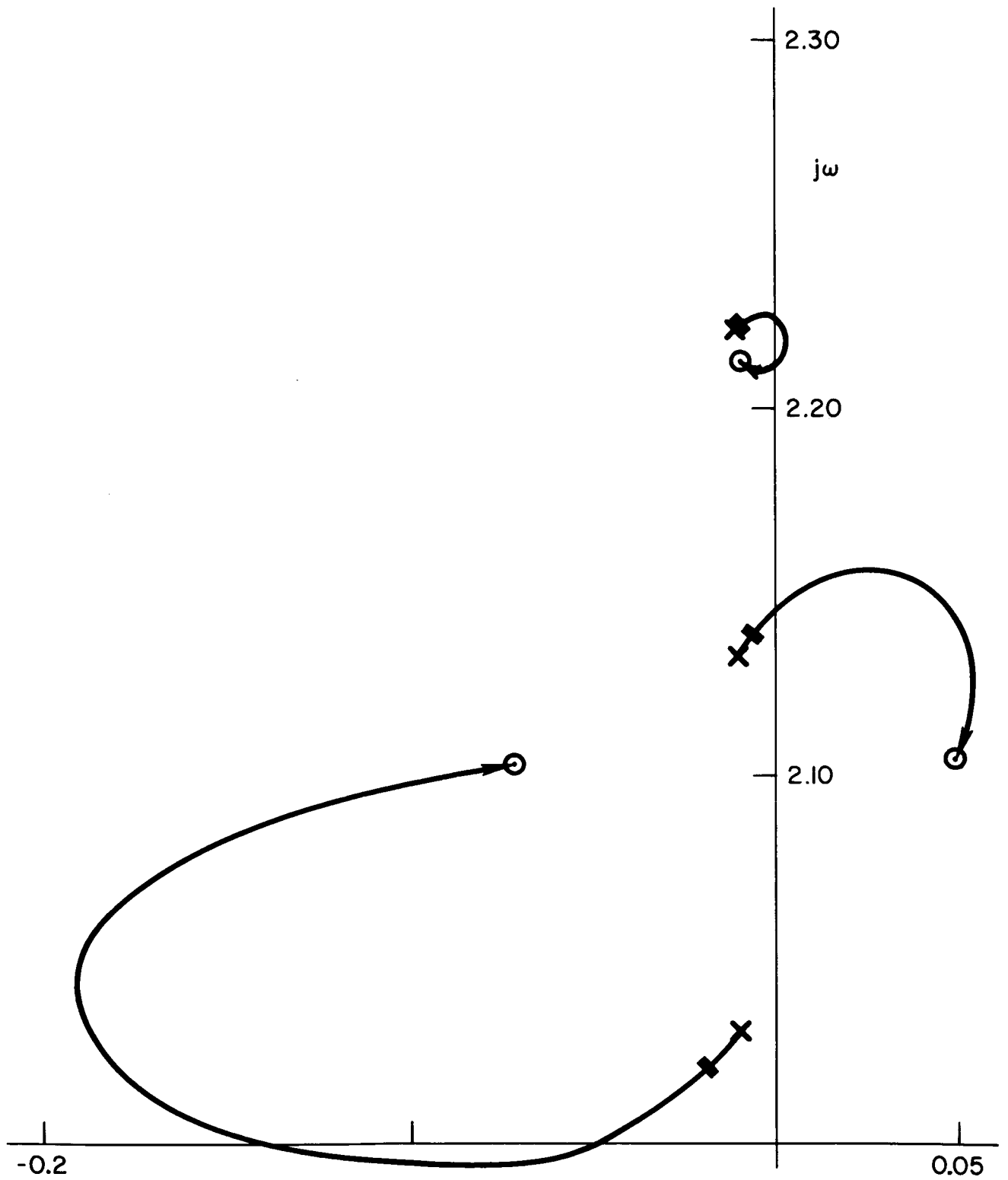


Figure F-3. Root Locus of Slosh Mode Region for Accelerometer (at 46.5) Loop at $t = 0$

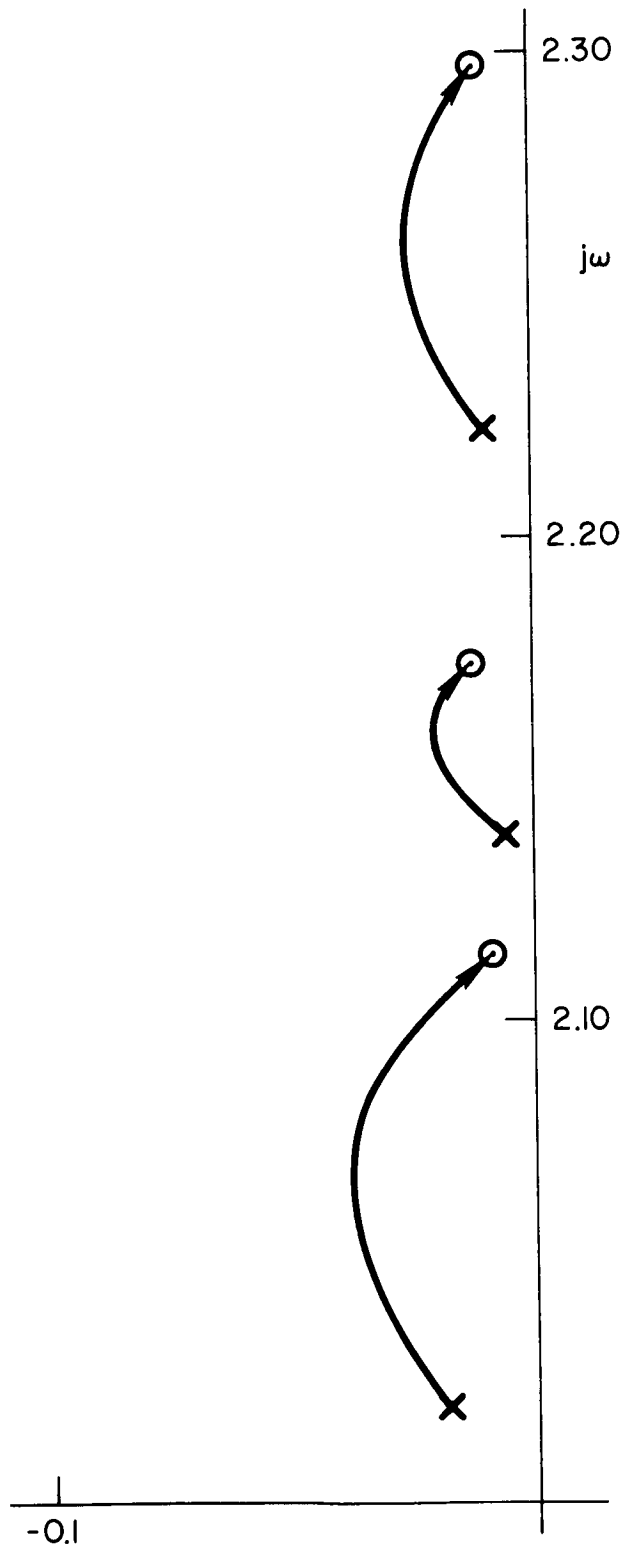


Figure F-4. Root Locus of Slosh Mode Region
for Rate Gyro (at 46.5) Loop at $t = 0$

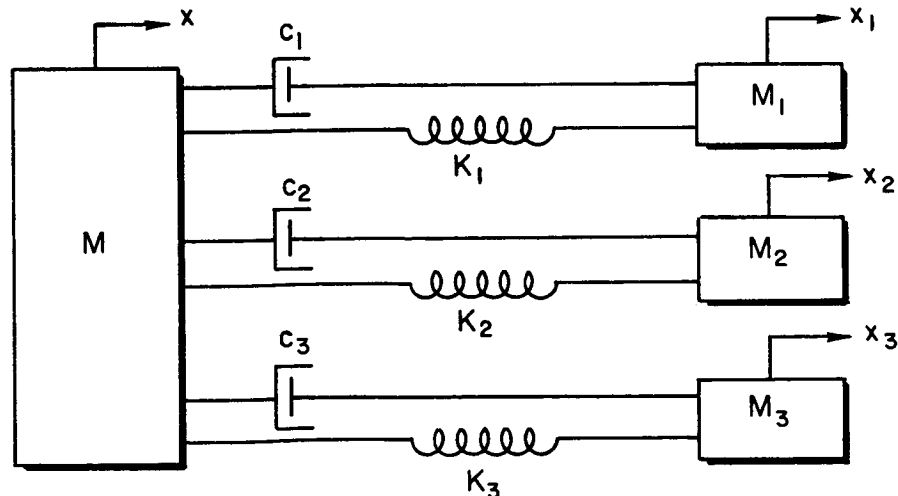
B. DECIDE WHAT TO DO TO OBTAIN THE DESIRED DAMPING

Increased slosh mode damping can be obtained by adding baffles to the tanks. The question is, "What is the minimum amount of baffling that will give $\Delta\zeta\omega = 0.04$ at the middle slosh mode pole and zero?" At a frequency of 3.0, $\Delta(\zeta\omega) = 0.04$ corresponds to a $\Delta\zeta$ value of 0.013. Thus, if a baffle will increase the uncoupled slosh mode damping ratio by 0.025 (Ref. 8 indicates baffling increases ζ from 0.005 to 0.030), it is reasonable to hope that the coupled damping ratio might increase by 0.013 in one of the slosh modes by adding a baffle to only one select tank.

The problem now becomes one of determining which tank to baffle to obtain the most damping in the middle slosh mode pole and zero. For simplicity it will be assumed that if the pole is damped by baffling a single tank, the corresponding zero will also be damped. This narrows the problem to finding out which tank to baffle in order to move the middle slosh mode pole the farthest to the left.

The problem is now stated in the form of a question: "For the mode of interest, in what tank will a baffle give the largest increase in the energy dissipation rate?" In order to answer this question a few pertinent equations must first be obtained. This is done using a simple model of the slosh dynamics.

For Model Vehicle No. 2 a slosh mode analog is given by the following model (Ref. 1), where the left-hand mass represents the rigid-body mass and the three other masses represent the sloshing masses:



The equations of motion for this model are given as

$$\ddot{M}\ddot{X} = -\sum_{i=1}^3 \left[C_i(\dot{X} - \dot{X}_i) + K_i(X - X_i) \right] \quad (\text{F-1})$$

and

$$M_i \ddot{X}_i = -C_i(\dot{X}_i - \dot{X}) - K_i(X_i - X) \quad (\text{F-2})$$

$$i = 1, 2, 3$$

The energy in the slosh mode of interest can be written as

$$E = \frac{1}{2} M \dot{X}^2 + \frac{1}{2} \sum_{i=1}^3 \left[M_i \dot{X}_i^2 + K_i (X_i - X)^2 \right] \quad (\text{F-3})$$

The dissipation rate is then given by

$$\frac{dE}{dt} = M \dot{X} \ddot{X} + \sum_{i=1}^3 \left[M_i \dot{X}_i \ddot{X}_i + K_i (X_i - X) (\dot{X}_i - \dot{X}) \right] \quad (\text{F-4})$$

Equation F-4 can be simplified by substituting in Eqs. F-1 and F-2, giving

$$\frac{dE}{dt} = -\sum_{i=1}^3 C_i (\dot{X}_i - \dot{X})^2 \quad (\text{F-5})$$

which is an obvious result. Now we can proceed to answer the original question. From the uncoupled equations of motion* it is clear that the uncoupled value of damping ($2\zeta_1\omega_1$) for each mode is C_i/M_i . Therefore, putting a baffle in tank j will give a change in C_j/M_j . The original question can thus be reformulated as: "In the mode of interest, what is j so that $|\Delta(dE/dt)|$ is greatest for a given magnitude of $\Delta(C_j/M_j)$?" To answer this, $\Delta(dE/dt)$ must be found. This is easily done using Eq. F-5. For small changes,

$$\Delta\left(\frac{dE}{dt}\right) \doteq \sum_{i=1}^3 \frac{\partial(dE/dt)}{\partial(C_i/M_i)} \Delta\left(\frac{C_i}{M_i}\right) \quad (\text{F-6})$$

*The uncoupled equations of motion can be obtained from Eq. F-2 by setting the displacement and velocity of the left-hand mass equal to zero, i.e., $X = \dot{X} = 0$. This then gives, after rearranging terms, $\ddot{X}_i + (C_i/M_i)\dot{X}_i + (K_i/M_i)X_i = 0$.

Therefore, using Eq. F-5,

$$\Delta\left(\frac{dE}{dt}\right) = -\sum_{i=1}^3 \left[M_i (\dot{X}_i - \dot{X})^2 \right] \Delta\left(\frac{C_i}{M_i}\right) \quad (F-7)$$

From Eq. F-7 it is seen that for only one nonzero $\Delta(C_i/M_i)$ the maximum value of $|\Delta(dE/dt)|$ is obtained by choosing i such that $M_i(\dot{X}_i - \dot{X})^2 \equiv Q_i$ is a maximum. Although this is the answer to the original question, it is not in a form that is readily useful because it involves velocities. It is therefore necessary to find an equivalent expression involving displacements. This is done as follows.

Due to the low damping, the motions of each of the masses is assumed to be essentially sinusoidal. Further, each mass is essentially either in phase or 180 deg out of phase with every other mass. As a result, the displacements of the masses can be written as

$$X = X_{\max} \sin \omega t \quad (F-8)$$

and

$$X_i = X_{i\max} \sin (\omega t + \phi_i) \quad (F-9)$$

where $\phi_i = \begin{cases} 0 \text{ deg if slosh mass is in phase} \\ \text{with rigid-body motion} \\ 180 \text{ deg if slosh mass is out of phase} \\ \text{with rigid-body motion} \end{cases}$

From Eqs. F-8 and F-9 the velocities are found to be

$$\dot{X} = \omega X_{\max} \cos \omega t \quad (F-10)$$

and

$$\dot{X}_i = \omega X_{i\max} \cos (\omega t + \phi_i) \quad (F-11)$$

Substituting these velocity equations into the expression to be maximized gives

$$Q_i = \omega^2 M_i \left[X_{i\max} \cos (\omega t + \phi_i) - X_{\max} \cos \omega t \right]^2 \quad (F-12)$$

Because the ω^2 does not affect the maximization, it will be disregarded. Also, the cosine functions can be changed to sine functions without affecting the maximum. But when this is done the terms within the square

brackets are recognized to be X_i and X . That is, Eq. F-12 becomes

$$Q_i = M_i(X_i - X)^2 \quad (F-13)$$

Equation F-13 gives a much more useful form of the expression to be maximized than did the earlier one involving velocities. Because only relative magnitudes of the displacements are required for a comparison (i.e., the scale factors is unimportant), the modal response ratios for the mode of interest can be used. As a parenthetic comment before giving an example, it is noted that the stated criterion leads to baffling the tank with the greatest "sloshing" energy (because $X_i - X$ is the "sloshing" within the tank).

As an example, the criterion will be applied to the second slosh mode at the $t = 80$ flight condition for Model Vehicle No. 2. The pertinent masses and modal response ratios are given in Table F-I:

TABLE F-I
NUMERICAL VALUES FOR MODEL VEHICLE NO. 2
SECOND SLOSH MODE AT $t = 80$ (REF. 1)

	LOWER TANK	MIDDLE TANK	UPPER TANK
M_i	11,612	18,399	11,173
$X_i - X$	-21.8	-13.4	-5.33

From these numbers and Eq. F-13 it is found that

$$\begin{aligned} Q_1 &= 5.52 \times 10^6 \\ Q_2 &= 3.30 \times 10^6 \\ Q_3 &= 0.317 \times 10^6 \end{aligned} \quad (F-14)$$

Because Q_1 is larger than either Q_2 or Q_3 , it is concluded that baffling the lower tank will increase the damping in the second slosh mode more than will a baffle in either of the other tanks. However, it will be noted that baffling the second tank does almost as much good as does baffling the first tank. Thus, if baffling one tank does not provide

sufficient damping of this mode, then the second tank should be baffled also. The third tank has relatively small contribution (i.e., less than 10 percent) and baffling here would be of little benefit.

C. COMPUTE THE NEW SLOSH MODE FACTORS THAT RESULT FROM BAFFLING THE LOWER TANK AT $t = 80$

For this computation the steps are straightforward, but the manipulations are quite laborious. Therefore, only a list of the steps taken will be given, along with the results.

Step 1 Rather than going back to the eleven-by-eleven matrix, an approximation (Ref. 1) was made in which only the two rigid-body equations, the three slosh mass equations, and the first bending mode equation were used. Further, simplifications were made in the elements of the resulting six-by-six matrix (so that the approximate factors from the six-by-six matrix are valid only in the frequency region of the slosh modes).

Step 2 The six-by-six matrix was used to obtain six-by-six determinants for the denominator and necessary numerators. These were easily reduced to four-by-four determinants by adding and subtracting rows, etc.

Step 3 The various four-by-four determinants were expanded to give the denominator and numerators for ϕ , η_1 , η_2 , etc. Then the polynomials were added appropriately to give the desired numerator sensor polynomial. The factors of the sensor polynomial and the denominator could then be used to evaluate the effects of adding baffling to the lower tank.

Step 4 The evaluation was carried out as follows. First, the above process was carried out with the numerical values appropriate for the missile without baffles. Then the process was repeated with numerical values appropriate for the situation with baffles in the lower tank. The changes in the pole and zero locations were noted. It is assumed that although the approximate factors for the denominator and numerators were not as accurate as would be desired, the changes in damping that were noted should nevertheless be indicative of the effects of adding baffling to the lower tank.

The results of the above procedure are presented in Table F-II. The approximate slosh mode factors (with and without baffles in the lower tank) are given for each individual numerator as well as for the accelerometer numerator and the denominator. Figure F-5 shows the approximate accelerometer poles and zeros (with and without baffles) superimposed on Fig. F-1. Again it is noted that although the pole and zero accuracy is not as good as might be desired, it is felt that the shifts in the pole

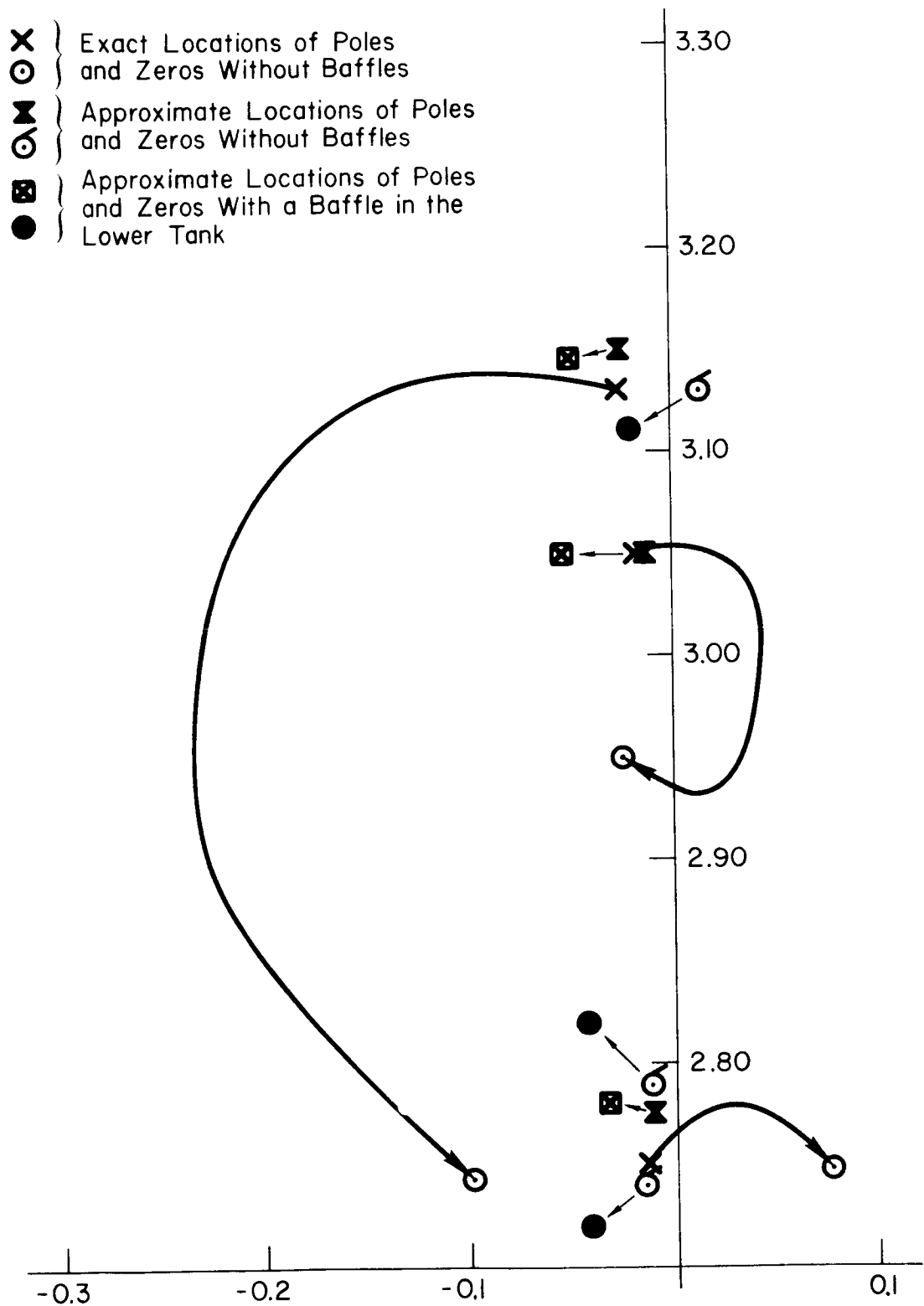


Figure F-5. Effect of Lower Tank Baffling on the Simplified Pole/Zero Locations; $t = 80$

TABLE F-II
SUMMARY OF RESULTS

	ζ_{s1}	ω_{s1}	ζ_{s2}	ω_{s2}	ζ_{s3}	ω_{s3}	
N_z	Without baffles	0.0148	2.765	-0.0045	2.764	0.0089	3.0271
	Baffles in lower tank	0.0335	2.758	0.0051	2.771	0.0056	3.0269
	$\Delta\zeta$	0.0187		0.0096		-0.0033	
N_ϕ	Without baffles	-0.0066	2.761	0.0161	2.762	0.0067	3.083
	Baffles in lower tank	0.0195	2.745	0.0152	2.785	0.0069	3.075
	$\Delta\zeta$	0.0261		-0.0009		0.0002	
N_{η_1}	Without baffles	0.0050	2.780	0.0050	2.793	0.0055	3.054
	Baffles in lower tank	0.0286	2.771	0.0044	2.804	0.0078	3.051
	$\Delta\zeta$	0.0236		-0.0006		0.0023	
N_{η_2}	Without baffles	0.0050	2.765	0.0078	2.975	0.0041	3.032
	Baffles in lower tank	0.0235	2.770	0.0122	2.971	0.0065	3.031
	$\Delta\zeta$	0.0185		0.0044		0.0024	
N_{η_3}	Without baffles	0.0050	2.769	0.0054	3.051	0.0087	3.1923
	Baffles in lower tank	0.0232	2.773	0.0099	3.049	0.0114	3.1906
	$\Delta\zeta$	0.0182		0.0045		0.0027	
N_{η_4}	Without baffles	0.0050	2.7627	-0.0197	2.973	0.0303	2.973
	Baffles in lower tank	0.0239	2.7651	-0.0182	2.959	0.0355	2.984
	$\Delta\zeta$	0.0189		0.0015		0.0052	
N_{a_z}	Without baffles	0.0055	2.74	0.0043	2.79	-0.0035	3.131
	Baffles in lower tank	0.0149	2.72	0.0147	2.82	0.0069	3.116
	$\Delta\zeta$	0.0094		0.0104		0.0104	
Δ	Without baffles	0.0050	2.776	0.0055	3.046	0.0086	3.153
	Baffles in lower tank	0.0113	2.780	0.0172	3.050	0.0155	3.145
	$\Delta\zeta$	0.0063		0.0117		0.0069	

and zero locations due to adding baffles are indicative of the added damping to be expected from adding baffles to the lower tank.

It is pointed out that the results show that the damping ratio in each of the three accelerometer zeros increased by about 0.010, whereas the damping ratio in the poles increased by about 0.0065 for the first and third slosh modes and by about 0.012 in the second (or middle) slosh mode. It was previously determined that an increase in damping ratio of about 0.013 was required to stabilize the middle slosh mode. Therefore, it appears that baffling the lower tank only may not add sufficient damping to stabilize this mode. In this event, the middle tank should also be baffled. However, final judgment must be delayed until the subsequent rate gyro loop closure is made. But, this is all only of academic interest at this point anyway, because the various assumptions and approximations that were made in simplifying the manipulators preclude basing a decision on small margins (stable or unstable). That is, the margin of stability or instability from this investigation appears to be within the magnitude of expected inaccuracies due to the simplifying assumptions. Therefore, the results will be summed up by stating that it appears feasible to stabilize the slosh modes with baffles in either the lower tank or the lower two tanks. But a more exact analysis must be used to arrive at a definite conclusion.

D. WAVE AMPLITUDE EFFECTS

The system stability analysis was based on the conventional linear model for slosh mode damping. As such, the damping is assumed to be constant and dependent on wall-wiping (unbaffled tank) and mixing (baffled tank). The damping is, however, strongly affected by the wave amplitude—at least in baffled tanks. This is shown in two versions of Miles' formula (Ref. 14) for the damping ratio as a function of baffle configuration and fluid slosh amplitude. Miles' experimentally verified formulas state that the damping ratio of the fluid mode increases with the wave amplitude, viz,

$$\begin{aligned} \zeta &= K_1 \sqrt{\eta_1} \\ \text{or } \zeta &= K_2 \eta_1 \end{aligned} \tag{F-15}$$

depending on the assumptions made. (η_1 is the wave amplitude; the constants K_1 and K_2 depend on tank diameter, baffle size, depth of the baffle below the liquid surface, etc.) The form of the expression is not as important here as is the fact that damping is related to wave amplitude (some slosh amplitude — limit cycle — must exist in order to achieve the damping increment given in the Model Vehicle No. 2 data).

A third source of damping is the control force applied by the gimbaled engine. This damping can be either positive or negative and depends on the relative phasing between the slosh mode and the closed-loop engine motion. The total slosh damping can thus be expressed (assuming the Miles' linear expression)

$$\begin{aligned}\zeta_T &= \zeta_w + \zeta + \Delta\zeta_{CL} \\ &= K\eta_1 + (\zeta_w + \zeta_{CL})\end{aligned}\tag{F-16}$$

This may be plotted as shown in the following sketch.

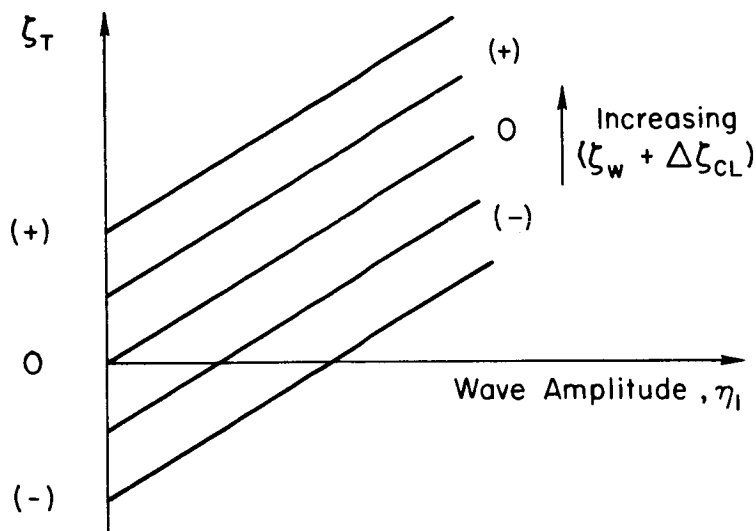


Figure F-6. Slosh Damping as a Function of Wave Amplitude

Obviously, if $(\zeta_w + \Delta\zeta_{CL})$ is positive a limit cycle need not exist and baffling, if employed, will increase the damping of any wave motion which may develop through disturbance inputs. If, however, $(\zeta_w + \Delta\zeta_{CL})$ is negative, a limit cycle will develop with a wave amplitude dependent on the value of $(\zeta_w + \Delta\zeta_{CL})$ and the tank baffle configuration.

The damping due to closed-loop phasing can be determined by inspection of a root locus plot of the slosh modes. For example, if the closed-loop root is to the right of its open-loop position, then the damping due to phasing is negative (see Fig. F-7).

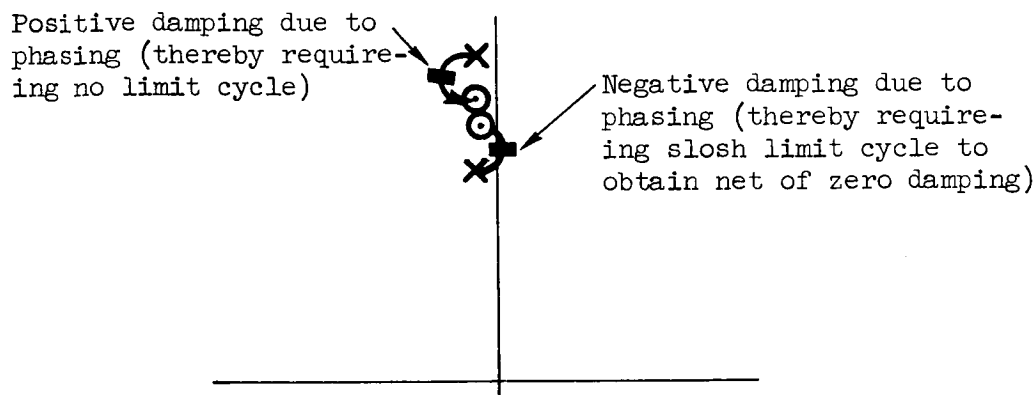


Figure F-7. Determination of Damping Due to Phasing from Root Locus

The amount of negative damping due to phasing determines the magnitude of the limit cycle to be expected, as indicated in Fig. F-6.

It is clear from the assumption of a damping ratio that increases with slosh amplitude that a slosh divergence is not possible. The amplitude will increase until just enough energy is dissipated to result in a limit cycle. However, the amplitude of slosh required to give the necessary damping ratio may exceed the limiting value as regards tank structural integrity or the limits in Eq. F-15.

The method of calculating the damping increase due to baffles indicated in Model Vehicle No. 2 is unknown (as well as the allowable wave amplitude which must be involved). Therefore it is still not possible to determine whether the single-tank baffling previously reported is or is not adequate. In any event, the actual determination of baffle location is beyond the scope of the current work and was attempted only as an interesting application of the results of the vehicle dynamics study. It does appear, though, that the physical insight of slosh mode response afforded by the vehicle dynamics report (Ref. 1) plus information on the allowable slosh wave amplitude (or forces) and the preferred equation relating fluid damping and wave amplitude will allow the control system analyst to assist the structural analyst in maximizing the beneficial effects of tank baffling.